quarterly

ISSN 1898-4088 (printed)
ISSN 2300-5319 (online)

2017
volume 11 no. 4

acta mechanica et automatica

CONTENTS

DE GRUYTER
OPEN

DOI 10.1515/ama-2017-0039

acta mechanica et automatica, vol.11 no.4 (2017)

EXPERIMENTAL INVESTIGATION OF AN AUTOMOTIVE MAGNETORHEOLOGICAL SHOCK ABSORBER

Łukasz JASTRZĘBSKI*, Bogdan SAPIŃSKI*

*Mechanical Engineering and Robotics, Department of Process Control, AGH University of Science and Technology, al. Mickiewicza 30, 30-059 Kraków, Poland

lukasz.jastrzebski83@gmail.com, deep@agh.edu.pl

received 24 May 2016, revised 2 October 2017, accepted 6 October 2017

Abstract: The study summarises the experimental examination of an automotive magnetorheological (MR) shock absorber under electrical and mechanical excitations, investigates its current and force responses and the energy dissipation in the system. The aim of experiments was to acquire measurement data that allows in next step of the research program to engineer an energy harvesting device for the absorber. The work covers basic technical data of the absorber, description of the experimental set-up, scenario of testing program and test results of the device. Of particular importance is the influence the operating current, piston displacement amplitude and piston velocity have on the absorber's response.

Key words: MR Shock Absorber, Vibration, Current Response, Force Response, Dissipated Energy

1. INTRODUCTION

The property of magnetorheological (MR) fluids manifesting itself by changes in the material's apparent viscosity when exposed to a magnetic field has made them attractive for use in many applications, including the automotive industry (Choi and Sung, 2008; Choi and Han, 2012; El-Kafafy et al., 2012; Sung and Choi, 2009). One of the most spectacular application in this field was the semi-active vehicle suspension system that utilized MR dampers for real-time control of the motion of a vehicle. Presently MR dampers are installed in various types of vehicles: passenger cars and sports vehicles, to improve the ride comfort by controlling undesired vibrations. The principal design parameters of MR dampers intended for vehicle suspension application are the magnetic gap in which MR fluid flows between upper and lower chambers, the radius of the piston, and bobbin structures involving the coil turns. By choosing appropriate values of these principal design parameters, successful vibration control can be implemented. Extensive research efforts have brought major headway in response time improvements, higher dynamic range, effective control and better response at low body velocities of MR dampers (Gołdasz and Dzierżek, 2016; Koo et al., 2006; Sapiński and Rosół, 2007; Strecker et al., 2015 a, b, c; Wu et al., 2011).

The aspect of MR damper applications that has received a great deal of attention recently is energy harvesting (Sapiński, 2014; Wang and Bai, 2013; Xinchun et al., 2015) whereby an MR damper in a typical confguration is driven by energy harvested from a vehicle while in motion. The mechanical energy that otherwise would be unused and lost through heat is converted into electricity and used for monitoring of an associated MR damper output.

The object of this study is the Magnetic Ride absorber used in cars of series Audi TT Quatro. The aim of the work is to evaluate the absorber's performance through experiments. The current responses of the device are determined when the amplifier is operated in the voltage and current mode, the force responses are determined when the device is subjected to a particular excitation from a range of displacements inputs. The obtained experimental results allow a special harvester to be designed such that the tested absorber can be energized (controlled) when implemented in a laboratory model of an automotive semi-active suspension system with energy harvesting capability

2. SPECIFICATION OF THE SHOCK ABSORBER

The structure of the investigated MR shock absorber is shown in Fig. 1. The device has a typical configuration of mono-tube flow-mode damper with an annular gap (Gołdasz and Sapiński, 2015). Geometrical parameters of the absorber are: piston stroke 178 mm, outer diameter of the cylinder 50 mm, the length with the piston in compression position 381 mm, the length with the piston in rebound position 559 mm. The cylinder is filled with 277 cm^3 of MR fluid. The shock absorber comprises an accumulator 65 cm^3 in volume, filled with nitrogen. The maximal current in the control coil should not exceed 5A. The device ought to be operated in the temperatures range (-30, 100) °C. The absorber's force response in the stroke center position is 335 N.

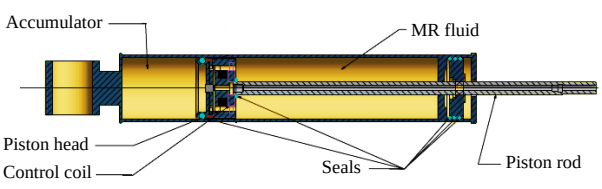

Fig. 1. Schematic diagram of the shock absorber

DOI 10.1515/ama-2017-0039

3. TESTING PROGRAM

The main purpose was to determine the current response in the absorber's control coil circuit to the applied step voltage excitations and the force response under the triangular and sine inputs (piston displacements).

Current responses were registered in the measurement system shown schematically in Fig. 2. The system comprises a power supply, an amplifier, a AD/DA board installed in a PC. To ensure the correct operation of the amplifier (Sapiński et al., 2012), it needs a symmetrical DC voltage supply ± 12 V. The amplifier can operate either in voltage mode or current mode (in this case with an integrated PID controller). The amplifier ensures that the maximal current supplying the coil should not exceed 7 A (the non-inverting operational amplifier OPA549 was used here). Integrated internal circuits in the amplifier, based on AD629, AD8622 operational amplifiers and 10 mΩ resistor, permit the measurements of voltage u and current i. Registered signals are converted into voltage signals in the range ± 10 V. Input voltage or current in an amplifier is controlled via an analogue input to which voltage u_c is supplied, in the range ± 10 V. The AD/DA board type RT-DAC 4 PCI [17] interacting with MATLAB/Simulink is used for generation of command signal u_c and for voltage and current measurements.

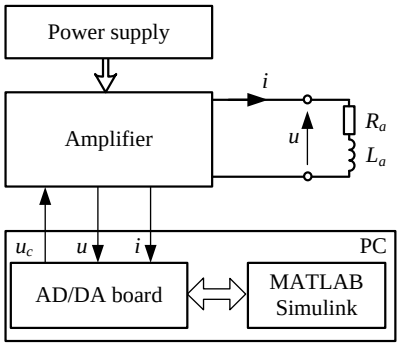

Fig. 2. Schematic diagram of the measurement system

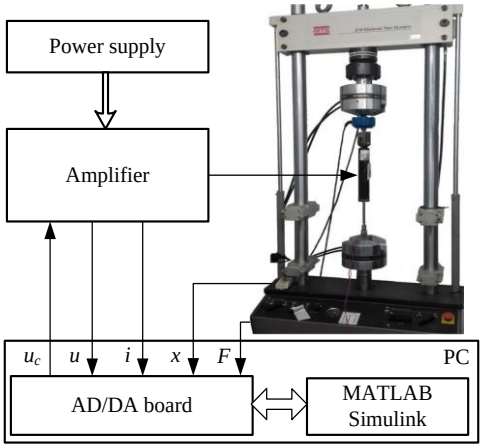

Fig. 3. Schematic diagram of the testing set-up

Force responses were registered using the MTS 810 testing machine-based set-up (see Fig. 3) and the components of the measurement system shown in Fig. 2. To an AD/DA board two voltage signals are supplied (in the range ± 10 V) corresponding to the piston displacement x and force F measured on the MTS tester. The maximal rate of the piston motion implemented on the MTS tester was 150 mm/s. The measurement range of the force sensor was ± 5 kN. Registered signals were sampled with the frequency 1 kHz and converted into voltage signals in the range ± 10 V.

The testing procedure involved two stages. In the first stage the current responses were registered under the applied square and sine voltage signals $u_k(t)$, governed by formulas (1) and (2), respectively:

$$u_k(t) = u_k(t+T) = \begin{cases} U_k & |t| \le \frac{T}{2} \\ 0 & |t| > \frac{T}{2} \end{cases} \tag{1}$$

T – period of the square voltage signal

$$u_k(t) = U_k \cdot \sin(2\pi f t) \tag{2}$$

f – frequency of the sine voltage signal.

Values U_k for the square and sine voltage signals were chosen such that the corresponding steady-state current levels I_k should be equal to 1, 3 and 5 A. The period T of the square voltage signal was 1 s and frequency f of the sine voltage signal $u_k(t)$ was varied in the range (0.1, 100) Hz with a step of 0.1 Hz. Signals were registered for 10 s.

Current responses of the control coil are graphed as time histories (see Fig. 4-6) and frequency characteristics expressing the magnitude of transfer admittance $|Y|$ in the function of frequency, governed by formula (3).

$$|Y_k(f)| = 20log\left(\frac{i_k^{RMS}}{u_k^{RMS}}\right) = 20log\left(\frac{\sqrt{\frac{1}{t}\int_0^t i_k^2(t)dt}}{\sqrt{\frac{1}{t}\int_0^t u_k^2(t)dt}}\right) \tag{3}$$

u_k^{RMS}, i_k^{RMS} – rms values of voltage and current.

In the second stage force responses were obtained under the triangular and sine signals of piston displacement. Under the triangular excitations, the piston in its back and forth positions moved at the constant speed 150, 100, 50 and 10 mm/s, respectively. The amplitude X_m of the applied excitation was 75, 25 and 5 mm. Frequencies f of the triangular input related to relevant amplitudes and velocities are summarised in Tab. 1. Amplitudes and frequencies registered under the sine excitations were identical as those under triangular inputs.

Tab. 1. Frequencies of the applied triangular excitation

Amplitude X_m / Velocity v	75 mm	25 mm	5 mm
150 mm/s	f = 0.5 Hz	f = 1.5 Hz	f = 7.5 Hz
100 mm/s	f = 0.33 Hz	f = 1 Hz	f = 5 Hz
50 mm/s	f = 0.16 Hz	f = 0.5 Hz	f = 2.5 Hz
10 mm/s	f = 0.033 Hz	f = 0.1 Hz	f = 0.5 Hz

4. RESULTS AND DISCUSSION

4.1. Current responses

Fig. 4 shows the current step responses $i_k(t)$ registered under the applied square voltage input $u_k(t)$ within one period. On that basis the resistance of the control coil was established (R=1.18

DOI 10.1515/ama-2017-0039

Ω). Fig. 5 and 6 shows the current responses $i_k(t)$ under the rising and trailing edge of the voltage signal $u_k(t)$ for the voltage and current modes of the amplifier operation.

Tab. 2 summarises the time constants T_{au} and T_{ad} of the control coil obtained for the rising and trailing edge and for two operation modes of the amplifier. The time constant T_{au} is defined as the time required to reach the 90% of the steady value of current I_k, whilst T_{ad} is expressed as 10% of I_k.

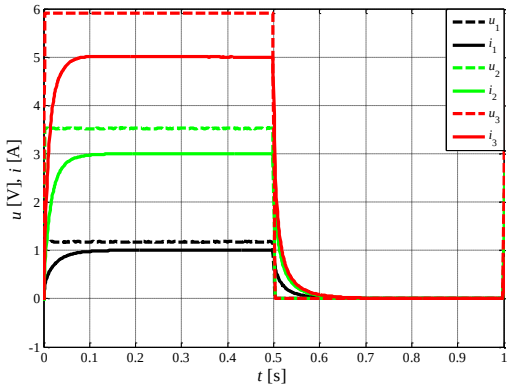

Fig. 4. Current response to a step variation of voltage

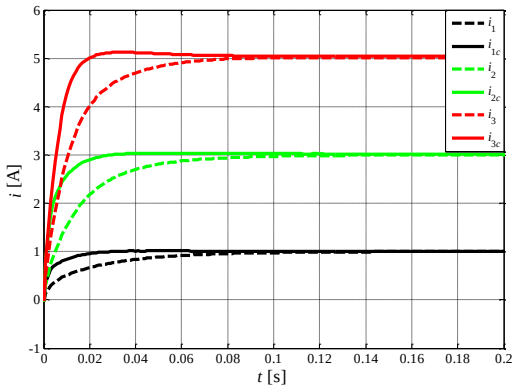

Fig. 5. Current response to a step variation of voltage – rising edge

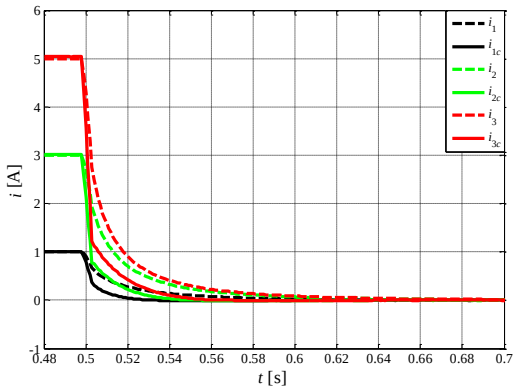

Fig. 6. Current response to a step variation of voltage – trailing edge

In the voltage mode, the time constants depend solely on properties of the control coil integrated in the shock absorber piston. As shown in Tab. 2, the higher the steady state value of current I_k, the lower the time constants T_{au} and T_{ad}, and in this mode of amplifier operation they do not differ by more than 15%. In the current mode, the values of time constants T_{au} and T_{ad} are 2-3.8 fold lower than those registered in the voltage mode. Fig. 7 plots the transfer admittance magnitude $|Y|$ of the control coil in the voltage mode. In the frequency range (0.1, 1) Hz the value of $|Y|$ does not change with varied frequency and is equal to $|Y|$=1.35 dB. Cut-off frequency values f_g for the steady-state current levels I_k 1, 3 and 5 A are 5.8, 6.5 and 7.1 Hz, respectively. Increasing the current I_k causes the cut-off frequency f_g to rise, which is confirmed by variability patterns of time constants. The rates of $|Y|$ decrease for frequencies $f>f_g$ and for steady-state current levels I_k: 1, 3 and 5 A they become 9, 11.4 and 12.3 dB/dec, respectively.

Tab. 2. Time constant of the control coil

Steady-state current level	Voltage mode		Current mode	
I_k	T_{au}	T_{ad}	T_{au}	T_{ad}
1 A	54 ms	47 ms	14 ms	14 ms
3 A	40 ms	43 ms	13 ms	16 ms
5 A	31 ms	34 ms	11 ms	17 ms

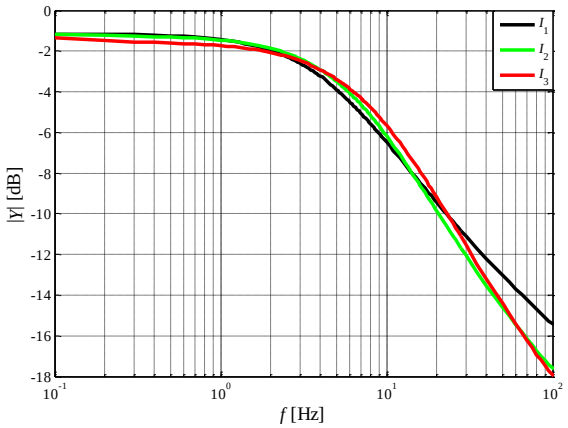

Fig. 7. Transfer admittance magnitude $|Y|$ vs frequency

4.2. Force responses

In the second stage the investigations focused on the effects of operating current I variations in the control coil, amplitudes of piston displacement X_m and piston velocity v on the magnitude of force generated by the shock absorber.

Effects of operating current

Fig. 8 and 9 plot the dependence of force F and displacement x under the triangular excitations (constant velocity v of the piston motion in compression and rebound positions: 50 and 150 mm/s), corresponding amplitudes X_m: 75 and 25 mm. To facilitate the analysis of results, the range of generated forces ΔF is defined as the difference of forces registered for the displacement x=0 mm in the back and forth cycle of the piston motion. An increase of current I from 0 to 5 A results in a nearly 14-fold increase of ΔF, irrespective of the displacement amplitude X_m. The average force value representing the shift of the force-displacement loop is associated with the reaction force of an integrated gas accumulator and is approximately equal to – 400 N.

Fig.10 plots the dependence of dissipated energy E_d within one cycle of the piston back-forth motion on the current level I. It appears that energy E_d tends to increase nonlinearly with increasing current level I. For piston motion velocities 150 and 100 mm/s, the values of E_d in the investigated range of current I are similar whilst for V=50

DOI 10.1515/ama-2017-0039

mm/s these values are significantly lower for I>1.5 A, irrespective of the amplitude X_m.

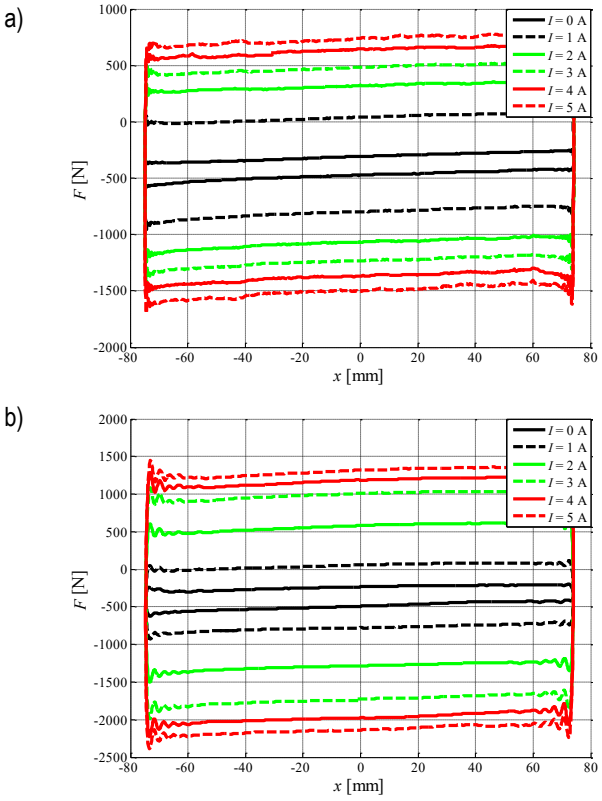

Fig. 8. Force vs displacement: a) V=50 mm/s; b) V=150 mm/s; X_m=75 mm

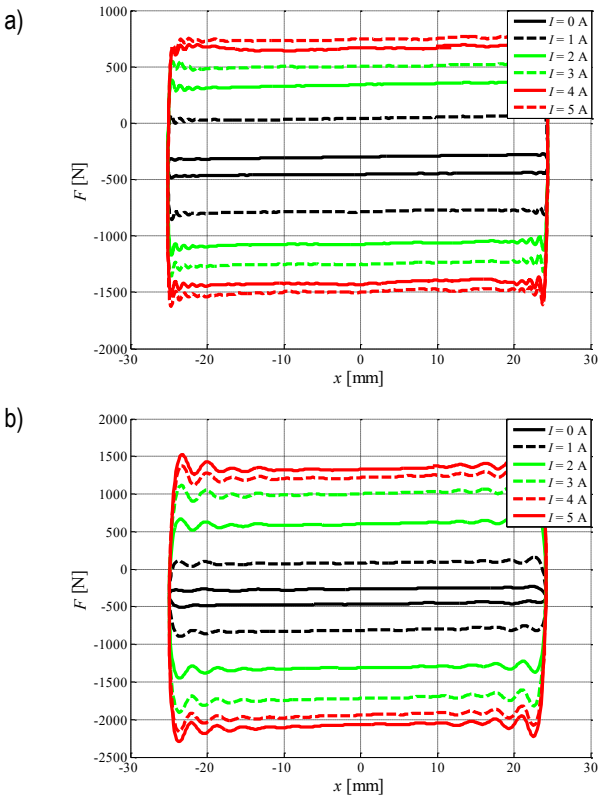

Fig. 9. Force vs displacement: a) V=50 mm/s; b) V=150 mm/s; X_m=25 mm

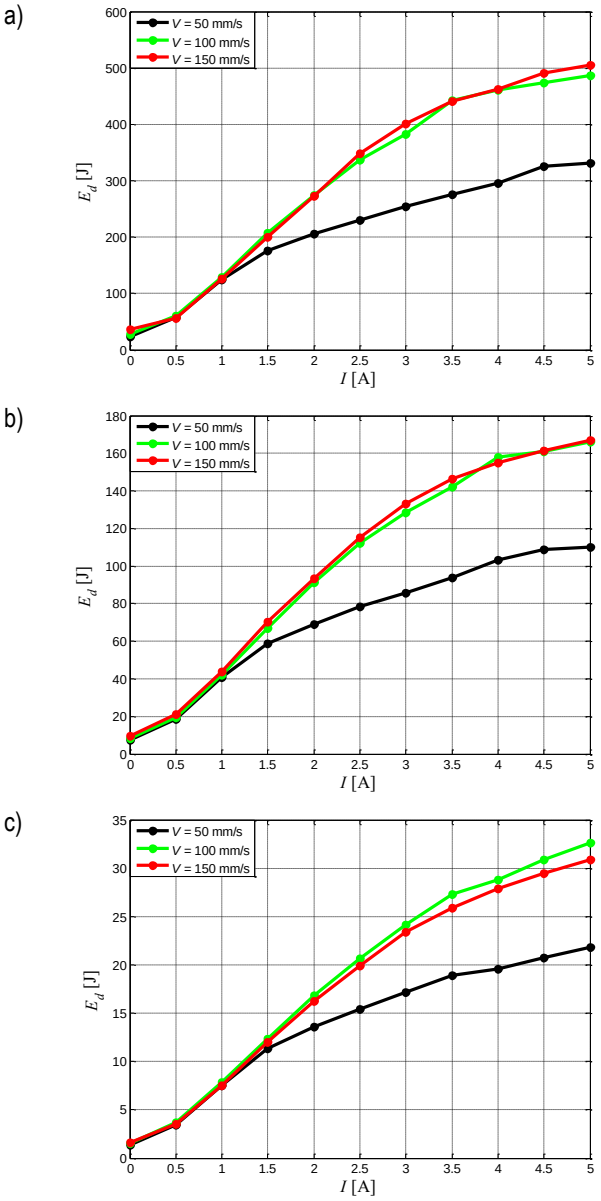

Fig. 10. Dissipated energy vs current: a) X_m=75 mm; b) X_m=25 mm; c) X_m=5 mm

Effects of piston displacement amplitude

Fig. 11 plots the force F vs piston displacement x dependence for the piston velocity V=150 mm/s and for the current levels I: 0, 1, 3, 5 A. It appears that the piston displacement amplitude X_m does not affect the range of generated forces ΔF, irrespective of the actual current level I. This observation is confirmed by the linear dependence between dissipated energy Ed and displacement amplitude X_m (see Fig. 12).

Effects of piston velocity

Fig. 13 plots the force F under the applied triangular excitation x with amplitude X_m=75 mm and for the current levels I: 0, 1, 3, 5 A. With no power supply to the coil and for velocities v in the interval (10; 100) mm/s, the range of force ΔF will not significantly change. ΔF will increase considerably (by nearly 56%) when the piston velocity becomes V=150 mm/s. For velocity V=50 mm/s (when I=1A) and V>100 mm/s (when I=3 A or I=5 A) there is a slight increase in ΔF. In the velocity range from 10 to 100 mm/s (when I=5A) there is a 8-fold increase in ΔF.

DOI 10.1515/ama-2017-0039

a)

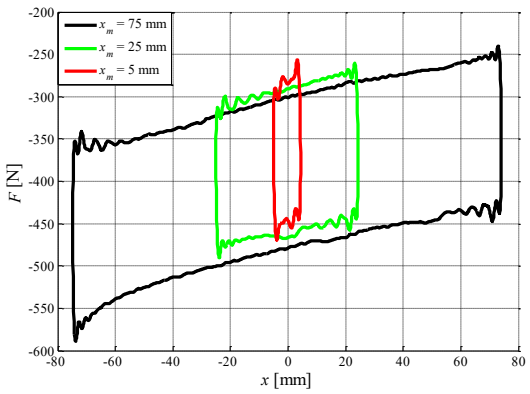

b)

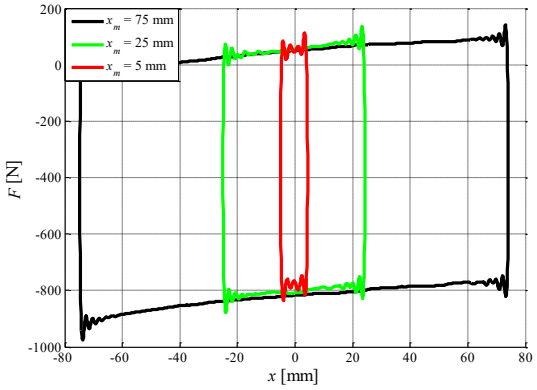

c)

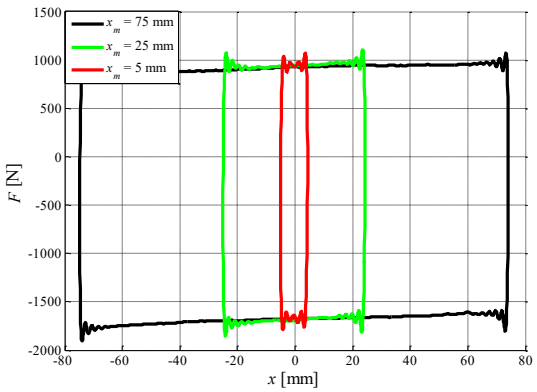

d)

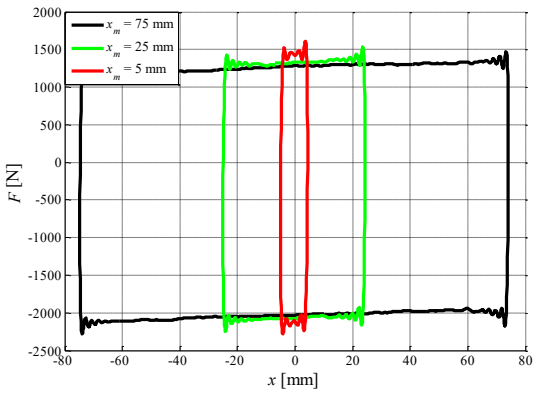

Fig. 11. Force vs displacement: a) *I*=0 A, b) *I*=1 A; c) *I*=3 A; d) *I*=5 A, *V*=150 mm/s

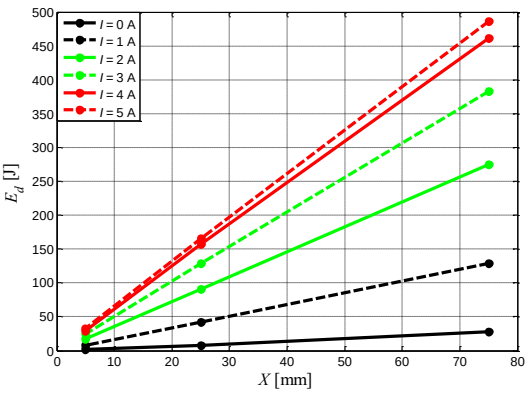

Fig. 12. Dissipated energy vs displacement amplitude; *V*= 150 mm/s

a)

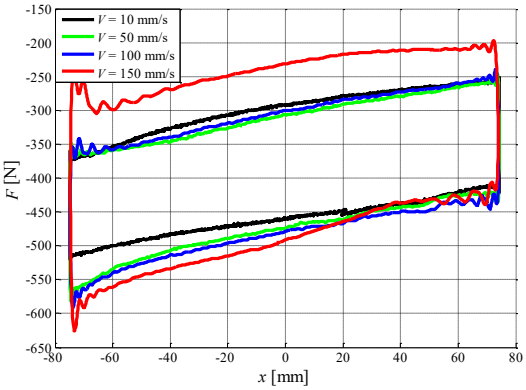

b)

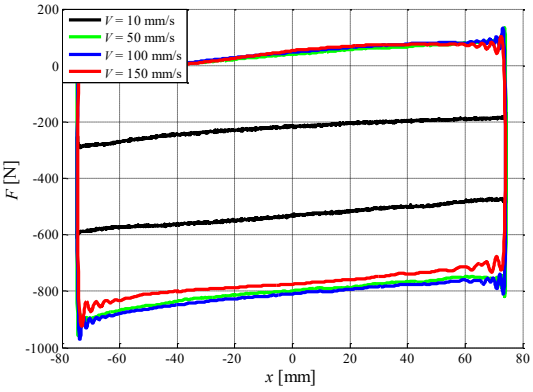

c)

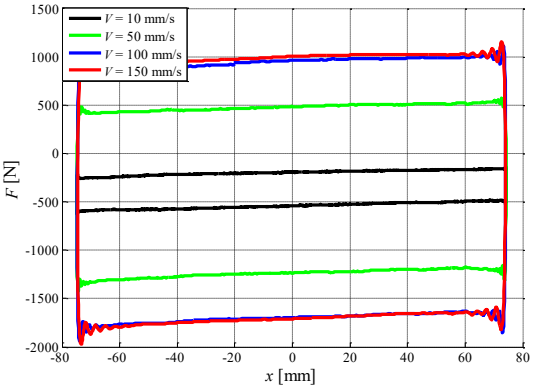

DOI 10.1515/ama-2017-0039

d)

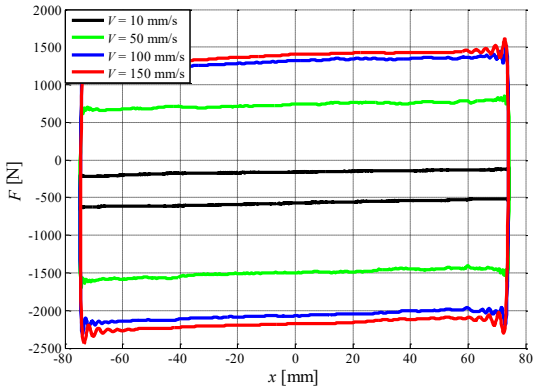

Fig. 13. Force vs displacement: a) *I*=0 A, b) *I*=1 A, c) *I*=3 A, d) *I*=5 A, X_m=75 mm

a)

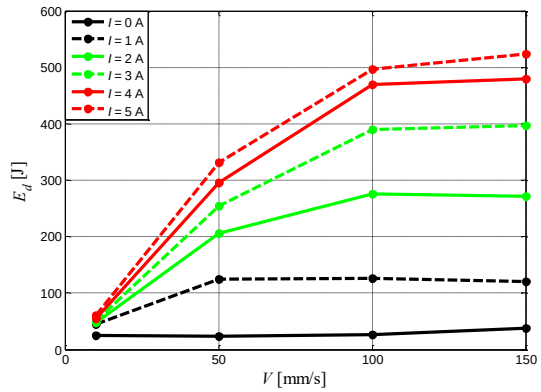

b)

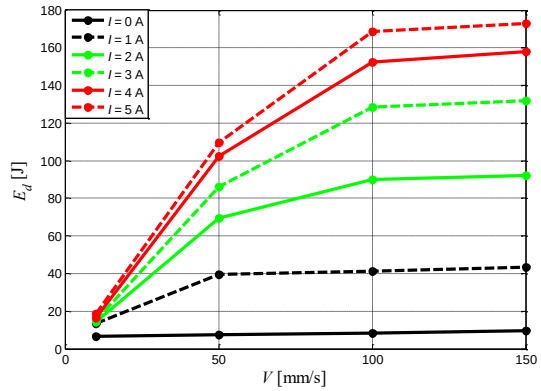

Fig. 14. Dissipated energy vs piston motion velocity: a) X_m=75 mm; b) X_m=25 mm

Fig. 14 plots the relationship between dissipated energy E_d and velocity V for varied current levels I. With no power supply to the coil, the influence that velocity v has on dissipated energy E_d is negligible; when the coil is power-supplied the situation is entirely different. E_d tends to grow significantly with velocity when V=50 mm/s (I≤1A) or V<100 mm/s (I>1A). Fig. 15 and 16 plot the dependence of F on piston displacement x and of the force F on piston velocity v under the sine excitation with the amplitude X_m=75 mm and frequency f=0.333 Hz (when the maximal velocity equals 150 mm/s), revealing a narrow hysteresis loop.

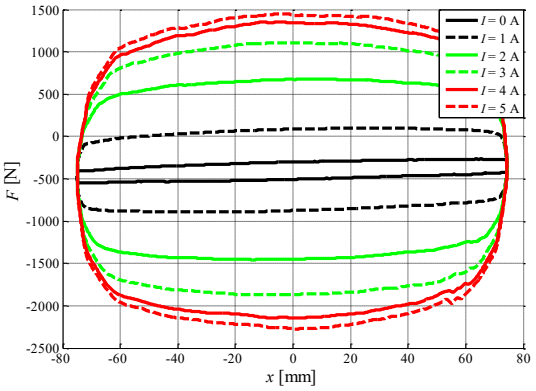

Fig. 15. Force vs displacement under sine excitations

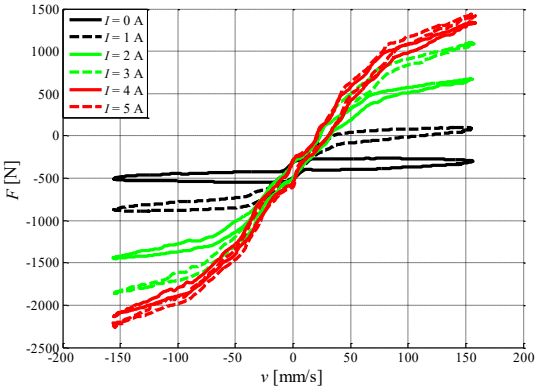

Fig. 16. Force vs velocity under sine excitation

5. SUMMARY

This study summarises the experimental testing of an automotive MR shock absorber under the electrical and mechanical excitations. The goal of the experiments was to acquire measurement data of the shock absorber. The main focus is on current and force responses of the device.

The obtained results lead the authors to the following conclusions:

- time constants T_{au} and T_{ad} derived basing on step responses (for the amplifier operated in the voltage mode) tend to decrease with increased current levels in the control coil,
- this variability patterns of time constants T_{au} and T_{ad} impact on the frequency characteristics (increasing the current levels leads to an increase of critical frequency f_g),
- current level has also influence on the rate of decrease of $|Y|$ in the frequency characteristics for $f>f_g$,
- when current level is increased from 0 to 5A, the range of force ΔF generated by the absorber at the piston velocity V=50 mm/s varies from 157 N to 2200 N, for V=150 mm/s the force ranges from 257 N to 2457 N,
- major determinants of the force range are the current level I and piston velocity v, whilst the effects of amplitude X_m are negligible.

The experimental data seems to be sufficient to formulate the design objectives of an energy harvesting device for the investigated shock absorber. The function of the harvester is to convert the energy of mechanical vibrations into electric energy required to power-supply (control) the shock absorber implemented in purpose-built laboratory model of a suspension system with

DOI 10.1515/ama-2017-0039

energy recuperation capability. As regards the obtained critical frequencies f_g, one has to bear in mind that the resonance phenomenon in the modeled system ought to occur at frequency f<5Hz.

REFERENCES

1. **Choi S.B., Han Y.M.** (2012), *Magnetorheological Fluid Technology Applications in Vehicle Systems*, Padstow, United States: CRC Press Taylor & Francis Group.
2. **Choi S.B., Sung K.G.** (2008), Vibration control of magnetorheological damper system subjected to parameter variations, *International Journal of Vehicle Design*, 45, 94–110.
3. **El-Kafafy M., El-Demerdash S., Rabeih A.** (2012), Automotive ride comfort control using MR fluid damper, *Engineering*, 4(4), 179–87.
4. **Gołdasz J., Dzierżek S.** (2016), Parametric study on the performance of automotive MR shock absorbers, *IOP Conf. Series: Materials Science and Engineering*, 148, 012004.
5. **Gołdasz J., Sapiński B**. (2015), *Insight into Magnetorheological Shock Absorbers*, Springer International Publishing AG Switzerland.
6. **Koo J.H.**, **Goncalves F.D.**, **Ahmadian M**. (2006), A comprehensive analysis of the time response of MR dampers, *Smart Materials and Structures*, 15, 351–358.
7. **Sapinski B.**, (2014), Energy harvesting MR linear damper: prototyping and testing, *Smart Materials and Structures*, 23, 035021.
8. **Sapiński B., Jastrzębski Ł., Rosół M**. (2012,) Power amplifier supporting MR fluid-based actuators, *Proceedings of 13th International Carpathian Control Conference ICCC 2012*, 612–616.
9. **Sapiński B., Rosół M**. (2007), MR damper performance for shock isolation, *Journal of Theoretical and Applied Mechanics*, 1(45), 133–146.
10. **Strecker Z., Mazurek I., Roupec J., Klapka M.** (2015), Influence of MR damper response time on semiactive suspension control efficiency, *Meccanica,* 50, 1949–1959.
11. **Strecker Z.**, **Roupec J.**, **Mazurek I.**, **Klapka M**. (2015), Limiting factors of the response time of the magnetorheological damper, *International Journal of Applied Electromagnetics and Mechanics*, 47(2), 541–550.
12. **Strecker Z., Roupec J., Mazurek I., Machacek O., Kubik M., Klapka M.** (2015), Design of magnetorheological damper with short time response, *Journal of Intelligent Material Systems and Structures*, Special Issue Article, 1–8.
13. **Sung K.G., Choi S.B**.(2009) Vibration control of vehicle suspension featuring magnetorheological dampers: road test evaluation, *Transactions of the Korean Society for Noise and Vibration Engineering*, Vol. 19 (3), 235–242.
14. **Wang D.H., Bai X.X.** (2013), A magnetorheological damper with an integrated self-powered displacement sensor, *Smart Materials and Structures*, 22, 075001.
15. **Wu G.**, **Feng Z.**, **Zhang G.**, **Hou Z.**, (2011), Experimental Study on Response Time of Magnetorheological Damper, 2nd International Conference on Artificial Intelligence, Management Science and Electronic Commerce (AIMSEC), 3968–3972.
16. **Xinchun G., Yonghu H., Yi R., Hui L., Jinping O.**, (2015), A novel self-powered MR damper: Theoretical and experimental analysis, Smart Materials and Structures, 24, 105033.
17. http://www.inteco.com.pl/

This work is supported by AGH University of Science and Technology under research program No. 11.11.130.958.

DOI 10.1515/ama-2017-0040

MULTISTAGE MECHANICAL TRANSMISSIONS WITH AUTOMATIC CONTROL FOR ADVANCED TRUCKS AND BUSES

Aleksandr BLOKHIN[*], Arcadiy NEDYALKOV[*], Lev BARAKHTANOV[*], Aleksandr TARATORKIN[*], Abram KROPP[*]

[*]Transport Systems Institute, Nizhny Novgorod State Technical University, Minin st.,24, Nizhny Novgorod, 603950, Russian Federation

alecsbl@mail.ru, centre@nntu.ru, barahtanov@yandex.ru, alexandr_tar@mail.ru, akropp@rambler.ru

received 28 March 2016, revised 15 October 2017, accepted 18 October 2017

Abstract: The study considers the basic trends of development of modern mechanical transmissions of trucks and buses. It provides the developed various series of multispeed transmissions with automatic control and a number of transmissions from 6 to 16 for trucks and buses. The paper shows the basic parameters of the standard series of new transmissions received on the basis of innovative technical solutions. It provides the results of experimental studies of 16-speed transmissions on a special test stand and on the road as part of a truck transmission. Theoretical and experimental data on the gear change time are compared.

Key words: Multistage Transmission, Pneumatic Actuator, Synchronization Process, Automatic Control, Command Control

1. TRENDS OF DEVELOPMENT OF MANUAL TRANSMISSIONS

The transmissions of vehicles around the world most often have multispeed mechanical synchronized gearboxes with a friction clutch having such advantages as small weight and size, high reliability and service life, low cost, high energy performance as well as ease of maintenance and repair.

In work (Crolla et al., 2009) the schemes and the general description of mechanical transmissions are presented, including with automated manual transmission (AMT), their advantages and disadvantages are described. It should be noted that at present AMT is widely used in vehicles, trucks, intercity buses and all-terrain vehicles. Overview of the types of actuators and control systems of ATM is presented in the paper Ali et al. (2004). Electro-hydraulic (Lucente et al., 2007), electro-pneumatic (Jiang et al., 2011) and electro-mechanical (Kuroiwa et al., 2004, Karpukhin et al., 2015) actuators are the most used. Electro-hydraulic and electro-mechanical actuators are mainly used in cars and light commercial vehicles (Kuroiwa et al., 2004, Song et al., 2010). Medium and heavy-duty trucks, intercity buses and all-terrain vehicles have compressors that provide air compression and receivers - cylinders, which compressed air is stored, and that is why electro-pneumatic actuators are used there. As you know, the energy of compressed air is used to brake vehicles, control transmission, power take, remote tire inflation, etc. In this paper we consider AMT for trucks and buses. Clutch control systems for trucks with electro-pneumatic actuators are considered in the work (Langjord, 2011). The gearshift process and synchronization are discussed in detail in the works Lovas et al., (2006), Ivarsson et al., (2010), Junnarkar and Raibhole (2017). In some papers, the influence optimization of transmissions shift schedules on the traction performance and fuel consumption of vehicles is considered (Liao and Quail, 2011).

For the majority of trucks, buses and road trains multispeed gearboxes are widely used. Their use ensures high traction and speed, reduced fuel consumption and improved environmental properties. Such gearboxes can be rationally used with automatic and command (semi-automatic) control (AMT), which allows us to realize the benefits of a wide range of gear ratios, creates a more comfortable environment for the driver and improves traffic safety.

The main trends in the development of modern manual transmissions are as follows:

1. Increase the density of ratios in the entire range of the gearboxes, which primarily takes place in the gear boxes of trucks and super heavy-duty vehicles.
2. Increase the range of ratios defining the limits of traction and speed characteristics of the vehicle. This allows to increase the traction of the vehicle or the road train and to reduce the slipping clutch operation at the same time, thereby increasing the reliability and longevity of its operation.
3. Adoption of new structural schemes of gearboxes, allowing to provide the required number of gears. This is achieved using multispeed gearboxes having a relatively small number of gear wheels and additional driving pairs of them in front of the main gear unit (splitter) or planetary synchronized range gear installed behind the main gear unit, or through the use of the so-called hybrids, including both the front splitter, and the planetary range gear.
4. The use of new design of compact energy-synchronizers using molybdenum covered friction cones, including double-cone ones.
5. The trend of setting gears on the shafts on needle bearings in the separators, which can significantly increase the speed mode of the gearbox, and improve the aligning of the gears on the shafts. This constructive solution in combination with a lubricant under pressure, which is especially necessary for heavy gearboxes, provides a guaranteed reliable operation of the unit.
6. The increasing use of the automated clutch control and gear shifting. Almost all well-known companies, such as, ZF, Volvo,

DOI 10.1515/ama-2017-0040

Mercedes-Benz, Scania, Renault, Eaton et al. establish a full-time or on-demand automated electro-pneumatic gearbox control.

7. We can see a trend of sharp increase of the engine torques while significantly increasing of the requirements to gearboxes for resources.

Creation of the units corresponding to these requirements demands a lot of experimental work related to the utmost optimization of each element of the gearbox. The created promising gearboxes should have simple design solutions, proven tests and they should surpass in the output parameters the best-known analogues of leading companies in the field of transmissions.

2. CHARACTERISTICS OF TRANSMISSIONS OF STANDARD SERIES

Taking into consideration the current trends of development and applying forward-looking solutions the specialists of the Nizhny Novgorod State Technical University named after R.E. Alekseev (NNSTU) and the COM Group (Russia, Naberezhnye Chelny, http://komgroup.ru) developed a standard series of advanced mechanical transmissions for light commercial vehicles, buses, road trains, heavy trucks and all-terrain vehicles for engines ranging from 75 to 750 kW (100 to 1000 HP) in a range of torques from 360 to 3500 Nm. Standard series (Tab. 1) includes five basic sizes of transmissions, three of which are 6-speed and two – multispeed, 8 and 16 speed gearboxes. The 8-speed gearbox consists of two gear units connected in one crankcase: from the basic 4-speed crankcase and 2-speed one.

Tab. 1. Basic parameters of standard series of advanced gearboxes

Modifications	Designation of the gearbox	Input point Nm	Number of gears	Range	Axle size on the ends of crankcase, mm	Center distance, mm	Weight, kg
1	M6-300	360	6	9.25	295	100	51.5
2	M6-700	750	6	9.10	380	135	120
3	M6-1100	1300	6	9.10	460	165	205
4	TM8-1300	1650	8	12.38	460	135	160
5	TM8-2000/1	2200	8	13.77	485	170	245
6	TM8-2700/2	2700	8	13.77	485	170	245
7	TM8-3500	3500	8	14.16	520	170	275
8	TM12-1800/1	1800	12	15.05	500	170	270
9	TM12-2200/2	2200	12	15.15	500	170	270
10	TM16-2000	2200	16	17.04	570	170	300
11	TM16-3000	3000	16	16.87	570	170	300
12	TM16-3500	3500	16	16.87	615	170	325

Execution of works included the creation of original calculation methods, the development of design, prototyping, development of special test methods and carrying out bench, resource and functional tests, finishing the design on the basis of the test results and release of drawing documentation for preparation of the serial production. By the number of transmissions of synchronized steps, the transmitted maximum torque and power, the range and density of a number of gear ratios the gearbox of standard series correspond to modern best analogues, in particular, such well-known ones as ZF, Volvo, Eaton, Mercedes-Benz, Scania, Renault. In addition, for all multispeed gearboxes we developed original friction clutch control mechanism shown in the works (Blokhin et al., 2015).

In Tab. 1 the weight of the gearbox is shown without the clutch case. Index / 1 - refers to the modification of the gearbox with a higher direct transfer. Index / 2 - refers to the modification with the higher overdrive. The TM index means that the kinematic scheme of a mechanical gearbox includes the main gear formed according to the three-shaft design, with the planetary range gear.

3. FEATURES OF THE DEVELOPED GEARBOX

Positive features of three types of sex-staged gearboxes, covering nearly 4 times the torque range - from 360 to 1300 Nm, are as follows:

- Axial dimensions, internal loss and weight of the gearboxes are located within 5-speed gearboxes or less. A wide range of gear ratios eliminates the necessity of splitters in the transfer gearbox for such vehicles as "Jeep" and other all-terrain vehicles, that simplifies and reduces the cost of the transmission unit;
- A single, unified system of automated electro-pneumatic control;
- A reduction in fuel consumption due to low internal losses and wide ratio coverage of the gearboxes.

For the whole family of the TM model of the multispeed gearboxes, two of which - TM8-1300 and TM 16-2000 are basic sizes and 9 modifications (taking into account the possibility of application of the highest transmission both direct and accelerating that at the extremely low cost expands the use of multispeed transmissions for a variety of engines and operating conditions of cars and trucks), were manufactured for the first time in the world with the use of a very simple three-shaft kinematic scheme without any additional supports and parasitic components when there are just three shafts, four supports and two crankcase parts. This allowed us to have an axial dimension of the base gearbox TM16-2000 85 mm less compared to the same ZF gearbox (model - Astronic 16AS 2200), although the latter has 2 intermediate shafts and a lower load-bearing capacity, which when converted to an equivalent load bearing capacity increases the difference in the axial envelope from 85 to 133.5 mm and this is without difference of 20 mm, due to the installation into the gearbox of two toothed couplings instead of the synchronizers. Thus, with the same functional capabilities the difference in the axial envelope reaches to 153.5 mm in favor of transmission TM16-2000. This, in particular, is one of the important indicators of the positive distinguishing features of the advanced technical level of the design solutions.

Small axial dimensions and mass parameters of the gearboxes even when with their relatively overestimated bearing capacity allows us to use the unit with a relatively small engine torque, because eventually the lowest limit of the use of the gearbox is determined by its dimensional and weight parameters. Small weight of the gearbox allows you to have a smaller number of sizes and, therefore, more mass production, which will help to reduce the cost of the unit.

At the same time we solved the problem of reducing of internal losses in gearboxes due to their original design, geometric and kinematic features. The internal losses in the gearbox TM16-2000 make 1.3 kW against 2.65 kW in a similar gearbox ZF S16-220

Aleksandr Blokhin, Arcadiy Nedyalkov, Lev Barakhtanov, Aleksandr Taratorkin, Abram Kropp
DOI 10.1515/ama-2017-0040

(based on the results of the ZF Company on measuring mode - direct transmission at 2000 rpm).

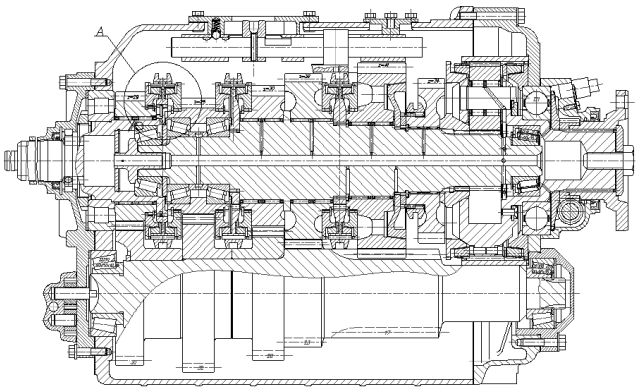

Fig. 1. Longitudinal section of a transmission TM16-2000

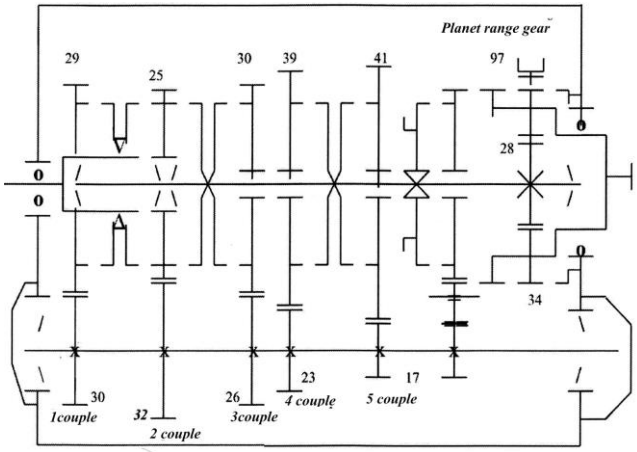

Fig. 2. Kinematic diagram of the transmission TM16-2000

The main features of multispeed designs (8-12) of the gearboxes of the developed standard series are as follows (Blokhin, 2016):

1. When designing the gearboxes we used the so-called modular principle, according to which the gearbox is made from functionally independent units and mechanisms, as opposed to the method of construction from the parts and units that are not able to perform the overall functional requirements. Modularity means maximum unification of the units and parts, and the maximum possible exception of the intermediate parts, which do not comply with clear functions. In this case, the gearbox is already a module that can be equipped with both automatic and manual control. In its turn, the gearbox module consists of module units: the unit of the planetary range gear with the control element; the gearshift; the units of primary, intermediate and the gearbox main shafts.
2. The source gear-box module differs from all known analogs by the following key features (see Fig. 1-2):

– Back support of the gearbox mainshaft is located not in the additional wall of the transmission housing, but in the the cage of the planetary range gear that reduces losses to zero at turning on the highest range of the range gear;
– Back support of the intermediate shaft is also located not in the additional wall, but in the crankcase of the range gear.
– This allowed us to have two walls (two body parts) instead of four (three in the housing parts and one of the steel plate) is performed in reverse direction compared to generally accepted one that unloads bearings of the supports and greatly reduces internal losses, as the forward support bearing of the main shaft rotates on a relatively low speed, and the bearing of external supports is much faster.

3. The design feature of the planetary shift stage compared to the widespread solutions is as follows:

– For the range shifting we used the axially movable ring gear with internal teeth, which considerably simplifies the construction of the shifting elements and reduces the overall axial size;
– Blockage of the planetary range gear is carried out when you connect the ring and sun gears. The traditional solution is to block by connecting the ring gear to the carrier. In the locking circuit used in the developed transmission, blockage is achieved 4 times faster; simultaneously it reduces synchronization time when the range gear is shifted from the lowest to the highest range 4-6 times. At the same time the axis of the sun gear and the satellites of the planetary range gear for any misalignment in the process of bending the output shaft are parallel, I. e, they are self-aligning. In the known transmissions their axis are crossed the greater the amount of torque is, not allowing the proper contact pattern on the mating gears and contributing to a reduction of their durability and reliability.

4. In the main gearbox, and the range gear we use compact synchronizers of the coupling type with molybdenum covered blocking rings. Three synchronizers of the main gear are unified. Similar synchronizers are used for planetary range gears. The TM series of boxes on the first gear used to provide additional cone reduction efforts at switching.
The design of synchronizers has the following features:

– Molybdenum consumption is reduced by 3 times by making the spiral grooves not on the molybdenum of the blocking ring, but on the ring gear that does not require expensive and complex process equipment required for processing of high hard molybdenum;
– A fairly time-consuming operation of the synchronizer clamps assembly with coil springs and crackers (9 items all together) is eliminated by using two spring rings;
– At the same time through the use of spring rings we eliminated the need for mating teeth on the couplings to limit the clutch stroke of the coupling that allows us to make the coupling on the universal standard equipment without using special very expensive broaching tools;
– The design of the locking ring is greatly simplified, only 3 teeth out of 63 have been left;
– The teeth blocking the synchronizer and shifting the gear are separated that maintains the geometry of the locking elements and increases their reliability during the operation;
– The width of the hub is increased to maximum, up to 32 mm in boxes TM 16-2000, and in the other modifications, that reduces the possibility of self-switching of the transmission.

5. The gearshift mechanism is configured as a separate unit and has the following features:

– It simplifies the structure of the body parts and the assembly of the gearbox;
– It reduces the length of the rods by 2-2.5 times;
– It uses high-tech unified forks made from sheet steel for three synchronizers.

DOI 10.1515/ama-2017-0040

6. In accordance with a pronounced trend observed in the world of automated control systems for manual transmissions (AMT), for the whole range of manual transmissions from M6-300 to TM16-3500 the automated control systems are applied. Thus, the following kinds of control are possible:

– Mechanical or pneumatic-mechanical (with servo- amplifier)
– Electro-pneumatic:
  – Command (semi-automatic);
  – Automatic.

For all modifications of the TM series of gearboxes there is a unified design of the pneumatic- mechanical, and the electro-pneumatic control, including the main, backup and disaster control unit.

Control of the main gear, splitter and the range gear is performed by means of electro-pneumatic devices, made in the form of independent units. This solenoid controls are mounted directly on the actuators, thereby reducing the required amount of the input air hoses and increase the speed and reliability of the control system.

It should be noted that in the process of work performance we used many years of experience in development of transmission of various dimensions and modifications, as well as control systems. The vast majority of technological and design solutions have been tested in the lab and on road, which ensures reliable operation of the applied constructional solutions and therefore gearboxes in general.

Fig. 3 shows the control system of the multispeed manual transmission and the clutch.

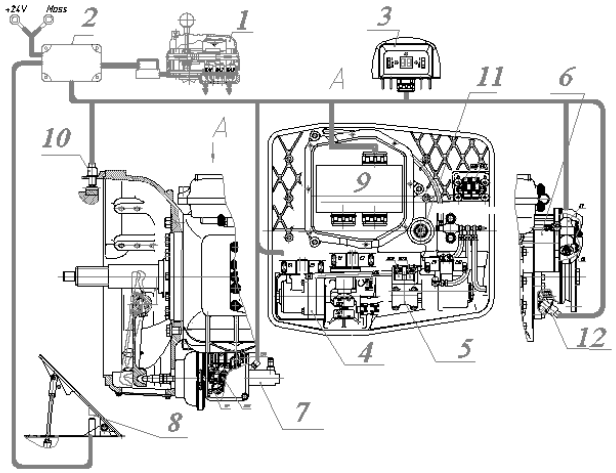

Fig. 3. The scheme of automatic transmission and clutch control:
1 – the controller; 2 – the matching unit; 3 – the monitor; 4 – the main gear control mechanism; 5 – the splitter control mechanism; 6 - splitter control mechanism; 7 - the clutch control mechanism; 8 – the accelerator pedal; 9 – the ecu; 10 – the engine speed sensor; 11, 12 - the intermediate and output shaft speed sensor

4. THE RESULTS OF LABORATORY BENCH TESTING

We have manufactured samples of gearboxes (Fig. 4) with a manual, semi-automatic and automatic control. We've carried out a full range of functional bench tests. We've completed long-run bench tests equivalent to 700 000 kilometers.

Experimental studies were carried out on a special stand for testing transmissions with automatic and command control (Patents of the Russian Federation for utility model №154871, №154102), manufactured in the NNSTU named after R.E. Alekseev (Fig. 5), (Blokhin et al., 2015, 2016, 2017). The stand allows studying the efficiency of the units of manual transmissions (the clutch, the divider, the main reduction gear box, the splitter, definition of the unit efficiency, study of the synchronization process, etc.) and mechatronic control systems for automatic or semi-automatic modes as.

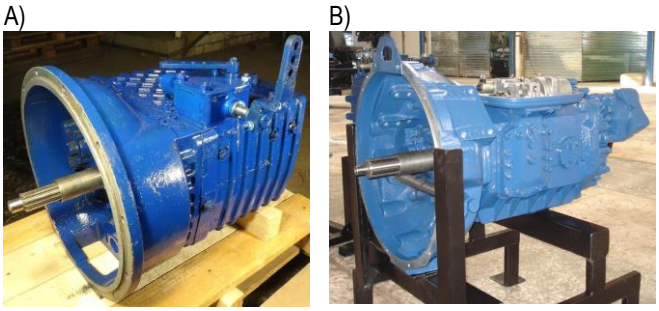

Fig. 4. Experimental samples of gearboxes: A) M6-700 b) TM8-2700

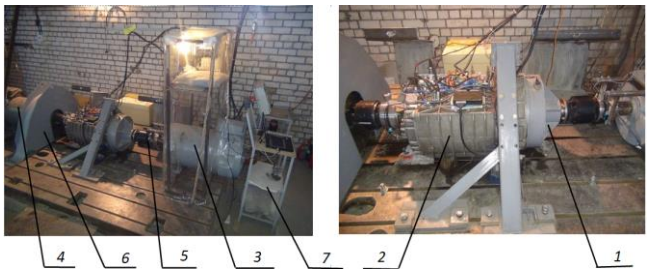

Fig. 5. The appearance of the stand for testing TM16-2000 transmissions with automatic control 1 – the clutch mechanism; 2 – the studied multistage transmission; 3 – the drive motor; 4 – the loading motor; 5 – the driveline; 6 – the inertial mass; 7 – the remote control

The studies were carried out on the test bench at the command and automatic modes at alternating pressure in the pneumatic system, different frequencies of rotation of the primary shaft and different values of diameter of the solenoid valve nozzle. Fig. 6 shows the results of the experimental studies.

Fig. 7 shows the results of experimental studies of sixteen staged transmission TM16-2000 with experimental samples of the automatic and command drive control in the following sequence 2-4-6-8. A signal from the microswitch of gears of the main gearbox is represented at channel №1, a signal from the pressure sensor in the accelerating mechanism of the clutch control is represented at channel №2, a signal from the pressure sensor in the power chamber of the clutch control mechanism is represented at channel №3 and a signal from the microswitch of the clutch mechanism is represented at channel №4. It is important to note that in the developed automatic transmissions the gearshift is always performed with the automatic clutch control (channels 2-4, Fig. 7).

According to the experimental studies we determined the main parameters of the switch-over process: the total turn-on time of the transmission; the clutch on / off time; time of the pressure rise in the power cylinder, the main gearbox, the divider, the splitter; the response time of the main gear mechanism and a divider in the selection and a given transmission; the dynamic moments on the motor shaft and the output shaft of the transmission; the rotational speed of the motor shaft and the output shaft of the transmission.

Aleksandr Blokhin, Arcadiy Nedyalkov, Lev Barakhtanov, Aleksandr Taratorkin, Abram Kropp
DOI 10.1515/ama-2017-0040

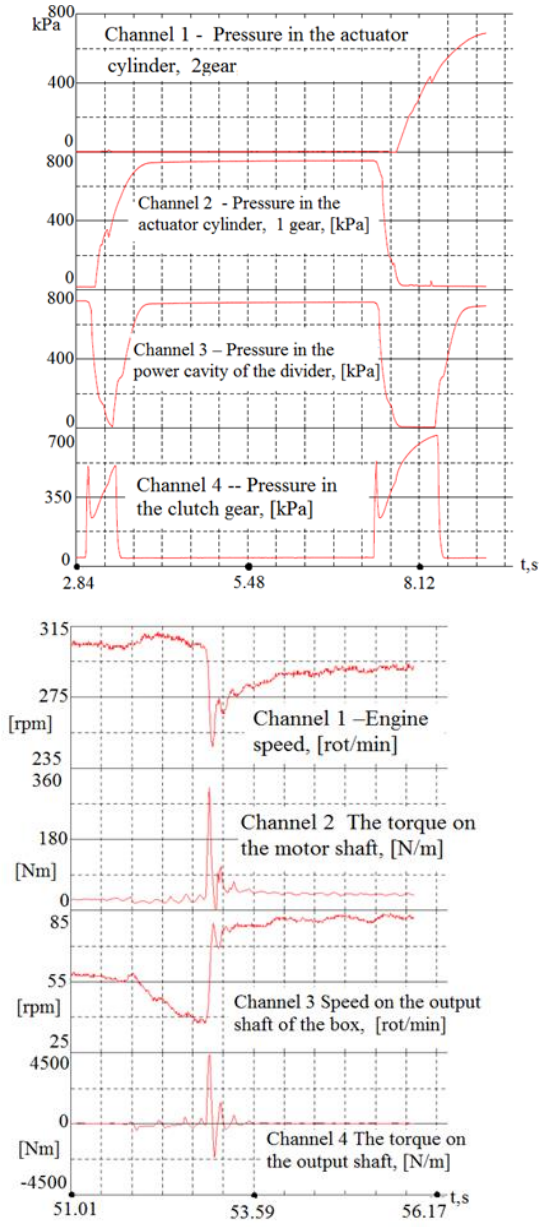

Fig. 6 . The results of the experimental studies

In addition, we determined the time of the clutch off\on, as one of the main parameters that characterize the quality of the clutch control. These parameters can be determined from Fig. 7, channels 2-3. The turn off time on average equals to 0.15 sec., and the turn on time equals to 0.30-0.35 sec., that is acceptable for heavy commercial trucks and buses.

Tab. 2 shows the results of the calculations and the experiments. Calculated values of synchronization time of certain stages and in all cycles of gear shifting differ from the experimental data by 10-25% maximum.

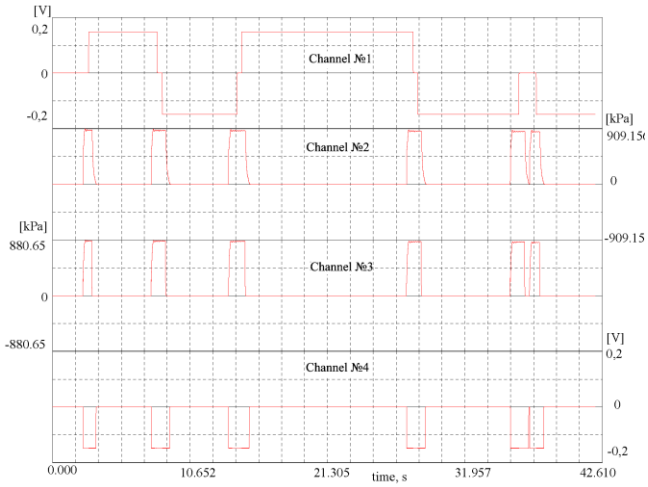

Fig. 7. The experimental data on the stand on the process of a gear shift in the transmission TM16-2000

Tab. 2. Results of the experimental and calculated values of the synchronization time. Type of lubrication oil - MC-20, temperature - 325-335^{0}K. Turnover of the secondary shaft n_2=0 equivalent moment of inertia including transmissions – y_1=0.472 nm*sec^2

№	Result Experiment/ Calculation	Pressure value, [N/m^2]	Rotational speed of the input shaft n_1, [rpm]	Nozzle diameter d, [м^2]	Time-to-contact friction cones, [s]	Synchronization time in critical discharge zone, [s]	Synchronization time in the subcritical discharge zone , [s]	Synchronization time in the zone of constant pressure, [s]	Total synchronization time, [s]
1	Exp.	$6.2\cdot10^5$	2000	$2\cdot10^{-3}$	0.17	0	0.29	0.6	0.79
2					0.18				0.83
3					0.18				0.82
4	Calc.				0.18				0.89
5	Exp.	$7.9\cdot10^5$	1060	$2\cdot10^{-3}$	0.13	0.04	0.30	0.033	0.36
6					0.14				0.35
7					0,13				0.33
8	Calc.				0.14				0.34
9	Exp.	$9.4\cdot10^5$	2600	$4\cdot10^{-3}$	0.04	0.034	0.14	0.335	0.51
10	Calc.				0.058				0.51

5. THE RESULTS OF ROAD TEST

After obtaining a satisfactory result at the test stand the sixteen speed transmission TM 16-2000 was installed on the vehicle KAMAZ-65117 (Fig. 8), (Blokhin et al., 2017). Its main technical parameters are presented in Tab. 3.

Figs. 9 and 10 show the waveforms, matching several startings of the vehicle KAMAZ-65117, having TM16-2000 transmission with automatic control on a flat supporting surface.

DOI 10.1515/ama-2017-0040

Fig. 8. The appearance of the vehicle KAMAZ 65117

Tab. 3. Main Specifications of KAMAZ-65117

The vehicle manufacturer	KAMAZ, Russia
The weight parameters and load	
The carrying capacity of the vehicle, kg	14500
The total mass of the vehicle, kg	24000
The load on the rear axles, kg	18000
The load on the front axle, kg	6000
Engine	
Engine model	KAMAZ 740.62.280
Max. useful torque Nm (kgc.m) at crankshaft speed, rev / min	1177 (120) 1300
Maximum net power, kW (hp) at crankshaft speed, rev / min	206 (280) 1900
Working volume, l	11.76
The location and number of cylinders	V-type, 8
Clutch	
Model	ZF SACHS MFZ 430
Transmission (gearbox)	
Model	TM16-2000
Main gear	
Gear ratio	5.94
Tires	
Tire size	295/80 R22.5
Tire brand	TYREX
Overall dimensions, mm	
Length x Width x Height	7800 x 2470 x730

On channel № 1 (Fig. 9) we can see the pressure in the power chamber of the automatic clutch control mechanism. The maximum value of pressure is about 8 atm. The pressure at which the regulation is provided by the clutch position corresponds to 2-2.2 bar. On channel № 2– we can the the pressure in the accelerator mechanism of the clutch control. Maximum pressure is a bit more than 8 atm., the pressure in the valves when the clutch position is being adjusted is 2.6-2.8 atm.

Channel № 3 is represented by the movement of the clutch fork rod. At the time of clutch engagement for gentle start of the vehicle the friction clutch plates differ by the amount of 70-80% of their maximum speed. Channel № 4 presents data on the response time of the microswitch of the clutch on the basis of the analysis which will determine the time of the on / off of the clutch and the total time of a gear change (on average about 0.7 seconds).

Fig. 10 shows the nature of the pressure measurement in the power of the main gearbox and cavities divider. The movement took place on 1 and 2 in the main transmission gearbox (respectively channels №5 and №6, Fig. 10) and the lower divider range (channel №7 Fig. 10).

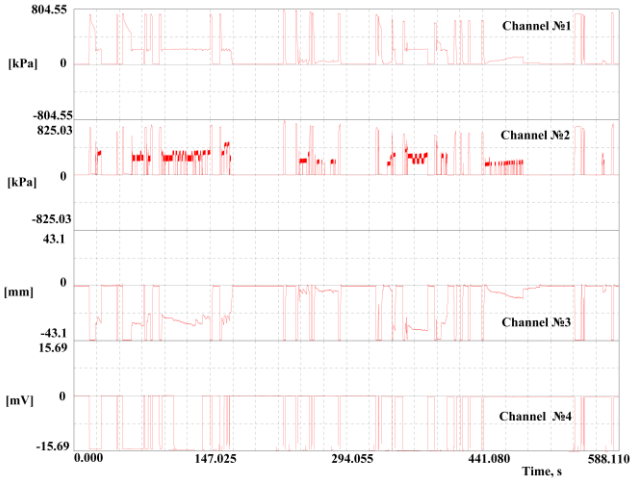

Fig. 9. Waveform of starting process of KAMAZ-65117 with TM16-2000 transmission: Channel №1 – The pressure in the power chamber of the automatic clutch control mechanism; Channel №2 – the pressure in the accelerator of the clutch control mechanism; Channel №3 – the movement of the clutch fork; Channel №4 – response time of the clutch mechanism

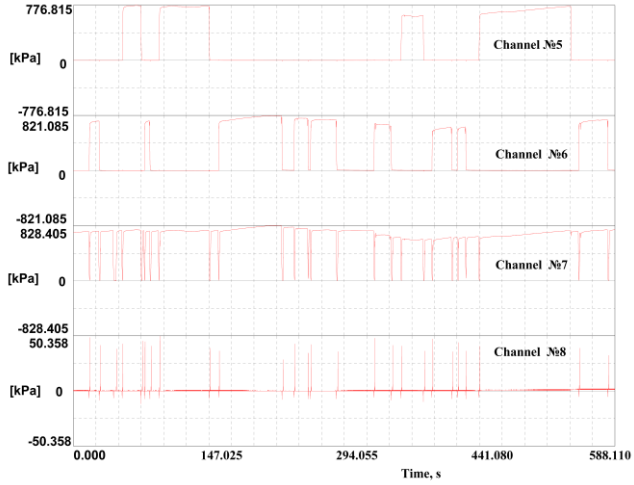

Fig. 10. Waveform of starting process of KAMAZ 65117 with TM16-2000 transmission: Channel №5 – The pressure in the power chamber of the main gear at turning on even gears; Channel №6 – The pressure in power chamber of the main gear at turning on even gears; Channel №7 – The pressure in the power chamber at the lower range of the splitter; Channel №8 – The pressure in the power chamber at the top range of the splitter

Analysis of the results of the road research showed that at ambient temperatures above 0°C the difference is 5-10% max. due to a more rapid decrease in pressure in the vehicle's receiver by several gear changes. At low outside temperatures, from -15°C to -20°C, the data of the laboratory and road conditions differ significantly, up to 35%. To some extent, this is due to additional freezing of the pipes when the vehicle is moving, which is difficult to simulate in our laboratory.

Thus, in general, there is a high qualitative and quantitative convergence with the results of laboratory tests on the stand, and the results of theoretical research.

DOI 10.1515/ama-2017-0040

6. CONCLUSION

1. The paper analyses the main trends in the development of mechanical staged gearboxes, on the basis of which we developed advanced standard series of manual gearboxes with automated control. .
2. It presents the characteristics of advanced manual gearboxes from the developed standard series for automobiles, road trains and heavy trucks with engines ranging from 75 to 750 kW (100 to 1000 hp) in the torque range from 360 to 3500 Nm.
3. It considers the basic design features of the unified technical multistage gearboxes on the basis of the leading technology solutions. We've found out that considering the number of gears of synchronized stages, transmitted maximum torque, power, range, density, number of gear ratios, and mass-dimensional parameters the gearboxes from the standard series rank with the best world analogues.
4. The paper contains a schematic diagram of automatic or command control of the developed multi-staged manual transmissions with microprocessor control.
5. It represents the results of experimental studies on the specialized stand, as well as comparison of theoretical and experimental data. The discrepancy between the data is max. 10-25%.
6. In general, there is a high qualitative and quantitative convergence of the road test results with the results of laboratory tests carried out on a special stand, and the results of theoretical research. At ambient temperatures above 0°C the difference is 5 ... 10% max, at lower temperatures, from -15°C to -20°C, the difference increases to 35%.

REFERENCES

1. **Ali A.I., Qin D., Attia N.A.** (2004), Review on development progress of automatic manual transmissions control, *Journal of Chongqing University - English Edition*, 3(2), 38-42.
2. **Blokhin A.** (2016), Robotic control system of the multistage manual transmission with friction clutch, *Research Journal of Applied Sciences*, 11(12), 1553-1558.
3. **Blokhin A., Barakhtanov L., Fadeev E., Denisenko E.** (2017) Research of robotised manual transmissions for all-terrain vehicles, *ARPN Journal of Engineering and Applied Sciences,* 12(1), 20-32.
4. **Blokhin A., Barakhtanov L., Koshurina A., Taratorkin A., Lubichev P.** (2015), Research of the Friction Clutch Automatic Control Performance at the Stand, *Proceedings of the 2015 International Conference on Electrical, Electronics and Mechatronics, AER - Advances in Engineering Research*, 34, 142-146.
5. **Crolla D.** [ed.] (2009), *Automotive Engineering: Powertrain, Chassis System and Vehicle Body*, Butterworth-Heinemann.
6. **Ivarsson M., Slund J., Nielsen L.** (2010), Impacts of AMT gear-shifting on fuel optimal look ahead control, *SAE Technical Paper* 2010-01-0370.
7. **Jiang M., Zhou J., Chen W., Zhang Y., Chen L.** (2011), Modeling and Simulation of AMT with MWorks, *Proceedings of the 8th International Modelica Conference*, 829-839.
8. **Junnarkar N.R., Raibhole V.N.** (2017), Development of Synchronizer Operation for integration in AMT Control Strategy, *IOSR Journal of Mechanical and Civil Engineering, 6th National Conference RDME*, 5, 40-45.
9. **Karpukhin K.E., Kozlov A.V., Bakhmutov S.V., Terenchenko A.S.** (2015), Comprehensive life cycle analysis of different types of energy storage for electric or hybrid vehicles, *ICAT 2015 Proceeding the international conference on automobile technology for Vietnam*, 7-14.
10. **Kuroiwa H., Ozaki N., Okada T., Yamasaki M.** (2004), Next-generation fuel-efficient automated manual transmission, *Hitachi Review* , 53(4), 205–209.
11. **Langjord H.** (2011), *Nonlinear Observer and Control Design for Electropneumatic Clutch Actuator*, Norwegian University of Science and Technology (NTNU).
12. **Liao Y., Quail A.** (2011), Experiment and Simulation of Medium-Duty Tactical Truck for Fuel Economy Improvement, *Energies*, 4, 276-293.
13. **Lovas L., Play D., Marialigeti J., Rigal J.F.** (2006), Mechanical behaviour simulation for synchromesh mechanism improvements, *Proceedings of the Institution of Mechanical Engineers, Journal of Automobile Engineering*, 220(7), 919-945.
14. **Lucente G., Montanari M., Rossi C.** (2007), Modelling of an automated manual transmission system, *Mechatronics*, (2-3), 73–91.
15. **Song X-Y, Sun Z-X, Yang X-J, Zhu G-M**. (2010), Modelling, control, and hardware-in-the-loop simulation of an automated manual transmission, *Proceedings of the Institution of Mechanical Engineers, Part D: Journal of Automobile Engineering*, 224(2), 143-160.

It should be noted that the this work was carried out at the NNSTU named after R.E. Alekseev, with financial support from the government in the face of the Russian Ministry of Education under the project: №14.Z50.31.0036

DE GRUYTER
OPEN

DOI 10.1515/ama-2017-0041 acta mechanica et automatica, vol.11 no.4 (2017)

ROLE OF MAGNETORHEOLOGICAL FLUIDS AND ELASTOMERS IN TODAY'S WORLD

Paweł SKALSKI*, Klaudia KALITA**

*Transport Department, Center of Transportation and Energy Conversion, Institute of Aviation, Al. Krakowska 110/114; 02-256 Warszawa, Poland
**Faculty of Mechanical Engineering and Aeronautics, Rzeszow University of Technology, Al. Powstańców Warszawy 8, 35-959 Rzeszów, Poland

pawel.skalski@ilot.edu.pl, klaud14@gmail.com

received 11 August 2016, revised 24 October 2017, accepted 30 October 2017

Abstract: This paper explains the role of magnetorheological fluids and elastomers in today's world. A review of applications of magnetorheological fluids and elastomers in devices and machines is presented. Magnetorheological fluids and elastomers belong to the smart materials family. Properties of magnetorheological fluids and elastomers can be controlled by a magnetic field. Compared with magnetorheological fluids, magnetorheological elastomers overcome the problems accompanying applications of MR fluids, such as sedimentation, sealing issues and environmental contamination. Magnetorheological fluids and elastomers, due to their ability of dampening vibrations in the presence of a controlled magnetic field, have great potential present and future applications in transport. Magnetorheological fluids are used e.g. dampers, shock absorbers, clutches and brakes. Magnetorheological dampers and magnetorheological shock absorbers are applied e.g. in damping control, in the operation of buildings and bridges, as well as in damping of high-tension wires. In the automotive industry, new solutions involving magnetorheological elastomer are increasingly patented e.g. adaptive system of energy absorption, system of magnetically dissociable [hooks/detents/grips], an vibration reduction system of the car's drive shaft. The application of magnetorheological elastomer in the aviation structure is presented as well.

Key words: Damper, Magnetorheological Fluid, Magnetorheological Elastomer, Smart Material, Shock Absorber, Application

1. INTRODUCTION

Scientists working in the area of material science, are contributing to the development of new materials or discovering new properties of already known materials. The 80's of the XX century were the beginning point of a rapid increase of interests in materials, which were named smart (Carlson, 2001; Kaleta, 2013; Bajkowski, 2014). This group of materials includes magnetorheological fluids and elastomers, which are characterized by the fact that they change their rheological properties under the influence of a magnetic field (Carlson 1999). The presented magnetorheological materials are very useful in solving damping problems, which are one of main engineering dilemmas of construction and exploitation of machines and devices (Bajkowski, 2014). A damper is a mechanical device that has a dulling or deadening influence. Shock absorber, or shock damper is what you call a mechanism used for absorbing or partially eliminating the energy of sudden impulses or shocks in machinery or structures (Carlson, 1994). Dampening devices have been around for a long time, even in early transportation means such as carriages. These devices have remained relevant for years, and with the fast development of technology, there is a constant need to improve and revolutionize dampening mechanics. An example of developments in dampening devices is the use of materials such as magnetorheological fluids, which have been used to create dampers with better functionality and performance. Magnetorheological dampers have a very broad range of use, from seismic response reduction, to shock absorbers used in vehicles in order to provide comfortable riding over a rough terrain, or in bumpers of automobiles for reducing impacts during accidents (Imthiyaz, 2014; Li et al., 2016; MAGNERIDE™ Controlled Suspension System, 2013; http://robohub.org/icelands-ossur-wins-popsci-best-of-whats-new-award-for-symbionic-leg/). These fluids, however, have a series of disadvantages (sedimentation, sealing). This encouraged new solutions using magnetorheological elastomers, which overcome some of the difficulties which MR fluids create. One of the main assets of MR elastomers is the lack of sedimentation, as the ferromagnetic particles are embedded in a polymer matrix, which gives them a small range of motion. The achievable yield stress in MR fluids is also something that raises concern, as these smart fluids typically work in the post- yield region, while MR elastomers work in the pre-yield region. To add to that, MR elastomers do not need channels or seals to hold or prevent leakage, as they have a solid state of matter (Kaleta, 2013).

These smart materials, however, are not only useful in dampening technology, but also in motor shaft sealing mechanics, industrial treatment of polished surfaces, medicine, vibration isolation and more (Bajkowski, 2004; Bajkowski, 2005; Bajkowski, 2006; Bajkowski, 2007; Bajkowski, 2014; Goncalves, 2005; Griffin, 1998; Lee et al., 1999; Lee et al., 2009; Milecki, 2001; Milecki, 2004; Milecki et al., 1999).

In the second Section the magnetorheological fluids and magnetorheological elastomers are described. Then, in the third Section the applications of such smart materials are shown. At the end, the paper is concluded.

2. SMART MATERIALS – MAGNETORHEOLOGICAL FLUIDS AND ELASTOMERS

As new technologies are being developed, smart materials have found a large number of applications over the years. These materials are unique, as their properties can be changed by an external stimuli. In the case of magnetorheological fluids and

DOI 10.1515/ama-2017-0041

elastomers, viscoelastic and rheological properties can be controlled by the application of a magnetic field (Schwartz, 2009). Thanks to their specific characteristics, these materials create the ability to build systems with adaptive properties, which was impossible to achieve with conventional materials (Kaleta, 2013).

2.1. Magnetorheological fluids

MR fluids state of matter can be changed with the use of different levels of a magnetic field. These fluids are composed of magnetic particles suspended in a viscous fluid. With the absence of a magnetic field these fluids have a low viscosity, as the particles are not arranged. The particles are of a small size, measuring between 3 and 10 microns (Tao, 2011). The magnetic particles of an MR fluid are additionally covered with a special layer, enhancing their magnetic susceptibility and reducing their tendency to form aggregations. Other substances, including anti-corrosion and anti-sedimentation substances, are also added in small amounts. The influence of a magnetic field causes changes in the physical properties of an MR fluid.The application of such a field forces the particles to acquire a magnetic dipole, and to then to move and align themselves along the lines of the magnetic flux. This change in the material appears as a rapid increase in apparent viscosity and the fluid developing into a quasi-solid state. The fluid develops controllable yield strength, while the change depends on the size and strength of the magnetic field, as well as the composition of the fluid. After the disappearance of an external magnetic field the liquid returns to its baseline. The structure of magnetorheological fluids, and the behavior of the fluids under no magnetic field and with applied magnetic field applied are presented in Fig. 1. Changes under the influence of a magnetic field appear in less than 10 milliseconds. Magnetorheological fluids retain their properties in the temperature range of -40 ÷150 [^{o}C], while the yield point value for these liquids is in the range of 50 ÷ 100 [kPa] (Carlson and Weiss, 1994).

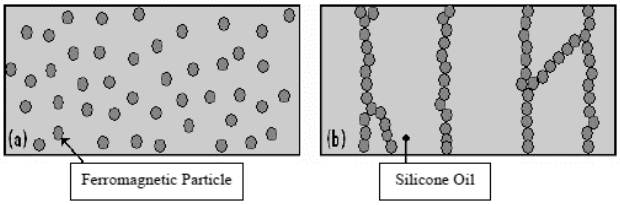

Fig. 1. Structure of magnetorheological fluids, ferromagnetic particles in a silicone oil suspension; (a) under no magnetic field, and (b) with magnetic field applied

Due to a difference in density and the force of gravity, the magnetic particles in a magnetorheological fluid settle out of the fluid in which they are entrained, making it lose its magnetic properties. Sedimentation is one of the greatest disadvantages of these smart materials, as additional measures have to be taken, e.g., introducing a single-walled carbon nanotube (SWNT) in CI based MR fluid (Fang et al., 2007), to create a device which overcomes this problem. Another problem that has to be dealt with is potential leakage into unwanted areas of the mechanism and thickening after prolonged use which creates the need of replacement. Nevertheless, the application set for MR fluids is vast, thanks to its precise controllability and dynamic response.

2.2. Magnetorheological elastomers

Magnetorheological elastomers generally consists of a natural or synthetic rubber matrix interspersed with micron sized (typically 3 to 5 microns) ferromagnetic particles. Elastomers such as rubber are used as they are generally soft and/ or deformable at room temperature, elastomers can have the ability to reversibly extend from 5-700% depending on the specific material. Thanks to a specially designed structure, the magnetic particles cannot move freely within the matrix. Therefore, there is no sedimentation. Magnetic field application stimulates a non-linear and reversible change of some of the properties. The limited movement of particles results in a quicker response to a magnetic field than in MR fluids. Magnetorheological elastomers work in the post-yield region, which differentiates them from MR fluids. There are two main types of MR elastomers: polarized elastomers (anisotropic) which have a strictly organized internal structure and isotropic elastomers (Kaleta, 2013). The difference between these two kinds of MR elastomers, is that, during the production of anisotropic elastomers, an external magnetic field is applied. Fig. 2. presents a SEM image of the two types of MR elastomer.

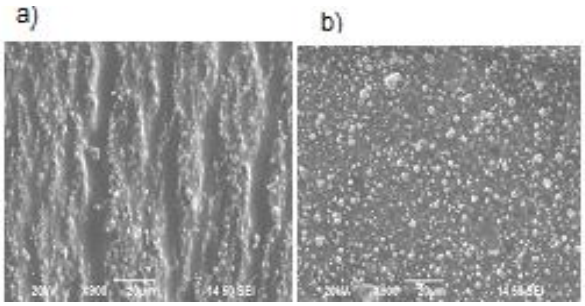

Fig. 2. SEM images of MREs: a) anisotropic MRE ; and b) isotropic MRE (Li et al., 2013)

What distinguishes anisotropic MR elastomers from MR fluids is that when the external magnetic field is removed, the anisotropic structure remains. The goal in the MR elastomers design is for the applied magnetic field to cause the greatest possible change in the materials properties. The size and shape of the magnetic particles, as well as the volume ratio of the magnetic particles to the matrix's material, have an important impact on the rheological effect (Kaleta, 2013). MR elastomers unique characteristics are what makes them have big market potential (Li et al., 2013).

3. MAGNETORHEOLOGICAL SMART MATERIALS IN APPLICATIONS

3.1. Applications of magnetorheological fluids

MR fluids have been found very useful in shock absorbers or dampers. These dampers are filled with a magnetorheological fluid, which, after the application of an external magnetic field changes from liquid to semi solid state, allowing the dampening characteristics to be controlled by the field. One of its main uses is

DOI 10.1515/ama-2017-0041

in semi-active vehicle suspensions which can adapt to road conditions (Carlson et al., 2000). One of the leaders in MR fluid technology in vehicle suspensions is LORD corp., which is the exclusive supplier of MR fluid technology to BWI for their Magneride primary suspension system for automotive applications. These systems are now used on more than 1,000,000 vehicles from multiple automotive OEMs including Ferrari, Audi, GM, Land Rover and others. Their MR fluids are of very high quality, advocated of having a fast response time, dynamic yield strength, temperature resistance as well as a hard settling resistance (Int. 1). This increase in commercial interest is largely due to the success of research projects and through the efforts of Lord Corporation. Schematics of LORD MR dampers are presented in Fig.3.

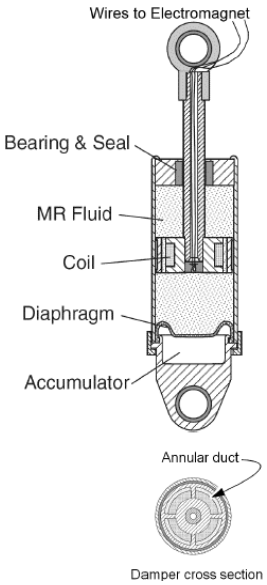

Fig. 3. Schematic of single ended MR damper and double ended MR damper, both produced by Lord (Spaggiari, 2013)

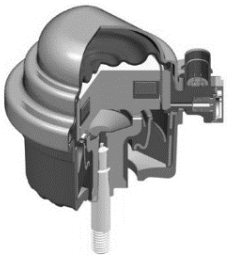

Fig. 4. BWIGroup powertrain mount using magneto-rheological technology (Magneto-Rheological Mounts, 2013)

Extensive analysis of the properties of magnetorheolgical fluids is included in Seval Genc's thesis (Genc, 2002), and the work of Fernando D. Goncalves (Goncalves, 2005). More information on MR fluids' properties can also be found in works: (Rabinow, 1948; Rabinow 1951; Nyawako and Reynolds, 2007).

BWIGroup, a leading global supplier of ride control systems, has introduced into production a powertrain mount using magneto-rheological technology (Fig. 4). The mount contains an electromagnetic coil that can generate a variable magnetic flux across the fluid passages. When the coil current is off, the MR fluid is not magnetised, the iron particles are randomly dispersed within the fluid, and the fluid behaves like conventional hydraulic oil. When the coil is energized, the magnetic field causes the particles to align into fibrous structures in the direction of the magnetic flux. The strength of the bond between the particles in the structures is proportional to the strength of the magnetic field, so changing the current provides real-time variable damping with a very large range of force variation (Fang et al., 2007).

Dampers and shock absorbers are used for example in vibration security systems, exploitation of buildings and bridges (Dyke et al., 1996; Dyke et al., 1998; Gordaninejad, 2002; Hiemenz and Wereley, 1999), and also in damping of vibrations of high – voltage wires (Sapinski et al., 2006; Sapinski and Snamina, 2007). The Dr. Franjo Tudjmann Bridge near Dubrovnik in Croatia has adaptive cable dampers installed which significantly reduce the oscillation amplitudes of the cables (Fig. 5.) (https://www.dywidag-systems.com/emea/projects/project-details/article/dr-franjo-tudjmann-bridge-dubrovnik-croatia.html).

Fig. 5. Cable vibration dampers based on MR fluid technology (https://www.dywidag-systems.com/emea/projects/project-details/article/dr-franjo-tudjmann-bridge-dubrovnik-croatia.html)

Magnetorheological dampers are also used in the process of vibration damping of car's suspension (Fig. 6) (Int. 3), in driver's seats in large trucks, to reduce harmful vibration that are transferred to the human body (Sassi et al., 2005; Park and Jeon, 2002), as well as in the construction of washing machines (Fig. 7). A simple, inexpensive magnetorheological fluid sponge designed for incorporation into washing machines consists of a steel bobbin and coil surrounded by a layer of foam saturated with MR fluid. The elements constitute a piston on the end of the shaft that is free to move axially inside a steel housing that provides the ma netic flux return path. The damping force is proportional to the sponge's active area (Carlson, 2002).

Fig. 6. MagneRide controlled suspension system-magneto-rheological damper technology (MAGNERIDE™ Controlled Suspension System, 2013)

DOI 10.1515/ama-2017-0041

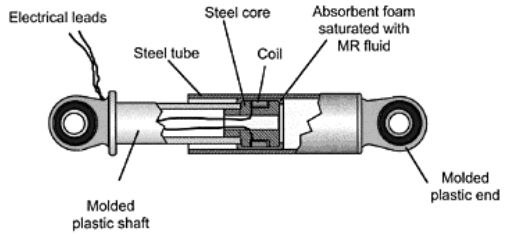

Fig. 7. Inexpensive magnetorheological fluid sponge designed for incorporation into washing machines (Carlson, 2002)

Because of the possibility of changing their physical quantities, these fluids find use in sealing technology in different mechanical elements, such as, motor shafts working under special conditions, e.g., in mines, ventilator shafts and in elements of bioreactors and chemical reactors, and other mechanical elements. They are also used in precise industrial processing of polished surfaces (Bajkowski, 2014). The sealing system presented in Fig. 8 consists of a permanent magnet 3 placed between two rings with a high magnetic permeability 4. The magnetic flux penetrates the rings 4 MR fluid 5 shaft 6 and ring 2 or bearing 7 (Muc and Barski, 2007).

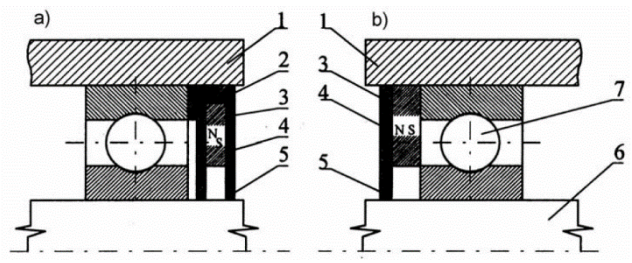

Fig. 8. Schematic of a sealing system in a motor bearing element with the use of MR fluids (Muc and Barski, 2007)

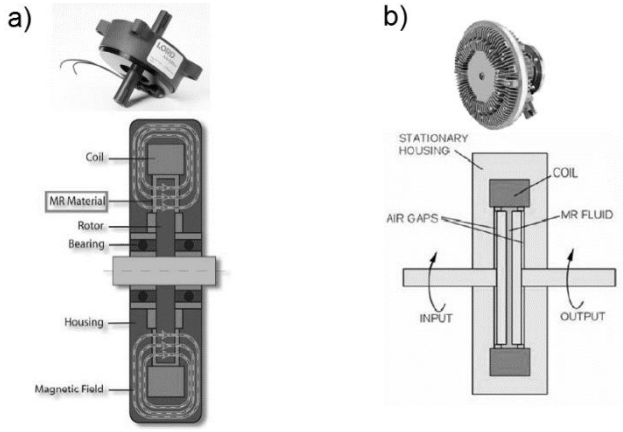

Fig. 9. Picture and schematic of a) MR based brake and b) clutch, both produced by Lord (Spaggiari, 2013)

Magnetorheological fluids are also used in the production of magnetorheological composites (Kaleta and Lewandowski, 2007; Kaleta et al., 2007), in the construction of clutches and brakes (Fig. 9) (Kikuchi et al., 2009; Kikuchi et al., 2010; Park et al., 2008; Spaggiari, 2013), robots (Yoon et al., 2003), in CD and DVD drives (Szeląg et al., 2000), in medical activities, such as devices for rehabilitation (Avraam, 2009; Carlson, 2001), or in-vitro methods (Flores and Liu, 2002), in printing (Muc and Barski, 2007), in suspension of planes and helicopters (Skorupka, 2010), in the construction of guns (Poynor, 2001; Bajkowski M., 2006).

Intensive work is being conducted on the broad use of magnetorheological fluids in medicine, especially orthopedics (Bajkowski, 2014). Examples are shown in Fig.10 and Fig. 11.

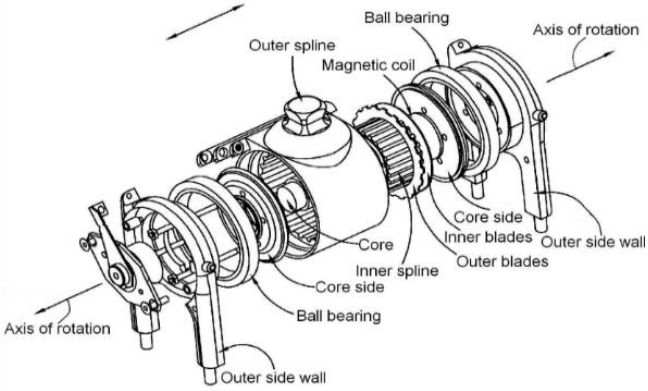

Fig. 10. A detailed exploded perspective view of a magnetorheologically actuated prosthetic knee (Thorarinsson, 2006)

Fig. 11. The microprocessor-controlled Rheo Knee This is the first prosthetic component to use magnetorheological fluid to control joint resistance (http://robohub.org/icelands-ossur-wins-popsci-best-of-whats-new-award-for-symbionic-leg/)

Another example of MR fluid application is in the stabilization of knee joints, elbows, and ankles after an operation or injury. The pressure applied to these joints can be controlled by magnetorheological dampers, which can help speed up the process of rehabilitation (Bajkowski, 2014).

There is also potential for MR fluid dampers to be used in aviation, with ongoing work on the application in the rotary wing industry to isolate vibrations from the aircraft structure and crew (Forte et al., 2004). There are three different ways in which MR fluid can be used: squeeze mode, valve mode and shear mode. The mode used depends on the designation of the damper. A device that uses squeeze mode has a layer of MR fluid that is placed between paramagnetic pole surfaces, while devices operating in shear mode have when a layer of MR fluid between two paramagnetic moving surfaces. Flow mode uses MR fluid to impede the flow of MR fluid from one reservoir to another. This last mode can be used in dampers and shock absorbers, by using the movement to be controlled to force the fluid through

DOI 10.1515/ama-2017-0041

channels, across which a magnetic field is applied (Olabi and Grunwald, 2007; Poynor, 2001). Aside from the other disadvantages of MR fluids mentioned previously, they also tend to be expensive and are still a limited feature.

More information about magnetorheological fluids and their applications can be found in the book J. Bajkowskiego (Bajkowski, 2014), and other publications (Skorupka, 2010; Kaleta, 2013; Milecki and Lawniczak, 1999; Sapinski, 2006; Goncalves, 2005; Schwartz, 2009; Muc and Barski, 2007; Carlson and Jolly, 2009; Spaggiari, 2013; Skalski, 2014; Tao, 2011; Genc, 2002).

3.2. Applications of magnetorheological elastomers

In comparison to MR fluids, MR elastomers are not widely used as dampening devices. Because of some of the downsides that MR fluids present, MR elastomers are starting to receive attention, as they have many potential engineering applications (Li et al., 2014). They have found function in developing adaptive tuned vibration absorbers and vibration isolation systems, since their stiffness changes within a magnetic field (Spaggiari, 2013; Carlson et al., 2000). A variable stiffness absorber based on magneto-rheological elastomer was designed, its features were published by The Transactions of Nonferrous Metals Society of China in 2009. Active and semi active vibration isolation systems based on magnetorheological materials were also created (Bazinenkov et al., 2004; Xiao et al., 2009; Spencer et al., 2007). The devices shown in Fig. 12 and Fig. 13 use coils to generate the magnetic field. There are, however, few designs of dampers using MR elastomer technology.

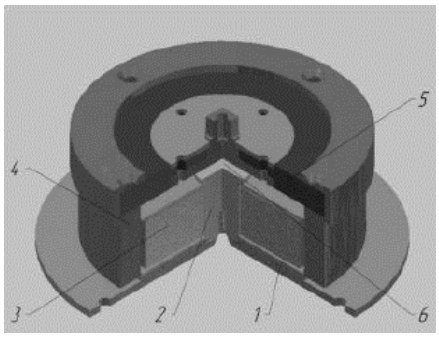

Fig. 12. The design of the damper based on MR elastomer: 1 – foundation, 2 – magnetic core, 3 – electromagnetic core, 4 – magnetic conductor rings, 5 – membrane of the MR elastomer, 6 – air gap (Bazinenkov et al., 2004)

Magnetorheological elastomers have a big potential, which can be used in the motorization industry. One of the solutions which includes MR elastomer is a patent (Watson, 1997) owned by Ford Motor Company, concerning the regulation of the suspension elements stiffness by implementing a sleeve with adjustable rigidity. In this solution, the magnetorheological elastomer is placed in between two sleeves; the one located inside is connected with the moving parts of the suspension, and the one on the outside is connected with the bodywork. An additional part of the system is a coil located in between the composite and the inside cylinder. The rigidity of the magnetorheological composite is regulated with the coil in which the magnetic field is induced. This solution can reduce the oversteer and understeer of a vehicle and can reduce the noise generated by the vibrations of a car body.

A similar solution was used to eliminate the vibrations of brake discs (Stewart, 1998). The previously described element consisting of the two cylinders' discs with a layer of magnetorheological elastomer in between them was used in this method. Rigidity of the composite changes as the electric current going through the coil (which is reeled around the layer of elastomer) varies. The current value is set by the control system based on the data received from the sensor in the braking system.

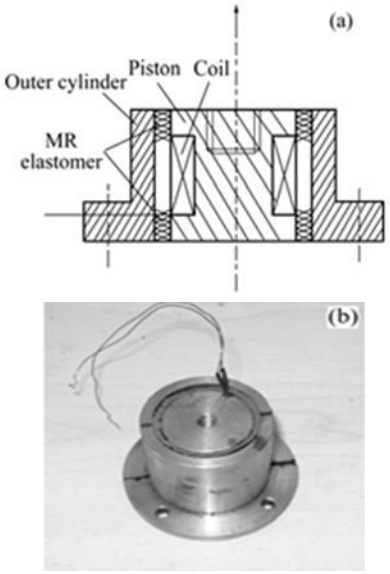

Fig.13. Schematic configuration (a) and photograph(b) of MRE absorber (Xiao et al., 2009)

A method of fast regulation of the physical properties of the elastomer elements in cars can be found in literature available on this topic (Elie, 1999). In traditional solutions the elastomer parts, such as, sleeves in the suspension, parts of the engine fastening, the propulsion transfer system and exhaust system have unchangeable physical properties. By replacing them with magnetorheological elastomer and adding a control system, it is possible to vary their rigidity, and therefore to adjust the level of noise and vibration, moreover to eliminate dipping of the car during braking, oversteer and understeer.

Thyssen Krupp AG company has developed a steering wheel column with an adaptive system of energy absorption in case of a crash, in which magnetorheological elastomer is applied to one of the elements (Klukowski, 2009). This solution differs from the previous one which has a metal element responsible for energy absorption. Due to the implementation of MRE, the new solution accommodates factors such as the vehicle's velocity and driver's mass.

General Motors has developed a system which absorbs energy during a crash (Barvosa-Carter, 2006). It can be installed inside headrests, seats, the dashboard, doors or over driver's and passengers' heads. This patented solution is composed of a rigid base and an elastic cover. In between them are the cylindrical elements made of magnetorheological elastomer with the coil reeled on them. The whole system is equipped with sensors and a control system.

Fig. 14 illustrates the reversibly expandable energy absorbing assembly in a pre-deployed, i.e. a stowed or original configuration. An exemplary reversibly expandable energy absorbing assembly, generally indicated as (10), utilizing actively controlled and engi-

DOI 10.1515/ama-2017-0041

neered materials comprises a flexible covering (12) attached to a rigid support structure 14 (Barvosa-Carter, 2006).

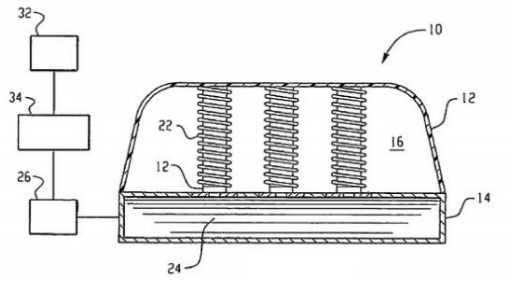

Fig. 14. A schematic illustrating an energy absorbing assembly in a stowed or pre-deployed configuration in accordance with the present disclosure (Barvosa-Carter, 2006)

Automotive companies have patented solutions which can have applications not only in the motorization industry, but in others as well. For instance, GM has developed a system of magnetically dissociable [hooks/detents/grips] which contains MR elastomer in its conformation (Ottaviani, 2006). This particular system can be used for vibration elimination.

Detents, which are opened and closed with the use of a magnetic field, were used to develop an entire system of separable securing of the various components of the car, for example closing the trunk lid or doors (Ottaviani, 2006). The proposed solution makes closing and opening of the lid easier, as well as absorbs more energy in case of an accident than the traditional single-point locks. As shown in Fig. 15 a releasable fastener system, generally indicated as (10), comprises a loop portion (12) and a hook portion (14). The loop portion (12) includes a support (16) and a loop material (18) disposed on one side thereof whereas the look portion (14) includes a support (20) and a plurality of closely spaced upstanding hook elements (22) extending from one side thereof. The hook elements (22) are formed of a magnetorheological elastomer that provides a shape changing and/or flexural modulus capability to the hook elements (22). The description can be find in (Ottaviani, 2006).

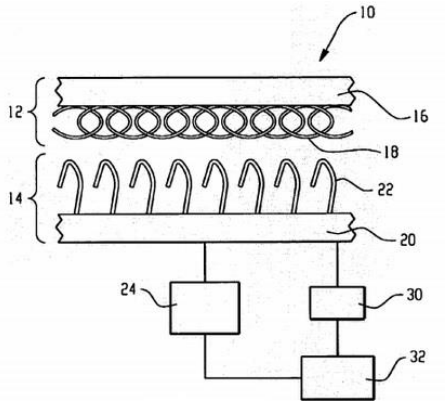

Fig. 15. A cross sectional view of a releasable fasting system (Ottaviani, 2006)

In the automotive industry, magnetorheological elastomers are used in the construction of engine covers or boots, for instance (Brei et al., 2006). In the proposed solution developed by General Motors Corporation and the University of Michigan, the cover, which in normal operation is close to the engine or luggage, deforms in the instance of a crash in such a way that it increases energy absorption.

Magnetorheological elastomer may be used as such a skin. Research is being done on the content of carbonyl iron particles, which are responsible for changing the rheology of the material in the presence of an external magnetic field. The first tests have shown that the properties of the material can be controlled by varying the external magnetic field. The process is completely reversible and the magnetorheological material bodes well in constructional solutions made of morphing structures. Fig. 16 shows a new magnetorheological elastomer destined for use in aviation structures (Skalski, 2014).

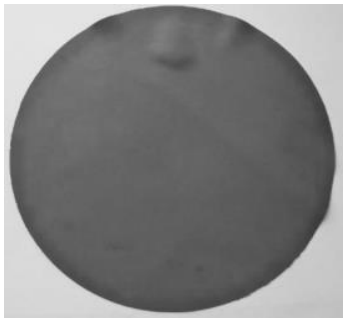

Fig. 16. View of a magnetorheological skin (Skalski, 2014)

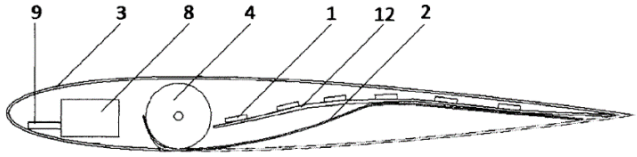

Fig. 17. A schematic view of the morphing structure with a magnetorheological elastomer (Skalski et al., 2014)

In the reported Polish patent (Skalski et al., 2014) an airfoil with a variable shape was described. It has an elastic coating made from an active material (magnetorheological elastomer) allowing to change the aerodynamic characteristics of an aircraft wing or a rotary blade during flight. In this solution (Skalski et al., 2014) presented in Fig.17, a thin layer of magnetorheological elastomer (2) was placed on the upper side of the reversed wing (3). Magnets (1) were placed underneath this surface (12) in order to generate a strong magnetic field that would attract the MR elastomer (2) and therefore change the overall profile of the wing. One end of the MR elastomer (2) is connected to a shaft (4), second end is fixed to the wing (3). The control module (9) is connected to the power supply (8). The control module controls (9) the servomechanism (Skalski et al., 2014).

4. CONCLUSIONS

To sum up, as new technologies are being developed, magnetorheological fluids and elastomers have found a large number of applications over the years. These materials are unique, as their properties can be changed by an external stimuli. In the case of magnetorheological fluids and elastomers, viscoelastic and rheological properties can be controlled by the application of an magnetic field. Thanks to their specific characteristics, these

DOI 10.1515/ama-2017-0041

materials create the ability to build systems with adaptive properties, which was impossible to achieve with conventional materials.

These smart materials are used e.g. in dampers, shock absorbers, clutches and brakes. Magnetorheological dampers and magnetorheological shock absorbers are applied e.g. in damping control, in the operation of buildings and bridges, as well as in damping of high-tension wires.

New solutions which regard implementing magnetorheological elastomers for automotive applications are constantly being patented/ licensed.

In the aerospace industry magnetorheological elastomers are desirable for use in morphing structures. Morphing in aerospace applications is becoming more and more popular due to the possibility of increasing the productivity and efficiency of flight. With MR elastomers, the development of new aircraft structures becomes possible. The main challenge for the next years and decades will be to adapt, at industrial level, developments made in laboratories, like new structures with more flexibility and ability to distort in a controlled way.

REFERENCES

1. **Avraam M.T.** (2009): *MR-fluid brake design and its application to a portable muscular rehabilitation device,* PhD thesis, Active Structures Laboratory Department of Mechanical Engineering and Robotics, Universite Libre de Bruxelles.
2. **Bajkowski J.** (2004), Modeling, mathematical description, simulation and experimental research of magnetorheological damper with influence of temperature, *Machine Dynamic Problems*, 28(3), 9-15.
3. **Bajkowski J.** (2014), *Magnetorheological fluids and dampers, Properties, structure, investigations, modeling and applications*, Transport and Communication Publishers, Warsaw (in Polish).
4. **Bajkowski J., Bajkowski M., Zalewski R.** (2007), *L'influence de la temperature sur le travail d'un amortiseur magnetorheologique,* XV French-Polish Seminar of Mechanics, France.
5. **Bajkowski J., Grzesikiewicz W., Holnicki J., Parafiniak M., Wołejsza Z.** (2005), *Analysis of the influance of magnetorheological damper on the airplane chassis during landing*, ECOMAS, Lizbona.
6. **Bajkowski M.** (2006), *Analysis of the influence of selected characteristics of a magnetorheological damper on change of dynamic properties of special object model*, PhD dissertation, Warsaw University of Technology, SiMR, Warsaw.
7. **Barvosa-Carter W., Johnson N.L., Browne A.L.** (2006), *Reversibly expandable energy absorbing assembly utilizing actively controlled and engineered materials for impact management and methods for operating the same*, US patent 7.140.478 B2.
8. **Bazinenkov A., Valery P. Mikhailov V.P.** (2004), Active and semi active vibration isolation systems based on magnetorheological materials, *Procedia Engineering*, 106, 170-174.
9. **Brei D., Redmond J., Wilmont A.L., Browne N.A., Johnson N.L., Jones G.L. (2006)**, *Hood lift mechanisms utilizing active materials and methods of use*, EU patent EP 1 617 022 A2.
10. **Carlson J. D.** (2001), What makes a good MR fluid?, *Proceedings of the Eighth International Conference*, Electrorheological Fluids and Magnetorheological Suspensions.
11. **Carlson J.D.** (1999), Low-cost MR fluid sponge devices, *Proceeding of the 7th international conference on ER fluids and MR suspensions*, World Scientific Publishing Co. Pte. Ltd., Honolulu Hawaii.
12. **Carlson J.D., Jolly M.R.** (2000), MR fluid, foam and elastomer devices, *Mechatronics*, 10, 555-569.
13. **Carlson J.D., Weiss K.D.** (1994), A growing attraction to magnetic fluids, *Machine Design*, 8, 61-66.
14. **Dyke S.J., Spemcer B.F., Sain M.K., Carlson J.D.** (1998), An experimental study of MR dampers for seismic protection, *Smart Mater Struct.*, 7, 693-703.
15. **Dyke S.J., Spencer B.F., Sain M.K., Carlson J.D.** (1996*),* Modeling and control of magnetorheological dampers for seismic response reduction, *Smart Materials and Structures*, 5(5), 565-575.
16. **Elie L.D., Ginder J.M., Mark J.S., Nichols M.E., Stewart W.M.** (1999), *Method for allowing rapid evaluation of chassis elastomeric devices in motor vehicles*, US patent 5.974.856.
17. **Fang F.F., Jang I. B., Choi H.J.** (2007), *Single-walled carbon nanotube added carbonyl iron suspension and its magnetorheology*, Department of Polymer Science and Engineering, Inha University, Incheon, 402-751, Republic of Korea.
18. **Flores G.A., Liu J.** (2002), In-Vitro blockage of a simulated vascular system using magnetorheological fluids as a cancer therapy*, European Cells and Materials*, 3, 9-11.
19. **Forte P., Paternò M., Rustighi E.** (2004), A Magnetorheological Fluid Damper for Rotor Applications, *International Journal of Rotating Machinery*, 10(3), 175-182.
20. **Genc S.** (2002*), Synthesis and properties of magnetorheological (MR) fluids*, PhD dissertation, University of Pittsburgh.
21. **Goncalves F.D.** (2005), *Characterizing the behavior of magnetorheological fluids at high velocities and high shear rates*, PhD thesis, Virginia Polytechnic, Blacksburg.
22. **Gordaninejad F., Sahdi M., Hansen B.C., Chang F.K.** (2002), Magneto-rheological fluid dampers for control of bridges, *J. of Int. Material Systems and Structures*, 13, 167-180.
23. **Griffin M.J., Wu X.** (1998), The influence of end-stop buffer characteristics on the severity of suspension seat-stop impacts, *Journal of sound and vibration*, 215(4), 989-996.
24. **Hiemenz G., Wereley N.** (1999), Seismic response of civil structures utilizing seni-active MR and ER bracing systems, J*ournal of intelligent material systems and structures*, Vol 10, Issue 8, 646-651.
25. **Imthiyaz T.A, Sundarrajan R., Prasaath G.T., Raviraj V.** (2014), Implementation of Magneto-rheological Dampers in Bumpers of Automobiles for Reducing Impacts during Accidents, *Procedia Engineering*, 97, 1220-1226.
26. **Kaleta J.** (2013), *Magnetic Materials SMART: Structure, manufacturing, investigations, properties, applications*, Publishing House of Wroclaw University of Technology, (in Polish).
27. **Kaleta J.Z., Lewandowski D.** (2007), Inelastic properties of magnetorheological composites: I. Fabrication, experimental tests, cyclic shear properties, *Smart Materials Structures*, 16, 1948-1953.
28. **Kaleta J.Z., Lewandowski D., Ziętek G.** (2007), Inelastic properties of magnetorheological composities: II: Model identification of parameters, *Smart Materials and Structures*, 16, 1954-1960.
29. **Kikuchi T., Ikeda K., Otsuki K., Kakehashi, Furusho J.** (2009), Compact MR fluid clutch device for human-friendly actuator, Journal of Physics, 149, 1-4.
30. **Kikuchi T., Otsuki K., Furusho J., Abe H.** (2010), Design and development of compact magnetorheological fluid clutch (CMRFC) with Multi-layered disks and micro-sized gaps, *Journal of the Society of Rheology*, 38, 17-22.
31. **Klukowski C.** (2009), *Steering column for a motor vehicle*, US patent 20090033082 A1.
32. **Lee H.G., Sung K.G., Chois S.B.** (2009), Ride comfort characteristics with different tire pressure of passenger vehicle featuring MR damper, *Journal of Physics*, 149, 1-4.
33. **Lee U., Kim D., Jeon D.** (1999), Design analysis and experimental evaluation of an ER and MR clutch, *Journal of intelligent materials and structures*, Vol 10, Issue 9, pp. 701-707.
34. **Li W.H., Zhang X.Z., Du H.** (2013), *Magnetorheological elastomers and their applications*, University of Wollongong, Research Online
35. **Li Y., Li J., Li W.,Du, H.** (2014), A state-of-the-art review on magnetorheological elastomer devices, *Smart Materials and Structures*, 23(12), 1-24.
36. **Li Z.X., Yu Chen Y., Yun-Dong Shi Y.** (2016), Seismic damage control of nonlinear continuous reinforced concrete bridges under extreme earthquakes using MR dampers, *Soil Dynamics and Earthquake Engineering*, 88, 386–398.

DOI 10.1515/ama-2017-0041

37. **Milecki A.** (2001), Investigation and control of magneto-rheological fluid dampers, *International journal of machine tools & manufacture*, 41, 379-391.
38. **Milecki A.** (2004), Modeling of magneto-rheological schock absorbers, *Archiwum technologii maszyn i automatyzacji* (In Polish), Vol 24, no. 2, 123-129.
39. **Milecki A., Ławniczak A.** (1999), *Electro- and Magnetorheological fluids and their applications in technics,* Publishing house of Poznan University of Technology (in Polish).
40. **Muc A., Barski M.** (2007), *Magnetorheological fluids and their practical applications*, Publishing house of Cracow University of Technology (in Polish).
41. **Nyawako D., Reynolds P.** (2007), Technologies for mitigation of human – induced vibrations in civil engineering structures, *The shock and vibration digest*, 39(6), 465-493.
42. **Olabi A. G., Grunwald A.** (2007), Design and application of magneto-rheological fluid, *Materials and Design*, 28, 2658-2664.
43. **Ottaviani R.A., Ulicny J.C., Golden M.A.** (2006), *Magnetorheological nanocomposite elastomer for releasable attachment applications*, US patent 6.877.193 B2.
44. **Park Ch., Jeon D.** (2002), Semiactive vibration control of a smart seat with an MR fluid damper considering its time delay, *Journal of intelligent material systems and structures*, 13, 521-524.
45. **Park E. J., Falcao L., Suleman A.** (2008), Multidisciplinary design optimization of an automotive magnetorheological brake design, *Computers and Structures*, 86, 207-216.
46. **Poynor J. C.** (2001), *Innovative Designs for Magneto-Rheological Dampers*, master thesis, Virginia Polytechnic, Blacksburg.
47. **Rabinow J.** (1948), *The magnetic fluid clutch*, AIEE Transactions, 67: 1308-1315.
48. **Rabinow J.** (1951), *Magnetic fluid torque and force transmitting device*, U.S. Patent 2, 575.
49. **Sapiński B.** (2006*), Magnetorheological dampers in vibration control*, AGH University of Science and Technology Press, Kraków
50. **Sapiński B., Snamina J.** (2007), Cable – MR damper system motion in transients, *Mechanics* 26, 22-29.
51. **Sapiński B., Snamina J., Maślanka M, Rosół M.** (2006), Facility for testing of magnetorheological damping systems for cable vibrations, *Mechnics*, 25/3, 135-
52. **Sassi S., Cherif K., Mezghani L., Thomas M., Kotrante A.** (2005), An innovative magnetorheological damper for automotive suspension: from design to experimental characterization, *Smart Mater. Struct.*, 14, 811-822.
53. **Schwartz M.** (2009), *Smart Materials*, Taylor and Francis Group
54. **Skalski P** (2014), *Morphing Structure with a Magnetorheological Material – Preliminary Approach*, Mechatronics 2013 Recent Technological and Scientific Advanced. Springer International Publishing, 219-226.
55. **Skalski P., Parafiniak M., Wysokiński D., Bednarski M.** (2014), *Aerodynamic profile with elastic skin of active material*, P-409202, Polish patent, 29.02.2016.
56. **Skorupka Z.** (2010), Magnetorheological fluids as method for active controlling of landing gear shock absorber characteristic, *Transactions of the Institute of Aviation*, 207, 36-48.
57. **Spaggiari A.** (2013), *Properties and applications of Magnetorheological fluids, Dept. of Engineering Sciences and Methods*, University of Modena and Reggio Emilia, Italy.
58. **Spencer B. F., Tomizuka M., Yun C. B., Chen W. M., Chen R. W.** (2007) World Forum on Smart Materials and Smart Structures Technology, *Proceedings of the World Forum on Smart Materials and Smart Structures Technology*, Taylor & Francis Group, 291-294.
59. **Stewart W.M., Ginder J.M., Ellie L.D., Nicholas M.E.** (1998), *Method and apparatus for reducing brake shudder*, US patent 5.816.587.
60. **Szeląg W., Nowak L., Myszkowski A.** (2000), Electromagnetic brake with magnetorheological fluid, Scientific Works of the Institute of Electric Machines, Drives and Measurements, 48, 206-213.
61. **Tao R**. (2011), Electro-Rheological Fluids And Magneto-Rheological Suspensions, *Proceedings of the 12th International Conference, World Scientific, Singapure*, 748.
62. **Thorarinsson E. T., Jonsdottir F., Palsson H.** (2006), *Design of a Magnetorheological Prosthetic Knee*, Department of Mechanical Engineering, University of Iceland.
63. **Watson J.R.** (1997*), Method and apparatus for varying the stiffness of a suspension busing*, US patent 5.609.353.
64. **Xiao-min D., Yu Miao, Liao C., Chen W.** (2009), *A new variable stiffness absorber based on magneto-rheological elastomer*, Transactions of Nonferrous Metals Society of China, 19, 611-615.
65. **Yoon S.-S., Kang S., Kim S.J., Kim Y.-H., Kim M., Lee C.** (2003), Safe arm with MR-based passive compliant joints and visco-elastic covering for service robot applications, *Intl. Conference on Intelligent Robots and Systems*, October, Nevada, 2191-2196.
66. BWI Group.com, MAGNERIDE™ CONTROLLED SUSPENSION SYSTEM (2013), http://www.bwigroup.com/en/pshow.php?pid=22; 08.08.2016.
67. BWI Group.com, MAGNETO-RHEOLOGICAL MOUNTS (2013) http://www.bwigroup.com/en/pshow.php?pid=26; 08.08.2016.
68. **Carlson J.D.** (2002), http://www.sensorsmag.com/sensors/electric-magnetic/controlling-vibration-with-magnetorheological-fluid-damping-999; 08.08.2016.
69. http://robohub.org/icelands-ossur-wins-popsci-best-of-whats-new-award-for-symbionic-leg/; 08.08.2016.
70. https://www.dywidag-systems.com/emea/projects/project-details/article/dr-franjo-tudjmann-bridge-dubrovnik-croatia.html; 08.08.2016.
71. Magneto-Rheological (MR) Fluid, "LORD is proud to be the exclusive supplier of MR Fluid technology…" Retrieved from: http://www.lord.com/products-and-solutions/active-vibration-control/industrial-suspension-systems/magneto-rheological-(mr)-fluid; 08.08.2016.

DE GRUYTER
OPEN

DOI 10.1515/ama-2017-0042 acta mechanica et automatica, vol.11 no.4 (2017)

SYNTHESIS OF BARIUM TITANATE PIEZOELECTRIC CERAMICS FOR MULTILAYER ACTUATORS (MLAs)

Mojtaba BIGLAR[*], Magdalena GROMADA[**], Feliks STACHOWICZ[*], Tomasz TRZEPIECIŃSKI[*]

[*]Faculty of Mechanical Engineering and Aeronautics, Department of Materials Forming, Rzeszow University of Technology, Powst. Warszawy 12, 35-959 Rzeszów, Poland
[**]Institute of Power Engineering, Ceramic Department CEREL, Research Institute, ul. Techniczna 1, 36-040 Boguchwała, Poland

m_biglar@prz.edu.pl, gromada@cerel.pl, stafel@prz.edu.pl, tomtrz@prz.edu.pl

received 4 May 2015, revised 21 November 2017, accepted 24 November 2017

Abstract: In this paper the characteristics of $BaTiO_3$ ceramics synthesized by solid state method is presented. In order to receive the monophase ceramics the double activation and calcination were applied. A spray drier was used to granulate the powder of $BaTiO_3$. Isostatic and uniaxial pressing were applied to manufacture the barium titanate pellets. The properties of fabricated $BaTiO_3$ ceramics were determined at different stages of production. After the sintering phase, the hardness, the bending strength, the fracture toughness, and the coefficient of thermal expansion of barium titanate sinter were estimated. The $BaTiO_3$ powder is characterized by spherical grains and the average size of 0.5 μm. The small value of the specific surface area of granulate ensured good properties of material mouldability and finally allowed to receive sinters of high density.

Key words: Barium Titanate, MLAs, Multilayer Actuators, Solid State, Piezoelectric Ceramics

1. INTRODUCTION

Barium titanate, revealing both ferroelectric and piezoelectric properties, is a very desirable perovskite-type ceramic material in the field of electroceramics and microelectronics (Biglar et al., 2015; Vijatović et al., 2008). BaTiO3 is destined for many applications in different industries, such as energy storage devices and multilayer actuators (MLAs) (Miot et al., 1995; Kao and Yang, 1999). These applications require materials with a good density, a high dielectric constant and a low loss factor. BaTiO3 has become one of the most important ferroelectric material. At Curie temperature the barium titanate transforms from paraelectric to ferroelectric phase (Ertuğ, 2013). Synthesis of materials with these properties needs highly pure, fine grained ceramics, which may be obtained from homogeneous reproducible powders of spherical particles (Miot et al., 1995; Kholodkova et al., 2012).

Choi et al. (2008) underline that MLCs have been investigated because their advantages are high precision, little noise and low power consumption, compared with conventional multilayer actuators (MLAs). Two types of multilayer actuators are considered, namely, stacked-disk and co-fired (Yoshikawa and Shrout, 1993). Fine grain powders used for fabrication piezoelectric materials has an effect on lower driving voltages and higher driving fields (Hackenberger et al., 1998; Luo et al., 2011).

The properties of barium titanate have been the subject of study of many authors (i.e., Cai et al., 2011; Prado et al., 2016; Zheng et al., 2012). The powder fabrication method and the synthesis procedure strongly influence the features of barium titanate (Moura et al., 2009; Stojanovic et al., 1999; Vijatović et al., 2008).

A lot of synthesis methods have been developed for the preparation of barium titanate powders. Both the conventional solid state reaction methods, chemical methods and mechanochemical used to prepare barium titanate have been described in the literature. Large scale production is based on solid state reactions of mixed powders BaCO3 and TiO2 at high temperatures. However, this procedure results in agglomeration, poor chemical homogeneity and formation of secondary phases which harm the electrical properties of BaTiO3 (Kim et al., 2009, Othman et al., 2014). However, the solid state method has the advantages of low production cost, precise stoichiometry control, operating simplicity and possibility of its application on mass production (Kao and Yang, 1999; Kholodkova et al., 2012).

Considering the disadvantages of solid state method, searching for development of barium titanate synthesis techniques was widely described by other authors. Wet-chemical methods at the temperature less than 100°C were applied for obtaining of 50-60 nm particles (Kholodkova et al., 2012). Nguyen et al. (2007) have developed the hydrothermal synthesis. This technique is used for producing oxide layers on ceramic surfaces. The main advantages of hydrothermal method is a simple procedure and low temperature treatment.

In this paper, the fabrication method and properties of barium titanate ceramics are described. The powder of BaTiO3 is synthetized by solid state method. The goal of the investigation is to prepare suitable material for MLAs. At the end of the paper, all properties influencing the application of obtained material for the multilayer actuator were discussed.

2. EXPERIMENTS

The powder of barium titanate was fabricated from the TiO_2 (99% of purity, Kronos, USA) and $BaCO_3$ (99.5% of purity, Chempur, Poland). The raw materials were mixed with isopropyl alcohol

DOI 10.1515/ama-2017-0042

and milled in the mixer mill for two hours. The obtained powder was calcined in the electrical furnace for 8 hours at 1100°C. The double milling and calcination were necessary to obtain monophase material. The diffraction patterns were recorded by X-ray X'PertPROX diffractometer equipped with a detector of Cu Kα radiation. The particle size distribution of powder was determined using Mastersize 2000 (Melvern, United Kingdom). The specific surface area of powders was determined by using Autosorb-1 analyzer (Quantachrome, USA).

The morphology of powder was evaluated based on the SEM micrographs made by using HITACHI S-3400N/2007 microscopy. To ensure good mouldability the $BaTiO_3$ powder was granulated with the use of Niro spray drier (GEA, Germany). The spray pressure was equal to the equivalent of 40 mm water column. The values of inlet and outlet temperatures were equal to 220°C and 80°C, respectively. The properties of received granulate i.e., the specific surface area and the phase composition were also determined. The isostatic and uniaxial pressing is used to manufacture the $BaTiO_3$ pellets.

The green pellets were sintered in the electrical furnace. The dilatometric curves were used to ensure the suitable sintering conditions. The maximal sintering temperatures were 1250, 1300, 1350, 1400 and 1450°C. The both cooling and heating rates were set to 100°C/h. Sintered pellets were denoted, respectively: $BaTiO_3$(0), $BaTiO_3$(1), $BaTiO_3$(2), $BaTiO_3$(3) and $BaTiO_3$(4).

The parameters characterizing the extent of material sintering: the apparent density, the apparent porosity, the water absorbability were estimated for sintered pellets by method taking advantages of Archimedes law. In the next stage, the pellet of the average density, sintered at 1300°C ($BaTiO_3$(1)) was considered and characterised in the direction of XRD and SEM.

The mechanical properties such as the hardness, the bending strength and the fracture toughness, and the coefficient of thermal expansion were determined based on the fabricated beams. These beams were manufactured according to the procedure used to fabricate $BaTiO_3$(1) pellets. The linear expansion coefficient was determined using a dilatometer (BÄHR-Gerätebau, Germany). The fracture toughness and Vickers hardness of $BaTiO_3$(1) were performed on 430/450SVD testing machine (Melit, Switzerland). The flexural strength of $BaTiO_3$(1) specimen was determined on a standard universal testing machine Z030 (Zwick/Roell, Germany) equipped with a 3-point bending device.

3. RESULTS AND DISCUSSION

The XRD pattern of powder of $BaTiO_3$ is shown in Fig. 1. The peaks of synthesized powder very well overlap with the standard ones. So, it was found that to obtain monophase powder the two mechanical activation and calcination processes are necessary.

An analysis of the morphology of barium titanate presented in Fig. 2a led to conclude that powder was characterized by uniform structure. The dimensions of the individual grains are very similar and equal to 0.5 μm (Fig. 2b). The small number of grains have an average diameter of about 1 μm.

In the Fig. 3 the distribution of particle size of $BaTiO_3$ powder is presented. The particle size distribution ranged between 0.3 μm and 80 μm.

However, the average particle size was equal to 1.59 μm. The grains of $BaTiO_3$ powder had a tendency to create agglomerates. The average size of the separate grain is almost three times smaller than the size of particles of agglomerates. The similar conclusion was found by Yoon and Lee (2004) who analysed the mean particle size and specific surface area of barium titanate fabricated also by solid state technique. In our investigations the specific surface area of powder particles was equal to approximately 1.9 m^2/g. Presented in Fig. 4 the XRD pattern of granulate, reveals also very well convergence to the standard pattern.

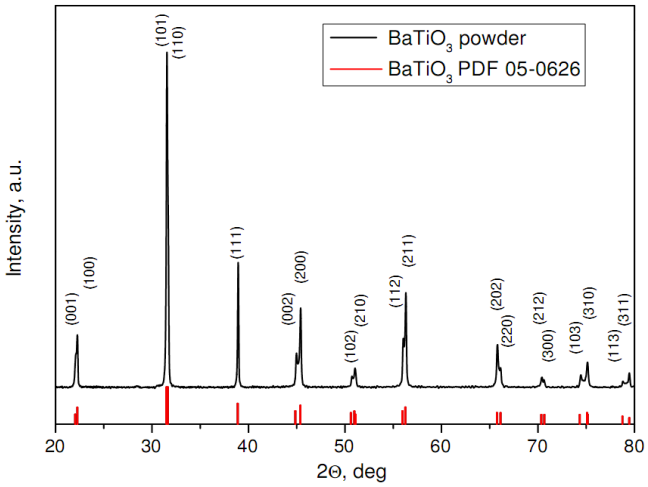

Fig. 1. XRD pattern of $BaTiO_3$ powder

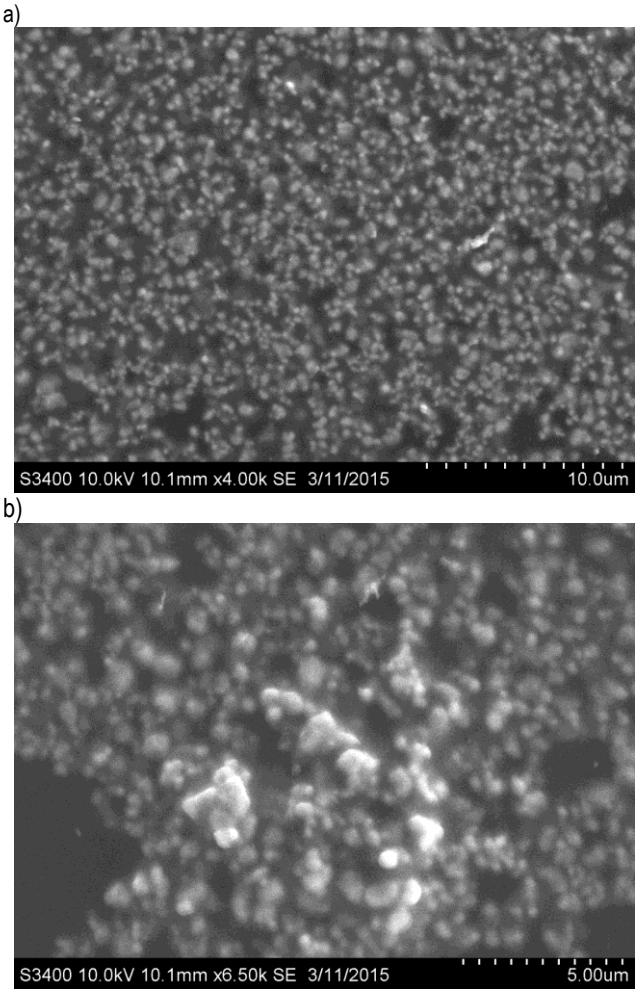

Fig. 2. SEM morphology of $BaTiO_3$ powder in two different magnifications: x4.00k (a) and x6.50k (b)

DOI 10.1515/ama-2017-0042

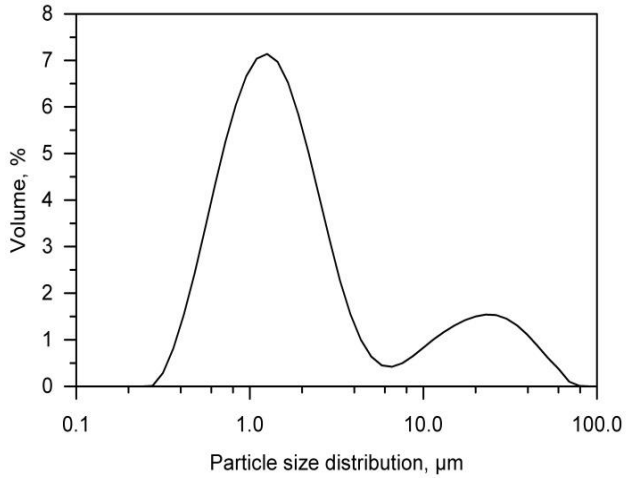

Fig. 3. The particle size distribution of $BaTiO_3$ powder

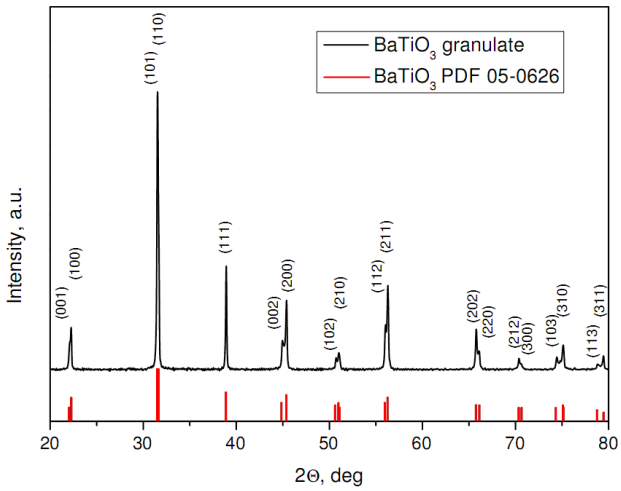

Fig. 4. XRD pattern of $BaTiO_3$ granulate

From data shown in Tab. 1 and Fig. 5 follows that the values of water absorbability and the apparent porosity of sintered pellets increase together with the maximal sintering temperature. The value of water absorbability increases with the sintering temperature (Tab. 1). Furthermore, the increasing in sintering temperature led to an increase of the apparent porosity (Fig. 5). In the range of apparent density between 5.80 and 5.87 g/cm^3 the values of apparent porosity are very similar. The values of relative density evaluated as the ratio of apparent density to the theoretical density are very similar (Table 1). Duran et al. (2002) and Miot et al. (1995) found that density of $BaTiO_3$ sintered pellets based on the value of lattice constant is equal to 6.02 g/cm^3. So, the obtained relative density is in agreement with the results of other authors.

Tab. 1. The physical properties of sintered pellets

Material type	Relative density, %	Water absorbability, %
$BaTiO_3(0)$	97.01	0.03
$BaTiO_3(1)$	96.68	0.05
$BaTiO_3(2)$	96.84	0.06
$BaTiO_3(3)$	96.35	0.07
$BaTiO_3(4)$	97.51	0.09

As we can see from the Fig. 6 the grains of barium titanate granulates exhibit a spherical shape that the dimensions varied between 25 μm and 35 μm. The spherical shape of granules is a result of granulation process. Before this process the $BaTiO_3$ powder was mixed with additives. So, the dimensions of powder granules did not change. During the granulation process the water slurry was sprayed. The specific surface area of $BaTiO_3$ granulate (1.18 m^2/g) is smaller than in the case of powder.

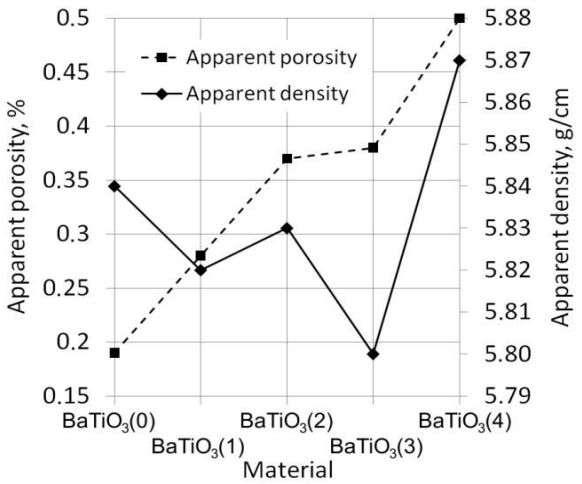

Fig. 5. Effect of material type on selected physical properties of sintered pellets

a)

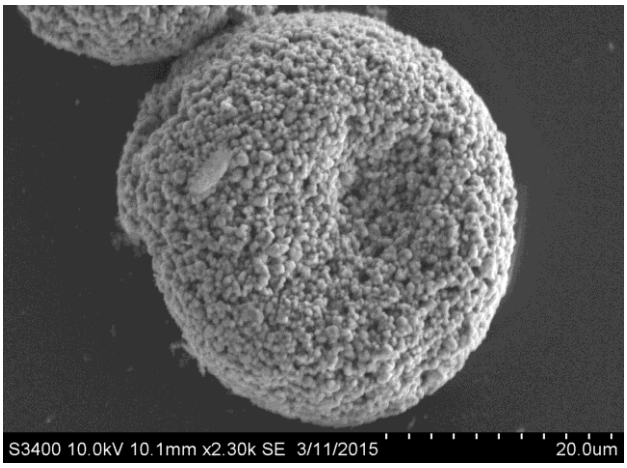

b)

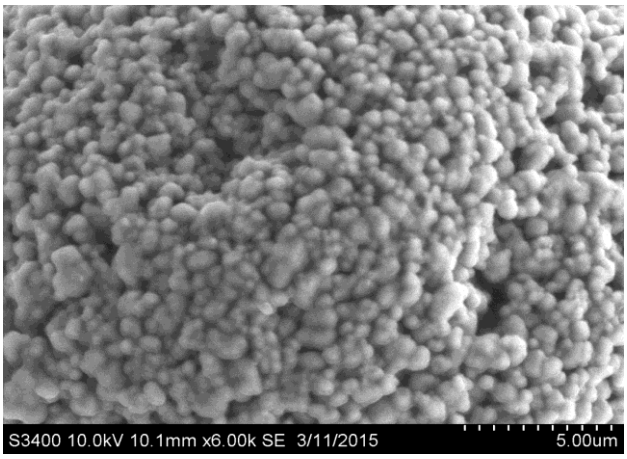

Fig. 6. SEM micrograph of $BaTiO_3$ granulate in two different magnifications: x2.30k (a) and x6.00k (b)

DOI 10.1515/ama-2017-0042

The pressing and sintering of the samples caused the improving of phase composition of $BaTiO_3$(1) pellet. The XRD pattern of $BaTiO_3$(1) presented in Fig. 7 is better than in the case of granulate.

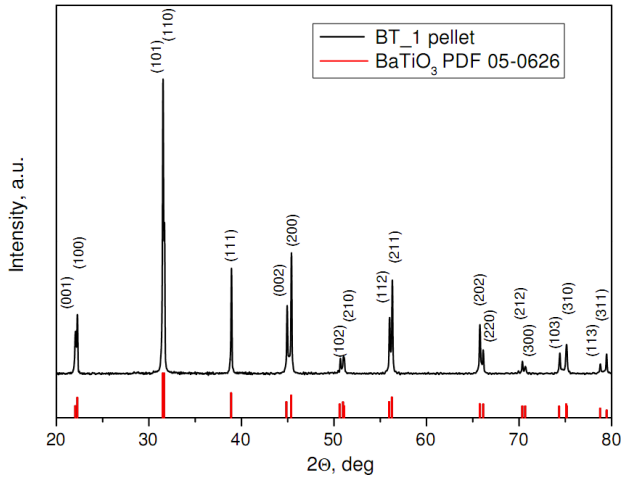

Fig. 7. XRD pattern of $BaTiO_3$(1) pellet

a)

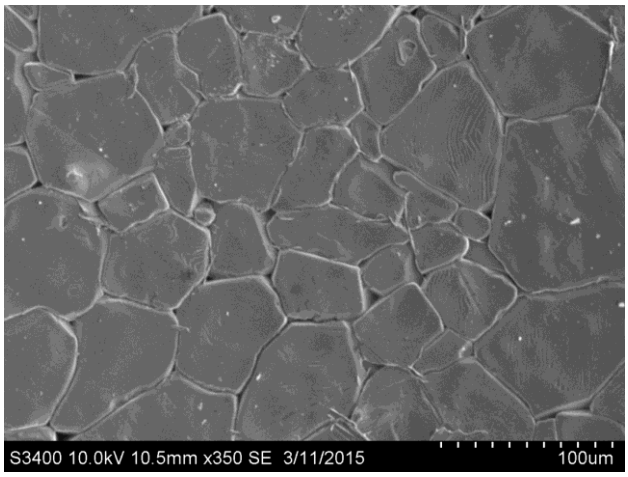

b)

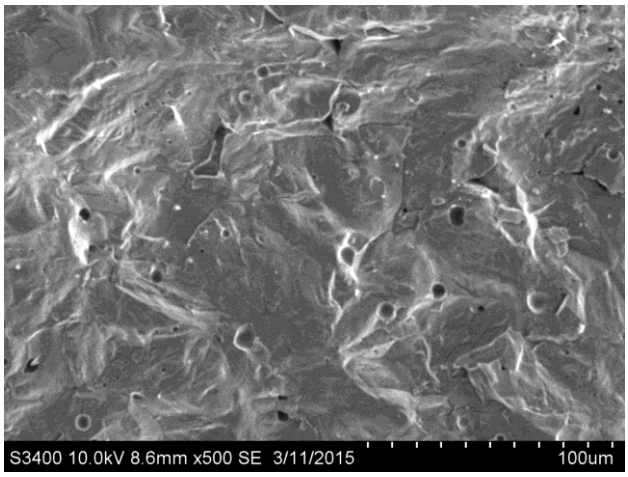

Fig. 8. SEM micrograph of $BaTiO_3$(1) pellet (a) and the fracture surface (b)

The SEM micrographs of $BaTiO_3$(1) pellet presented in Fig. 8a reveal the densification of the grains due to compacting process. The small pores indicated in the Fig. 8b are a result of densification process and correspond to the density of $BaTiO_3$(1) pellet shown in Tab. 1. The smaller pores have a dimension of a few micrometers which is in agreement with the results of Yoon and Lee (2004). The size of the grains is very diversified. In the microstructure the large number of the grains with the size of 60-90 μm, and smaller number of grains with size between 1 and 3 μm are observed (Fig. 8a).

To confirm the application of sintered $BaTiO_3$ ceramic in multilayer actuators the additional mechanical properties i.e., the hardness, the flexural strength, the fracture toughness and the coefficient of thermal expansion were determined. The value of fracture toughness of 0.83 $MPa \cdot m^{1/2}$ is comparable with the results of research of perovskite-type $BaTiO_3$ ceramics conducted by Hwang and Niihara (1998). The hardness of the $BaTiO_3$(1) beam was equal to 3.09 GPa, the value of the bending strength was 78.1 MPa, while the coefficient of thermal expansion reached $4.75 \cdot 10^{-6}$ 1/K.

4. CONCLUSIONS

The spherical grains of the size about 500 nm were indicated on SEM micrographs of powder but these small grains have an easy tendency to create agglomerates. The small value of the specific surface area of both powder and granulate ensured the good properties of material mouldability and finally allowed to receive sinters of high density. Obtainment of the high density of sinters was confirmed by the results of the apparent density and additionally photos of microstructure. The purity of powder, granulate and sinters was controlled by determining the phase compositions, which in all cases revealed the almost perfect barium titanate phase. The values of hardness, flexural strength, fracture toughness and coefficient of thermal expansion confirmed the usability of prepared perovskite-type $BaTiO_3$ ceramic material on multilayer actuators. The microstructure of the pellets is comparable with the results found in the literature. However, to increase the dielectric constant of $BaTiO_3$, it is expected to produce fine-grained microstructure of ceramic material. It is possible, by special thermal treatment of $BaTiO_3$ pellets to get the smaller size of particles.

REFERENCES

1. **Biglar M., Gromada M., Stachowicz F., Trzepieciński T.** (2015), Optimal configuration of piezoelectric sensors and actuators for active vibration control of a plate using a genetic algorithm, *Acta Mechanica*, 226(10), 3451-3462.
2. **Cai W., Fu C., Gao J., Guo Q., Deng X., Zhang C.** (2011), Preparation and optical properties of barium titanate thin films, *Physica B*, 406, 3583-3587.
3. **Choi M.-S., Kim S.-H., Kim Y.-H., Kim I.W., Jeong S.-J., Song J.-S., Lee J.-S.** (2008), Application of Ag–ceramic composite electrodes to low firing piezoelectric multilayer ceramic actuators, *Journal of Electroceramics*, 20, 225-229.
4. **Duran P., Gutierrez D., Tartaj J., Moure C.** (2002), Densification behaviour, microstructure development and dielectric properties of pure $BaTiO_3$ prepared by thermal decomposition of (Ba,Ti)-citrate polyester resins, *Ceramics International*, 28, 283-292.

DOI 10.1515/ama-2017-0042

5. **Ertuğ B.** (2013), The overview of the electrical properties of barium titanate *American Journal of Engineering Research*, 2(8), 1-7.
6. **Hackenberger W.S., Pan M.-J., Vedula V., Pertsch P., Cao W., Randall C.A., Shrout T.R.** (1998), Effect of grain size on actuator properties of piezoelectric ceramics, *Smart Structures and Materials 1998: Smart Materials Technologies*, 3324, 28-34.
7. **Hwang H.J, Niihara K.** (1998), Perovskite-type $BaTiO_3$ ceramics containing particulate SiC: Part II Microstructure and mechanical properties, *Journal of Materials Science*, 33, 549-558.
8. **Kao C.F., Yang W.D.** (1999), Preparation of barium strontium titanate powder from citrate precursor, *Applied Organometallic Chemistry*, 13, 383-397.
9. **Kholodkova A., Danchevskaya M., Fionov A.** (2012), Study of nanocrystalline barium titanate formation in water vapour conditions, NANOCON Conference, 23-25.10.2012, Brno, Czech Republic.
10. **Kim H.-T., Kim J.-H., Jung W.-S., Yoon D.-H.** (2009), Effect of starting materials on the properties of solid-state reacted barium titanate powder, *Journal of Ceramic Processing Research*, (10)6, 753-757.
11. **Luo J, Qiu J., Zhu K., Du J.** (2011), Effects of the calcining temperature on the piezoelectric and dielectric properties of 0.55PNN-0.45PZT ceramics, *Ferroelectric*, 425(1), 90-97.
12. **Miot C., Proust C., Husson E.** (1995), Dense ceramics of $BaTiO_3$ produced from powders prepared by a chemical process, *Journal of European Ceramic Society*, 15, 1163-1170.
13. **Moura F., Simoes A.Z., Aguiar E.C., Nogueira I.C., Zaghete M.A., Varela J.A., Longo E.** (2009), Dielectric investigations of vanadium modified barium zirconium titanate ceramics obtained from mixed oxide method, *Journal of Alloys and Compounds*, 479, 280-283.
14. **Nguyen D.Q., Lebey T., Castelan P., Bley V., Boulos M., Guillemet-Fritsch S., Combettes C., Durand B.** (2007), Electrical and physical characterization of bulk ceramics and thick layers of barium titanate manufactured using nanopowders, *Journal of Materials Engineering and Performance*, 16(5), 626-634.
15. **Othman K.I., Hassan A.A., Abdelal O.A.A., Elshazly E.S., Ali M.E.-S., El-Raghy S.M., El-Houte S.** (2014), Formation mechanism of barium titanate by solid-state reactions, *International Journal of Scientific& Engineering Research*, (5)7, 1460-1465.
16. **Prado L.R., de Resende N.S., Silva R.S., Egues S.M.S., Salazar-Banda G.R.** (2016), Influence of the synthesis method on the preparation of barium titanate nanoparticles, *Chemical Engineering and Processing: Process Intensification*, 103, 12-20.
17. **Stojanovic B.D.** (1999), *Advanced in Sintered Electronic Materials, Advanced Science and Technology of Sintering*, Kluwer Academic/Plenum Publishers, New York.
18. **Vijatović M.M., Bobić J.D., Stojanović B.D.** (2008), History and challenges of barium titanate: Part II, *Science of Sintering*, 40, 235-244.
19. **Yoon D.-H., Lee B.I.** (2004), Processing of barium titanate tapes with different binders for MLCC applications: Part I: Optimization using design of experiments, *Journal of European Ceramic Society,* 24, 739-752.
20. **Yoshikawa S., Shrout T.** (1993), Multilayer piezoelectric actuators – structures and reliability, AIAA/ASME/ASCE /AHS/ASC Structures, Structural Dynamics, and Materials Conference, 34th and AIAA/ASME Adaptive Structures Forum, La Jolla, CA, 19-22.04.1993, Technical Papers. Pt. 6, 3581-3586.
21. **Zheng P., Zhang J.L., Tan Y.Q., Wang C.L.** (2012), Grain-size effects on dielectric and piezoelectric properties of poled $BaTiO_3$ ceramics, *Acta Materialia*, 60, 5022-5030.

The research leading to these results has received funding from the People Programme (Marie Curie Actions) of the European Union's Seventh Framework Programme FP7/2007-2013/ under REA grant agreement No. PITN-GA-2013- 606878.

DOI 10.1515/ama-2017-0043

THERMAL STRESSES DUE TO FRICTIONAL HEATING WITH TIME-DEPENDENT SPECIFIC POWER OF FRICTION

Katarzyna TOPCZEWSKA*

*Faculty of Mechanical Engineering, Department of Mechanics and Applied Computer Science, Bialystok University of Technology, ul. Wiejska 45C, Bialystok 15–351, Poland

k.topczewska@doktoranci.pb.edu.pl

received 12 July 2017, revised 21 November 2017, accepted 24 November 2017

Abstract: In this paper influence of temporal profile of the specific friction power (i.e. the product of the coefficient of friction, sliding velocity and contact pressure) on thermal stresses in a friction element during braking was investigated. Spatio-temporal distributions of thermal stresses were analytically determined for a subsurface layer of the friction element, based on the model of thermal bending of a thick plate with unfixed edges (Timoshenko and Goodier , 1970). To conduct calculations, the fields of dimensionless temperature were used. These fields were received in the article (Topczewska, 2017) as solutions to a one-dimensional boundary-value problem of heat conduction for a semi-space heated on its outer surface by fictional heat flux with three, different time profiles of the friction power.

Key words: Frictional Heating, Temperature, Thermal Stresses, Time-Dependent Power of Friction

1. INTRODUCTION

As a result of friction, on the disc-pad contact surface during braking, high temperature and thermal stresses appear in friction elements. In these conditions the abrasive wear process is intensified and braking efficiency is significantly lower. When thermal stresses exceed the ultimate strength of the friction material, then plastic deformations and thermal cracks on the brake disc surface may arise (Yevtushenko and Kuciej, 2010b; Kim et al. 2013; Wu et al. 2016). Therefore, thermal calculations of working elements are pivotal stage during braking systems design.

Analytical equations to determine temperature and thermal stresses, generated as a result of frictional heating, are predominantly obtain from solution to a one-dimensional thermal problem of friction (Evtushenko et al., 2000; Yevtushenko et al., 2012; 2014). Acceptance of a one-dimensional heat conduction model is reasoned for high values of Peclet number (for braking at high speed) (Blok, 1955). One of the approach to formulate thermal problems of friction during braking is based on a virtual separation of friction elements and heating their working surfaces by the heat fluxes with intensity proportional to the specific power of friction (Talati and Jalalifar, 2009; Yevtushenko and Kuciej, 2010b). Using this approach, in the paper (Evtushenko and Kutsei, 2006) distributions of the non-stationary temperature and thermal stresses for a semi-infinite solid heated on its outer surface by the frictional heat flow modelled by a pulse with rectangular or triangular shape. Thermal problem of friction for a strip – semi-space (pad – calliper) tribosystem with linear time profile of frictional heat flux intensity effects on the outer surface of the strip were formulated and solved in the article (Yevtushenko et al., 2011).

In the literature there is a lack of exact solutions to this type of problems with temporal profile of heat flux adequately described the real braking processes. The experimental study (Chichinadze, 1967) shows that this quantity may have a various forms, depends on working conditions, thermal stability of the friction pair and the way of contact pressure regulation.

Influence of temporal profile of specific friction power on spatio-temporal distribution of the temperature in a friction element during single braking was investigated in the article (Topczewska, 2017). For this purpose a one-dimensional boundary-value problem of heat conduction for a homogeneous semi-space (brake disc) heated on its outer surface by the frictional heat flux was formulated and analytically solved. This problem was considered with three different time profiles of specific friction power (Chichinadze, 1967). Obtained solutions determine transient fields of dimensionless temperature in the heated element. Based on received results it was established that temporal profile of the intensity of frictional heat flux has essential influence on temperature distribution in the working elements of brakes.

The main aim of this work is to investigate the influence of selected time profiles of intensity of the frictional heat flux on quasi-static distribution of the thermal stresses in the friction element.

2. TEMPERATURE

It was assumed, that a homogeneous half-space (brake disc), from the initial moment $t = t_0 = 0$ to the end of the braking process ($t = t_s$), is heated on its free surface $z = 0$ (friction surface) (Fig. 1) by the frictional heat flux with intensity proportional to the specific power of friction $q_i(t) = q_0\, q_i^*(t),\ i = 1,2,3$ (Chichinadze, 1967):

$$q_1^*(t) = 3(1 - t/t_s)^2,\ q_2^*(t) = 6\, t/t_s\,(1 - t/t_s),$$
$$q_3^*(t) = 6\left(\sqrt{t/t_s} - t/t_s\right), \qquad 0 \le t \le t_s. \tag{1}$$

where $q_0 = fV_0p_0$.

Temporal profiles of the heat flux intensities (1) are characterized by that the braking work in the moment of standstill is equal for all these processes.

DOI 10.1515/ama-2017-0043

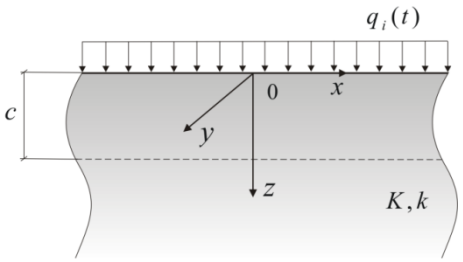

Fig. 1. Scheme of the problem

Solutions to above-mentioned formulated thermal problem of friction, which were found in the paper (Topczewska, 2017), are the following distributions of dimensionless temperature $T_i^*, i = 1,2,3$:

$$T_1^*(\zeta,\tau) = 2\sqrt{\tau}\{3\,\mathrm{ierfc}Z - 2\tau^*\big[2(1+Z^2)\mathrm{ierfc}Z - \mathrm{Zerfc}Z + 0.2\tau^{*2}[(8+18Z^2+4Z^4)\mathrm{ierfc}Z - Z(7+2Z^2)\mathrm{erfc}Z]\big\},$$

$$\zeta \geq 0, 0 \leq \tau \leq \tau_s, \tag{2}$$

$$T_2^*(\zeta,\tau) = 4\tau^*\sqrt{\tau}\{[2(1+Z^2)\mathrm{ierfc}Z - \mathrm{Zerfc}Z] - 0.2\tau^*[(8+18Z^2+4Z^4)\mathrm{ierfc}Z - Z(7+2Z^2)\mathrm{erfc}Z]\},$$

$$\zeta \geq 0, 0 \leq \tau \leq \tau_s, \tag{3}$$

$$T_3^*(\zeta,\tau) = \tau^*\{3\sqrt{\pi\tau_s}(\mathrm{erfc}Z - 2Z\mathrm{ierfc}Z) - 4\sqrt{\tau}[2(1+Z^2)\mathrm{ierfc}Z - \mathrm{Zerfc}Z]\},\ \zeta \geq 0, 0 \leq \tau \leq \tau_s, \tag{4}$$

where

$$\zeta = \frac{z}{a}, \tau = \frac{kt}{a^2}, \tau_s = \frac{kt_s}{a^2}, T_0 = \frac{q_0 a}{K}, T_i^* = \frac{T_i - T_a}{T_0}, Z = \frac{\zeta}{2\sqrt{\tau}}, \tag{5}$$

$a = \sqrt{3kt_s}$ is effective depth of the heat penetration inside brake disc (Chichinadze et al., 1979), T_a is initial temperature, K, k are thermal conductivity and thermal diffusivity, respectively.

Based on the solutions (2)–(4) and the model of temperature bending of a thick plate with unfixed edges, the distributions of quasi-static thermal stresses in heated brake disc will be received.

3. THERMAL STRESSES

Distribution of the transient temperature field in a brake disc (2)–(4), due to its free surface heating by the frictional heat flux with intensities (1), generate temperature strains and stresses, which may initiate the superficial cracks of the disc material. Experimental research shows that the strongest influence on the material cracking along the direction of the disc sliding, according to the scheme of the process (Fig. 1), has lateral normal component of stress tensor σ_y (acting along the y-axis) (Jewtuszenko et al., 2015). For a one-dimensional model of frictional heating in the direction perpendicular to the friction surface – z, lateral and longitudinal normal components of the stresses are equal $\sigma_y = \sigma_x = \sigma$ (Timoshenko and Goodier, 1970). However, in case of plane state of stresses, normal component of the stress tensor σ_z, which acts in the direction of heating, is negligible.

In accordance with model of thermal bending of a thick strip of the thickness $c = a$ ($\zeta = 1$) with unfixed ends, the dimensionless field of lateral thermal strains $\varepsilon_{y,i}^*(\zeta,\tau) = \varepsilon_i^*(\zeta,\tau)$ we find from the equation (Timoshenko and Goodier, 1970):

$$\varepsilon_i^*(\zeta,\tau) = \int_0^1 T_i^*(\zeta,\tau)d\zeta + 12(\zeta - 0.5)\int_0^1 (\zeta - 0.5)T_i^*(\zeta,\tau)d\zeta,$$

$$0 \leq \zeta \leq 1, 0 \leq \tau \leq \tau_s. \tag{6}$$

where $T_i^*(\zeta,\tau), i = 1,2,3$ are fields of the dimensionless temperature (2)–(4).

Writing the thermal strains (6) in the form:

$$\varepsilon_i^*(\zeta,\tau) = \bar{T}_i^*(\tau)(4 - 6\zeta) + 6M_i^*(\tau)(2\zeta - 1), \tag{7}$$

where dimensionless mean temperature $\bar{T}_i^*(\tau)$ and temperature momentum $M_i^*(\tau)$, for three intensities of heat flux (1), we determine from the equations:

$$\bar{T}_i^*(\tau) = \int_0^1 T_i^*(\zeta,\tau)d\zeta,\ \ M_i^*(\tau) = \int_0^1 \zeta T_i^*(\zeta,\tau)d\zeta, \tag{8}$$

and substituting the dimensionless temperatures (2)–(4), to the relations (8), we have:

$$\bar{T}_1^*(\tau) = 4\tau\{3I_0(\tau) - 2\tau^*[2I_0(\tau) + 2I_2(\tau) - J_1(\tau)] + 0.2\tau^{*2}[8I_0(\tau) + 18I_2(\tau) + 4I_4(\tau) - 7J_1(\tau) - 2J_3(\tau)]\}, \tag{9}$$

$$M_1^*(\tau) = 8\tau\sqrt{\tau}\{3I_1(\tau) - 2\tau^*[2I_1(\tau) + 2I_3(\tau) - J_2(\tau)] + 0.2\tau^{*2}[8I_1(\tau) + 18I_3(\tau) + 4I_5(\tau) - 7J_2(\tau) - 2J_4(\tau)]\}, \tag{10}$$

$$\bar{T}_2^*(\tau) = 8\tau\tau^*\{[2I_0(\tau) + 2I_2(\tau) - J_1(\tau)] - 0.2\tau^*[8I_0(\tau) + 18I_2(\tau) + 4I_4(\tau) - 7J_1(\tau) - 2J_3(\tau)]\}, \tag{11}$$

$$M_2^*(\tau) = 16\tau\sqrt{\tau}\tau^*\{[2I_1(\tau) + 2I_3(\tau) - J_2(\tau)] - 0.2\tau^*[8I_1(\tau) + 18I_3(\tau) + 4I_5(\tau) - 7J_2(\tau) - 2J_4(\tau)]\}, \tag{12}$$

$$\bar{T}_3^*(\tau) = 2\sqrt{\tau}\tau^*\{3\sqrt{\pi\tau_s}[J_0(\tau) - 2I_1(\tau)] - 8\sqrt{\tau}[I_0(\tau) + I_2(\tau) - 0.5J_1(\tau)]\}, \tag{13}$$

$$M_3^*(\tau) = 4\tau\tau^*\{3\sqrt{\pi\tau_s}[J_1(\tau) - 2I_2(\tau)] - 8\sqrt{\tau}[I_1(\tau) + I_3(\tau) - 0.5J_2(\tau)]\}, \tag{14}$$

where integrals $I_k(\tau)$ and $J_k(\tau)$ are defined by the following formulas:

$$I_k(\tau) = \int_0^X Z^k \mathrm{ierfc}Z\, dZ, k = 0,1,2 \ldots \tag{15}$$

$$J_k(\tau) = \int_0^X Z^k \mathrm{erfc}Z\, dZ, k = 0,1,2 \ldots \tag{16}$$

where Z has the form (5) and $X = (2\sqrt{\tau})^{-1}$.

Integrals $I_k(\tau)$ (15), we transform to the following form:

$$I_k(\tau) = \frac{1}{\sqrt{\pi}}N_k(\tau) - J_{k+1}(\tau), k = 0,1,2 \ldots \tag{17}$$

where $N_k(\tau) = \int_0^X Z^k e^{-Z^2}\, dZ, k = 0,1,2 \ldots$ (18)

Applying the recursive formula (Prudnikov et al., 1998):

$$J_k(\tau) = \frac{k(k-1)}{2(k+1)}J_{k-2}(\tau) + \left(X^2 - \frac{k}{2}\right)\frac{X^{k-1}}{k+1}\mathrm{erfc}X - \frac{X^k e^{-X^2}}{\sqrt{\pi}(k+1)}, \tag{19}$$

and $J_0(\tau) = \sqrt{\pi}^{-1} - \mathrm{ierfc}X, J_1(\tau) = \frac{1}{4}\mathrm{erfc}X - \frac{1}{2}X\mathrm{ierfc}X,$ (20)

integrals $J_k(\tau), k = 0,1,2 \ldots$ (16) we write in the form:

$$J_2(\tau) = \frac{1}{3\sqrt{\pi}}\left[1 - e^{-X^2}(X^2+1)\right] + \frac{X^3}{3}\mathrm{erfc}X, \tag{21}$$

$$J_3(\tau) = \frac{1}{8}\left[\frac{3}{2}\mathrm{erf}X - \frac{Xe^{-X^2}}{\sqrt{\pi}}(2X^2+3)\right] + \frac{X^4}{4}\mathrm{erfc}X, \tag{22}$$

$$J_4(\tau) = \frac{2}{5\sqrt{\pi}}\left[1 - e^{-X^2}\left(\frac{1}{2}X^4 + X^2 + 1\right)\right] + \frac{X^5}{5}\mathrm{erfc}X, \tag{23}$$

DOI 10.1515/ama-2017-0043

$$J_5(\tau)=\frac{5}{8}\left[\frac{1}{2}\mathrm{erf}X-\frac{Xe^{-X^2}}{3\sqrt{\pi}}\left(\frac{4}{5}X^4+2X^2+3\right)\right]+\frac{X^6}{6}\mathrm{erfc}X, \quad (24)$$

$$J_6(\tau)=\frac{6}{7\sqrt{\pi}}\left[1-e^{-X^2}\left(\frac{1}{6}X^6+\frac{1}{2}X^4+X^2+1\right)\right]+\frac{X^7}{7}\mathrm{erfc}X, \quad (25)$$

Using the relations (Prudnikov et al., 1986):

$$N_k(\tau)=\frac{k-1}{2}N_{k-2}(\tau)-\frac{X^{k-1}}{2}e^{-X^2}, k=0,1,2\ldots \quad (26)$$

where $N_0(\tau)=\frac{\sqrt{\pi}}{2}(1-\mathrm{erfc}X),\ N_1(\tau)=\frac{1}{2}\left(1-e^{-X^2}\right),$ (27)

we find the integrals $N_k(\tau), k=0,1,2\ldots$ (18):

$$N_2(\tau)=\frac{1}{4}\sqrt{\pi}\mathrm{erf}X-\frac{X}{2}e^{-X^2}, \quad (28)$$

$$N_3(\tau)=\frac{1}{2}\left[1-e^{-X^2}(X^2+1)\right], \quad (29)$$

$$N_4(\tau)=\frac{3}{8}\sqrt{\pi}\mathrm{erf}X-\frac{X}{2}e^{-X^2}\left(X^2+\frac{3}{2}\right), \quad (30)$$

$$N_5(\tau)=1-e^{-X^2}\left(\frac{1}{2}X^4+X^2+1\right). \quad (31)$$

Substituting the relations (20)–(25) and (27)–(31) to the formula (17) we obtain:

$$I_0(\tau)=\frac{1}{4}\mathrm{erfc}X+\frac{X}{2\sqrt{\pi}}e^{-X^2}-\frac{X^2}{2}\mathrm{erfc}X, \quad (32)$$

$$I_1(\tau)=\frac{1}{6\sqrt{\pi}}\left(1-e^{-X^2}\right)+\frac{1}{3}X^2\mathrm{ierfc}X, \quad (33)$$

$$I_2(\tau)=\frac{1}{16}\mathrm{erf}X+\frac{X}{8\sqrt{\pi}}e^{-X^2}(2X^2-1)-\frac{X^4}{4}\mathrm{erfc}X, \quad (34)$$

$$I_3(\tau)=\frac{1}{10\sqrt{\pi}}\left[1+e^{-X^2}(2X^4-X^2-1)\right]-\frac{X^5}{5}\mathrm{erfc}X, \quad (35)$$

$$I_4(\tau)=\frac{1}{16}\mathrm{erf}X+\frac{X}{24\sqrt{\pi}}e^{-X^2}(4X^4-2X^2-3)-\frac{X^6}{6}\mathrm{erfc}X, \quad (36)$$

$$I_5(\tau)=\frac{1}{7\sqrt{\pi}}\left[1+e^{-X^2}\left(X^6-\frac{1}{2}X^4-X^2-1\right)\right]-\frac{X^7}{7}\mathrm{erfc}X. \quad (37)$$

Substituting the solutions (20)–(25) and (32)–(37) to the dimensionless mean temperature $\bar{T}_i^*(\tau)$ and temperature momentum $M_i^*(\tau)$ (9)-(14), and received results to the equation (7), we obtain fields of dimensionless lateral deformations $\varepsilon_i^*(\zeta,\tau),\ i=1,2,3$.

Knowing the dimensionless temperature (2)–(4) and thermal strains (7), distributions of the dimensionless thermal stresses $\sigma_i^*(\zeta,\tau)$ in the brake disc for three intensities of the frictional heat flux (1), we determine from the equations (Timoshenko and Goodier, 1970):

$$\sigma_i^*(\zeta,\tau)=\varepsilon_i^*(\zeta,\tau)-T_i^*(\zeta,\tau), \quad (38)$$

$$0\le\zeta\le1, 0\le\tau\le\tau_s, i=1,2,3$$

where $\sigma_i(\zeta,\tau)=\sigma_0\sigma_i^*(\zeta,\tau), \sigma_0=\frac{\alpha E T_0}{1-\nu}.$ (39)

E is Young's modulus, α is linear thermal expansion coefficient and ν is Poisson's ratio.

4. NUMERICAL ANALYSIS

Based on obtained analytical solutions, numerical analysis of the transient distributions of the temperature and quasi-static thermal stresses in a brake disc (half-space) for selected braking modes, i.e. for three different intensities of frictional heat fluxes (1). The following dimensionless parameters: spatial coordinate ζ, time τ and braking time $\tau_S=1$, which are determined by the equations (5) were used to perform numerical calculations.

Spatio-temporal distributions of the dimensionless temperature $T_i^*(\zeta,\tau),\ i=1,2,3$ generated due to frictional heating of the working surface $\zeta=0$ by the heat fluxes with three intensities (1) and corresponding distributions of the quasi-static normal thermal stresses $\sigma_i^*(\zeta,\tau),\ i=1,2,3$ were presented in the Fig. 2. As follows from the functions (equations (1)), which describe the intensities of the frictional heat fluxes effects on the working surface of the brake disc, the profile of the first one $q_1^*(\tau)$ is characterized by the fact, that the maximum value occurs at the initial moment of braking ($\tau=0$) and afterwards it decreases with time to zero at the moment of standstill $\tau=\tau_S=1$. However intensities $q_i^*(\tau),\ i=2,3$ increase from zero at the initial moment ($\tau=0$) to the maximum values at $0.5\tau_s$ for $i=2$ and at $0.25\tau_s$ for $i=3$. After reached maximum value of the heat flux intensities they decrease to zero at the stop moment. Distributions of the temperature inside the brake disc, generated due to heating friction surface by the heat flux with the foregoing intensities, are shown in Fig. 2 a,c,e. Conducted analysis of the spatio-temporal distributions of temperature allow to establish, that the time of appearance of the maximum heat flux value has crucial influence both on the time of appearance maximum temperature on the friction surface, and on the temperature distribution inside the brake disc. If the maximum value of heat flux occurs in the initial stage of braking ($q_1^*(\tau)$) maximum value of temperature $T_{1,\max}^*=1.2$ is reached at $\tau_{\max}\cong0.317\,\tau_s$. The time of appearance of the maximum temperature on the working surface of the disc increases with increasing the time to reach maximum value of frictional heat flux. For the intensities of heat flux $q_2^*(\tau)$ time $\tau_{\max}=0.75\,\tau_s$ $(T_{2,\max}^*=1.17)$ and for $q_3^*(\tau)$ $\tau_{\max}\cong0.62\,\tau_s$ $(T_{3,\max}^*=1.09)$.

In Fig. 2b,d,f, the dimensionless distributions of the quasi-static thermal stresses $\sigma_i^*,\ i=1,2,3$ are presented, corresponding to the spatial-time distributions of the dimensionless temperature (Fig. 2a,c,e.) in the brake disc. Overall character of the change of stresses state in the consider zone of the brake disc $0\le\zeta\le1$ is similar for all analyzed time profiles of the frictional heat flux intensities. In the initial stage of braking, in the subsurface region of the disc $0\le\zeta\le0.2$, the compressive stresses $\sigma_i^*<0$ are generated. Value of these stresses decreases with time, to the sign change – which means that the tensile stresses take place. The time of change compressive stresses $\sigma_i^*<0$ into tensile stresses $\sigma_i^*>0$ depends on the time of appearance of maximum temperature value on the friction surface of the disc, i.e. the faster the maximum temperature is reached, the earlier becomes that change. In the case of heat flux intensity $q_1^*(\tau)$ when the temperature achieved the greatest value at the time moment $\tau_{\max}\cong0.317\,\tau_s$ the time of the change of stress sign (appearance of the isoline of zero stress level) on the working surface and inside the disc is equal to $\tau=0.53$ (Fig. 2b). Whereas for the fluxes $q_i^*(\tau),\ i=2,3$ the change of the compressive stresses into tensile stresses, in the consider zone $0\le\zeta\le0.2$, occurs at the time $\tau=0.88$ (Fig. 2d) and $\tau=0.8$ (Fig. 2f). Similar character of the stresses appearance and its change can be observed in the region $0.75\le\zeta\le1$. In the early stage of the heating process, the compressive stresses are generated, but their values are lower in comparison with the subsurface zone of the disc. Afterwards the stresses values decreases with time, to the sign change and the tensile stresses appear, in the similar way as in the subsurface region but also with lower values.

DOI 10.1515/ama-2017-0043

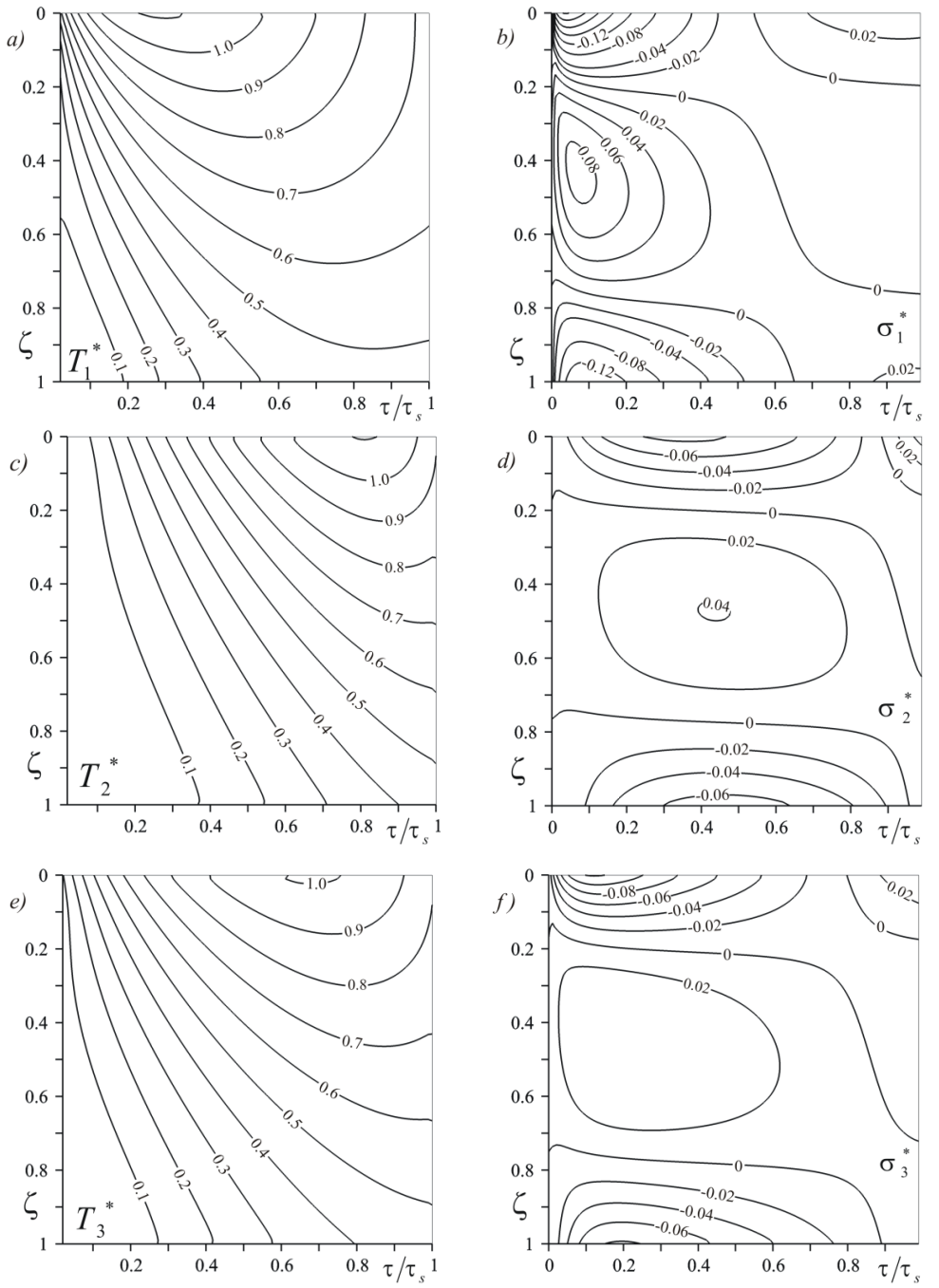

Fig. 2. Spatio-temporal distributions of the dimensionless temperatures T_i^*: $a)\ i = 1;\ c)\ i = 2;\ e)\ i = 3$; and the transverse thermal stresses σ_i^*: $b)\ i = 1;\ d)\ i = 2;\ f)\ i = 3$; inside the brake disc, for three time profiles of the heat flux intensities

Between the above-mentioned regions, in the initial stage of braking, the tensile stresses are generated, which in the all consider cases of frictional heating is present in the whole time interval $0 < \tau \leq \tau_s$. The greatest value of the normal compressive stresses in this region occurs in the case of the frictional heating of the disc by the heat flux with intensity $q_1^*(\tau)$ and is equal $\sigma_1^* = 0.08$ (Fig. 2b). Stresses appear in this zone, in the early stage of braking – at time moment $\tau \approx 0.04$. The time of occurrence of the maximum compressive stresses is almost equal to the time of appearance of the maximum values of tensile stresses on the heated surface, and for intensities of frictional heat fluxes $q_i^*(\tau),\ i = 2{,}3$ is $\tau \approx 0.4$ (Fig. 2d) and $\tau \approx 0.16$ (Fig. 2f), respectively. After reaching the maximum value, these stress decrease with time, and the region of its occurrence "narrows" and "moves" towards the depth $\zeta = 1$, to the replacement of the compressive stresses, adjacent to this region.

Evolutions of the dimensionless thermal stresses on the friction surface of the disc for three frictional heating modes are presented in Fig. 3. On the friction surface $\zeta = 0$, the maximum values of the dimensionless compressive stresses $\sigma_{1,\min}^* = -0.29$, $\sigma_{2,\min}^* = -0.12$, $\sigma_{3,\min}^* = -0.13$ are reached at the time moments $\tau = 0.04$, $\tau = 0.4$ and $\tau = 0.16$, respectively. After achieving the greatest value of the temperature (Fig. 2 a,c,e), compressive stresses on the heated surface disappear with time, and at the moments $\tau = 0.53$ $(q_1^*(\tau))$, $\tau = 0.88$ $(q_2^*(\tau))$ and $\tau = 0.8$ $(q_3^*(\tau))$ the sign of thermal stress change and tensile stresses appear, accompanied by the temperature decrease to the standstill moment. In cases $q_i^*(\tau),\ i = 2{,}3$ tensile stresses

DOI 10.1515/ama-2017-0043

monotonically increase and reach maximum values $\sigma^*_{2,\max} = 0.05$ and $\sigma^*_{3,\max} = 0.04$ at the end of the braking process $\tau = \tau_S = 1$. Whereas, in the process $q^*_1(\tau)$ stresses increase, reaching the maximum value $\sigma^*_{1,\max} = 0.04$ at the moment $\tau = 0.88$ and next, we can observe a slight fall of this value to the standstill.

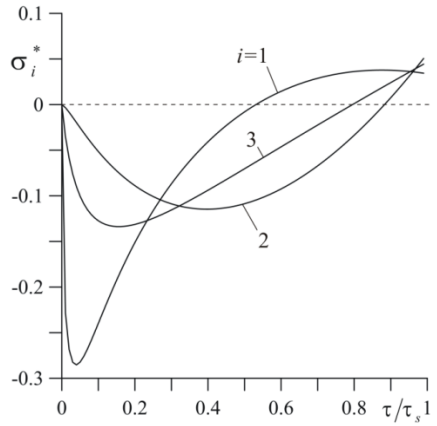

Fig. 3. Evolutions of the dimensionless transverse thermal stresses σ^*_i, $i = 1,2,3$ for three temporal profiles of the intensities of frictional heat flux, on the working surface of the disc $\zeta = 0$.

5. CONCLUSIONS

In this paper fields of the dimensionless thermal stresses in the brake disc heated by the frictional heat flux with intensity defined by three different temporal profiles were analytically determined. Conducted analysis allow us to make the following conclusions:

- in the initial stage of braking, adjacent to the friction surface the compressive stresses appear, subsequently decrease to zero, then the tensile stress zone arise and persist until the end of braking;
- increase of the time of achieving the maximum value of the specific friction power, results in increase of the time of occurrence of stress sign change on the heated surface;
- rapid decrease of the disc temperature before the stop moment, causes the appearance of the tensile stresses with higher value on the friction surface. Exceed of the ultimate strength of the friction material by the value of this stress can cause the initiation of the superficial thermal cracks;
- values and distribution of the thermal stresses, generated inside the heated brake disc, depends mainly on temporal profile of the specific friction power.

Nomenclature: a – effective depth of heat penetration [m]; c – thickness of the strip [m]; E – Young's modulus [MPa]; $\mathrm{erf(x)}$ – Gauss error function; $\mathrm{erfc(x)} = 1 - \mathrm{erf(x)}$ – complementary error function; $\mathrm{ierfc(x)} = \pi^{-1/2}\exp(-\mathrm{x}^2) - \mathrm{xerfc(x)}$ – integral of complementary error function; K – thermal conductivity [W K^{-1} m^{-1}]; k – thermal diffusivity [m^2 s^{-1}]; q – intensity of the heat flux [W m^{-2}]; q^* – dimensionless intensity of the heat flux; T – temperature [K]; T^* – dimensionless temperature; T_a – initial temperature [K]; T_0 –temperature scaling factor [K]; t – time [s]; t_s– braking time [s]; xyz – spatial coordinates [m]; α – linear thermal expansion coefficient [K^{-1}]; ε^* – dimensionless thermal strain; σ_0 –stress scaling factor [MPa]; σ – normal component of stress tensor [MPa]; σ^* – dimensionless component of stress tensor; τ – dimensionless time (Fourier number); τ_s – dimensionless braking time; ζ – dimensionless depth.

REFERENCES

1. **Abramowitz M., Stegun I.A.** (1972), *Handbook of Mathematical Functions with Formulas*, Graphs, and Tables, National Bureau of Standards, Washington.
2. **Blok H.** (1955) The dissipation of frictional heat, *Applied Scientific Research*, Section A. (2–3), 151–181.
3. **Chichinadze A.V.** (1967) *Calculation and study of external friction during braking*, Nauka, Moscow, (in Russian).
4. **Chichinadze A.V., Braun E.D., Ginsburg A.G., Ignat'eva Z.V.** (1979), *Calculation, Test and Selection of Frictional Couples*, Nauka, Moscow (in Russian).
5. **Evtushenko A., Kutsei M.** (2006) Initiating of thermal cracking of materials by frictional heating, *Journal of Friction and Wear*, 27(2), 9-16.
6. **Evtushenko O.O., Ivanyk E.H., Horbachova N.V.** (2000) Analytic methods for thermal calculation of brakes, *Materials Science*, 36(6), 857-862.
7. **Jewtuszenko O., Kuciej M., Tołstoj–Sienkiewicz J.** (2015) *Transients and quasi-stationary friction temperature fields*, Oficyna Wydawnicza Politechniki Białostockiej, Białystok (in Polish).
8. **Kim S.W., Segu D.Z., Kim S.S.** (2013) The Thermo-mechanical Cracking Analysis of Break System, *Procedia Engineering*, 68, 586-592.
9. **Prudnikov A.P., Brychkov Yu. A., Marichev O. I.** (1986), *Integrals and Series*, Vol. 1: Elementary Functions, Gordon and Breach, New York.
10. **Prudnikov A. P., Brychkov Yu. A., Marichev O. I.** (1998) *Integrals and Serie*s, Vol. 2, Special Functions, New York-London,Taylor & Francis.
11. **Talati F., Jalalifar S.** (2009) *Analysis of heat conduction in a disk brake system*, Heat Mass Transfer, 45, 1047-1059.
12. **Timoshenko S.P., Goodier J.N.** (1970) *Theory of Elasticity,* McGraw-Hill, New York.
13. **Topczewska K.** (2017) Frictional heating with time-dependent specific power of friction, *Acta Mechanica et Automatica*, 11(2), 111-115.
14. **Wu S.C., Zhang S.Q., Xu Z.W.** (2016) Thermal crack growth-based fatigue life prediction due to braking for a high-speed railway brake disc, *International Journal of Fatigue*, 87, 359-369.
15. **Yevtushenko A.A., Kuciej M.** (2010a) Two heat conduction problems with frictional heating during braking, *J. Theor. Appl. Mech.*, 48(2), 367–380.
16. **Yevtushenko A.A., Kuciej M.** (2010b) Two calculation schemes for determination of thermal stresses due to frictional heating during braking, *Journal of Theoretical and Applied Mechanics*, 48(3), 605-621.
17. **Yevtushenko A.A., Kuciej M., Yevtushenko O.O.** (2011) Temperature and thermal stresses in material of a pad during braking, *Arch. Appl. Mech.*, 81, 715-726.
18. **Yevtushenko A.A., Kuciej M.** (2012) One-dimensional thermal problem of friction during braking: The history of development and actual state, *International Journal of Heat and Mass Transfer*, 55(15), 4148-4153.
19. **Yevtushenko A.A., Kuciej M., Yevtushenko O.** (2014), The asymptotic solutions of heat problem of friction for a three-element tribosystem with generalized boundary conditions on the surface of sliding, *International Journal of Heat and Mass Transfer*, 70, 128-136.

This work is part of the project no. MB/WM/18/2017 which is carried out in the Faculty of Mechanical Engineering, Bialystok University of Technology.

DE GRUYTER
OPEN

DOI 10.1515/ama-2017-0044 acta mechanica et automatica, vol.11 no.4 (2017)

THE FINITE ELEMENT ANALYSIS OF OSTEOPOROTIC LUMBAR VERTEBRAL BODY BY INFLUENCE OF TRABECULAR BONE APPARENT DENSITY AND THICKNESS OF CORTICAL SHELL

Oleg ARDATOV[*], Algirdas MAKNICKAS[**], Vidmantas ALEKNA[***], Marija TAMULAITIENĖ[***], Rimantas KAČIANAUSKAS[**]

[*]Faculty of Mechanics, Department of Biomechanics, Vilnius Gediminas Technical University, Basanavičiaus 28, 03224 Vilnius, Lithuania
[**]Faculty of Mechanics, Institute of mechanical Science, Vilnius Gediminas Technical University, Basanavičiaus 28, 03224 Vilnius, Lithuania
[***]Faculty of Medicine, Čiurlionio 21, 03101 Vilnius, Lithuania

oleg.ardatov@vgtu.lt, algirdas.maknickas@vgtu.lt, vidmantas.alekna@mf.vu.lt, marija.tamulaitiene@mf.vu.lt, rimantas.kacianauskas@vgtu.lt

received 30 May 2016, revised 22 November 2017, accepted 27 November 2017

Abstract: Osteoporosis causes the bone mass loss and increased fracture risk. This paper presents the modelling of osteoporotic human lumbar vertebrae L1 by employing finite elements method (FEM). The isolated inhomogeneous vertebral body is composed by cortical outer shell and cancellous bone. The level of osteoporotic contribution is characterised by reducing the thickness of cortical shell and elasticity modulus of cancellous bone using power-law dependence with apparent density. The strength parameters are evaluated on the basis of von Mises-Hencky yield criterion. Parametric study of osteoporotic degradation contains the static and nonlinear dynamic analysis of stresses that occur due to physiological load. Results of our investigation are presented in terms of nonlinear interdependence between stress and external load.

Key words: Bone Tissue Elasticity, Finite Element Method, Lumbar Vertebrae, Osteoporosis

1. INTRODUCTION

Osteoporosis is a disease characterized by low bone mass and micro-architectural deterioration of bone tissue. Due to the process of osteoporotic degradation, the thickness of cortical bone and apparent density of cancellous bone are significantly reduced. Osteoporosis is one of the major health problems, especially in elderly populations, and is associated with fragility fractures. Various social and medical aspects of the osteoporosis has been studied worldwide (Agarwal and Kalia, 2014; Lin and Lane, 2004, Cooper et al., 2011; Cummings and Melton III, 2002). Although osteoporotic fractures can occur anywhere in the human body, vertebral fractures are the most common among them, particularly in the elderly population. Vertebral fractures result in pain, functional disability, affects the quality of life, and is associated with the increased mortality (Melton III et al., 2013; Johnell et al., 2004).

It could be mentioned that this disease affects over 200 million people over the world. It is estimated that one in three women and one in five men over the age of fifty worldwide will sustain an osteoporotic fracture. Hip and spine fractures are the two most serious fracture types, associated with substantial pain and suffering, disability, and even death. In 2010, 22 million women and 5.5 million men were estimated to have osteoporosis in the European Union; and among 3.5 million new fragility fractures, 520,000 vertebral fractures were sustained. The economic burden of incident and prior fragility fractures was estimated at € 37 billion (Svedbom et al., 2013).

The modern understanding of the osteoporosis has been gained by the cooperative interaction of several scientific disciplines. Apart in depth knowledge of the bone biology, specific understanding of biomechanical behaviour is required. In combination with other studies, the mechanistic approach based on biomechanics and the numerical finite element analysis provide useful tools for research on the bone fragility and support a clinical prediction of bone fractures. The biomechanical research, when compared to the branches of traditional aeronautical and civil engineering, provides not only a new application area but also a raft of challenges relating to the simulation of living tissues. Comprehensive discussion on the role of computational biomechanical simulations was raised up in the review paper (Doblare et al., 2004). The approach integrating numerical simulations, experiments and theoretical knowledge as the major focus of future research was pointed out. Application of computational simulations of factors and parameters that are difficult or impossible to examine experimentally will reduce or even replace experimental and clinical trials.

Adequacy of the finite element simulations essentially depends on the choice of mechanical approach and the development of proper finite model. Generally, mechanical FE simulations are aimed to calculate variations of mechanical stress and strain fields while evaluation of strength, fracture risk and others synonymous parameters is performed in secondary part of simulation.

The FE models applied for mechanical analysis of the spine range from sub-micron scale assessment of vertebral bone up to the analysis of the whole spine and surrounding structures. Developments of the entire human spine scale FE models and their simulations are rather limited (Watanabe et al., 2001; Okamoto et al., 2014). Here, vertebrae are connected via intervertebral

discs (IVD) and posterior elements having a relatively complex geometry. Numerical results obtained by applying a three-dimensional FE model of the human body (Okamoto et al., 2014) illustrate that maximal stresses are distributed along the entire skeleton, but fractures and dangerous deformation are concentrated in the local fragment of three vertebrae. Eight well-established FE models of the lumbar spine (L1-L5) created by different research centres around the globe were compared to in vitro and in vivo measurements (Dreischarf et al., 2014).

The earlier developments of spinal finite element models with a view to a standardized framework of verification, validation and sensitivity analysis were examined in the review paper (Jones and Wilcox, 2008). The scope of the above paper was restricted to review models of the vertebra, the intervertebral discs and short spinal segments. Several tendencies concerning various aspects of vertebral models could be distinguished in this review and in the further developments. The FE models largely depend on the material properties, geometry, meshing technique, etc.

Regarding these results and extremely large difficulties in forming of the real geometry of spine, most of the studies focus on the simplified models. Recent developments are limited by smaller fragments of vertebrae (Łodygowski et al., 2005; Su et al., 2009), but majority of the studies concerns vertebral body in isolation (Jones and Wilcox, 2008; Crowford et al., 2003; Maquer et al., 2015; Provatidis et al., 2010), using also the simplified shape by excluding the posterior elements (McDonald et al., 2010; Garo et al, 2011).

Vertebral body under consideration mainly comprises cancellous bone core consisting of the trabecular network surrounded by compact bone in a form of external thin cortical shell. Character of these properties plays crucial role in development of the finite element models. It is obvious that the mechanical properties of the bone tissues in vertebral body are directly influenced by their microstructure (Bono and Einhorn, 2003). Thereby, the measurement of bone mineral density is useful method in evaluation of fracture risk. Osteoporotic changes of the skeleton may be also quantified by the density- dependent bone strength degradation described by power-laws (Doblare et al., 2004). Compressive review and summary of elasticity–density relationships is are also presented by Helgason et al. (2008). Some recommendations are made for the application of elasticity–density relationships to subject-specific finite element studies (Helgason et al., 2008).

Discrete structure of the bone tissue may be transferred to FE models in a number of ways. The voxel-based finite element models are patient-specific or specimen-specific models (Jones and Wilcox, 2008). The sample of vertebral body was generated on the basis of QCT (Crawford et al., 2003). Here, material properties are then defined on an element-by-element basis using densities derived from the scanned image data. This method represents a clinically feasible approach, unable to distinguish properties of the cortical shell. Presented applications illustrate, see (Jones and Wilcox, 2008) and (Crawford et al., 2003), that finite element model-derived estimates of strength are better predictors of in vitro vertebral compressive strength than clinical measurements of bone density using a computer tomography.

A generic FE models are based on continuum description. Characterization of porous discrete micro-structure of trabecular tissues is non-unique and is still under development. The purely elastic inhomogeneous lumbar spine (L3 -L4) model including on the lumbar intervertebral disc, was considered (Su et al., 2009). In Crawford et al., (2003), by imaging observed inhomogeneity was implemented by nine elastic isotropic regions with different elasticity constants. Some of the models include plasticity (Macdonald et al., 2010; Garo et al., 2011). An anisotropic elastic–visco-plastic-damage model was applied by Wolfram et al. (2012).

The two-scale modelling approach proposed in series of works, where the macroscopic constitutive behaviour is determined on the properties of microstructure. Microscopic lattice network is used by McDonald et al. (2010). More comprehensive but computationally expensive approach used in Wierszycki et al. (2014) determines macroscopic constants directly on the detailed geometry of cancellous bone microstructure, where a porous representative cell of trabeculae of a cancellous bone is considered to be 3D solid body.

For identification of loading level and strength of bone the classical continuum-level yield criteria are frequently adopted to the strength criteria. Hereby, the von Mises yield criterion is the mostly used criterion (Provatidis et al., 2010) applied for vertebral trabecular bone. A fabric-dependent, orthotropic Tsai–Wu yield criterion is proposed in Wolfram et al., 2012].

Qualitative verification of the FE models largely depends on the model geometry and meshing technique. Geometry models of vertebrae can be divided into two categories (Jones and Wilcox, 2008). Geometry of models, whose are classified to the first category, is obtained on the data of a particularly measured in vitro specimens and all voxel-based models belong to them. Generic models are computationally generated parametrical models whose values reflect an average of the real sizes. Continuum models of this category are used to represent inhomogeneous vertebra. This approach is basically applied for representation of anatomical geometry of cortical shell. The treatment of the cortical shell by FE differs across the range of single vertebral models. In several cases, thin (McDonald et al., 2010) or thick (Garo et al., 2011) shell elements may be used but 3D tetrahedral or brick elements still prevail.

Simulation of the spine fragment involves the intervertebral discs (IVD) (Jones and Wilcox, 2008). The IVD presents a complex inhomogeneous, anisotropic and porous structure, which behaviour is governed by biochemical processes as well as mechanical properties. Simulation of the mechanical behaviour of disc has led to a number of different approaches (Dreischarf et al., 2014; Łodygowski et al., 2005; Jaramillo et al., 2015. FE simulation of osteoporotic vertebrae loaded via healthy and degenerated intervertebral disc calibrated against in vitro tests was demonstrated in Crawford et al. (2003). The three different viscoelastic models of disc were considered in Gohari et al. (2013) and three different viscoelastic finite element models were prepared for lumbar motion segment (L4/L5).

In most of applications, the investigations were restricted by static loading, while consideration of the dynamic loads are rather limited (Garo et al., 2011; El-Rich et al., 2009). The present study is aimed at numerical investigating the influence of osteoporotic degradation of L1 lumbar vertebral body on the mechanical strength characterization. Evaluation of the contribution of time-dependent load and degradation of mechanical properties is addressed due to dynamic load.

2. METHODS AND MATERIALS

2.1. Problem formulation

The Von Mises-Hencky criterion is applied on research

DOI 10.1515/ama-2017-0044

of stresses, which occur on cortical shell of the model. The selection of this criterion is based on mechanical properties of the bone, which seem to behave as a ductile material (Dreischarft et al., 2014; Wolfram et al., 2012).

It is defined in Eq. (1) below, where σ_1, σ_2 and σ_3 are the maximum, intermediate, and minimum principal stresses respectively. σ_y is a yield stress (40 MPa). This value is specific for osteoporotic bone (Nazarian et al., 2008).

$$\sqrt{\frac{(\sigma_1-\sigma_2)^2+(\sigma_2-\sigma_3)^2+(\sigma_3-\sigma_1)^2}{2}} = \sigma_y. \quad (1)$$

In nonlinear dynamic analysis, the equilibrium equations of the dynamic system at time step $t+\Delta t$ are:

$$[M]^{t+\Delta t}\{U''\}^{(i)} + [C]^{t+\Delta t}\{U'\}^{(i)} + {}^{t+\Delta t}[K]^{(i)}\,{}^{t+\Delta t}\{\Delta U\}^{(i)} = {}^{t+\Delta t}\{R\} - {}^{t+\Delta t}\{F\}^{(i-1)}, \quad (2)$$

where: *[M]* – mass matrix of the system, *[C]* – damping matrix of the system, ${}^{t+\Delta t}[K]^{(i)}$ – stiffness matrix of the system, ${}^{t+\Delta t}\{R\}$ – vector of externally applied nodal loads, ${}^{t+\Delta t}\{F\}^{(i-1)}$ - vector of internally generated nodal forces at iteration *(i-1)*, ${}^{t+\Delta t}[\Delta U]^{(i)}$ – vector of incremental nodal displacements at iteration *(i)*, ${}^{t+\Delta t}\{U'\}^{(i)}$ – vector of total velocities at iteration *(i)*, $[M]^{t+\Delta t}\{U''\}^{(i)}$ – vector of total accelerations at iteration *(i)* where damping matrix *[C]* was neglected or *[C]=0*.

Using implicit time integration Newmark-Beta scheme and employing a Newton's iterative method, the above equations are cast in the form:

$${}^{t+\Delta t}[K]^{(i)}\ \{\Delta U\}^{(i)} = {}^{t+\Delta t}\{R\}^{(i)}, \quad (3)$$

where: ${}^{t+\Delta t}\{R\}^{(i)}$ – the effective load vector and ${}^{t+\Delta t}[K]^{(i)}$ – the effective stiffness matrix.

The three-dimensional static and dynamic analysis was performed using BRIGADE/Plus software.

2.2. Geometry of the model

The inhomogeneous lumbar vertebrae body consists of two basic structural members – outer cortical shell fulfilled by inner bone tissue. The initial anatomical geometry of the vertebral body is developed by using DICOM format data and the model is illustrated in Fig. 1. The height of the lumbar vertebral body model is approximately equal to 30 mm, the cross-sectional size is approximately equal to 40 mm. Two intervertebral disks of 10 mm thickness were also included to reflect boundary conditions with the neighbour trabecular.

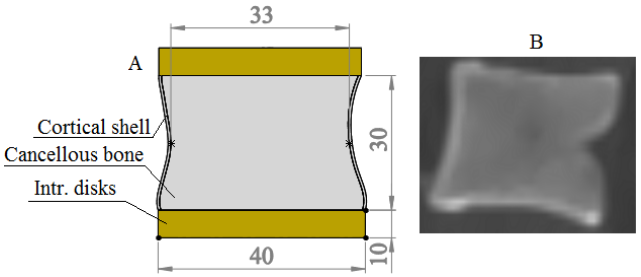

Fig. 1. A) Frontal section view of the model, B) initial DICOM data format (sagittal view)

2.3. Mechanical properties of structural members

Surrounding compact bone (cortical shell) is modelled as isotropic elastoplastic continuum as described in McDonald et al., (2010). The inner cancellous bone is transversally isotropic and perfectly elastic. The stress-strain curve for cortical bone is presented in Fig. 2. Intervertebral disks were assumed isotropic and perfectly elastic. Mechanical properties of model members are presented in Tab. 1.

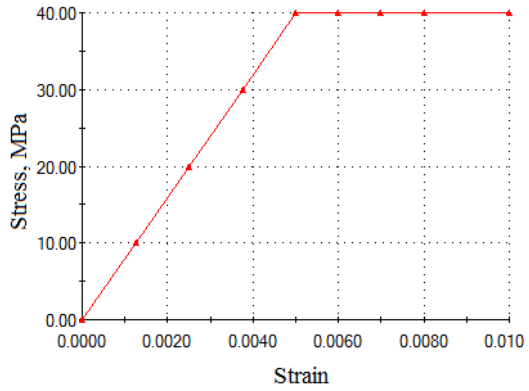

Fig. 2. Stress-strain curve for cortical bone (E=8 GPa)

The influence of osteoporosis is modelled by changing the thickness of cortical shell. In this research, we were investigating three models with thickness of 0.2, 0.4 and 0.5 mm first used in McDonald (2010) and Kim et al. (2013). Osteoporotic changes of the vertebrae is also characterised by decreasing modulus of elasticity of cancellous bone. Modulus of cancellous bone is determined according to power-law equations, which reflect the impact of apparent density. The selection of this equation is based on alignment of our research and data published by Helgason et al. (2008).

$$E_{cancellous} = 4.730\rho^{1.56}, \quad (4)$$

where: ρ – apparent density. In current research, it is in range between 0.10 and 0.30 g/cm^3.

Tab. 1. Elasticity constants and density parameters

Part of the model	E_z, MPa	$E_x=E_y$, MPa	ν_z	$\nu_x=\nu_y$	ρ, g/cm^3
Cortical shell	8000	8000	0.300	0.300	-
Cancellous bone	130-720	42-240	0.300	0.200	0.10-0.30
Intervertebral disk	10	10	0.495	0.495	-

2.4. Loads and boundary conditions

The bone is subjected by the physiological loads, which occur through daily activities. Generally, it presents the axially acting pressure load in the range between 0.15 and 0.75 MPa (Fig. 3).

These values are equivalent to 160-810 N compressive force.

Due to nonlinear dynamic analysis, the load depends on the displacement values while it's direction during compression changes with the deformed shape of the model.

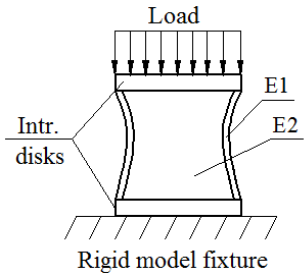

Fig. 3. Schematization of load due to compression test, E1 – cortical shell; E2 – cancellous bone

Time variation of the load is shown in Fig. 4 and is determined to simulate the effect of dynamic load bearing. The character of time curve is based on analysis of jumps using force platform (Linthorne, 2010). It is easy to find that in the first stage until 0.15 MPa the loading is low and has static character while in the second stage in the range of 0.15 and 0.75 MPa nonlinear behaviour is expected. Load was applied vertically on the surface of superior intervertebral disk. The bottom intervertebral disk was constrained from any motion.

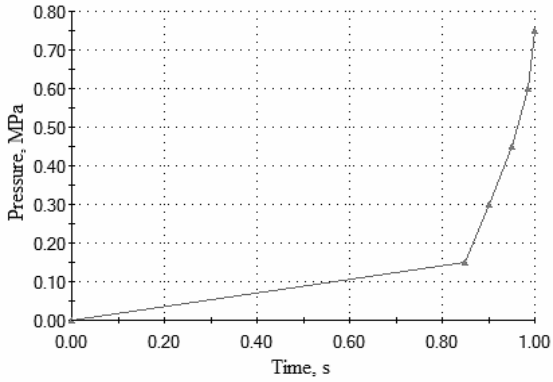

Fig. 4. Variation of dynamic load in time

2.5. Meshing

The model was meshed with triangular finite elements due to its curvature. The cortical and trabecular bone is presented as 3D structure and meshed by using volume tetrahedral finite elements. The number of finite elements of cortical bone was 7686 and the number of nodes – 16597, as for the most important part of the model. The number of finite elements of cancellous bone was 12915, the number of nodes – 18313. The number of finite elements of intervertebral disks was only 3224 and the number of nodes – 5677, for it's not the primary part of the model. The model is characterized by 113 274 degrees of freedom. BRIGADE/Plus software was used. The meshed model is presented in Fig. 5.

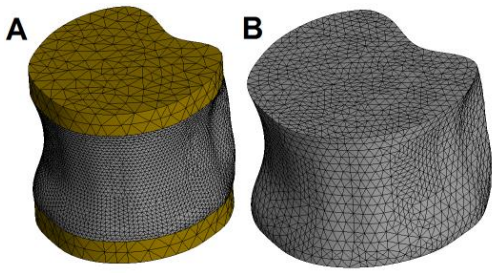

Fig. 5. Meshed parts of the model with finite elements: A) – intervertebral disks and cortical shell, B) – cancellous bone

3. NUMERICAL RESULTS AND DISCUSSION

The numerical results of both static, dynamic analysis and their comparison are presented below. Also, the comparison between static and dynamic results is performed and presented graphically.

3.1. Static analysis

Stress distribution on cortical shell of the model is shown in Fig. 6. It shows that the highest von-Mises stresses occurred in the middle of the cortical shell on the front side of the model, and on its posterior side (Fig. 6).

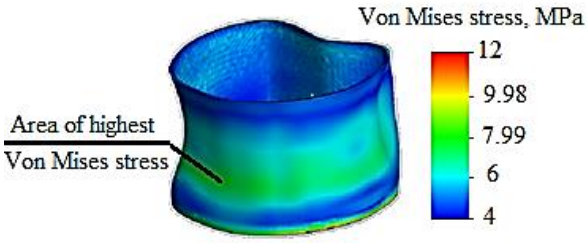

Fig. 6. Distribution of stress on cortical shell of the model under 0.3 MPa load, with apparent density of cancellous bone 0.2 g/cm^3

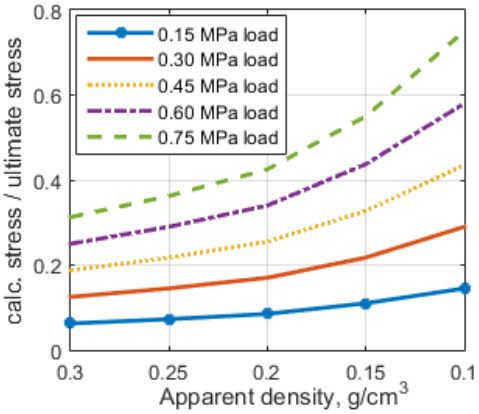

Fig. 7. Relation between calculated and maximum Von Mises stress on cortical shell of the model versus apparent density and load for thickness of cortical shell 0.5 mm

Fig. 7 shows a relation between calculated and ultimate (σ_{ult}=40 MPa) Von Mises stress on cortical shell (0.5 mm thickness) of the model versus apparent density and different load

DOI 10.1515/ama-2017-0044

values. The results show, that maximum calculated stress reaches 70% of ultimate stress due to 0.75 MPa load on model with apparent density of 0.1 g/cm^3, though, it doesn't reach the value of ultimate stress (40 MPa). It proves that cortical shell plays important role in whole strength of lumbar vertebral body and despite of poor apparent density (0.1 g/cm^3) of cancellous bone, still can carry compression load safely.

Figs. 8 and 9 show a relation between calculated and ultimate Von Mises stress for models with 0.4 and 0.2 mm cortical shell thickness. Maximal stress is about 35 MPa due to minimum apparent density. It reaches 87% of ultimate stress and it is 25% higher than for the model with 0.5 mm thickness of cortical shell.

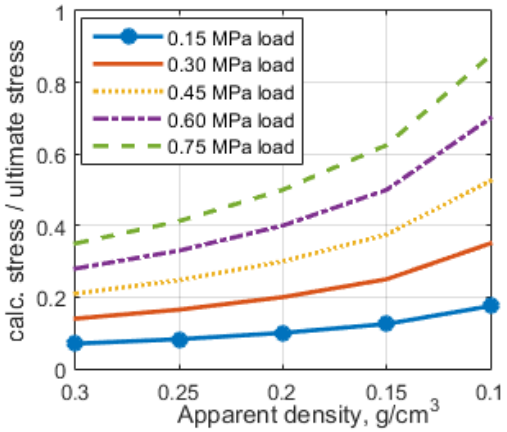

Fig. 8. Relation between calculated and maximum Von Mises stress on cortical shell of the model versus apparent density and load for thickness of cortical shell 0.4 mm

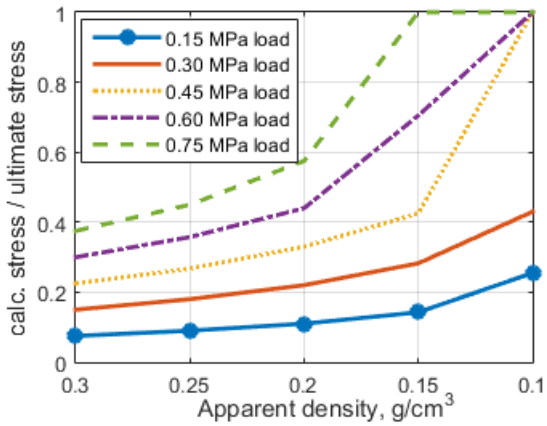

Fig. 9. Relation between calculated and maximum Von Mises stress on cortical shell of the model versus apparent density and load for thickness of cortical shell 0.2 mm

Fig. 9 shows that strength load is 0.45 MPa, while apparent density of cancellous bone is less than 0.15 g/cm^3.

Obtained results are in good agreement with research of Kim et al. (2013), with difference about 5-10% for the model with low apparent density and thickness of cortical shell 0.2 mm. The maximum compressive load for model with 0.2 mm cortical shell thickness is 0.45-0.60 MPa (in addiction to apparent density), while McDonald (MacDonald et al., 2010) reports this value up to 0.99 MPa.

3.2. Dynamic analysis

The stresses distribution in lumbar vertebra during dynamical analysis was computed. It is easy to see, that stress concentrators are more contrast, than due to static analysis. The highest value of stress appeared in the middle of cortical shell and it is in a good agreement with clinical observations (Agrawal and Kalia, 2014; Lin and Lane, 2004; Cooper et al., 2011; Cummings and Melton III, 2002; Melton III et al., 2013). The distribution of Von Mises stress on cortical shell of the model is shown in Fig. 10.

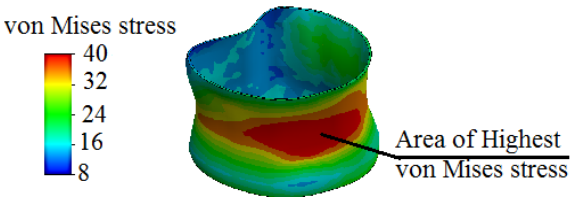

Fig. 10. Distribution of Von Mises stress on cortical shell of the model due to dynamic load

Fig. 11 shows a relation between calculated and maximum (σ_{ult}=40 MPa) Von Mises stress on cortical shell (0.5 mm thickness) of the model versus apparent density and different load values.

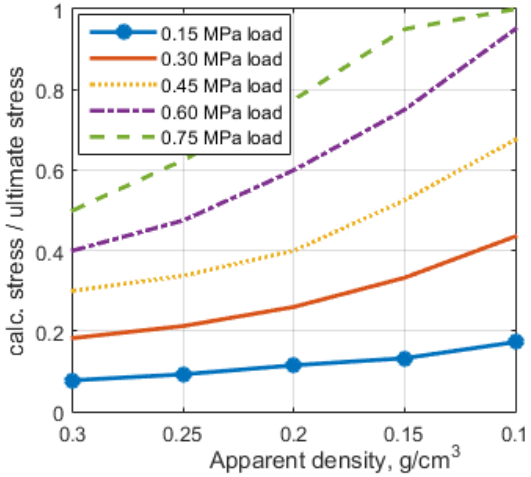

Fig. 11. Relation between calculated and maximum Von Mises stress on cortical shell of the model versus apparent density and load. Thickness of cortical shell is 0.5 mm

Fig. 11 shows that failure of the model is expected due to 0.6 MPa load while density of cancellous bone is less than 0.1 g /cm^3.

Relations between calculated and maximum Von Mises stress on cortical shell of the model with 0.4 and 0.2 mm thicknesses versus apparent density and load are presented in Figs. 12, 13 and 14. It shows, that failure of the model is expected due to 0.45 MPa load while medium apparent density ~0.2 g/cm^3 occurs.

Oleg Ardatov, Algirdas Maknickas, Vidmantas Alekna, Marija Tamulaitienė, Rimantas Kačianauskas DOI 10.1515/ama-2017-0044

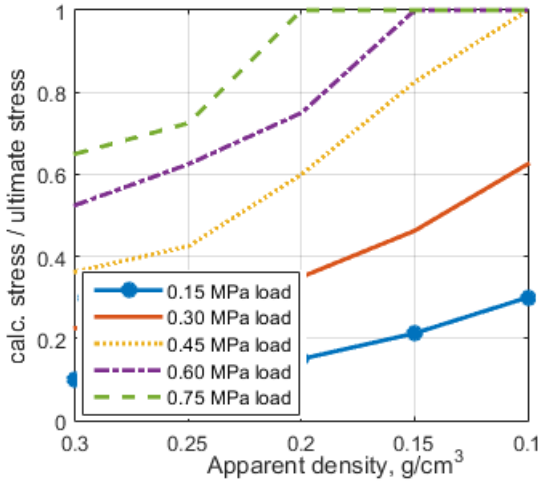

Fig. 12. Relation between calculated and maximum Von Mises stress on cortical shell of the model versus apparent density and load. Thickness of cortical shell is 0.4 mm

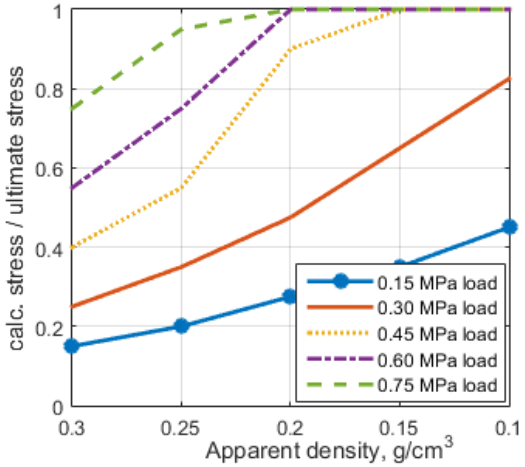

Fig. 13. Relation between calculated and maximum Von Mises stress on cortical shell of the model versus apparent density and load. Thickness of cortical shell is 0.2 mm

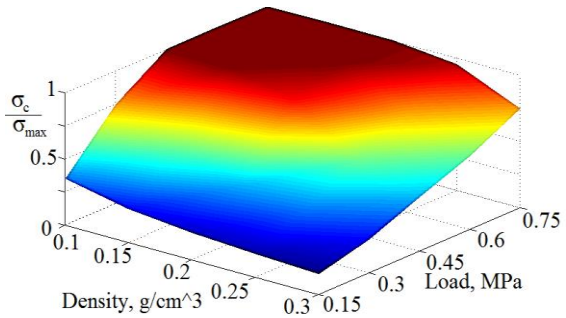

Fig. 14. Relation between calculated and maximum Von Mises stress on cortical shell of the model versus apparent density and load (3D view)

3.3. Comparison between static and dynamic results

Distribution of stress due to dynamical load is more varied and there is the higher risk of shell overloading. The failure of the model is obtained by external 0.45 MPa load due to 0.15 g/cm^3 bone density in case of dynamical analysis. The same effect was observed in terms of static analysis, for 0.45 MPa load and 0.10 g/cm^3 cancellous bone density. It shows that dynamic loads are more dangerous for lumbar body (Fig. 15).

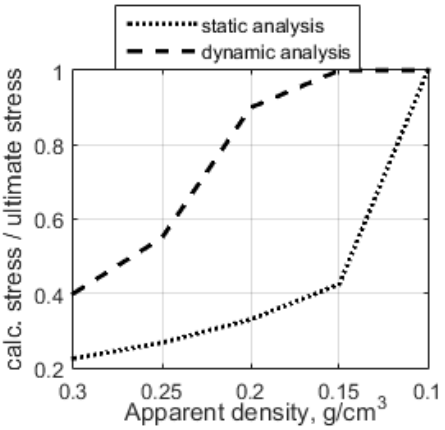

Fig. 15. Dependence between von Mises stress, and density of trabecular bone in model with 0.2 mm shell thickness due to 0.45 MPa load

The comparison of calculated and ultimate stress in linear static and nonlinear dynamic analysis gives notably higher result for nonlinear dynamics load and is highest for 0.75 MPa and lowest apparent density of trabecular bone (0.1 g/cm^3). It is presented in Figs. 16-18.

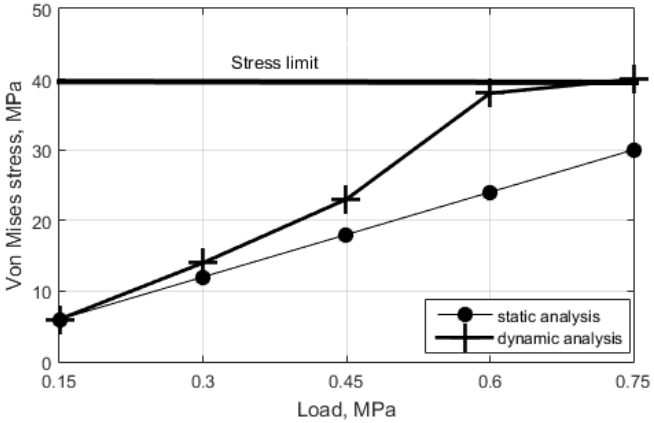

Fig. 16. Difference between Von Mises stress values due to static and dynamic load for model with 0.5 mm cortical shell thickness

Fig. 16 shows the difference between Von Mises stress values due to static and dynamic load for model with 0.5 mm cortical shell thickness. Now we observe that the difference between results of static and dynamic analysis increases as load enhances. Ratio between stress values due to 0.45 MPa load is 20%, while it increases up to 40% due to 0.60 MPa load. Due to 0.75 MPa load value of stress reaches critical value in case of dynamic load, while the strength capacity is more than 25% in case of static load.

Fig. 17 shows the difference between Von Mises stress values due to static and dynamic load for model with 0.4 mm cortical shell thickness. In this case, the ratio between stress values due to 0.15 MPa load is less than 25% while it reaches 50% due to 0.45 MPa load, and strength capacity of dynamic load is exceeded, while it has a 15% reserve due to static load.

DOI 10.1515/ama-2017-0044

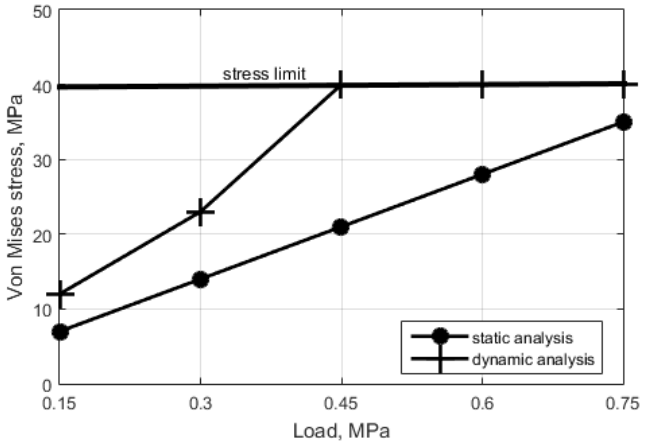

Fig. 17. Difference between Von Mises stress values due to static and dynamic load for model with 0.4 mm cortical shell thickness

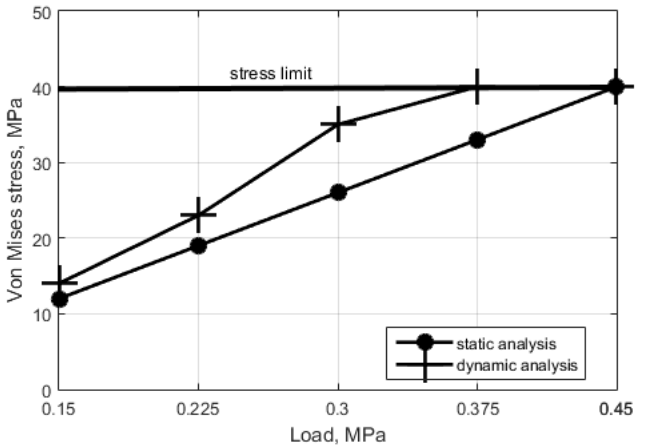

Fig. 18. Difference between Von Mises stress values due to static and dynamic load for model with 0.2 mm cortical shell thickness

Fig. 18 shows the difference between results of static and dynamic analysis for model with 0.2 mm thickness of cortical shell. The difference in results exceeds 25% due to 0.3 MPa load while the difference between stress values due to 0.15 MPa load is only 15%. In both cases critical value of stress is reached due to 0.45 MPa load.

The results obtained also show that stress greatly depends on both thickness of cortical shell and apparent density of cancellous bone, though the primary role is being played by cortical shell, as it carries the major part of the load. On the other hand, a quality of cancellous bone, which is determined by its density, affects the value of stresses. In comparison, the value of failure of the model will be expected due to 0.45 MPa load for model with 0.2 thickness of cortical shell (Fig. 13, 14, 15, 18), since apparent density of cancellous bone is smaller than 0.15 g/cm^3. Also, the results of our research show, that static analysis is not reliable enough for predicting strength capacity of the osteoporotic lumbar vertebrae, with the variance in range of the results up to 50%.

4. CONCLUSION

The proposed model which consisted of cortical shell, cancellous bone and intervertebral disks was treated for various grades of degenerative diseases. The numerical test was performed by applying the FEM tools. The problem was solved using tetrahedral finite elements according to complicated curvature of the model. The optimal mesh and number of finite elements were figured up on the basis of calculation accuracy and calculation time ratio. The von-Mises stress, which was assumed to verify the strength properties, was determined for three different thicknesses of cortical shell and different apparent density of cancellous bone (in range of 0.1—0.3 g/cm^3).

The results showed that the von-Mises stress was substantially higher under relatively low levels of apparent density, and critical due to thinner cortical shell, which suggests the high fracture risk even during daily activities. The results also showed that cortical shell is the most important component in aspect of lumbar body strength and the decrease of its thickness from 0.5 mm down to 0.2 mm leads to bone overloading.

In addition, this model can be individualized according to the peculiar anatomical properties of the patient. For that case the DICOM format file should be extracted and processed using CAD software. Then the mechanical properties based on apparent density should be supplied to the developed model and the numerical results of both static and dynamic loading could be used in order to verify the stressed state of the model.

REFERENCES

1. **Agrawal A., Kalia R.** (2014), Osteoporosis: current review, *J. Orthop. Traumatol. Rehabil.,* 7, 101-102.
2. **Bono C.M., Einhorn T.A.** (2003),Overview of osteoporosis: pathophysiology and determinants of bone strength., *Eur. Spine J*., 12, 90–96.
3. **Bouzakis K.D., Mitsi S., Michailidis N., Mirisidis I., Mesomeris G., Maliaris G., Korlos A., Kapetanos G., Antonarakos P., Anagnognostidos K.** (2004), Loading simulation of lumbar spine vertebrae during a compression test using the finite elements method and trabecular bone strength properties, determined by means of nanoindentations, *J. Musculoskelet. Neuronal Interact.*, 4, 152–158.
4. **Cooper C., Cole Z.A. Holroyd C.R.**, et al. (2011), Secular trends in the incidence of hip and other osteoporotic fractures, *Osteoporos Int*., 22, 1277–1288.
5. **Crawford R.P., Cann C.E., Keaveny T.M.** (2003), Finite element models predict in vitro vertebral body compressive strength better than quantitative computed tomography, *Bone*, 33, 744–750.
6. **Cummings S.R., Melton III L.J.**. (2002), Epidemiology and outcomes of osteoporotic fractures, *Lancet* 359,1761–1767.
7. **Doblaré M., Garcia J.M., Gómez M.J.** (2004), Modelling bone tissue fracture and healing: a review, *Eng. Fract. Mech*., 71, 1809–1840.
8. **Dreischarf M., Zander T., Shirazi-Adl A., Puttlitz C.M., Adam C.J., Chen C.S.**, et al. (2014),Comparison of eight published static finite element models of the intact lumbar spine: Predictive power of models improves when combined together, *J. Biomech*., 47, 1757–1766.
9. **El-Rich M., Arnoux P.J., Wagnac E., Brunet C., Aubin C.E.** (2009),Finite element investigation of the loading rate effect on the spinal load-sharing changes under impact conditions, *J. Biomech.*, 42, 1252–1262.
10. **Garo A., Arnoux P.J., Wagnac E., Aubin C.E.** (2011), Calibration of the mechanical properties in a finite element model of a lumbar vertebra under dynamic compression up to failure, *Med. Biol. Eng. Comput.* 49, 1371–1379.
11. **Gohari E., Nikkhoo M., Haghpanahi M., Parnianpour M.** (2013), Analysis of different material theories used in a FE model of a lumbar segment motion, *Acta Bioeng. Biomech*., 15, 33–41.
12. **Helgason B., Perilli E., Schileo E., Taddei F., Brynjólfsson S.S., Viceconti M.** (2008), Mathematical relationships between bone density and mechanical properties: A literature review, *Clin. Biomech*., 23, 135–146.

13. **Jaramillo H.E., Gomez L., Garcia J.J.** (2015), A finite element model of the L4-L5-S1 human spine segment including the heterogeneity and anisotropy of the discs, *Acta Bioeng. Biomeechanics*., 17, 15–24.
14. **Johnell O., Kanis J.A., Odén A., Sernbo I., Redlund-Johnell I., Petterson C.**, et al. (2004), Mortality after osteoporotic fractures, *Osteoporos. Int.*, 15, 38–42.
15. **Jones A.C., Wilcox R.K.**, (2008), Finite element analysis of the spine: Towards a framework of verification, validation and sensitivity analysis, *Med. Eng. Phys*., 30, 1287–1304.
16. **Lin J.T., Lane J.M.** (2004), Osteoporosis: a review., *Clin. Orthop. Relat. Res*., 425, 126–34.
17. **Linthorne N. P.** (2010), Analysis of standing vertical jumps using a force platform, *The Journal of Sports Science and Medicine*, 9, 282-287
18. **Kim Y.H., Wu M., Kim K.** (2013), Stress analysis of osteoporotic lumbar vertebra using finite element model with microscaled beam-shell trabecular-cortical structure, *Journal of Applied Mathematics*, 2013, 146-152.
19. **Łodygowski T., Kakol W., Wierszycki M., Ogurkowska B.M.** (2005), Three-dimensional nonlinear finite element model of the human lumbar spine segment, *Acta Bioeng. Biomech*., 7, 17–28.
20. **McDonald K., Little J., Pearcy M., Adam C.** (2010), Development of a multi-scale finite element model of the osteoporotic lumbar vertebral body for the investigation of apparent level vertebra mechanics and micro-level trabecular mechanics, *Med. Eng. Phys*., 32, 653–661.
21. **Maquer G., Schwiedrzik J., Huber G., Morlock M.M., Zysset P.K.** (2015), Compressive strength of elderly vertebrae is reduced by disc degeneration and additional flexion, *J. Mech. Behav. Biomed. Mater*. 42, 54–66.
22. **Melton III L.J., Achenbach S. J. Atkinson E.J., Therneau T.M., Amin S.** (2013), Long-term mortality following fractures at different skeletai sites: a population-based cohort study, *Osteoporos Int.*, 24, 1689–1696.
23. **Nazarian A., von Stechow D., Zurakowski D., Muller R., Snyder B.D.** (2008), Bone Volume Fraction Explains the Variation in Strength and Stiffness of Cancellous Bone Affected by Metastatic Cancer and Osteoporosis, *Calcified Tissue International,* 83, 368-379.
24. **Okamoto Y., Murakami H., Demura S., Kato S., Yoshioka K., Hayashi H.**, et al. (2014), The effect of kyphotic deformity because of vertebral fracture: a finite element analysis of a 10° and 20° wedge-shaped vertebral fracture model, *Spine J*., 15, 713–720.
25. **Provatidis C., Vossou C., Koukoulis I., Balanika A., Baltas C., Lyritis G.** (2010),A pilot finite element study of an osteoporotic L1-vertebra compared to one with normal T-score., *Comput. Methods Biomech. Biomed. Engin*., 13, 185–95.
26. **Su J., Cao L., Li Z., Yu B., Zhang C., Li M.** (2009), Three-dimensional finite element analysis of lumbar vertebra loaded by static stress and its biomechanical significance, *Chinese J. Traumatol*., 12, 153–156.
27. **Svedbom A., Hernlund E., Ivergård M., Compston J., Cooper C., Stenmark J., McCloskey E.V, Jönsson B., Kanis J.A.** (2013), The EU review panel of the IOF. Osteoporosis in the European Union: a compendium of country-specific reports, *Arch. Osteoporos*., 8, 137-138.
28. **Watanabe I., Furusu K., Kato C., Miki K., Hasegawa J.** (2001), Development of practical and simplified human whole body FEM model*, JSAE Rev.*, 22, 189–194.
29. **Wierszycki M., Szajek K., Łodygowski T., Nowak M.** (2014), A two-scale approach for trabecular bone microstructure modeling based on computational homogenization procedure, *Comput. Mech*., 54, 287–298.
30. **Wolfram U., Gross T., Pahr D.H., Schwiedrzik J., Wilke H.J., Zysset P.K.** (2012), Fabric-based Tsai-Wu yield criteria for vertebral trabecular bone in stress and strain space, *J. Mech. Behav. Biomed. Mater*., 15, 218–228.

DE GRUYTER
OPEN

DOI 10.1515/ama-2017-0045 acta mechanica et automatica, vol.11 no.4 (2017)

ASYMPTOTIC APPROXIMATIONS TO THE NON-ISOTHERMAL DISTRIBUTED ACTIVATION ENERGY MODEL FOR BIO-MASS PYROLYSIS

Alok DHAUNDIYAL[*], Suraj B. SINGH [**]

[*]Faculty of Mechanical Engineering, Mechanical Engineering PhD School, Szent Istvan University, Godollo, Hungary
[**] Department of Mathematics, Statistics and Computer Science, Govind Ballabh Pant University of Agriculture and Technology, Pantnagar, Uttarakhand 263153, India

Dhaundiyal.Alok@phd.uni-szie.hu, drsurajbsingh@yahoo.com

received 17 June 2016, revised 23 November 2017, accepted 28 November 2017

Abstract: This paper describes the influence of some parameters significant to biomass pyrolysis on the numerical solutions of the non-isothermal nth order distributed activation energy model (DAEM) using the Gamma distribution and discusses the special case for the positive integer value of the scale parameter (λ), i.e. the Erlang distribution. Investigated parameters are the integral upper limit, the frequency factor, the heating rate, the reaction order, and the shape and rate parameters of the Gamma distribution. Influence of these parameters has been considered for the determination of the kinetic parameters of the non-isothermal nth order Gamma distribution from the experimentally derived thermoanalytical data of biomass pyrolysis. Mathematically, the effect of parameters on numerical solution is also used for predicting the behaviour of the unpyrolysized fraction of biomass with respect to temperature. Analysis of the mathematical model is based upon asymptotic expansions, which leads to the systematic methods for efficient way to determine the accurate approximations. The proposed method, therefore, provides a rapid and highly effective way for estimating the kinetic parameters and the distribution of activation energies.

Key words: Biomass Pyrolysis, Distributed Activation Energy Model (DAEM), Non- Isothermal Kinetics, Gamma Distribution, Asymptotic Expansion, Erlang Distribution

1. INTRODUCTION

There are various possible ways of converting biomass into valuable products (Szczodrak and Fiedurek, 1996). One of them is pyrolysis, which comes under purview of thermochemical processes. While biomass undergoes pyrolysis process, it changes into gases, liquid oil and char. The details studies related to pyrolysis and thermal analysis is reported by Colomba Di Blasi (Blasi, 2008) and John E White (White and Legendre, 2011). Thermogravimetric analysis (TGA) is mainly used for experimental observation of pyrolysis decomposition (Brown, 2001). The main objective of thermogravimetric analysis is to measure changes of mass as functions of time or temperature.

Mathematically, it becomes complicated to describe biomass decomposition kinetics, as several reactions take place and their mechanism is unknown. There are various models which have been used to explain biomass pyrolysis, such as single-reaction and multi-reaction models (Carpart et al., 2004; Conesa et al., 1995; Conesa et al, 2001; Pysiak and Badwi, 2004; Mysyk et al. 2005; CriadoJ Pérez-Maqueda, 2005). The most common approach used is isoconversional model, which assumes that kinetic parameters, such as the frequency factor and activation energies, are not constant during the process of decomposition. Another model, which is also used for determination of kinetic parameters, is the lumped kinetics model. It postulates that an ultimate number of parallel n^{th} order reactions take place. These partial reactions provide the information about overall decomposition run. However, hitherto, the most accurate and up-to-date approach has been implemented for the modeling of biomass pyrolysis is the distributed activation energy model (DAEM) (Burnham and Braun, 1999; Burnham et al.,1995; Galgano and Blasi, 2003; Ferdous et al., 2002). Comparatively, the principle of the lumped kinetic model is very similar to the DAEM. The only difference is in the number of expected decomposition reactions. However, lumped kinetic model contains around one-hundred decomposition reactions, it would be approaching the distributed activation kinetic model.

The numerical solutions obtained, after implementing the asymptotic expansion, of the kinetic model are used to determine the kinetic parameters. To predict realistic results, the parameters affecting the behaviour of numerical solution must be estimated. The effect of these parameters on the single –reaction models has been reviewed in literature (Brown, 2001). The distributed activation energy model (DAEM) has proven very successful to describe the pyrolysis of different types of biomass. Our study mainly focuses on the relevant parameters which affect the kinetics of pyrolysis. The DAEM also applies to the pyrolysis of other conventional sources of energy like coal, residual oils, resin chars (Teng and Hsieh, 1999) and kerogen (Lakshmanan and White, 1994). This analytical method is not only used for thermal decomposition of plant, or animal biomass (Giuntoli et al., 2009; Lapuerta et al., 2004), but also for thermal decomposition of other materials such as medical wastes (Zhu et al., 2009), waste car tyres ([Koreňová et al., 2006), printed circuit board wastes (Quan et al., 2009), or sewage sludge (Otero et al. 2008; Folgueras et al. 2003). Approximation to the non-isothermal distribution requires

DOI 10.1515/ama-2017-0045

many evaluations of double exponential term (DExp) which involves rapidly varying functions, and this leads to significant numerical difficulties. In addition to that the double exponential term arising in the DAEM, is investigated for the non-isothermal temperature profile only. This double exponential term acts over a narrow range of activation energies, which varies as time proceeds. While approximating, the significant part of our analysis is to identify the importance of relative step width of the double exponential term as compared to the width of the initial distribution of volatiles released during pyrolysis. The main aim of this study is to use asymptotic methods to make accurate approximation to the integrals, and thereby predict the behaviour of the non-isothermal nth order DAEM by considering the effect of some relevant parameters on the pyrolysis of biomass and discuss the behaviour of distribution for the special case (Erlang distribution).

2. THE NON-ISOTHERMAL NTH ORDER DAEM USING THE GAMMA DISTRIBUTION AND ITS ASYMPTOTIC APPROXIMATION

The concept of distributed activation energy was originally propounded by Vand (1943). Pitt applied DAEM to the problem of coal devolatilization (Pitt, 1962). Later, it was used by Hanbaba and his co-workers (Hanbaba, 1968), and Anthony (Anthony, 1974). Postulation of the model states that the decomposition mechanism takes many independent, parallel, first order chemical reactions with different activation energies which reflect variations in the bond strength of constituent of biomass. The development of the model here follows Howard (Howard,1981) and Solomon and Hamblen (Solomon and Hamblen, 1983). Assume biomass's constituents are numbered $i = 1,2,3 \dots \dots n$, and the released (volatilized mass fraction for the ith constituent is $V_i(t)$. The initial mass of constituent i in the coal is V_i^*. Each reaction is assumed to be first order, so that the rate of pyrolysis is given by equation (1)

$$\frac{dV_i}{dt} = k_i(V_i^* - V_i) \tag{1}$$

The rate coefficient is taken to be Arrhenius in the form

$$k_i = k_{0i}e^{-\frac{E_i}{RT}},$$

where $\mathrm{k_{0i}}$ is the pre-exponential or frequency factor (s^{-1}), E_i is the apparent activation energy for constituent i (kJ/mol), R is ideal gas constant, and $T(t)$ is the time-dependent temperature (K) regime of the biomass.

Equation (1) can be written as:

$$(V_i^* - V_i) = e^{-\int_0^t k_i dt}$$

For $\mathrm{i} = 1$, the model is referred to as the single first-order reaction model (SFOR). In DAEM, the dependence on volatile number i is substituted by a continuous distribution function of activation energy E, so that the total fraction of volatile available to release from biomass is considered to follow distribution correctly (Equation (2)).

$$dV^* = f(E)dE$$

The solution then becomes:

$$\frac{V^*-V}{V^*} = \int_0^\infty \exp\left(-\int_0^t k_0(E)e^{-\frac{E}{RT}}\right) f(E)dE \tag{2}$$

The main purpose of using this model is to assume the initial distribution of volatile $f(E)$, the pre-exponential factors $k_0(E)$, and then find the resulting time-dependence of the volatiles. This model involves reaction time scale, which gained lot of acceptance as it is most significant part of biomass devolatilization (Howard, 1981; Suuberg, 1983). The problem relating to DAEM is that the function $f(E)$ and $k_0(E)$ are highly correlated, hence it is very complicated for us to determine both functions accurately. A common assumption has been considered to assume the constant value of pre-exponential or frequency factors k_0. By doing so, though analysis gets easier, but study is more focused towards the uncertainty of reactant distributions. In this paper, approximation for the time-dependence of the volatiles is evaluated first, which is given by equation (2), where $k_0(E)$ is replaced by the constant k_0. The non-isothermal nth DAEM is given by equation (3)

$$1 - X = \begin{cases} \int_0^\infty \exp\left[-\int_0^t k_0 \exp\left(\frac{-E}{RT}\right) dt\right] f(E)dE \ \ (\text{first order reaction}) \\ \int_0^\infty \left[1 - \left(1 - n\int_0^t k_0 \exp\left(\frac{-E}{RT}\right) dt\right)\right]^{\left(\frac{1}{1-n}\right)} f(E)dE \ \ \text{for } n \neq 1 \end{cases} \tag{3}$$

where $(1 - \mathrm{X})$ is the mass fraction of released volatile, n is the order of reaction, and $f(E)$ is the distribution of activation energies.

Mainly, $\mathrm{f(E)}$ is a Gaussian distribution function. As the selection of an appropriate distribution function for the molecular activation energies is very important component of our study, so it would be beneficial to select an asymmetric distribution for modeling the kinetics of biomass pyrolysis, such as the Gamma distribution, over a symmetrical one (Skrdla and Roberson, 2005).

Moreover, the Gamma distribution is mathematically flexible and expressed as:

$$f(E) = \frac{E^{(\lambda-1)}e^{-\frac{E}{\eta}}}{\eta^\lambda \Gamma(\lambda)} \text{ for } E > 0 \tag{4}$$

where λ is positive scale parameter expressed in kJ/mol and, η is dimensionless positive shape parameter.

The mean and the variance of distribution are given by equation (5) and equation (6) respectively:

$$E_0 = \frac{\lambda}{\eta} \tag{5}$$

$$\sigma^2 = \frac{\lambda}{\eta^2} \tag{6}$$

Primarily, the Erlang distribution was given by A. K. Erlang to examine the telephonic-traffic engineering. Later, it was implemented in the field of stochastic and biomathematics (Robeva, 2010). Basically, the Erlang distribution is a special case of the Gamma distribution for the integer values of the scale parameter λ. For η =1, the distribution is exponential. For values of $\eta \geq 1$, the distribution becomes 'bell shaped', and positively skewed. With increase in the value of η, the Gamma distribution approaches the Gaussian distribution more and more closely. In addition, attribute of distribution curve is also decided by the scale and shape parameters. However, the wide distribution pattern is chosen to simplify the given numerical problem of DAEM. Here, variance and mean of distribution functions are dependent on these parameters, which are evaluated with the help of equations (5) and (6).

DOI 10.1515/ama-2017-0045

3. SYSTEMATIC APPROXIMATIONS

The integrand in equation (3) (first order) consists of two terms. The first term (DExp) of equation (3) is function of time, which in fact depends on the temperature history experienced experimentally by the biomass sample. The second part is invariant of time, and depends on the distribution of volatiles in the sample. The behaviour of temperature dependent part is considered first, and approximations are derived that is useful to solve the double exponential term. The ramping temperature history only has been investigated, together with the Gamma distribution of volatiles.

3.1. The double exponential simplification

Approximations to the double exponential are considered, where T varies linearly with time and having constant slope that indicates the heating rate (θ) of sample E can take any positive value. The approach considered here is similar to that of Niksa and Lau (Niksa and Lau, 1993) and it involves much systematic and accurate approximation.

$$\mathrm{DExp} = \exp\left(-\int_0^t k_0 e^{-\frac{E}{RT}}\, dt\right)$$

For approximation of double exponential term, the first step is to consider the typical values of dependent parameters and functions. The frequency factors ($\mathrm{k_0}$) are typically in range of $\mathrm{k_0} \sim 10^{10} - 10^{13}\mathrm{s}^{-1}$, whereas the activation energies domain lies between 100-300 kJ/mol. The temperature dependence, however, consider according to the specified experimental requirement. It varies from biomass to biomass, but typically the range of temperature varies as:

$$1000\,°C \leq T \leq 2000\,°C$$

Note: The DAEM model is also applicable to the combustion related problems where the extensive range of temperature is incorporated, and hence it is useful to extrapolate the simplification made in the higher specified regimes of temperature, which is mentioned above.

To demonstrate the proposed method, the ramping profile of temperature has been considered as follows

$$\mathrm{T} = \theta \mathrm{t},$$

If the temperature is taken to ramp linearly, DExp becomes:

$$\mathrm{DExp} = \exp\left(-\int_0^t k_0\, e^{-\frac{E}{R\theta t}}\, dt\right)$$

The integral in the exponent is approximated by using the conventional Laplace approach where the parameter $\frac{\mathrm{E}}{\mathrm{R\theta t}}$ is assumed to be large and hence the dominant contribution from the integral is nearest to the maximum temperature experienced by the biomass sample.

$$\exp\left(-\int_0^t k_0\, e^{-\frac{E}{R\theta t}}\, dt\right) \sim \exp\left(\frac{-k_0\, R\theta t^2}{E} e^{-\frac{E}{R\theta t}}\right) \quad (7)$$

as $\frac{E}{R\theta t} \to \infty$

This approximate function can be written in the form:

$$\sim \exp\left(-\exp\left(\frac{E_s - E}{E_w}\right)\right)$$

where again the function switches rapidly from zero to one with respect to increment of activation energy E, over a range of step size $\mathrm{E_w}$ around the central value $\mathrm{E_s}$, which can be approximated as follows:

$$g(E) = \left(\frac{E_s - E}{E_w}\right)$$

Then equation (7) can be rewritten as:

$$\exp\left(-\exp\big(g(E)\big)\right)$$

where:

$$g(E) \equiv -\frac{E}{R\theta t} + \ln\left(\frac{k_0 R\theta t^2}{E}\right)$$

Expand $\mathrm{g(E)}$ with the help of Taylor series around $\mathrm{E_s}$ by:

$$g(E) \sim g(E_s) + (E - E_s) g'(E_s) + \frac{(E-E_s)^2}{2!} g''(E_s) + \ldots \quad (8)$$

Using equation (8) and the predefined function $\mathrm{g(E_s)}$, $\mathrm{E_s}$ and $\mathrm{E_w}$ are chosen such that:

$$g(E_s) = 0 \text{ and } g'(E_s) = \frac{-1}{E_w}$$

After solving these, we have:

$$E_s = R\theta t Y(k_0 t) \text{ and } E_w = \left(\frac{R\theta t E_s}{R\theta t + E_s}\right)$$

where $\mathrm{Y(x)}$ is Lambert W function defined to be one of the real roots of the equation:

$$Y\, e^Y = x.$$

Approximation for the small and the large values of x (corresponding to short and long times) (Armstrong and Kulesza, 1981) can be taken as:

$$Y \sim x - x^2, x \ll 1,$$

and

$$Y \sim \ln\left(\frac{x}{\ln\left(\frac{x}{\ln x}\right)}\right), x \gg 1.$$

DExp has been varied like a smoothed step-function, rising rapidly (for the large values of $\mathrm{k_0 t}$) from zero to one in a range of activation energies of the step width $\mathrm{E_w}$ around the central value $\mathrm{E = E_s}$, where both $\mathrm{E_s}$ and $\mathrm{E_w}$ vary with time. In equation (3), DExp is multiplied by the initial distribution $\mathrm{f(E)}$. The initial distribution is supposed to be centered around a value E0 and has a width designated by σ. The Gamma distribution function has been used, which is demarcated by the special case, i.e the Erlang distribution for its practical scope. The distribution can be either wide or narrow. Here we have discussed the wide distribution case only, where the initial distribution function $\mathrm{f(E)}$ is relatively wide in compare with the width of DExp. Moreover, the

shape of the total integrand also depends on the distribution chosen. When the initial distribution is relatively wide compared to E_w, the total integrand behaves similar to an initial distribution $f(E)$. But as time proceeds, it is progressively shifted from the left by the step-like DExp. The location of the maximum of the total integrand can move significantly, and the shape becomes quite skewed.

From equations (3) and (7), the remaining mass fraction equation can be expressed as:

$$1 - X = \int_0^\infty \exp\left(-\exp\left(\frac{E_s - E}{E_w}\right)\right)\frac{E^{(\lambda-1)}e^{-\frac{E}{\eta}}}{\eta^\lambda \Gamma(\lambda)}\, dE$$

Let:

$$h(E) = -\exp\left(\frac{E_s - E}{E_w}\right) - \frac{E}{\eta},$$

then:

$$1 - X = \int_0^\infty \exp\big(h(E)\big)\frac{E^{(\lambda-1)}}{\eta^\lambda \Gamma(\lambda)}\, dE$$

where E_s and E_w are function of t as mentioned earlier.

Energy is now rescaled as $y = \frac{E}{E_0}$, so that the problem becomes:

$$1 - X = \frac{\alpha}{\Gamma(\lambda)}\int_0^\infty y^{(\lambda-1)}\exp\big(h(y)\big)\, dy \quad (9)$$

$$h(y) = -\exp\left(\frac{y_s - y}{y_w}\right) - \left(\sigma\sqrt{y}\right)^2 \quad (10)$$

where the constant parameter $\alpha = \frac{\sigma^{2\lambda}}{E_0}$. Note that in practice $\alpha \ll 1$. Time is also rescaled as $\tau = k_0 t$.

For linear ramping temperature $T = \theta t$,

$$y_s = \frac{R\theta\tau Y(\tau)}{k_0 E_0}, y_w = \frac{y_s}{\big(1 + Y(\tau)\big)}$$

Note: The ramping temperature can be generalized to the case of non-zero initial temperature T_0 by simply replacing t with $t + \frac{T_0}{\theta}$ everywhere, else analysis will be changed.

Approximations to equation (10) are studied by considering the initial distribution, centered around $y = 1$ with width $\sqrt[2\lambda]{\alpha}$, while DExp jumps from zero to one around $y = y_s$ with a width y_w.

3.2. The wide distribution case

3.2.1. Gamma distribution (Generalized form of the Erlang distribution)

The initial distribution much wider than DExp is considered. In this limit, as previously discussed, DExp jumps from zero to one near $y = y_s$ in a manner that has previously been approximated by the step function (Howard, 1981; Suuberg, 1983; Vand, 1943; Pitt, 1962). To apply this, the limit $y_w \sqrt[2\lambda]{\alpha} \ll 1$ is taken:

$$H(y - y_s) = \begin{cases} 0, y < y_s \\ 1, y \geq y_s \end{cases}$$

Equation (9) can be rewritten for first order and n[th] order reactions

Case 1: For first order ($n = 1$)reaction

$$1 - X = \frac{\alpha}{\Gamma(\lambda)}\int_0^\infty \left(\exp\left(-\exp\left(\frac{y_s - y}{y_w}\right)\right) - H(y - y_s)\right) y^{(\lambda-1)}\exp\left(-\left(\sigma\sqrt{y}\right)^2\right)\, dy + \frac{\alpha}{\sigma^{2\lambda}\Gamma(\lambda)}\,\Gamma(\lambda, \sigma^2 y_s)$$

where $\Gamma(\lambda, \sigma^2 y_s)$ is the upper incomplete Gamma function.

The second integral in this equation is a complementary error function, therefore easily computed. In fact, many previous simplifications (the step-function approximations) used just this term and neglected the first integral. The first integral term is the initial distribution multiplied by a function that is very small everywhere except in a neighbourhood of size y_w around the point $y = y_s$. This integrand can, therefore, be approximated by expanding the initial distribution term with the help of Taylor series about $y = y_s$.

Let:

$$Z(y) = y^{(\lambda-1)}\exp\left(-\left(\sigma\sqrt{y}\right)^2\right)$$

$$Z(y) \sim Z(y_s) + (y - y_s)Z'(y_s) + \frac{(y-y_s)^2}{2!}Z''(y_s) + \frac{(y-y_s)^3}{3!}Z'''(y_s) + \ldots$$

$$Z(y) \sim Z(y_s) + (y - y_s)Z'(y_s) + \frac{(y-y_s)^2}{2!}Z''(y_s) + \frac{(y-y_s)^3}{3!}Z'''(y_s)$$

$$\sim \exp\left(-\left(\sigma\sqrt{y_s}\right)^2\right)\Big[y_s^{(\lambda-1)} - (y - y_s)y_s^{(\lambda-2)}(-\lambda + \sigma^2 y_s + 1) + \frac{(y-y_s)^2}{2}y_s^{(\lambda-3)}\big(\sigma^4 {y_s}^2 + 2(1-\lambda)\sigma^2 y_s + (\lambda^2 - 3\lambda + 2)\big) - \frac{(y-y_s)^3}{6}y_s^{(\lambda-4)}(\sigma^6 {y_s}^3 + 3(1-\lambda)\sigma^4 {y_s}^2 + (3\lambda^2 - 9\lambda + 6)\sigma^2 y_s - \lambda^3 + 6\lambda^2 - 11\lambda + 6)\Big]$$

Substituting $\frac{y - y_s}{y_w} = x, dy = y_w\, dx$ in equation (9), we have:

$$\sim \exp\left(-\left(\sigma\sqrt{y_s}\right)^2\right)\Big[y_s^{(\lambda-1)} - y_w x y_s^{(\lambda-2)}(-\lambda + \sigma^2 y_s + 1) + \frac{(y_w x)^2}{2}y_s^{(\lambda-3)}\big(\sigma^4 {y_s}^2 + 2(1-\lambda)\sigma^2 y_s + (\lambda^2 - 3\lambda + 2)\big) - \frac{(y_w x)^3}{6}y_s^{(\lambda-4)}(\sigma^6 {y_s}^3 + 3(1-\lambda)\sigma^4 {y_s}^2 + (3\lambda^2 - 9\lambda + 6)\sigma^2 y_s - \lambda^3 + 6\lambda^2 - 11\lambda + 6)\Big]$$

$$1 - X \sim \frac{\alpha}{\Gamma(\lambda)}\int_0^\infty \big(\exp(-\exp(-x)) - H(x)\big)\exp\left(-\left(\sigma\sqrt{y_s}\right)^2\right)\Big[y_s^{(\lambda-1)} - y_w x y_s^{(\lambda-2)}(-\lambda + \sigma^2 y_s + 1) + \frac{(y_w x)^2}{2}y_s^{(\lambda-3)}\big(\sigma^4 {y_s}^2 + 2(1-\lambda)\sigma^2 y_s + (\lambda^2 - 3\lambda + 2)\big) - \frac{(y_w x)^3}{6}y_s^{(\lambda-4)}(\sigma^6 {y_s}^3 + 3(1-\lambda)\sigma^4 {y_s}^2 + (3\lambda^2 - 9\lambda + 6)\sigma^2 y_s - \lambda^3 + 6\lambda^2 - 11\lambda + 6)\Big] y_w dx + \frac{\alpha}{\sigma^{2\lambda}\Gamma(\lambda)}\,\Gamma(\lambda, \sigma^2 y_s)$$

or

$$1 - X \sim \frac{\alpha}{\Gamma(\lambda)}\exp\left(-\left(\sigma\sqrt{y_s}\right)^2\right) y_s^{(\lambda-1)} y_w \Big[L_0 - \frac{y_w}{y_s}L_1(-\lambda + \sigma^2 y_s + 1) + \frac{1}{2}\left(\frac{y_w}{y_s}\right)^2 L_2\big(\sigma^4 {y_s}^2 + 2(1-\lambda)\sigma^2 y_s + (\lambda^2 - 3\lambda + 2)\big) -$$

DOI 10.1515/ama-2017-0045

$$\frac{1}{6}\left(\frac{y_w}{y_s}\right)^3 L_3(\sigma^6 {y_s}^3 + 3(1-\lambda)\sigma^4 {y_s}^2 + (3\lambda^2 - 9\lambda + 6)\sigma^2 y_s - \lambda^3 + 6\lambda^2 - 11\lambda + 6)\Big] + \frac{\alpha}{\sigma^{2\lambda}\Gamma(\lambda)}\,\Gamma(\lambda, \sigma^2 y_s) \quad (11)$$

We know that:

$$\frac{\Gamma(\lambda, \sigma^2 y_s)}{\Gamma(\lambda)} = 1 - P(\lambda, \sigma^2 y_s)$$

where $\mathrm{P}(\lambda, \sigma^2 \mathrm{y_s}) = \frac{\gamma(\lambda, \sigma^2 \mathrm{y_s})}{\Gamma(\lambda)}$ is the lower cumulative distribution for Gamma random variables and $\gamma(\lambda, \sigma^2 \mathrm{y_s})$ is the lower incomplete gamma function.

$$L_0 \approx -0.5772,\ L_1 \approx -0.98906,\ L_2 \approx -1.81496, L_3 \approx -5.89037$$

The remaining integral terms are evaluated by the expression:

$$L_n \equiv \int_{-\infty}^{\infty} x^n \left(e^{-e^{-x}} - H(x)\right) dx$$

Case 2: For nth order reaction $(\mathbf{n \neq 1})$

Invoking the equation (3), we can derive the result for nth order reaction. As stated earlier, the term $\left(\frac{\mathrm{E}}{\mathrm{R\theta t}}\right)\rightarrow\infty$, the exponential term raised to power$\left(\frac{1}{1-\mathrm{n}}\right)$, will vary from zero to one, and is approximated by using the binomial expansion. Hence, the equation (3) is written as:

$$(1-X)_{n^{th}} \sim \int_0^{\infty} \left[1 - \exp\left(\frac{E_s - E}{E_w}\right) + \frac{n}{2}\exp\left(2\left(\frac{E_s - E}{E_w}\right)\right) - \frac{(2n-1)}{6}\exp\left(3\left(\frac{E_s - E}{E_w}\right)\right) + \cdots\right] \frac{E^{(\lambda-1)} e^{-\frac{E}{\eta}}}{\eta^{\lambda}\Gamma(\lambda)} dE$$

$$(1-X)_{n^{th}} \sim \int_0^{\infty} \left[1 - \exp\left(\frac{y_s - y}{y_w}\right) + \frac{n}{2}\exp\left(2\left(\frac{y_s - y}{y_w}\right)\right) - \frac{(2n-1)}{6}\exp\left(3\left(\frac{y_s - y}{y_w}\right)\right) + \cdots\right] \frac{\alpha\, y^{(\lambda-1)}\exp(-(\sigma\sqrt{y})^2)}{\Gamma(\lambda)} dy$$

After applying the wide distribution limit, the above equation is expressed in the form of Heaviside or unit step function as:

$$(1-X)_{n^{\mathrm{th}}} \sim \int_0^{\infty} \left[1 - \left(\exp\left(\frac{y_s - y}{y_w}\right) - H(y_s - y)\right) + \frac{n}{2}\left(\exp\left(2\left(\frac{y_s - y}{y_w}\right)\right) - H(y_s - y)\right) - \frac{(2n-1)}{6}\left(\exp\left(3\left(\frac{y_s - y}{y_w}\right)\right) - -H(y_s - y)\right) + \cdots\right] \frac{\alpha\, y^{(\lambda-1)}\exp(-(\sigma\sqrt{y})^2)}{\Gamma(\lambda)} dy$$

or:

$$(1-X)_{n^{\mathrm{th}}} \sim \frac{\alpha}{\sigma^{2\lambda}}\left(1 + \frac{(n-5)}{6}\frac{\Gamma(\lambda, \sigma^2 y_s)}{\Gamma(\lambda)}\right) + \frac{\alpha}{\Gamma(\lambda)}\exp\left(-\left(\sigma\sqrt{y_s}\right)^2\right) {y_s}^{(\lambda-1)} y_w \left(\left[\left(P_0 + \frac{n}{2}M_0 - \frac{(2n-1)}{6}N_0\right) - \frac{y_w}{y_s}\left(P_1 + \frac{n}{2}M_0 - \frac{(2n-1)}{6}N_1\right)(-\lambda + \sigma^2 y_s + 1) + \frac{1}{2}\left(\frac{y_w}{y_s}\right)^2 \left(P_2 + \frac{n}{2}M_2 - \frac{(2n-1)}{6}N_2\right)\left(\sigma^4 {y_s}^2 + 2(1-\lambda)\sigma^2 y_s + (\lambda^2 - 3\lambda + 2)\right) - \frac{1}{6}\left(\frac{y_w}{y_s}\right)^3 \left(P_3 + \frac{n}{2}M_3 - \frac{(2n-1)}{6}N_3\right)(\sigma^6 {y_s}^3 + 3(1-\lambda)\sigma^4 {y_s}^2 + (3\lambda^2 - 9\lambda + 6)\sigma^2 y_s - \lambda^3 + 6\lambda^2 - 11\lambda + 6)\right]\right) \quad (12)$$

3.2.2. Erlang Distribution (Generalized Chi-squared distribution) (for the positive integer value of $\boldsymbol{\lambda > 0}$)

Case 1: First order reaction

For Erlang distribution, we can rewrite the equation (11) as:

$$1 - X \sim \frac{\alpha}{(\lambda-1)!}\exp\left(-\left(\sigma\sqrt{y_s}\right)^2\right) {y_s}^{(\lambda-1)} y_w \left[L_0 - \frac{y_w}{y_s}L_1(-\lambda + \sigma^2 y_s + 1) + \frac{1}{2}\left(\frac{y_w}{y_s}\right)^2 \mathrm{L}_2\left(\sigma^4 {y_s}^2 + 2(1-\lambda)\sigma^2 y_s + (\lambda^2 - 3\lambda + 2)\right) - \frac{1}{6}\left(\frac{y_w}{y_s}\right)^3 L_3(\sigma^6 {y_s}^3 + 3(1-\lambda)\sigma^4 {y_s}^2 + (3\lambda^2 - 9\lambda + 6)\sigma^2 y_s - \lambda^3 + 6\lambda^2 - 11\lambda + 6)\right] + \frac{\alpha}{\sigma^{2\lambda}(\lambda-1)!)}\,\Gamma(\lambda, \sigma^2 y_s) \quad (13)$$

In case of the Erlang distribution, we have:

$$\frac{\Gamma(\lambda, \sigma^2 y_s)}{(\lambda-1)!} = Pr(\lambda, \sigma^2 y_s) \approx 1 - \sum_{f=0}^{\lambda-1} \frac{1}{f!} e^{-(y_s \sigma^2)} (\sigma^2 y_s)^f$$

where $\mathrm{Pr}(\lambda, \sigma^2 \mathrm{y_s})$ is the cumulative distribution for the Poisson random variable.

Case 2: nth order reaction

The nth order reaction case of the Erlang distribution is expressed as:

$$(1-X)_{n^{th}} \sim \frac{\alpha}{\sigma^{2\lambda}}\left(1 + \frac{(n-5)}{6}\frac{\Gamma(\lambda, \sigma^2 y_s)}{(\lambda-1)!}\right) + \frac{\alpha}{(\lambda-1)!}\exp\left(-\left(\sigma\sqrt{y_s}\right)^2\right) {y_s}^{(\lambda-1)} y_w \left(\left[\left(P_0 + \frac{n}{2}M_0 - \frac{(2n-1)}{6}N_0\right) - \frac{y_w}{y_s}\left(P_1 + \frac{n}{2}M_0 - \frac{(2n-1)}{6}N_1\right)(-\lambda + \sigma^2 y_s + 1) + \frac{1}{2}\left(\frac{y_w}{y_s}\right)^2 \left(P_2 + \frac{n}{2}M_2 - \frac{(2n-1)}{6}N_2\right)\left(\sigma^4 {y_s}^2 + 2(1-\lambda)\sigma^2 y_s + (\lambda^2 - 3\lambda + 2)\right) - \frac{1}{6}\left(\frac{y_w}{y_s}\right)^3 \left(P_3 + \frac{n}{2}M_3 - \frac{(2n-1)}{6}N_3\right)(\sigma^6 {y_s}^3 + 3(1-\lambda)\sigma^4 {y_s}^2 + (3\lambda^2 - 9\lambda + 6)\sigma^2 y_s - \lambda^3 + 6\lambda^2 - 11\lambda + 6)\right]\right) \quad (14)$$

The values of coefficients are estimated as:

$P_0 \approx -0.36788$, $P_1 \approx -0.23576$, $P_2 \approx -0.17273$, $P_3 \approx -0.13607$,

$M_0 \approx -0.56767$, $M_1 \approx -0.35150$, $M_2 \approx -0.25250$, $M_3 \approx -0.19642$,

$N_0 \approx -0.68326$, $N_1 \approx -0.41102$, $N_2 \approx -0.29061$, $N_3 \approx -0.22387$.

The remaining integral terms are evaluated as:

$$P_n \equiv \int_{-\infty}^{\infty} x^i \left(\exp(-x) - U(x)\right) dx,\ i = 0,1,2,3 \ldots.$$

$$M_n \equiv \int_{-\infty}^{\infty} x^i \left(\exp(-2x) - U(x)\right) dx,\ i = 0,1,2,3 \ldots$$

$$N_n \equiv \int_{-\infty}^{\infty} x^i \left(\exp(-3x) - U(x)\right) dx,\ i = 0,1,2,3 \ldots$$

DOI 10.1515/ama-2017-0045

4. APPLICATION OF THE FOREST WASTE

For application perspective, the thermogravimetric analysis has been performed upon the sample of pine needles. The date of elemental composition and the calorific value have been obtained by using the CHNO-S analyser, and the bomb calorimeter, whereas the thermal degradation of the same sample has been carried out under the presence of inert atmosphere of nitrogen, and with the help of TG/DTG (SDT Q600 (TA, Perkin Elmer)) analyser. The range of temperature varied from 292 K to 873K in the furnace. The thermocouple type 'R' has been used to measure the sample and the furnace temperature. A vertical TG/DCS holder was used to hold the sample. To perform pyrolsis, a nitrogen purge flow rate was set at 100 ml/min, whose function is to remove the product gases. Thermogravimetric measurements are done at the heating rate of 10 °C/min. Al_2O_3 crucibles are used. The furnace space is inertized in order to eliminate the remaining oxygen. The mass of the samples is in between 20 mg to 21 mg.

Thermogravimetric data has used for the prediction of nth-order DAEM using the Gamma distribution (Fig. 8). Equations (11), (12), (13), and (14) are solved by using algorithm on the Matlab software. Each parameter is compared and reiterated until the root mean square error between experimental and simulated values is not less than equal to the maximum permissible error.

Tab. 1. Elemental composition and the high heating value (H.H.V) of pine needle sample

C%	H%	N %	O %	S%	Ash%	*H.H. V (kJ/kg)	**V.M %
53.7	5.21	0.61	32.13	0.22	4.72	19.5	70.1

*H.H. V- Higher heating value
**V.M - Volatile matter

Tab. 2. Comparative illustration of Gamma and Erlang distributions with other distribution types

Distribution Types	Upper limit of '*dE*' integrals	Frequency factor (min^{-1})
Gaussian (Dhaundiyal and Singh, 20016)	80 kJ/mol	1.75 E+06
Weibull (Dhaundiyal and Singh ,2016)	23 kJ/mol	10E+03
Gamma	150 kJ/mol	0.0015
Erlang	150 kJ/mol	0.0015

Tab. 3. Computed root mean square error

Distribution function	Root mean squared error (RMSE)**
Gamma	10E-02 to 10E-03
Erlang	10E-02 to 10E-03

$$RMSE^{**} = \sqrt{\frac{\sum_{i=1}^{N}\left((1-X_i)_{Experimental} - (1-X_i)_{Evaluated}\right)}{N}}$$

where N is number of data points.

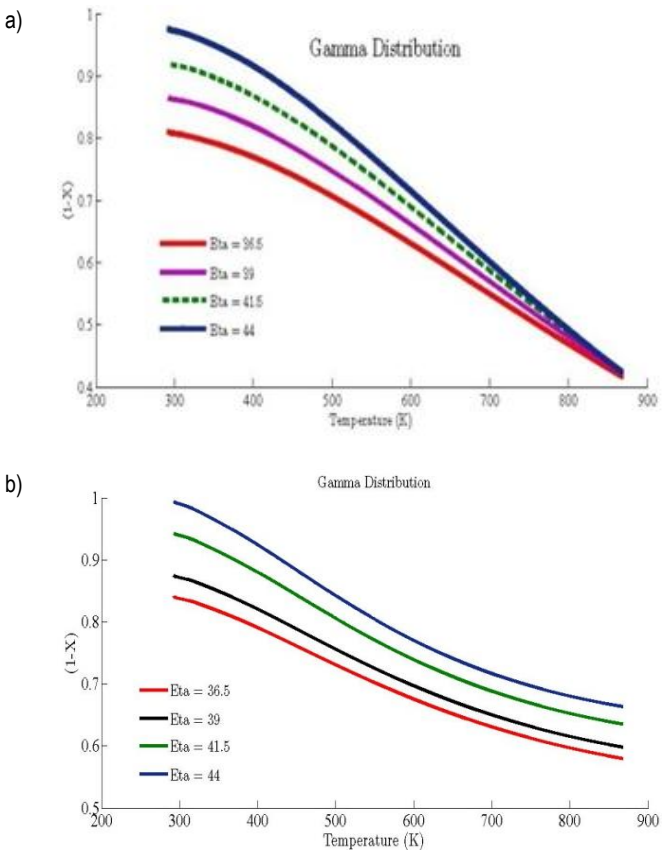

Fig. 1. Effect of shape parameter of the Gamma distribution (η) on the numerical results (k_0 = 5.7E-04 min^{-1}, θ = 10 °C/min, T_0 =293 K and λ = 45.5 kJ/mol; (a) first order reaction, (b) n^{th} order reaction, n = 8.5)

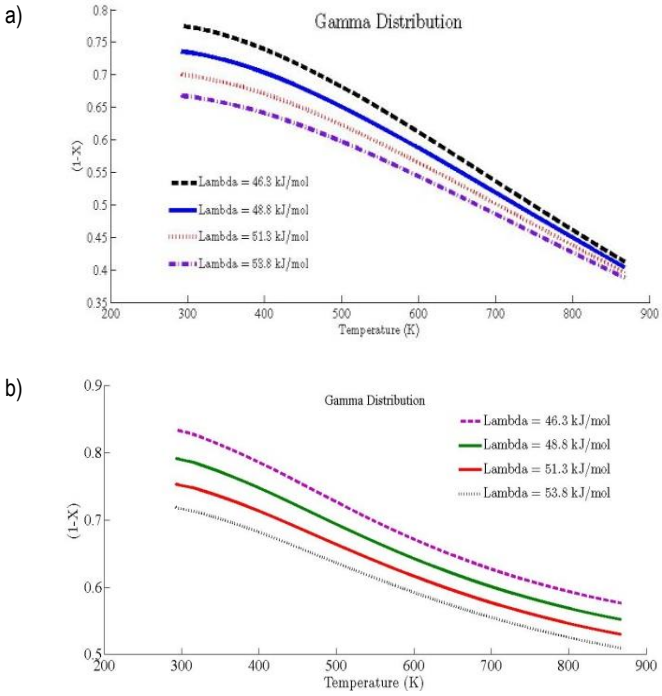

Fig. 2. Effect of scale parameter of the Gamma distribution (λ) on the numerical results (k_0= 5.7E-04 min^{-1}, θ = 10 °C/min, T_0 = 293 K and η = 35; (a) first order, (b) n^{th} order, n = 8.5)

DOI 10.1515/ama-2017-0045

a)

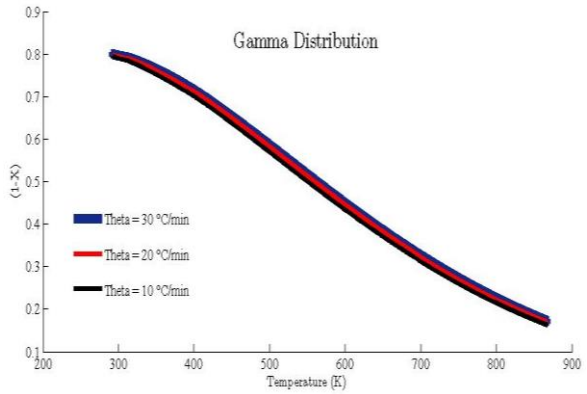

b)

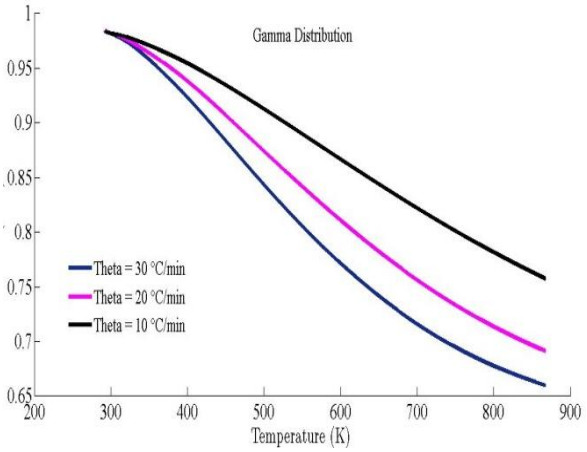

Fig. 3. Effect of heating rate on the numerical results (k_0= 5.7E-04 min^{-1}, λ = 45.5 kJ/mol, T_0 =293 K and η = 35; (a) first order, (b) nth order, n = 8.5)

a)

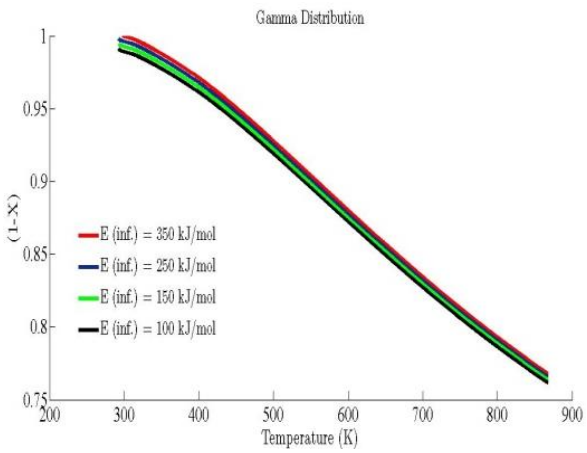

b)

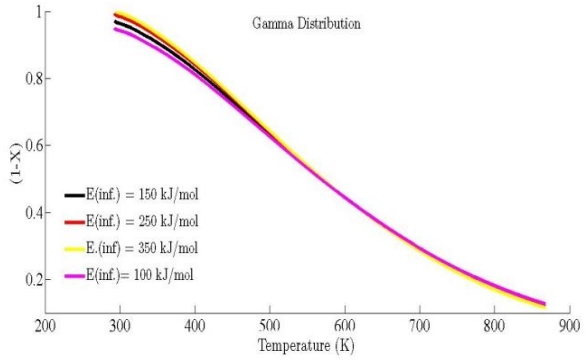

Fig. 4. Effect of upper limit (E∞) of dE integral on the numerical results (k_0 = 5.7E-04 min^{-1}, λ = 45.5 kJ/mol, T_0 =293 K and η= 35; (a) first order, (b) nth order, n= 8.5)

a)

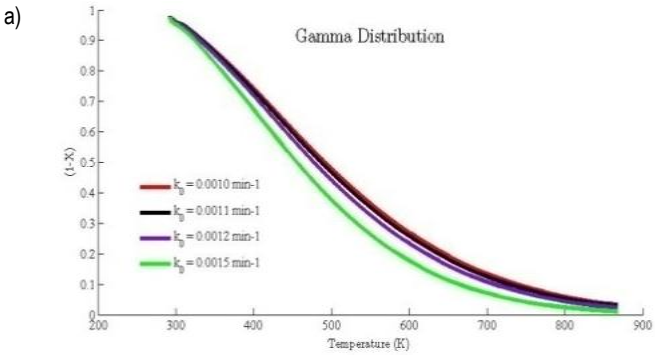

b)

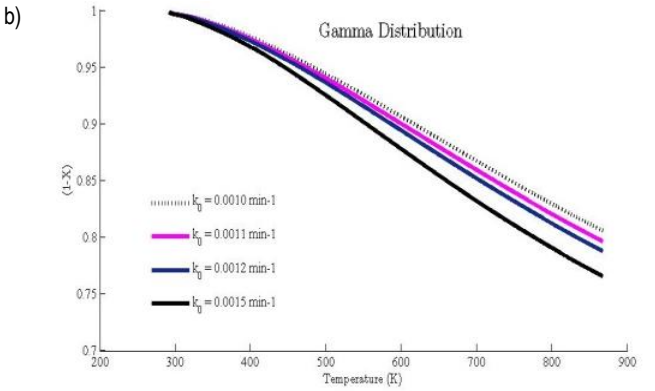

Fig. 5. Effect of frequency factor (k_0) on the numerical results (λ = 45.5 kJ/mol, T_0 = 293 K and η = 35; (a) first order, (b) nth order, n = 8.5)

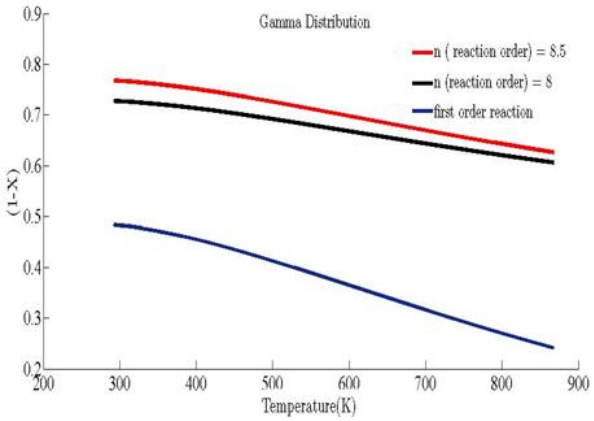

Fig. 6. Effect of reaction order (n) on the numerical results (λ = 45.5 kJ/mol, T_0 =293 K; and η = 35)

a)

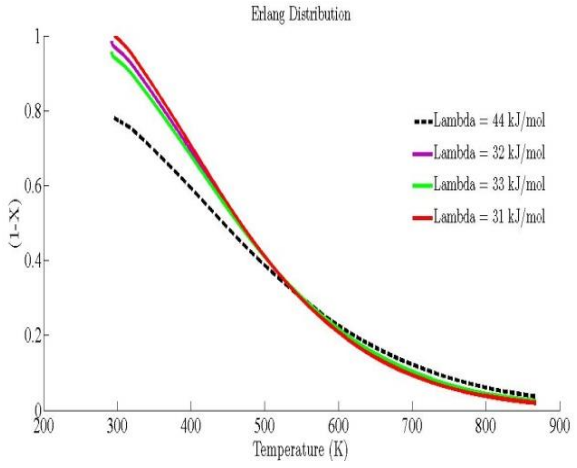

DOI 10.1515/ama-2017-0045

b)

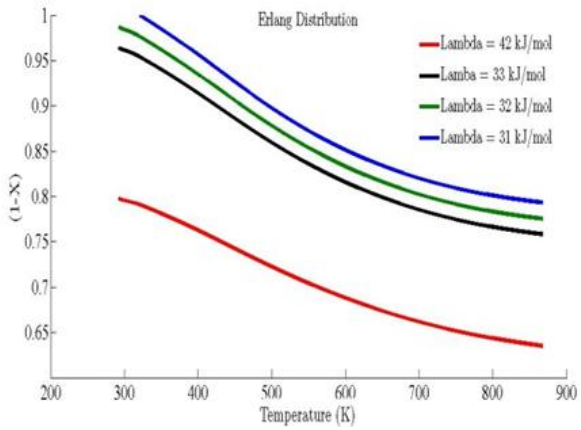

Fig. 7. Effect of scale parameter of the Erlang distribution (λ) on the numerical results (k_0= 0.0047 min^{-1}, θ = 10 °C/min, T_0 =293 K and η = 32; (a) first order, (b) nth order, n = 6.8)

a)

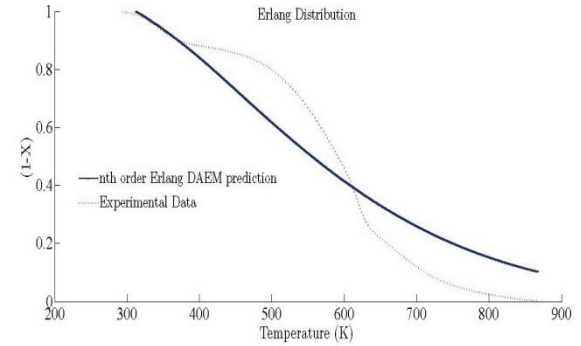

b)

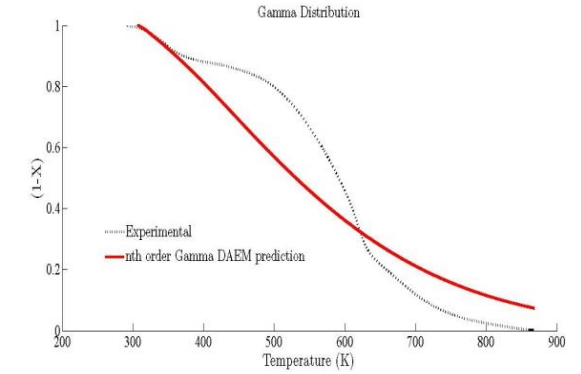

Fig. 8. Comparison between the experimental data and the nth order DAEM prediction (a) The Erlang Distribution (b) The Gamma Distribution

5. RESULTS AND DISCUSSION

The shape parameter has been obtained for Gamma distribution by using the asymptotic approximation and the energy rescaling (y) of activation energies. The influence of shape parameter of Gamma distribution on the numerical results is shown in Fig. 1. At the beginning of pyrolysis, the remaining mass fraction $(1-\mathrm{X})$ (equations 11 and 12) must be at vicinity of one. On the contrary, in Fig. 1, it is observed that the remaining mass fraction is less than one. However, as the value of shape parameter approaches $44 \leq \eta$, the upper half of curve approaches one. The distribution exhibits no inflexion for the lower value of shape parameter $39 \geq \eta$ and the remaining mass fraction curves lead towards right as parallel to each other. The effect of scale parameter values (λ) of Gamma distribution on the numerical result is shown in Fig. 2. The decrease in the value of scale parameter, λ, reduces the slope of the remaining mass proportion $(1-\mathrm{X})$ (equations 11and 12) curves. The effect of positive integer value of scale parameter of Erlang distribution is depicted in Fig. 7. It is observed that the behaviour of scale parameter (λ) for Erlang distribution is opposite to that of Gamma distribution. As the value of $\lambda \leq 33$, the remaining mass fraction curve has proximity with one for the Erlang distribution, which implies the good approximation is obtained at the beginning of pyrolysis. The variation has been observed as the second term is almost negligible in equation (14), and the remaining mass fraction behaves like the cumulative distribution function. The effect of heating rate on numerical results is illustrated in Fig. 3, where it is seen that the remaining mass proportion is slightly increased with the heating rate. It has been observed that the mass fraction curves are shifted up the temperature scale with an increase in the heating rate. The influence of the outer limit of '$\mathrm{d}E$' on the numerical results of the non-isothermal nth order DAEM is shown in Fig. 4. It reveals that remaining mass proportion is at vicinity of one for $\mathrm{E}_{\infty} \leq 150\ \mathrm{J/mol}$ values. When the values of E are more than 250 J/mol, the results are not accurate and closely proximate to each other. Hence, 150 J/mol is used as the upper limit of the $\mathrm{d}E$ integral. The effect of the frequency factor (k_0) values on the numerical results is shown in Fig. 5. According to these curves, increase in k0 values causes $(1-\mathrm{X})$ (equations 11 and 12) curves to shift towards the left direction. The effect of the reaction order (n) values on the numerical result is illustrated in Fig. 6. As the order of reaction increases, the lower half range of $(1-\mathrm{X})$ (equations 11 and 12) curves shifted up. The prediction of nth order DAEM is depicted in Fig. 8. In the beginning of pyroylsis, Erlang distribution (Fig. 8a) and Gamma distribution (Fig. 8b) are in good agreement with the thermogravimetric data, but as time increases, the gamma distribution has relatively provided an accurate approximation for the conversion occurred at the higher temperature.

Variation in the upper limit of activation energy and frequency factors for the different distribution function is shown in Tab. 3. But, in case of the Gamma and the Erlang distributions, it was found that evaluation of kinetic parameters at single heating rate led to the compensatory effect (Doyle,1962). Root mean squared error between Erlang and Gamma distribution functions is illustrated in Tab. 3.

6. CONCLUSIONS

In the asymptotic approximation of the nonisothermal nth order for knowing the influence of parametric values on the pyrolysis kinetics, 150 J/mol value is used as the limit of the outer dE integral. The variation of the frequency factor, heating rate, the reaction order, the shape, and the scale parameter of the Gamma distribution as well as Erlang distribution affect the form of remaining mass fraction curves. We also studied the influence of some parameters. The special case of Gamma distribution has been discussed to know the more practical aspect regarding the distribution behaviour at lower and higher temperature regimes. It has been concluded that the Gamma distribution provides better approximation for conversion rate at higher temperature than that of the Erlang distribution. The Erlang distribution is found to be more suiTab. for pyrolysis reaction that took place for the lower

DOI 10.1515/ama-2017-0045

temperature regimes. Moreover, the results are very helpful to determine the kinetic parameters of the nonisothermal n^{th} order Gamma DAEM from the thermo analytical data of biomass pyolysis. It can also be concluded from comparative illustration that the two asymmetrical distribution functions (Weibull and Gamma) does not provide the same results (Tab. 3.)

REFERENCES

1. **Anthony D.B. (1974),** Rapid devolatilization and hydrogasification of pulverized coal, DSc. thesis, Massachusetts Institute of Technology.
2. **Armstrong R., Kulesza B.L.J.** (1981), *An approximate solution to the equation x = exp (−x/ϵ)*, Bull. Institute of Mathematics and its Applications, 17, 56.
3. **Brown M. E**. (2001), *Introduction to Thermal Analysis, Techniques and Applications*, Kluwer Academic Publisher, Dordrecht.
4. **Burnham A.K., Braun R.L.** (1999),Global kinetic analysis of complex materials, *Energy Fuels*, 13, 1-22.
5. **Burnham A.K., Schmidt B.J., and Braun R.L** (1995), A test of parallel reaction model using kinetic measurements on hydrous pyrolysis residues, *Geochem*, 23, 931-939.
6. **Capart R, Khezami L., Burnham A.K.** (2004), Assessment of various kinetic models for the pyrolysis of microgranular cellulose, *Thermochim. Acta*, 417(1), 79-89.
7. **Conesa J. A., Marcilla A., Caballero J. A., Font R.** (2001), Comments on the validity and utility of the different methods for kinetic analysis of thermogravimetric data, *J. Anal. Appl. Pyrolysis*, 617, 58–59.
8. **Conesa J.A., Caballero J.A., Marcilla A., Font R**. (1995), Analysis of different kinetic models in the dynamic pyrolysis of cellulose, *Thermochim. Acta*, 254, 175-192.
9. **Criado J.M., Pérez-Maqueda L.A**. (2005), Sample controlled thermal analysis and kinetics, *J. Therm. Anal. Cal.*, 80, 27-33.
10. **Dhaundiyal A., Singh S.B.** (2016), Asymptotic approximations to the distributed activation energy model for non-isothermal pyrolysis of loose biomass using the Weibull distribution, *Archivum Combustionis*, 36(2), 131-146.
11. **Dhaundiyal A., Singh S.B. (**2016), Proceedings of the Latvian Academy of Sciences, Section B. Natural, *Exact, and Applied Sciences*, 70, 64–70.
12. **Di Blasi C.** (2008), Modeling chemical and physical processes of wood and biomass pyrolysis, *Progress in Energy and Combustion Science*, 34, 47-90.
13. **Doyle C.D**. (1962), Estimating isothermal life from thermogravimetric data, *J. Appl. Polym. Sci*. 6, 639-642.
14. **Ferdous D, Dalai A.K, Bej S.K., Thring R.W.** (2002), Pyrolysis of lignins, experimental and kinetics studies, *Energy Fuels*, 16, 1405–1412
15. **Folgueras M.B., Diaz R.M., Xiberta J., Prieto I**. (2003), Thermogravimetric analysis of the co-combustion of coal and sewage sludge, *Fuel*, 82, 2051-2055.
16. **Galgano A., Blasi C.D.** (2003), Modeling wood degradation by the unreacted-core-shrinking approximation, *Eng. Chem. Res*, 42, 2101-2111.
17. **Giuntoli J., de Jong W., Arvelakis S., Spliethoff H., Verkooijen A.H.M.** (2009), Quantitative and kinetic TG-FTIR study of biomass residue pyrolysis, Dry distiller's grains with solubles (DDGS) and chicken manure, *Journal of Analytical and Applied Pyrolysis*, 85(1), 301-312.
18. **Hanbaba P., van Heek K.H, Jüntgen H., Peters W.** (1968), Non-isothermal kinetics of coal pyrol-yse , Part II , Extension of the theory of the evolution of gas and experimental confirmation of bituminous coal, *Fuel Chemistry*, 49(12), 1968, 368-376.,
19. **Howard J.B.** (1981), Fundamentals of Coal Pyrolysis and Hydropyrolysis, in Chemistry of Coal Utilization, (M.A.Elliott, Ed) Wiley & Sons.
20. **Koreňová Z., JumaM., Annus J., Markoš J., Jelemensky L.** (2006), Kinetics of pyrolysis and properties of carbon black from a scrap tire, *Chemical Papers*, 60, 422–426.
21. **Lakshmanan C.C., White N.** (1994), A new distributed activation energy model using Weibull distribution for the representation of complex kinetics, *Energy Fuels*, 8, 1158–1167.
22. **Lapuerta, M., Hernández, J.J., Rodríguez, J.** (2004), Kinetics of devolatilisation of forestry wastes from thermogravimetric analysis, *Biomass and Bioenergy,* 27(4),385–91.
23. **Mysyk R.D., Whyman G.E., Savoskin M.V., Yaroshenko A.P**. (2005), Theoretical model and experimental study of pore growth during thermal expansion of graphite intercalation compounds, *J. Therm. Anal and Cal.*, 79(3), 515-519.
24. **Niksa S., Lau, C-W.** (1993), Global rates of devolatilization for various coal types Combust, *Flame*, 94, 293-307
25. **Otero M., Calvo L.F., Gil M.V., García A.I., Morán A**. (2008), Cocombustion Of Different Sewage Sludge and Coal, A non-isothermal thermogravimetric kinetic analysis, *Bioresource Technology*, 99, 6311-19.
26. **Pitt G.J.** (1962), The kinetics of the evolution of volatile products from coal, *Fuel*, 1, 267-274
27. **Pysiak J.J., Badwi Y.Al.** (2004), *Kinetic equations for thermal dissociation processes*,76, 521–528
28. **Quan C., Li A., Gao N.** (2009), Thermogravimetric analysis and kinetic study on large particles of printed circuit board wastes, *Waste Management*, 29, 2353–2360.
29. **Robeva R., Davies R., Hodge T., Enyedi A**. (2010), Mathematical Biology Modules Based on Modern Molecular Biology and Modern Discrete Mathematics, CBE Life Sciences Education (*The American Society for Cell Biology*), 9 (3), 227–240.
30. **Skrdla P.J., Roberson R.T.** (2005), Semiempirical equations for modeling solid-state kinetics based on a Maxwell-Boltzmann distribution of activation energies, applications to a polymorphic transformation under crystallization slurry conditions and to the thermal decomposition of AgMnO4 crystals, *J. Phys. Chem. B*, 109, 10611- 10619.
31. **Solomon P.R., Hamblen D.G.** (1983), Finding Order in Coal Pyrolysis Kinetics, Topical Report Submitted to the U.S. Department of Energy. *Progr. Energy Combust. Sci.,* 9, 323-361.
32. **Suuberg E.M.** (1983), Approximate solution technique for nonisothermal, Gaussian distributed activation energy models, *Combust. Flame*, 50,243-245
33. **Szczodrak J., Fiedurek J. (**1996), Technology for conversion of lignocellulosic biomass to ethanol, *Biomass and Bioenergy*, 34, 367-375.
34. **Teng H., Hsieh C.T.** (1999), Influence of surface characteristics on liquid-phase adsorption of phenol by activated carbons prepared from bituminous coa, *Ind. Engg. Chem. Res*, 37, 3618-3624.
35. **Vand V.** (1943), A theory of the irreversible electrical resistance changes of metallic films evaporated in vacuum, *Proc. Phys. Soc.*,55, 222-246
36. **White J.E., Catallo W.J., Legendre B.L.** (2011), Biomass pyrolysis kinetics, A comparative critical review with relevant agriculture residue case studies, *J. Anal. Appl. Pyrolysis*, 91 (1), 1-33,
37. **Zhu H.M., Yan J.H., Jiang X.G., Lai Y.E., Cen K.F**(2009), Analysis Of Volatile Species Kinetics During Typical Medical Waste Materials Pyrolysis Using A Distributed Activation Energy Model, *Journal of Hazardous Materials*, 162(2), 646-651.

DE GRUYTER
OPEN

DOI 10.1515/ama-2017-0046

TRANSIENT ANALYSIS OF A RAILGUN WITH PERMANENT MAGNETS SUPPORT

Andrzej WAINDOK*, Paweł PIEKIELNY*

*Faculty of Electrical Engineering, Automatic Control and Informatics, Department of Electrical Engineering and Mechatronics, Opole University of Technology, ul. Prószkowska 76, 45-758 Opole, Poland

a.waindok@po.opole.pl, bp.piekielny@po.opole.pl

received 10 October 2016, revised 30 November 2017, accepted 4 December 2017

Abstract: The calculation and measurement results of transients for an electrodynamic accelerator with permanent magnet support have been presented in this paper. The calculations have been made using the magnetostatic model in the Maxwell software, as well as using a Matlab/Simulink transient model. The waves of mechanical parameters (projectile velocity and acceleration, force) and electric ones (excitation current and capacitor voltage) have been analyzed for different supply conditions (voltage value, capacitance). The efficiency and projectile energy have been studied as well. The mathematical models have been verified experimentally using the original laboratory stand. A good conformity between calculation and measurement results has been obtained.

Key words: Electrodynamic Accelerators with Permanent Magnets, Field-Circuit Modelling, Transient Calculation, Measurement Verification

1. INTRODUCTION

Electrodynamic accelerators (railguns) have become increasingly popular in recent years. There are carried out many works and researches in terms of both military (McNab and Beach, 2007; Gosiewski and Kłoskowski, 2008; Hundertmark et al., 2013) and industrial applications (Poniaev et al., 2015; Hogan et al., 2013; Domin and Kluczczyński, 2013) of the device. The railguns are an alternative for coilgun constructions (Waindok and Mazur, 2011; Piskur, 2010), mostly due to better performance (efficiency, projectile velocity). A disadvantage of such electrodynamic accelerator is the high cost of assembling and problem with rails and electric contact degradation (Cooper et al., 2007; Tang et al., 2015; Wild et al., 2014). Another problem is a very high current peak of kA to even MA appearing in some milliseconds. The efficiency of the device is low, as well.

In order to increase the efficiency of the railgun there is a need not only to perform the experimental work, but also to create a proper calculation model, which would simulate the physical object with sufficient accuracy (Kluszczyński and Domin, 2015). The proper model could be used, for example, in order to increase the thrust, without increasing the excitation current (Waindok and Piekielny, 2013; Gieras et al., 2011). One of the method is the optimization of the magnetic circuit. It requires the development of a magnetostatic model using field analysis, for example 3D finite element method (FEM). The transient model is very important as well. It enables to follow the influence of supplying parameters and initial conditions on the waves connected with discharges, which allows to improve the efficiency of the whole system.

In the paper, the calculation and measurement results for the original electrodynamic accelerator with iron core and permanent magnets have been presented. The device has been developed in the Department of Electrical Engineering and Mechatronics at Opole University of Technology. The calculations have been carried out using a field-circuit model of the device (Zimon et al., 2012). For magnetostatic analysis, the Maxwell software has been used. The parameters obtained in the field calculations have been used in the transient (circuit) model, which has been implemented in the Matlab/Simulink software.

2. PHYSICAL MODEL

The picture of the accelerator with ferromagnetic core and permanent magnets is presented in Fig. 1a. The magnetic field has two sources: a current flowing through the circuit and permanent magnets. The iron core has been used in order to focus the magnetic field lines in the projectile area. Therefore, in relation to the core-less accelerator, the thrust could be increased for the same excitation current value.

Before construction of a prototype, some calculations have been carried out in order to set up the dimensions of the core and permanent magnets (Fig. 1b). The following design constraints have been assumed: a cross-section of each rail less than 100 mm^2, the distance between them a=12 mm, the length of the device l=200 mm. The non-linear characteristic of the core has been measured and taken into account (Fig. 2). The measurement has been performed for a ring-shaped magnetic sample (Tumanski, 2011). The sinusoidal voltage supply system has been used. The magnetic field strength in the magnetic circuit has been determined with using the Ampere's circuital law. The magnetic flux density value in the sample has been determined according to Faraday's law, using the mean value of the induced voltage.

The projectile core of 25 mm length (Fig. 3) has been made of PF CC 201 material (textolite). The PF CC 201 has been chosen due to its ease processing, low mass (m=2.5 g), relatively

DOI 10.1515/ama-2017-0046

high stiffness and high heat resistance. The reduction of the mass allows to take the shot at smaller values of the excitation current. The active part of the projectile is made of an OFC (Oxygen-Free Copper) wire, which ensures a good electric contact between rails and the projectile. The OFC wire was selected due to high conductivity and friction resistivity, which is very important in dynamic systems with high current values. The rails have been made of brass.

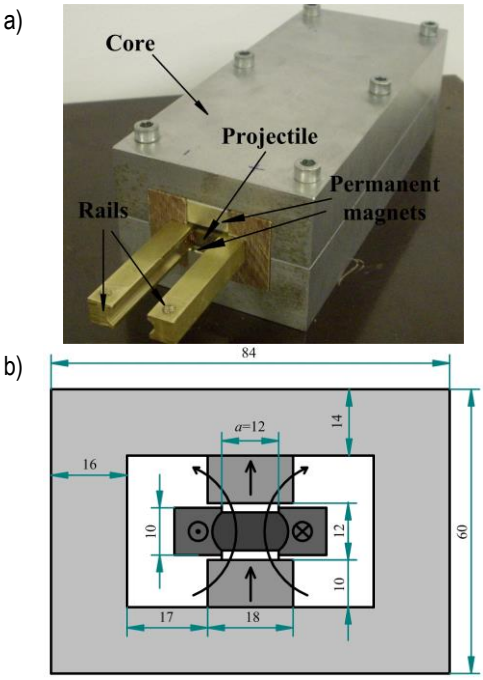

Fig. 1. Electrodynamic accelerator with ferromagnetic core and permanent magnets: a) picture of the prototype; b) cross-section (dimensions in mm)

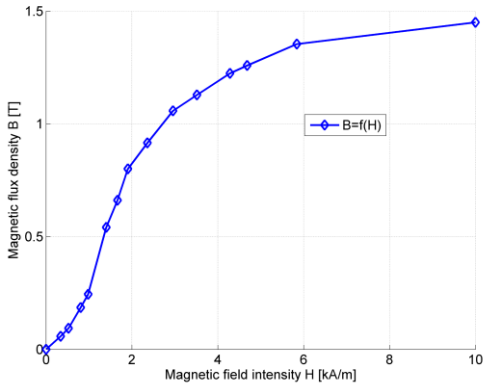

Fig. 2. Measured B/H curve of the used ferromagnetic core

Fig. 3. Picture of the projectile

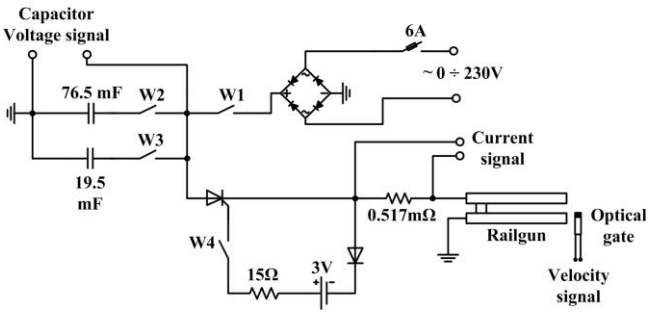

Fig. 4. Electrical circuit diagram

The electrical circuit diagram of the original laboratory stand (Piekielny, 2015) is shown in Fig. 4. It consists of two main parts: the power supply circuit and measuring system. The power source is a capacitor bank with a total capacity of 96 mF and nominal voltage of 350 V. To trigger the shot a high power thyristor was used (model T95-1900 from Kubara LAMINA Company). During the shot the following signals are recorded using an oscilloscope: the voltage on the capacitor bank *U*, the excitation current *I* and the average muzzle velocity of the projectile *v*. The current measurement was made by recording the voltage drop on a 0.517 mOhm resistance. Velocity of the projectile was determined by measuring the flying time through the optical gate.

3. MATHEMATICAL MODEL

In order to determine the magnetic field integral parameters, the finite element method, implemented in the program Maxwell, has been used. The voltage boundary conditions were assumed on the rails ends (Fig. 5). On the outer boundaries the zero Dirichlet condition has been assumed. The eddy current effect has been neglected. Using this model, the integral parameters of the field have been determined. The magnetic flux on the surface *S* (limited by the rails and projectile, Fig 6) was calculated with using the expression:

$$\Phi = \int_S \mathbf{B}\cdot\mathbf{n}dS \tag{1}$$

where: Φ – magnetic flux on the surface *S*, $\mathbf{B}$ – magnetic flux density vector, $\mathbf{n}$ – unit vector normal to surface *S*, S – surface limited by the rails and projectile, parallel to the plane YZ (Fig. 6).

Lorentz force **F** acting on the projectile was calculated according to equation:

$$\mathbf{F} = \int_\Omega (\mathbf{J}\times\mathbf{B})d\Omega \tag{2}$$

where: $\mathbf{J}$ – current density vector in the projectile, Ω – volume of the projectile.

The dynamic inductance L_d of the accelerator was determined by the expression:

$$L_d = \frac{\partial\Phi}{\partial i} = \frac{1}{i}\frac{\partial W_m}{\partial i} \tag{3}$$

where: i – current flowing through the rails, W_m – magnetic energy.

In order to select the proper mesh discretization, the calculations for two different meshes have been made (Fig. 5). In the first case an adaptive method for mesh generation has been used. The algorithm has created quite coarse mesh presented in Fig. 5a. In the second case, the maximum size of the mesh elements in each sub-area has been forced (Fig. 5b), which signif-

DOI 10.1515/ama-2017-0046

icantly increases the number of elements (dense mesh). In table 1, the calculation results for both types of mesh have been given. Due to small differences between obtained results (below 1.1% in case of thrust and below 0.2% for excitation current) and due to significantly shorter calculation time, the coarse mesh generated by an adaptive method, has been used. It should be mentioned, that the calculation time for magnetostatic models is a very important quantity, since the calculations of integral parameters (magnetic flux, force and inductance) are made for different positions of the projectile and different excitation current values.

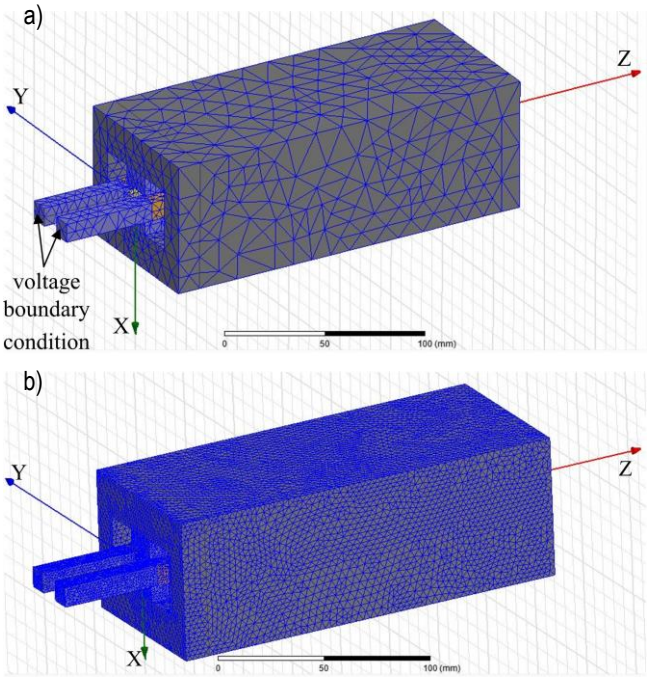

Fig. 5. Two analyzed discretization meshes: a) coarse mesh; b) dense mesh

Tab. 1. Comparison of the calculation results for two different meshes

Mesh type	Voltage	Excitation current	Force	Calc. time	Number of elements
-	*U* [V]	*I* [A]	*F* [N]	*t* [h:m:s]	*n*
Dense	150	26274.13	543.26	7:28:09	1230778
Coarse	150	26227.46	537.45	0:02:48	60046

The analysis of accelerator operation is based not only on static, but also on the dynamic calculations. Thus, a field-circuit model have been developed for a transient analysis. The equations describing the dynamic model of the railgun have been obtained with using the Euler-Lagrange method:

$$\frac{d}{dt}\begin{bmatrix} v \\ i \end{bmatrix} = \begin{bmatrix} -\frac{D}{m} & 0 \\ -\frac{\frac{\partial \Psi(i,x)}{\partial x}}{L_d(i,x)} & -\frac{R}{L_d(i,x)} \end{bmatrix}\begin{bmatrix} v \\ i \end{bmatrix} + \begin{bmatrix} \frac{F(i,x)}{m} \\ -\frac{\frac{q}{C}}{L_d(i,x)} \end{bmatrix} \tag{4}$$

The first equation describes the mechanical part of the system, while the second one describes the electrical part. The above equations have been implemented in the Matlab–Simulink software. The values of force and magnetic flux vs. position and excitation current values have been calculated with using the FEM magnetostatic model and included in the form of Look-up tables.

4. MAGNETOSTATIC CALCULATION RESULTS

The current density and the thrust values, as well as magnetic field distribution have been determined for different values of the excitation voltage (-60 V to 200 V). In Fig. 7a an exemplary distribution of the current density (for *U*=150 V) has been shown (the projectile is placed in position z_i=3 cm (Fig.6).

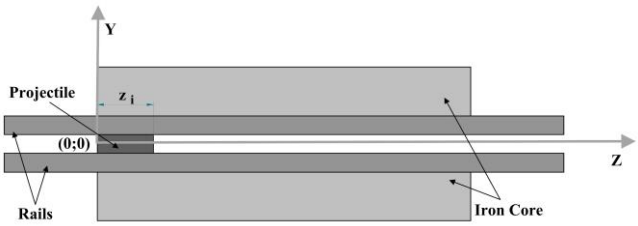

Fig. 6. Initial position of the projectile

The highest value of the current density is observed in the area of the projectile, on the inner edges of the conductive part (more than 3 kA/mm^2). In Fig. 7b the magnetic flux density distribution for *U*=150 V has been depicted. Accordingly to the current density distribution, the highest value of the magnetic flux density is observed in the projectile area (about 4.13 T). Such a high value is due to high current density value. In the iron parts of the railgun, the magnetic density value is much lower (below 2 T).

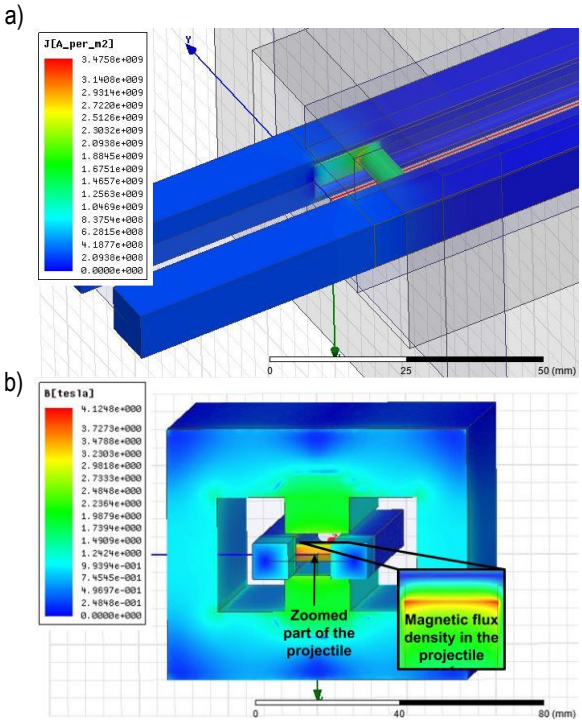

Fig. 7. Calculation results for U=150 V: a) current density distribution in the rails and projectile; b) magnetic flux density distribution

The calculation results for electrodynamic force and magnetic flux vs. excitation current value *I* and projectile position z are presented in Fig. 8. The force value is almost insensitive vs. projectile position and changes exponentially vs. excitation current value. The magnetic flux changes linearly both vs. *I* and z. According to equation (4), in calculation of transients the dynamic

DOI 10.1515/ama-2017-0046

inductance L_d is an important parameter. The graph of the L_d=f(z, i) has been presented in Fig. 9. Its value weakly depends on the excitation current and is linearly dependent on the projectile position coordinate.

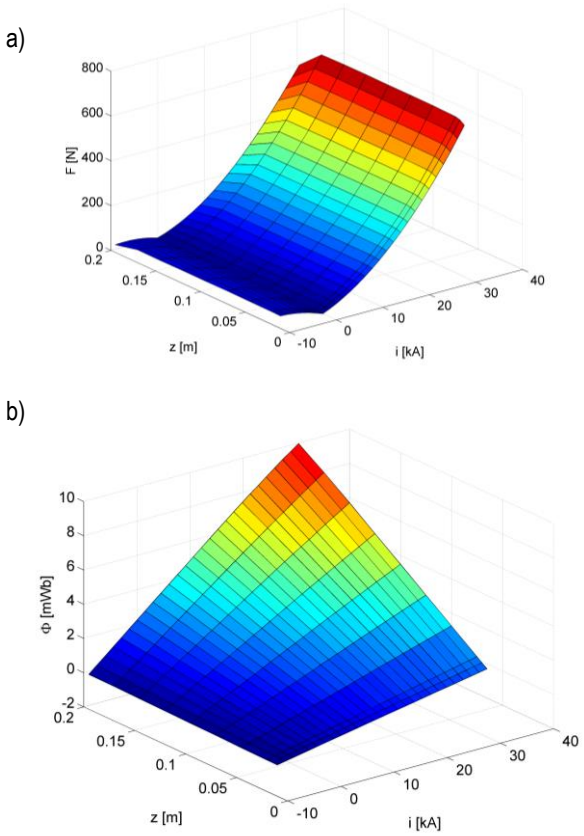

Fig. 8. Integral parameters vs. projectile position and excitation current value: a) electrodynamic force; b) magnetic flux

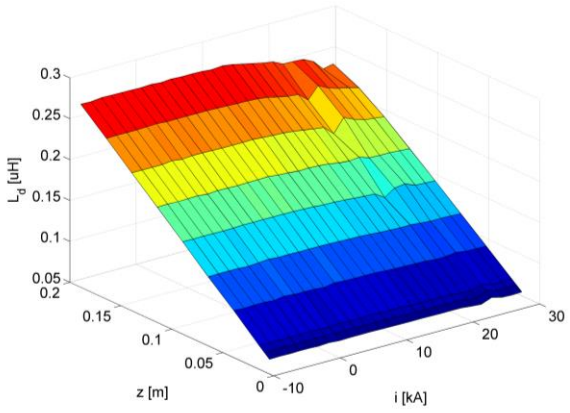

Fig. 9. Dynamic inductance vs. current value and projectile position

5. TRANSIENT CALCULATION AND MEASUREMENT RESULTS

The measurements for different capacitors and voltage values have been made. Some results are presented in Fig. 10. Increasing of the capacitance values raises the discharge time and slightly increases the peak current value (Fig. 10a). The capacitor voltage level affects only the current value – increasing of the voltage increases the current in approximately a linear way (Fig. 10b).

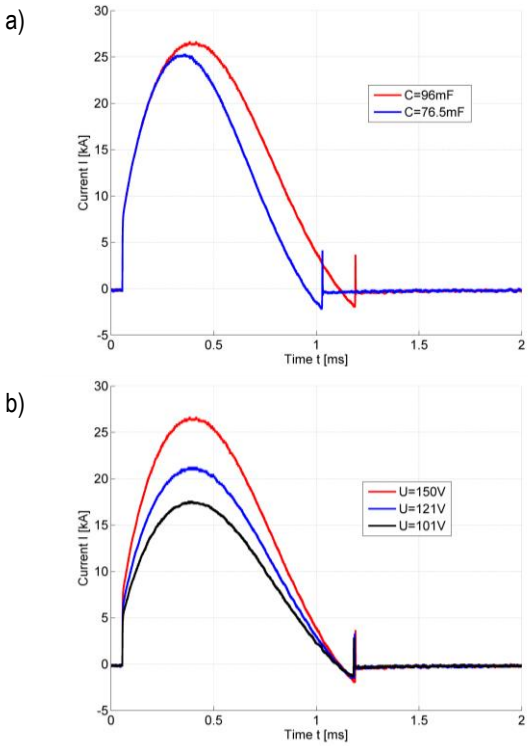

Fig. 10. Current excitation waves for different supply parameters: a) constant voltage value (U=150 V) - different capacity values; b) constant capacitance value (C=96 mF) - variable voltage values

Using the original laboratory stand, a measurement verification of the selected calculation results have been carried out. The resistance and inductance of supply cables were assumed to be equal R=2.75 mOhm and L=0.98 μH, respectively. Due to the motion of the projectile additional parameters have to be included i.e. mass of the projectile m=4.51 g, coefficient of the kinetic friction D=0.2 Ns/m and the value of the air resistance coefficient C_x=1.05.

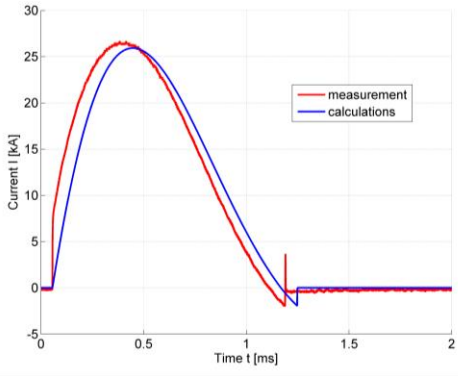

Fig. 11. Calculation and measurement results of the current waveform for U=150 V and C=96 mF

In Fig. 11, results of calculated and measured current waveforms for U=150 V and C = 96 mF are presented. The current peak visible in the measurement results is due to commutation

DOI 10.1515/ama-2017-0046

of the thyristor, which switches off the inductive circuit under non-zero conditions and generates a voltage disturbance in the circuit. The current is measured based on the voltage drop on the resistor. Thus the voltage disturbance is visible in measured waves.

There are also visible differences between measured and calculated shape of current waves (Fig. 11). Therefore, some modifications have been proposed in the mathematical model. From the experimental research came out, that in the system some time lags are existing between the thyristor triggering time and the response time of the circuit rails-projectile. The system behaves in some ways like a transmission line. Therefore, in the mathematical model, a fixed time delay block for the inductance value has been added. The delay time has been chosen based on the experimental tests as Δt=4.4 μs. After the delay time, the static inductance value of the accelerator circuit raises from 0 to 0.98 μH. The results for the modified field-circuit model have been presented in Fig. 12a. In the case of current wave, a very good conformity between calculation and measurement results is observed. The measured voltage wave on the capacitors differs slightly from the calculated one (Fig. 12b). However, the mathematical model is sufficiently precise and could be used in future calculations. The negative value of the capacitor voltage is caused by the finite switching-off time of the thyristor (about 100 μs).

The measurement verification of the projectile velocity has been made, as well (Tab. 2). The differences between calculated and measured results do not exceed 10 % and are observed for the lowest velocity values. In the case of the highest observed velocities, the difference does not exceed 1.1 %.

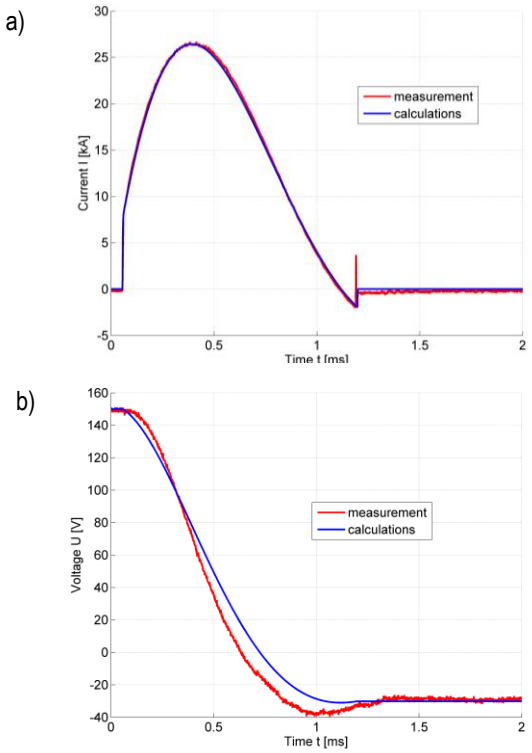

Fig. 12. Measurement verification of the modified field-circuit model for U=150 V and C=96 mF: a) excitation current vs. time; b) voltage waves

Tab. 2. The dynamic parameters for different power supply configurations

Voltage	Capacity	Calculated current peak	Measured current peak	Calculated velocity	Measured velocity	Force
U [V]	C [mF]	I_{max} [A]	I_{max} [A]	v [m/s]	v [m/s]	F_{max}[N]
150	96.0	26422	26692.5	61.35	60.98	549.74
150	76.5	24868	25145.1	47.86	47.71	501.30
121	96.0	21303	21276.6	42.23	44.64	395.18
121	76.5	20045	20116.1	32.57	34.53	361.22
101	96.0	17767	17620.9	30.62	33.78	302.03
101	76.5	16715	16769.8	23.29	25.83	276.39

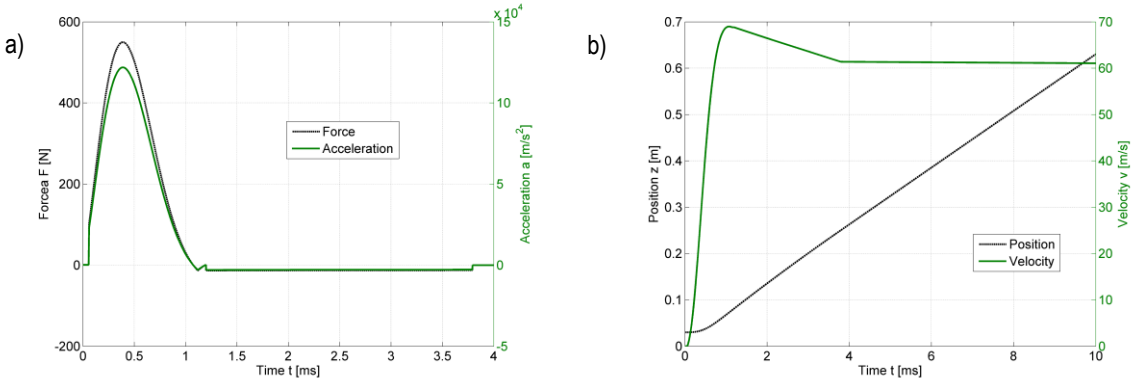

Fig. 13. Calculated waves (U=150 V, C=96 mF): a) force and acceleration; b) position and velocity

Using the field-circuit model, some additional calculations have been carried out. They concern quantities, which are very difficult to measure, i.e. thrust, acceleration, velocity and position of the projectile. The initial position of the projectile equal to z_i=3 cm has been included in the model. In Fig. 13 some results are presented. The shape of force and acceleration waves is the same (Fig. 13a). The maximum value of the acceleration reaches very high value (121890 m/s^2), which is due to small mass of the

DOI 10.1515/ama-2017-0046

movable element and due to relatively high force (peak value of 549.74 N). Waveforms of the position and velocity (Fig. 13b) indicate, that the duration of force and current impulses (about 1 ms) is much shorter than the duration of the projectile movement in rails (about 4 ms). It means, that the capacitance could be increased in order to exploit the full potential of the presented accelerator.

6. CONCLUSIONS

A study of the mathematical and physical models of the electrodynamic accelerator (railgun) with permanent magnets support has been presented in the paper. The obtained results allow to formulate some conclusions:

- the capacitance value has an impact mainly on the duration of current pulse. Increasing the capacity influences only slightly the peak value of the excitation current (Fig. 10a).;
- the initial capacitor voltage value affects mainly the excitation current value (Fig. 10b).;
- mathematical models which do not take into account the additional time delay in the system do not simulate the physical object with a sufficient precision (Fig. 11).;
- for the correct calculation of the projectile velocity, an appropriate choice of the friction coefficient value is important.

The efficiency of the railgun has been determined as well. The measurement results have been presented in Tab. 3. In our tests the efficiency value did not exceed 1 % and increases along with the energy value. The future works will be focused on increasing this parameter.

Tab. 3. Measured efficiency of the investigated accelerator

Voltage	Capacity	Energy stored in the capacitors	Kinetic energy of projectile	Efficiency
U [V]	C [mF]	E [J]	E [J]	η [%]
150	96.0	1068.75	8.39	0.78
150	76.5	843.75	5.13	0.61
121	96.0	695.45	4.49	0.65
121	76.5	549.04	2.69	0.49
101	96.0	484.55	2.57	0.53
101	76.5	382.54	1.50	0.39

The level of complexity of the phenomena occurring in the electrodynamic accelerator is relatively high. Thus, some further investigations for improving both physical and computational models are planned. In particular, the development of the experimental stand will be carried out.

REFERENCES

1. **Cooper K.P., Jones H.N., Meger R.A.** (2007), Analysis of railgun barrel material, *IEEE Transactions on Magnetics*, 43(1), 120-125.
2. **Domin J., Kluszczynski K.** (2013), Hybrid pneumatic-electromagnetic launcher - general concept, mathematical model and results of simulation, *Przegląd Elektrotechniczny*, 89(12), 21-25.
3. **Gieras J. F., Piech Z. J., Tomczuk B.** (2011), *Linear synchronous motors*, CRC Press, Taylor & Francis Group.
4. **Gosiewski Z., Klosowski P.** (2008), Support of work of electromagnetic gun by using permanent magnets, *Bulletin of the Military University of Technology*, 57(3), 87-95.
5. **Hogan J.D., Spray J.G., Rogers R.J., Vincent G., Schneider M.,** (2013), Dynamic fragmentation of planetary materials: ejecta length quantification and semi-analytical modelling, *International Journal of Impact Enginee-ring*, 62, 219–228.
6. **Hundertmark S., Schneider M., Simicic D., Vincent G.,** (2013), Experiments to increase the used energy with the PEGASUS railgun installation, http://arxiv.org/pdf/1402.6094v1.pdf.
7. **Kluszczynski K., Domin J.** (2015), Two module electromagnetic launcher with pneumatic assist: modelling, computer simulations and laboratory investigations, *COMPEL (The International Journal for Computation and Mathematics in Electrical and Electronic Engineering)*, 34(3), 691-709.
8. **McNab I.R., Beach F.C.** (2007), Naval railguns, *IEEE Transactions on Magnetics*, 43(1), 463-468.
9. **Piekielny P.** (2015), The measurement stand for the testing of the electrodynamic accelerator parameters, *Zeszyty Naukowe Politechniki Opolskiej*, 71, 53-54.
10. **Piskur P.** (2010), *Multiparameter optimization of construction and control of an electromagnetic launcher for application in linear drive of machining tool*, Ph.D. theses, Koszalin University of Technology, Department of Mechatronics, Nanotechnology and Vacuum Technology, Koszalin, Poland. (in polish)
11. **Poniaev S.A., Bobashev S.V., Zhukov R.O., Sedov A.I., Izotov S.N., Kulakov S.L., Smirnova M.N.,** (2015), Small-size railgun of mm-size solid bodies for hypervelocity material testing, *Acta Astronautica*, 109, 162-165.
12. **Tang L., He J., Chen L., Xia S., Feng D., Li J., Yan P.,** (2015), Study of some influencing factors of armature current distribution at current ramp-up stage in railgun, *IEEE Transactions on Plasma Science*, 43(5), 1585-1591.
13. **Tumanski S.** (2011), *Handbook of Magnetic Measurements*, CRC Press.
14. **Waindok A., Mazur G.** (2011), Mutual inductances in a mathematical model of the three-stage reluctance accelerator, *3rd International Students Conference on Electrodynamics and Mechatronics (SCE III)*, Opole, Poland, 115-118.
15. **Waindok A., Piekielny P.** (2013), Analysis of selected constructions of the electrodynamic accelerator, *International Symposium on Electrodynamic and Mechatronic Systems (SELM)*, Zawiercie, Poland, 51-52.
16. **Wild B., Schuppler C., Alouahabi F., Schneider M., Hoffman R.** (2014), The influence of the rail material on the multishot performance of the Rapid Fire Railgun (RAFIRA), *17th International Symposium on Electromagnetic Launch Technology (EML)*, La Jolla, CA, USA.
17. **Zimon J., Tomczuk B., Wajnert D.** (2012), Field-circuit modeling of AMB system for various speeds of the rotor, *Journal of Vibroengineering*, 14(1), 165-170.

DOI 10.1515/ama-2017-0047

BOUNDARY ELEMENT ANALYSIS OF ANISOTROPIC THERMOMAGNETOELECTROELASTIC SOLIDS WITH 3D SHELL-LIKE INCLUSIONS

Iaroslav PASTERNAK[*], Heorhiy SULYM[**]

[*]Department of Computer Engineering, Lutsk National Technical University, Lvivska Str 75, 43018 Lutsk, Ukraine
[**]Department of Mechanics and Applied Computer Science, Bialystok University of Technology, ul. Wiejska 45C, 15-351 Bialystok, Poland

yaroslav.pasternak@gmail.com, h.sulym@pb.edu.pl

received 21 April 2017, revised 5 December 2017, accepted 8 December 2017

Abstract: The paper presents novel boundary element technique for analysis of anisotropic thermomagnetoelectroelastic solids containing cracks and thin shell-like soft inclusions. Dual boundary integral equations of heat conduction and thermomagnetoelectroelasticity are derived, which do not contain volume integrals in the absence of distributed body heat and extended body forces. Models of 3D soft thermomagnetoelectroelastic thin inclusions are adopted. The issues on the boundary element solution of obtained equations are discussed. The efficient techniques for numerical evaluation of kernels and singular and hypersingular integrals are discussed. Nonlinear polynomial mappings are adopted for smoothing the integrand at the inclusion's front, which is advantageous for accurate evaluation of field intensity factors. Special shape functions are introduced, which account for a square-root singularity of extended stress and heat flux at the inclusion's front. Numerical example is presented.

Key words: Anisotropic, 3D, Thermomagnetoelectroelastic, Crack, Thin Inclusion

1. INTRODUCTION

Rapid development of modern multi-field materials and micro-electro-mechanical technologies raises increasing attention to their modeling and simulation. Particular interest is focused on the issues of fracture mechanics of cracked and inhomogeneous thermomagnetoelectroelastic (TMEE) materials. Since TMEE materials are anisotropic by nature, their analysis is more complicated than those of isotropic materials.

The boundary element method (BEM) is widely applied in the crack analysis (Aliabadi, 1997), since it allows accurate evaluation of field intensity factors at the crack front and requires only boundary mesh. Various boundary element techniques were proposed for 3D crack analysis in multi-field materials (e.g. see Pan and Yuan (2000), Rungamornrat et al. (2015), Muñoz-Reja et al. (2016)). Nevertheless, only recently (Pasternak et al., 2017) it was developed general 3D BEM for analysis of 3D cracks in anisotropic medium, which couples both thermal and magneto-electro-mechanical fields.

Another issue is the analysis of thin 3D inclusions. Various techniques are introduced to study soft or rigid inhomogeneities; however, they are mainly limited to the cases of planar perfectly rigid inclusions (Mykhas'kiv et al. (2010), Selvadurai (2000, 2002)). Also the models of thin inclusions should be accounted for in the modeling of semi-permeable cracks.

Therefore, this paper utilizes previously developed dual boundary integral equations (Pasternak et al., 2017) for obtaining the dual BEM for TMEE solids containing discontinuity surfaces (heat flux, stress, electric displacement, magnetic induction, temperature, displacement, electric and magnetic potentials discontinuity). Models of soft semi-permeable shell-like inclusions are introduced and incorporated in the obtained integral equations for obtaining the solution to 3D crack and inclusion problems. The issues on the efficient numerical evaluation of kernel functions, integration of singular and hypersingular integrals and accurate determination of field intensity factors are discussed in details.

2. GOVERNING EQUATIONS OF HEAT CONDUCTION AND THERMOMAGNETOELECTROELASTICITY

According to Pasternak et al. (2017), in a fixed Cartesian coordinate system $Ox_1x_2x_3$ the equilibrium equations, the Maxwell equations (Gauss theorem for electric and magnetic fields), and the balance equations of heat conduction in the steady-state case can be presented in the following compact form

$$\tilde{\sigma}_{Ij,j} + \tilde{f}_I = 0,\ h_{i,i} - f_h = 0, \tag{1}$$

where the capital index varies from 1 to 5, while the lower case index varies from 1 to 3, i.e. $I = 1,2,\ldots,5$. $i = 1,2,3$. Here and further the Einstein summation convention is used. A comma at subscript denotes differentiation with respect to a coordinate indexed after the comma, i.e. $u_{i,j} = \partial u_i / \partial x_j$.

In the assumption of small strains and fields' strengths the constitutive equations of linear thermomagnetoelectroelasticity in the compact notations are as follows (Pasternak et al., 2017):

$$\tilde{\sigma}_j = \tilde{C}_{IjKm}\tilde{u}_{K,m} - \tilde{\beta}_{Ij}\theta,\ h_i = -k_{ij}\theta_{,j}, \tag{2}$$

where:

$$\tilde{u}_i = u_i, \tilde{u}_4 = \phi, \tilde{u}_5 = \psi; \tilde{f}_i = f_i, \tilde{f}_4 = -q, \tilde{f}_5 = b_m;$$
$$\tilde{\sigma}_{ij} = \sigma_{ij}, \tilde{\sigma}_{4j} = D_j, \tilde{\sigma}_{5j} = B_j;$$
$$\tilde{C}_{ijkm} = C_{ijkm}, \tilde{C}_{ij4m} = e_{mij}, \tilde{C}_{4jkm} = e_{jkm}, \tilde{C}_{4j4m} = -\kappa_{jm},$$

DOI 10.1515/ama-2017-0047

$$\tilde{C}_{ij5m} = h_{mij}, \tilde{C}_{5jkm} = h_{jkm}, \tilde{C}_{5j5m} = -\mu_{jm}, \tilde{\beta}_{ij} = \beta_{ij},$$
$$\tilde{C}_{4j5m} = -\gamma_{jm}, \tilde{C}_{5j4m} = -\gamma_{jm};$$
$$\tilde{\beta}_{4j} = -\chi_j, \ \tilde{\beta}_{5j} = \nu_j (i, j, k, m = 1,2,3); \quad (3)$$

σ_{ij} is a stress tensor; f_i is a body force vector; D_i is an electric displacement vector; q is a free charge volume density; B_i is a magnetic induction vector; b_m is a body current; h_i is a heat flux; f_h is a distributed heat source density; u_i is a displacement vector; ϕ, ψ are the electric and magnetic potentials, respectively; θ is a temperature change with respect to the reference temperature; C_{ijkm} are the elastic stiffnesses (elastic moduli); k_{ij} are heat conduction coefficients; e_{ijk}, h_{ijk} are piezoelectric and piezomagnetic constants; κ_{ij}, μ_{ij}, γ_{ij} are dielectric permittivities, magnetic permeabilities and electromagnetic constants, respectively; β_{ij}, χ_i and ν_i are thermal moduli, pyroelectric coefficients and pyromagnetic coefficients, respectively.

Thus, the problem of linear thermomagnetoelectroelasticity is to solve partial differential equations (1) and (2) under the given boundary conditions and volume loading. Since magneto-electro-mechanical fields do not influence temperature field in the considered problem (uncoupled thermomagnetoelectroelasticity) the first step is to solve the heat conduction equation and the second one is to determine mechanical, electric and magnetic fields acting in the solid.

3. DUAL BOUNDARY INTEGRAL EQUATIONS AND MODELS OF 3D SOFT SHELL-LIKE INCLUSIONS

For modeling of solids with thin inhomogeneities, a coupling principle for continua of different dimension is often used (Sulym, 2007). This principle involves the replacement of a thin inclusion with a surface of a field discontinuity for stress, electric displacement, displacement, electric potential, temperature, and heat flux. Frequently a median surface of a thin inhomogeneity is chosen as the discontinuity surface. The inclusion is thus removed from consideration as a geometrical object, and it is assumed that the thermal, electric and mechanical influence of the inclusion is reduced to the influence of the above-mentioned discontinuity surface (Fig. 1). Thus, according to a discontinuity function method (Sulym, 2007), the study of a stress state of a solid (an exterior problem) is reduced to the study of the influence of unknown discontinuity functions and is considered without account of the inclusion's material properties. It is clear that the thermoelectroelastic state of the solid depends on these discontinuity functions, material properties of the solid, the geometrical features of the problem, the contact conditions at the thin inhomogeneity interface, and the external load.

On the other hand, due to a small thickness of the inclusion, the extended tractions and displacements, temperature and heat flux at the faces of the inclusion are related with each other. Corresponding relations, which include thermo-magneto-electro-mechanical properties of the inclusion and its thickness, are called the mathematical model of a thin inclusion. This model does not depend on the properties of a medium containing an inclusion, and it can be considered as an interior problem. There are only three basic requirements for the mathematical model of a thin inclusion (Sulym, 2007): (a) the number of equations should equal to the number of the unknown discontinuity functions; (b) the model should be simple for further solution of the obtained system of equations; and (c) the model should simulate essential features of thermoelectroelastic behavior of the inclusion.

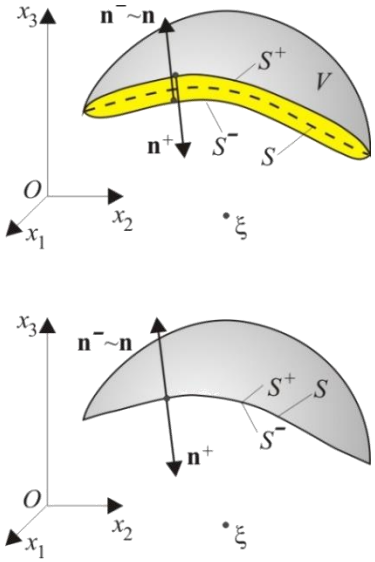

Fig. 1. Simplification of a thin inclusion

Since the coupling principle and a discontinuity function method consider exterior and interior problems independently, several inclusion models, which simulate different features of the inhomogeneity, can be developed for the same exterior problem, and using the same inclusion model one can solve different exterior problems.

According to the philosophy of the discontinuity function approach the exterior problem of 3D TMEE is reduced to the following system of dual boundary integral equations (see Pasternak et al. (2017)):

– heat conduction

$$\frac{1}{2}\Sigma\theta(\mathbf{x}_0) = \iint_S \Theta^*(\mathbf{x}, \mathbf{x}_0)\Sigma h_n(\mathbf{x})dS(\mathbf{x}) - \text{CPV}\iint_S H^*(\mathbf{x}, \mathbf{x}_0)\Delta\theta(\mathbf{x})dS(\mathbf{x}),$$
$$\frac{1}{2}\Delta h_n(\mathbf{x}_0) = n_i(\mathbf{x}_0)\Big[\text{CPV}\iint_S \Theta_i^{**}(\mathbf{x}, \mathbf{x}_0)\Sigma h_n(\mathbf{x})dS(\mathbf{x}) - \text{HFP}\iint_S H_i^{**}(\mathbf{x}, \mathbf{x}_0)\Delta\theta(\mathbf{x})dS(\mathbf{x})\Big], \quad (4)$$

– TMEE

$$\frac{1}{2}\Delta\tilde{t}_I(\mathbf{x}_0) = n_j\Bigg[\text{CPV}\iint_S D_{IjK}(\mathbf{x}, \mathbf{x}_0)\Sigma\tilde{t}_K(\mathbf{x})dS(\mathbf{x}) - \text{HFP}\iint_S S_{IjK}(\mathbf{x}, \mathbf{x}_0)\Delta\tilde{u}_K(\mathbf{x})dS(\mathbf{x}) + \text{CPV}\iint_S Q_{Ij}(\mathbf{x}, \mathbf{x}_0)\Delta\theta(\mathbf{x})dS(\mathbf{x}) + \iint_S W_{Ij}(\mathbf{x}, \mathbf{x}_0)\Sigma h_n(\mathbf{x})dS(\mathbf{x})\Big], \quad (5)$$

where $\Sigma f = f^+ + f^-$; $\Delta f = f^+ - f^-$; n_p is a unit outwards normal vector to the surface S (or its faces S^+ and S^-), which replaces an inclusion; $\tilde{t}_I = \tilde{\sigma}_{Ij}n_j$ is an extended traction vector; $h_n = h_i n_i$; CPV stands for the Cauchy Principal Value of the integral, and HFP stands for the Hadamard Finite Part of the integral. All the kernels are given explicitly by Pasternak et al. (2017).

DOI 10.1515/ama-2017-0047

The interior problem is then solved as follows. Using the philosophy of the discontinuity function method and the coupling principle (Fig. 1) for the development of a shell-like inclusion model, one withdraws the inclusion from consideration as a geometrical object, and transfers the contact tractions, displacements, surface charges, electric potential, temperature, and heat flux onto its median surface S (accordingly onto the faces S^+ and S^-, Fig. 1). Thus, the problem is reduced to the determination of the thermomagnetoelectroelastic state of a solid with the surface S of thermo-magneto-electro-mechanical field discontinuities. After development of the interaction conditions for a thin inhomogeneity along with the integral equations (4)–(5) concerning abovementioned field discontinuities for a solid, the thermoelectroelastic state of the latter can be determined.

Consider the thermomagnetoelectroelastic state at a certain point y on the median surface of a thin transversely isotropic pyroelectric inclusion. Assume that the Ox'_3 axis of a local coordinate system $Ox'_1x'_2x'_3$ is directed along the normal vector $n^+(y)$ of the surface S^+ at the point y. All vectors in the local coordinate system are related with those of the global one by the relations $\tilde{t}' \ \ I = \Omega IJ\tilde{t}J$, $\tilde{t}_I = \Omega_{JI}\widetilde{t'}_J$, where Ω is a rotation matrix. The origin of the local coordinate system is placed at the median surface of the thin inclusion. Thus, $\tilde{f}(-h) = \tilde{f}^+$ and $\tilde{f}(h) = \tilde{f}^-$, where $\tilde{f}$ is one of the scalars θ, h_n or vectors $\tilde{u}_i$, $\tilde{t}_i$; $2h = 2h(y)$ is the thickness of the inclusion at y. With the account of the identity $n^{\pm} = -n^{i\pm}$, the conditions of a perfect thermal, mechanical, magnetic and electric contact of the inclusion and the solid are $\theta^{\pm} = \theta^{i\pm}$, $h_n^{\pm} = -h_n^{i\pm}$, $\tilde{u}_i^{\pm} = \tilde{u}_i^{i\pm}$, $\tilde{t}_i^{\pm} = -\tilde{t}_i^{i\pm}$. Here the non-italic superscript "i" denotes values concerned with the inclusion.

According to Eq. (2), heat flux and extended stress inside the inclusion in the local coordinate system equal

$$h'_3 = -k'^{\mathrm{i}}_{3j}\theta'_{,j}; \quad \widetilde{\sigma}' \ \ I3 = C'^{\mathrm{i}}_{I3Km}\widetilde{u}' \ \ K,m - \widetilde{\beta}'I3\mathrm{i}\theta. \quad (6)$$

Integrating Eq. (6) over the thickness of the inclusion one can obtain

$$\begin{aligned}
&\int_{-h}^{h} h'_3 dx'_3 = -k'^{\mathrm{i}}_{33}\left[\theta(h)-\theta(-h)\right] \\
&\quad -k'^{\mathrm{i}}_{31}\int_{-h}^{h}\theta'_{,1}dx'_3 - k'^{\mathrm{i}}_{32}\int_{-h}^{h}\theta'_{,2}dx'_3, \\
&\int_{-h}^{h}\tilde{\sigma}'_{I3}dx'_3 = C'^{\mathrm{i}}_{I3K3}\left[\tilde{u}'_K(h)-\tilde{u}'_K(-h)\right] \\
&\quad + C'^{\mathrm{i}}_{I3K1}\int_{-h}^{h}\tilde{u}'_{K,1}dx'_3 + C'^{\mathrm{i}}_{I3K2}\int_{-h}^{h}\tilde{u}'_{K,1}dx'_3 - \tilde{\beta}'^{\mathrm{i}}_{I3}\int_{-h}^{h}\theta dx'_3.
\end{aligned} \quad (7)$$

According to the mean value theorem,

$$\begin{aligned}
&\int_{-h}^{h} h'_3 dx'_3 = 2h\cdot h'^{\mathrm{avr}}_3 \\
&\quad \approx h(\mathbf{y})\left[h_n^{\mathrm{i}}(h)-h_n^{\mathrm{i}}(-h)\right] = h(\mathbf{y})\Delta h_n(\mathbf{y}), \\
&\int_{-h}^{h}\theta dx'_3 = 2h\cdot\theta^{\mathrm{avr}} \\
&\quad \approx h(\mathbf{y})\left[\theta(h)+\theta(-h)\right] = h(\mathbf{y})\Sigma\theta(\mathbf{y}); \\
&\int_{-h}^{h}\tilde{\sigma}'_{I3}dx'_3 = 2h\tilde{\sigma}'^{\mathrm{avr}}_{I3} \\
&\quad \approx h(\mathbf{y})\left[\tilde{t}'^{\mathrm{i}}_I(h)-\tilde{t}'^{\mathrm{i}}_I(-h)\right] = h(\mathbf{y})\Delta\tilde{t}'_I(\mathbf{y}).
\end{aligned} \quad (8)$$

For simplification of the model one can withdraw the interaction of thermo-magneto-electro-mechanical fields in the directions normal and tangential to the inclusion's median surface (as in the model of Winkler elastic foundation) by assuming that

$$\begin{aligned}
&\int_{-h}^{h}\theta'_{,1}dx'_3 = 0, \int_{-h}^{h}\theta'_{,2}dx'_3 = 0; \\
&\int_{-h}^{h}\tilde{u}'_{K,1}dx'_3 = 0, \int_{-h}^{h}\tilde{u}'_{K,2}dx'_3 = 0.
\end{aligned} \quad (9)$$

In this case it is also assumed that

$$\Sigma h_n(\mathbf{y}) = 0\,, \ \ \Sigma\tilde{t}_I = 0\,, \quad (10)$$

which allows to satisfy balance equations (1) identically.

Then, according to Eqs. (6)–(9), one can obtain

$$\begin{aligned}
&\Delta h_n(\mathbf{y}) = \frac{k'^{\mathrm{i}}_{11}(\mathbf{y})}{h(\mathbf{y})}\Delta\theta(\mathbf{y}), \\
&\Delta\tilde{t}'_I(\mathbf{y}) = -\frac{C'^{\mathrm{i}}_{I3K3}(\mathbf{y})}{h(\mathbf{y})}\Delta\tilde{u}'_K(\mathbf{y}) - \tilde{\beta}'^{\mathrm{i}}_{I3}\Sigma\theta(\mathbf{y}).
\end{aligned} \quad (11)$$

Transforming (11) to global coordinates the following model of he thin thermomagnetoelectroelastic inclusion is obtained

$$\begin{aligned}
&\Delta h_n(\mathbf{y}) = \frac{k'^{\mathrm{i}}_{11}(\mathbf{y})}{h(\mathbf{y})}\Delta\theta(\mathbf{y}); \\
&\Delta\tilde{\mathbf{t}}(\mathbf{y}) = -\frac{\mathbf{V}(\mathbf{y})}{h(\mathbf{y})}\Delta\tilde{\mathbf{u}}(\mathbf{y}) - \mathbf{v}(\mathbf{y})\Sigma\theta(\mathbf{y}).
\end{aligned} \quad (12)$$

Here $\mathbf{V} = \boldsymbol{\Omega}^{\mathrm{T}}\mathbf{C}'^{\mathrm{i}}_{33}\boldsymbol{\Omega}$, $\mathbf{v} = \boldsymbol{\Omega}^{\mathrm{T}}\tilde{\boldsymbol{\beta}}'^{\mathrm{i}}_3$.

Reducing Eqs (4), (5), (10), (12) one obtains the sought system of integral equations for a solid containing thin soft semi-permeable shell-like inclusion

– heat conduction

$$\begin{aligned}
&\frac{k'^{\mathrm{i}}_{11}}{2h}\Delta\theta(\mathbf{x}_0) = \\
&\quad -\mathrm{HFP}\iint_S H_i^{**}(\mathbf{x},\mathbf{x}_0)n_i(\mathbf{x}_0)\Delta\theta(\mathbf{x})dS(\mathbf{x}),
\end{aligned} \quad (13)$$

– TMEE

$$\begin{aligned}
&-\frac{V_{IK}(\mathbf{x}_0)}{2h(\mathbf{x}_0)}\Delta\tilde{u}_K(\mathbf{y}) = \\
&\quad n_j(\mathbf{x}_0)\left[-\mathrm{HFP}\iint_S S_{IjK}(\mathbf{x},\mathbf{x}_0)\Delta\tilde{u}_K(\mathbf{x})dS(\mathbf{x})\right. \\
&\quad \left.+\mathrm{CPV}\iint_S\left[Q_{Ij}-H^*(\mathbf{x},\mathbf{x}_0)v_I(\mathbf{x}_0)\right]\Delta\theta(\mathbf{x})dS(\mathbf{x})\right].
\end{aligned} \quad (14)$$

Thus the problem is reduced to determination of unknown temperature and extended displacement discontinuities from the system of integral equations (13), (14). It should be mentioned that for the sake of compactness the terms accounting for external boundaries of the solid (which thermo-magneto-electro-mechanical loading is assumed to be given) are not written here. The explicit expressions for integral equations of external problem accounting for external boundaries of a solid can be found in (Pasternak et al., 2017). These terms are just the regular integrals, and for infinite medium they can be reduced to certain spatial functions.

DOI 10.1515/ama-2017-0047

4. NUMERICAL SOLUTION OF OBTAINED EQUATIONS

Since the singularities of obtained kernels are the same as for 3D cracks, the solution strategy is the same as presented in (Pasternak et al., 2017). The median surface of thin inclusion is meshed with quadrilateral discontinuous boundary elements. Special shape functions are used to catch the square-root singularity, which also arises at inclusions front (see Sulym (2007)). Numerical evaluation of singular and hypersingular integrals is held with the help of modified Kutt's quadrature. Polynomial mappings are used to smoothen the integrand.

According to Sulym (2007) the field intensity factors vector at some point of inclusion's front is defined as

$$\tilde{\mathbf{k}}^{(1)} = \lim_{\mathbf{x}\to\mathbf{x}(A)} \sqrt{\frac{\pi}{8s(\mathbf{x})}}\, \mathbf{L}\cdot\Delta\tilde{\mathbf{u}}^{*}(\mathbf{x}), \tag{15}$$

where $\tilde{\mathrm{k}}^{(1)} = [\mathrm{K_{II}}, \mathrm{K_I}, \mathrm{K_{III}}, \mathrm{K_D}, \mathrm{K_B}]^{\mathrm{T}}$; $\mathrm{K_I}$, $\mathrm{K_{II}}$, $\mathrm{K_{III}}$ are the stress intensity factors; $\mathrm{K_D}$, $\mathrm{K_B}$ are electric displacement and magnetic induction intensity factors; L is a Barnett – Lothe tensor evaluated in the local coordinate system; and $\mathrm{s(x)}$ is an arc length evaluated from x to the selected point along the cross section of the crack with the normal plane.

These field intensity factors for soft semi-permeable inclusions are close to those of a crack; therefore, they can be accurately determined numerically by the technique proposed by Pasternak et al. (2017).

5. NUMERICAL EXAMPLE

Consider a transversely isotropic pyroelectric medium, which has the following properties of barium titanate (BaTiO3) (Dunn, 1993):

- elastic moduli (GPa): $C_{11} = C_{22} = 150$; $C_{33} = 146$; $C_{12} = C_{13} = C_{23} = 66$; $C_{44} = C_{55} = 44$; $C_{66} = (C_{11} - C_{12})/2 = 42$;
- piezoelectric constants (C/m^2): $e_{31} = e_{32} = -4.35$; $e_{33} = 17.5$; $e_{15} = e_{24} = 11.4$;
- dielectric constants (nF/m): $\kappa_{11} = \kappa_{22} = 9.86775$; $\kappa_{33} = 11.151$;
- heat conduction coefficients (W/(m·K)): $k_{11} = k_{22} = k_{33} = 2.5$;
- thermal expansion coefficients (K^{-1}): $\alpha_{11} = \alpha_{22} = 8.53 \cdot 10^{-6}$; $\alpha_{33} = 1.99 \cdot 10^{-6}$;
- pyroelectric constants (GV/(m·K)): $\lambda_3 = 13.3 \cdot 10^{-6}$;
- the rest of constants are equal to zero.

Here the Voigt notation is used in the indices of elastic moduli and piezoelectric constants, which changes the index pairs in Eq (3) with a single index as $11 \leftrightarrow 1$; $22 \leftrightarrow 2$; $33 \leftrightarrow 3$; $23{,}32 \leftrightarrow 4$; $13{,}31 \leftrightarrow 5$; $12{,}21 \leftrightarrow 6$.

Consider the thermoelectroelastic problem for a penny-shaped disk inclusion of radius R, which lays in the isotropy plane $\mathrm{Ox_1x_2}$. The medium is loaded with uniform heat $\mathrm{h_0}$ flowing along the polarization direction $\mathrm{Ox_3}$, which does not cause tertiary pyroelectricity (Pasternak et al., 2014). The median surface of inclusion is meshed with only 12 quadrilateral discontinuous boundary elements (Fig. 2).

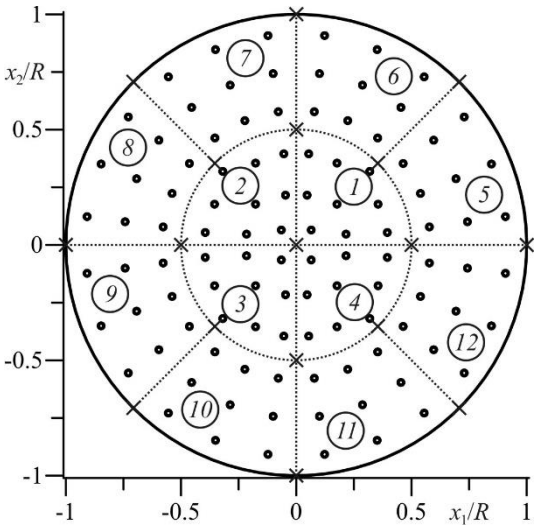

Fig. 2. Boundary element mesh of the disk inclusion

Four central boundary elements Nos 1–4 use general quadratic shape functions, while other elements (Nos 5–12) utilize special shape functions to account for the square root singularity of stress and heat flux at the inclusion front (Pasternak et al., 2017).

Inclusion's material is characterized by its relative rigidity, permeability and thermal conductivity, which are assumed the same in this study, i.e. $C^{\mathrm{i}}_{33} = \mathrm{r}C_{33}$, $\kappa^{\mathrm{i}}_{33} = r\kappa_{33}$, $k^{\mathrm{i}}_{33} = rk_{33}$, where r is the dimensionless parameter. The thickness of inclusion is equal to $2h = 0.02R$. It is also assumed that the plane $\mathrm{Ox_1x_2}$ has zero temperature (with respect to the reference one). The normalization factors are equal to $K_\sigma = h_0\beta_{11}R\sqrt{\pi R}/k_{11}$, $K_{h1} = -2h_0\sqrt{R/\pi}$.

Fig. 3 depicts normalized stress intensity factors at inclusion's front for very small values of parameter $\mathrm{r} < 10^{-4}$. They are close to those calculated for a thermally insulated impermeable crack by Pasternak et al. (2017), which validates proposed model of thin shell-like soft weakly permeable inclusion.

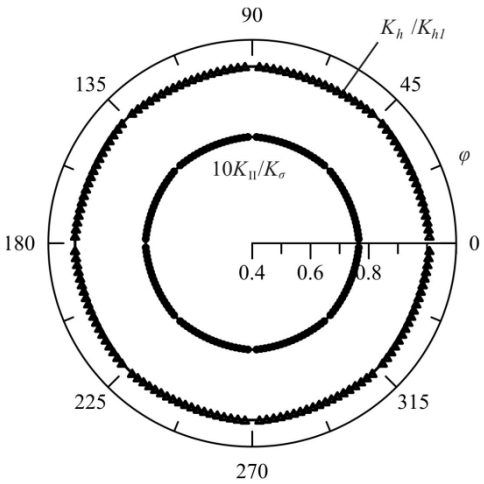

Fig. 3. Field intensity factors of a very soft inclusion

Fig. 4 depicts change in field intensity factor $\mathrm{K_{II}}$ depending on the parameter r. The normalization factor is $\mathrm{K_{II}}$ of a corresponding penny-shaped crack.

DOI 10.1515/ama-2017-0047

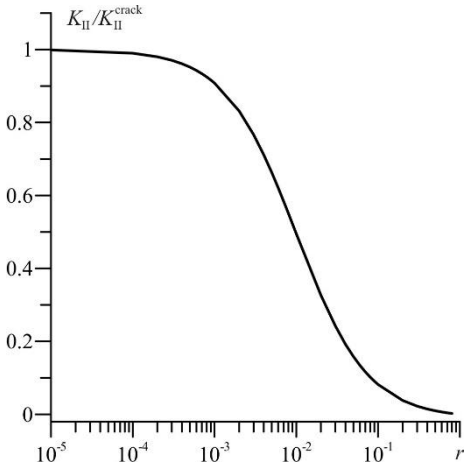

Fig. 4. Dependence of field intensity factor on r

One can see that the field intensity factor decrease monotonously on r. It is also visible that the proposed inclusion model does not sufficiently describe rigid inclusions. For $r > 1$ field intensity factors and thus discontinuity functions are zero, the same as for a homogeneous material without inclusion. Therefore, another models should be developed to address this case.

REFERENCES

1. **Aliabadi M.H.** (1997) Boundary element formulations in fracture mechanics, *Applied Mechanics Review*, 50, 83–96.
2. **Dunn M.L.** (1993) Micromechanics of coupled electroelastic composites: effective thermal expansion and pyroelectric coefficients, *J Appl Phys*, 73, 5131–5140.
3. **Muñoz-Reja M.M., Buroni F.C., Sáez A., García-Sánchez F.** (2016) 3D explicit-BEM fracture analysis for materials with anisotropic multifield coupling, *Applied Mathematical Modelling*, 40, 2897–2912.
4. **Mykhas'kiv V.V., Khay O.M., Zhang Ch., Bostrom A.** (2010) Effective dynamic properties of 3D composite materials containing rigid penny-shaped inclusions, *Waves in Random and Complex Media*, 20(3), 491–510.
5. **Pan E., Yuan F.G.** (2000) Boundary element analysis of three-dimensional cracks in anisotropic solids, *Int. J. Numer. Meth. Engng.*, 48, 211–237.
6. **Pasternak Ia., Pasternak R., Pasternak V., Sulym H.** (2017) Boundary element analysis of 3D cracks in anisotropic thermomagnetoelectroelastic solids, *Engineering Analysis with Boundary Elements*, 74, 70–78.
7. **Pasternak Ia., Pasternak R., Sulym H.** (2014) Temperature field and heat flux that do not induce stress and electric displacement in a free thermoelectroelastic anisotropic solid, *Mechanics Research Communications*, 57, 40–43.
8. **Rungamornrat J., Phongtinnaboot W., Wijeyewickrema A.C.** (2015) Analysis of cracks in 3D piezoelectric media with various electrical boundary conditions, *International Journal of Fracture*, 192, 133–153.
9. **Selvadurai A.P.S.** (2000) An inclusion at a bi-material elastic interface, *Journal of Engineering Mathematics*, 37, 155–170.
10. **Selvadurai A.P.S.** (2002) Mechanics of a rigid circular disc bonded to a cracked elastic half-space, *Int. J. of Solids and Structures*, 39, 6035–6053.
11. **Sulym H.T.** (2007) *Bases of mathematical theory of thermoelastic equilibrium of deformable solids with thin inclusions*, Research and Publishing center of NTSh, Lviv, (in Ukrainian).

The present paper is financially supported by the Ministry of Science and Higher Education of Poland (research project No S/WM/4/2017) and realized in Bialystok University of Technology.

DE GRUYTER
OPEN

DOI 10.1515/ama-2017-0048

acta mechanica et automatica, vol.11 no.4 (2017)

DRY ICE COMPACTION IN PISTON EXTRUSION PROCESS

Jan GÓRECKI*, Ireneusz MALUJDA*, Krzysztof TALAŚKA*, Dominik WOJTKOWIAK*

*Chair of Basics of Machine Design, Faculty of Machines and Transport,
Poznan University of Technology, ul. Piotrowo 3, 60-965 Poznań, Poland

jan.gorecki@put.poznan.pl, ireneusz.malujda@put.poznan.pl, krzysztof.talaska@put.poznan.pl, dominik.wojtkowiak@put.poznan.pl

received 6 June 2017, revised 5 December 2017, accepted 8 December 2017

Abstract: The article presents the results of research on the effect of extrusion tube geometry on the axial force being the key parameter of the dry ice piston extrusion process. The tests were carried out with the experimental set-up based on a cylindrical extrusion tube used alone and supplemented with reducer (orifice). The focus of the experiments was to determine the effect of compression tube reducer on the value of the force of resistance FOP in the dry ice compression process. Its value can subsequently be used as the basis for establishing guidelines for designing and building machines for compression and pelletizing of dry ice.

Key words: Dry Ice, Carbon Dioxide, Compaction, Agglomeration Process, Extrusion Tube Reducer

1. INTRODUCTION

Waste materials generated during production processes can be recovered and reused, for example as raw materials. An example of such materials is carbon dioxide generated in production of ammonia compounds (Chen et al., 2014). The amount of carbon dioxide generated in these processes is the highest on a percentage basis among all other sources of carbon dioxide emissions (Fig. 1). Carbon dioxide is liquefied through compression and in this form it can be stored for further processing. The amounts of carbon dioxide generated in production processes often exceeds own needs of the factor. Hence, the surplus amounts are often supplied to other companies (Chen et al., 2014; Vansant, 2013).

Expansion of liquid carbon dioxide produces carbon dioxide snow (Liu et al., 2012; Liu et al., 2010). The product has a temperature of -78.8°C and sublimates at room temperatures (Chen et al., 2014; Masa et al., 2016; Mazzoldi et al., 2008; Uhlmann et al., 2010). This is why it is popularly known as dry ice. Maintaining low temperature accompanied with sublimation at normal temperatures make it particularly suitable for food industry applications (including dry ice blasting, disinfection in the food production, carbonating of water, low temperature storage of food products, etc.) (Dong et al., 2012; Li et al., 2016; Liu and Calvert et al., 2012; Liu and Hirama et al., 2012; Masa et al., 2016; Otto et al., 2011; Spur, 1999; Ulhmann et al., 2010; Witte et al., 2017; Yamaguchi et al., 2011).

Dry ice snow can be then densified (compacted) to reduce storage volume and slow down the process of sublimation. Compression extends the time for which dry ice remains in solid phase thus improving the characteristics desired in refrigeration applications (Chen et al., 2014; Górecki et al., 2015 and 2016; Masa et al., 2016).

Dry ice compaction machines are most often based on hydraulic or crankshaft mechanisms. The review of available sources does not provide sufficient data needed for a detailed analysis of the dry ice extrusion process. Such analysis is indispensable for evaluation of the process itself and to put forward solutions to improve its efficiency.

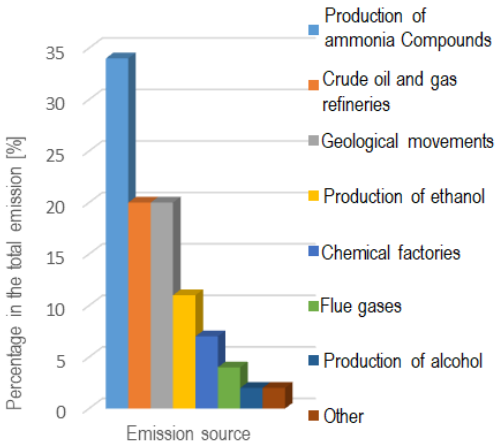

Fig. 1. Main sources of CO_2 (Spur, 1999)

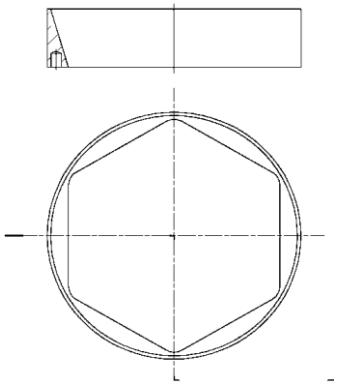

Fig. 2. Extrusion tube reducer

The present research concerns piston extrusion technique implemented with a specifically designed and built machine including

DOI 10.1515/ama-2017-0048

a multi-channel die and extrusion tube assembly. The paper focuses on the results of testing the compression tube reducer (Fig. 2), described in the patent application No. P.419432 which is an important part of the extrusion assembly having an effect on the compression efficiency. This concerns in particular reduction of the resisting surface area S_{PP} (Fig. 4).

2. DESIGN OF EXTRUSION TUBE ASSEMBLY USED IN THE PISTON TYPE EXTRUSION MACHINE

The design of the extrusion tube used in the analysed piston extrusion machine is presented in Fig. 3. The analysed dry ice snow compression method features a sequence of operations performed in a loop. In the first step the snow particles 5 are introduced into the cylindrical tube 2 of D_K diameter where they are compressed through piston displacement 1. The process of compression continues until the resistance force F_{OP} caused by friction and shaping of the pellet in the die 3 equals the force F_t applied to the piston 1. In the next step the compacted material moves through the die plate until the piston has reached its end position at which point it starts to reciprocate to the initial position.

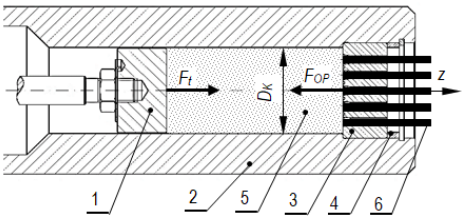

Fig. 3. Piston-type extrusion assembly 1 – piston, 2 – extrusion tube, 3 – multi-channel die, 4 – spacing ring, 5 – dry ice snow, 6 – compressed dry ice snow

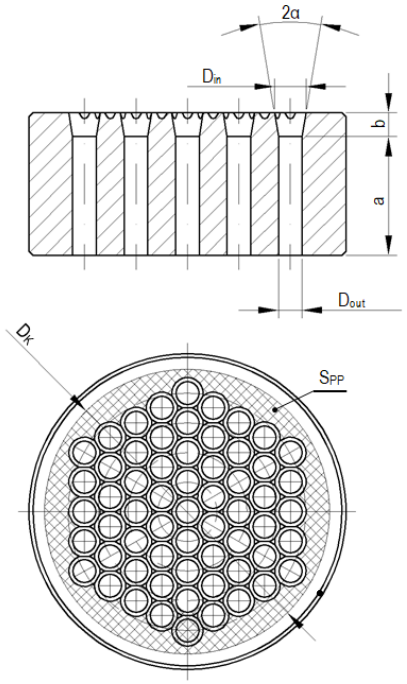

Fig. 4. Multi-channel die, D_{in} – channel inlet diameter, D_{out} – channel outlet diameter, a – length of barrel section, b – length of conical section, 2α – angle of convergence of the conical section, D_K – extrusion chamber diameter, S_{PP} – area of resisting surface

The efficiency of the piston extrusion process depends primarily on the design of the die plate including partly cylindrical and partly conical channels (Fig. 4). The die geometry influences the movement resistance as well as the final shape of the pellet. There are 61 channels, each comprising a conical section of length *b* and *2α* angle of convergence followed by cylindrical (barrel) section of length *a* and diameter D_{out}. The die channels are all arranged within a hexagon with sides the length of *e*. Since the die is mounted within a cylindrical extrusion tube (No. 2 in Fig. 3) the die plate surface S_{PP} is perpendicular to axis Z.

In order to determine the minimum external force F_t applied on the piston to effect densification of dry ice snow the test procedure described in literature was used (Drzymała, 1988; Górecki et al., 2013; Malczewski, 1992). The test apparatus was MTS strength tester, model Insight 50 kN which allowed recording the force and displacement values at 10 Hz frequency.

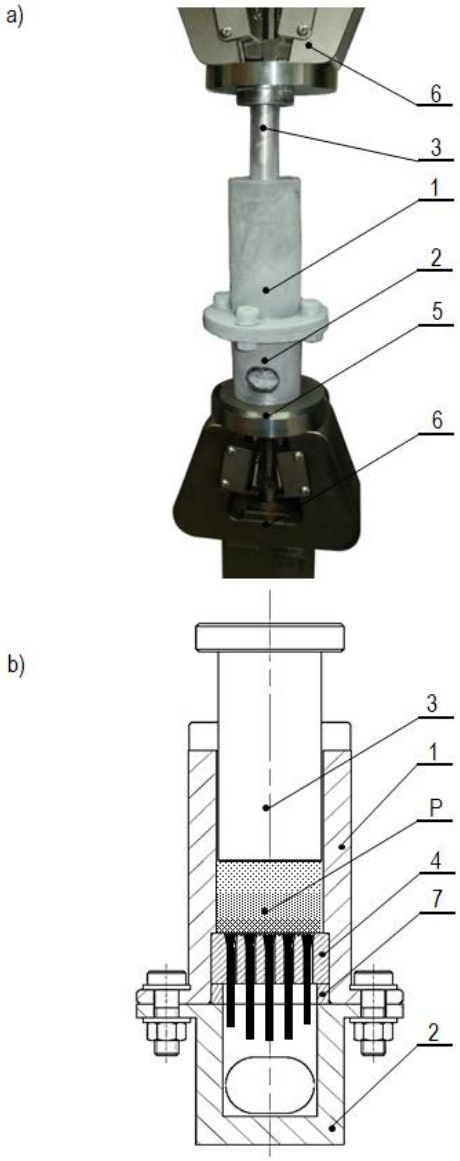

Fig. 5. Test set-up a) grips of the MTS strength tester including the test assembly and alignment jig, b) cross-section of the test assembly 1 – cylindrical extrusion tube, 2 – base of the test assembly, 3 – piston, 4 – multi-channel die plate 5 – right-angle jig, 6 – grips of the strength tester, 7 – spacing ring, P – compressed dry ice snow (Górecki et al., 2013)

DOI 10.1515/ama-2017-0048

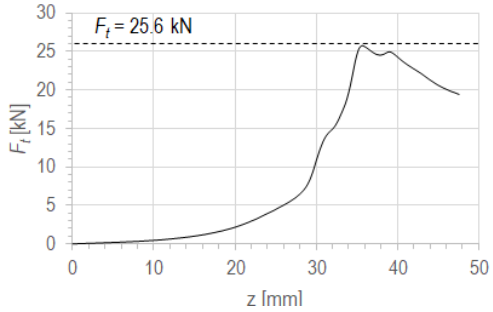

Fig. 6. Dry ice snow compression curve in a multi-channel die extrusion system

A special test assembly was used in the tests (Fig. 5). In order to minimize the measurement error due to eccentric mounting of the compression head, the grips were equipped with a right-angle jig to align the compression force in the direction perpendicular to the specimen cross-section 5.

Before starting the test the compression chamber 1 was filled with crushed dry ice. Subsequently the piston 3 was inserted into the extrusion chamber 2. The test set-up was complete with the test assembly fitted in the grips of the strength tester. The scale was zeroed and the procedure was started by lowering the piston 3 downwards at a constant speed. When F_t reached the level of F_{OP} the material started being pushed through the multi-channel die 4.

The test was repeated ten times and the results were averaged and presented as compression curves representing the change of force F_t as a function of piston displacement Z (Fig. 6).

The average force F_t is 25.6 kN.

3. COMPRESSION TUBE REDUCER

The value of F_{OP} force is influenced by the geometric parameters of the parts making up the compression chamber. One of them is the compression chamber reducer (Fig. 7, 8). The purpose of this piece is to reduce the area of the resistance surface S_{PP}.

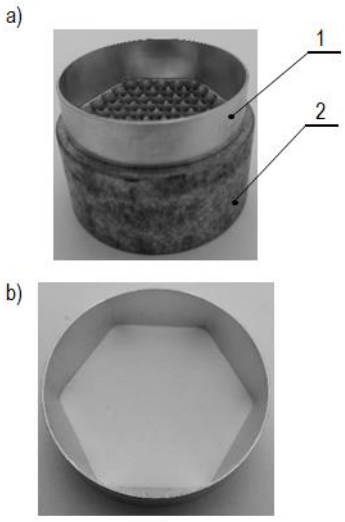

Fig. 7. Assembly comprising the multi-channel die plate and compression tube reducer a) entire assembly, b) stress concentration reducer: 1 – reducer piece, 2 – multi-channel die plate

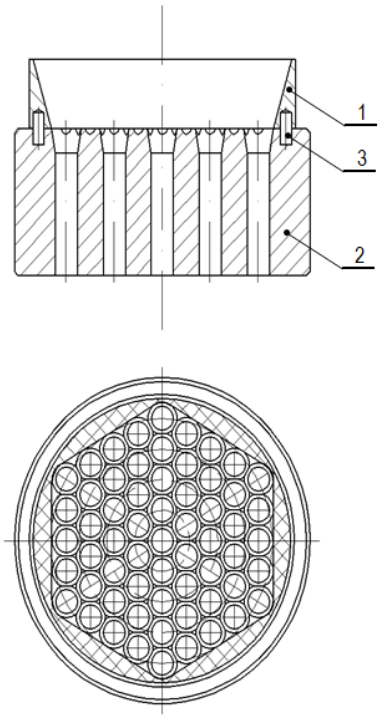

Fig. 8. Assembly comprising the multi-channel die plate and compression tube reducer: 1 – compression tube reducer, 2 – multi-channel die plate, 3 – locating pin, SPP – resisting surface (P.419432)

Since the shape of the reducer is not circularly symmetric (due to circular to hexagonal shape transition) two locating pins 3 were used to align the elements (Fig. 8).

The assembly obtained in this way can be fitted in the tube in which dry ice snow is compressed by a crank-driven piston (Fig. 9).

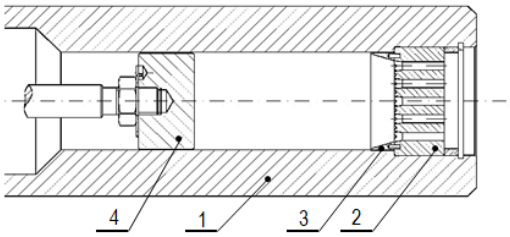

Fig. 9. The processing assembly of the piston extrusion machine: 1 – cylindrical extrusion tube, 2 – multi-channel die plate, 3 – compression tube reducer, 4 – piston (P.419432)

Reduction of the resisting surface S_{PP} obtained by fitting the reducer affects the experimentally determined force applied on the piston F_t'.

The test procedure was the same as described in the previous chapter. The test set-up was also the same (Fig. 10a) except that this time it included the compression tube reducer assembly besides the multi-channel die plate 4, 5 (Fig. 10b).

Based on the above described kinematic structure the design of the research

The test results were averaged and presented as a compression curve representing the change of force F_t' as a function of piston displacement z (Fig. 11).

DOI 10.1515/ama-2017-0048

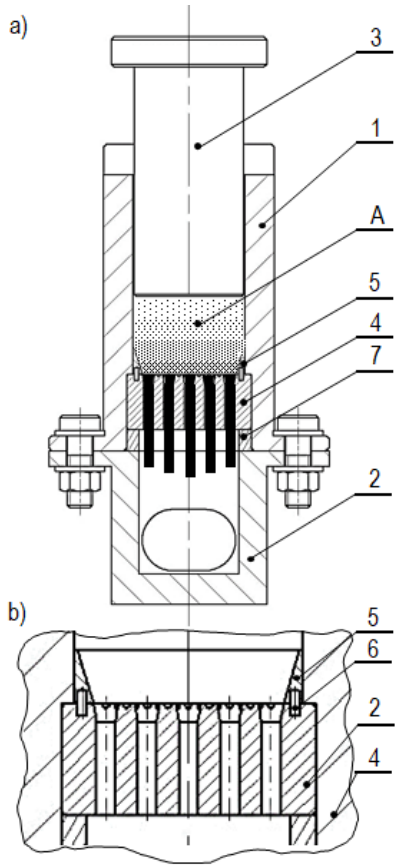

Fig. 10. Test assembly a) test assembly cross-section, b) location of the reducer piece in the test assembly: 1 – extrusion tube, 2 – base of the test assembly, 3 – piston, 4 – multi-channel die plate, 5 – tube reducer, 6 – locating pin, 7 – spacing ring, A – compressed dry ice snow

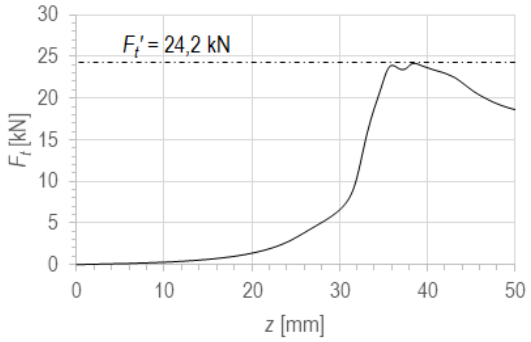

Fig. 11. Compression curve obtained with the multi-channel die plate and compression tube reducer assembly

The average value of the applied force F_t' was 24.2 kN. Hence we get a difference of 1,5 kN between the values of F_t and F_t'.

4. SUMMARY

The tests of the compression tube reducer described in the patent application No. P.419432 have confirmed its influence on the value of the resistance force F_{OP}. As it can be figured out from the diagram, the force decreased by 1.5 kN i.e. by ca. 5.8%.

Considering the value of compression stresses in commercial dry ice extrusion machines there is a need for further research in order to build mathematical models describing the relation between the resistance force F_{OP} and the compression tube parameters. These mathematical models will be used to determine the optimum parameters of the compression assemblies of dry ice snow compression machines.

REFERENCES

1. **Chen L., Zhang X.** (2014), A review study of solid-gas sublimation flow refrigeration: From basic mechanism to alications, *International Journal od Refrigeration*, 40, 61-83.
2. **Dong S., Song B., Hansz B., Liao H.L., Coddet C.,** (2012) Modeling of dry ice blasting and its alication in thermal spray, *Material Research Innovations*, 16, 61-66.
3. **Drzymała Z.** (1988), *Basics of Compaction Engineering of Material Compaction* (in polish), PWN, Warsaw.
4. **Górecki J., Malujda I., Talaśka K.** (2013), Research on Densification of solid carbon dioxide, *Journal of Mechanical and Transportation Engineering*, 65(4), 5-12.
5. **Górecki J., Malujda I., Talaśka K.** (2016), Investigation of internal friction of agglomerated dry ice, *Procedia Engineering*, 136, 275-279.
6. **Górecki J., Malujda I., Talaśka K., Kukla M., Tarkowski P.** (2016), Influence of the Value of Limit Densification Stress on the Quality of the Pellets During the Agglomeration Process of CO_2, *Procedia Engineering*, 136, 269-274.
7. **Li M., Liu W., Qing X., Ye Y., Liu L., Tang Z. Wang H., Dong Y., Zhang H.,** (2016), Feasibility Study of a New Approach to Removal of Paint Coatings In Remanufacturing, *Journal of Materials Processing Technology*, 234, 102-112.
8. **Liu Y., Calvert G., Hare C., Ghadiri M., Matusaka S.** (2012), Size measurement of dry ice particles produced form liquid carbon dioxide, *Journal of Aerosol Science*, 48, 1-9.
9. **Liu Y., Hirama D., Matusaka S.** (2012), Particle removal proces during alication of impinging dry ice jet, *Powder Technology*, 2017, 607-613.
10. **Liu Y., Maruyama H., Matsusaka S.** (2010), Agglomeration process of dry ice particles produced by expanding liquid carbon dioxide, *Advanced Powder Technology*, 21, 652-657.
11. **Malczewski J.** (1992), *Mechanic of bulk materials, unit operations* (in polish), Warsaw, OWPW.
12. **Masa V., Kuba P.** (2016) Efficient use of compressed air for dry ice blasting, *Journal of Cleaner Production*, 111, 76-84.
13. **Mazzoldi A., Hill T., Colls J.** (2008), CO_2 transportation for carbon capture and storage: Sublimation of carbon dioxide from a dry ice bank, *International Journal of Greenhouse Gas Control*, 2, 210-218.
14. **Otto C., Zahn S., Rost F., Zahan P., Jaros D., Rohm H.,** (2011) Physical Methods of cleaning and Disinfection of Surfaces, *Food Engineering Review*, 3, 171-188.
15. **Patent application** No. P.419432, Piston assembly designed for dry ice snow compression, Polish Patent Office, Poland.
16. **Spur G., Uhlmann E., Elbing F.** (1999), Dry-ice blasting for cleaning: process, optimization and alication, Wear, *233–235*, 402–411.
17. **Uhlmann E., Kretzschmar M., Elbing F., Mihotovic V.** (2010), *Deburring with CO_2 Snow Blasting*, In: Aurich J., Dornfeld D. (eds) Burrs - Analysis, Control and Removal. Springer, Berlin, Heidelberg.
18. **Vansant J.,** (2013), *Carbon dioxide emission and merchant market in the European union*, In Aresta M. (eds) Carbon Dioxide Recovery and Utilization, Springer Science & Business Media.
19. **Witte A., Bobal M., David R., Blattler B., Schoder D. Rossmanith P.** (2017), Investigation of the potential of dry ice blasting for cleaning and disinfection in the food production environment, *LWT - Food Science and Technology*, 75, 735-741.
20. **Yamaguchi H., Niu X., Sekimoto K., Neksa P.** (2011), Investigation of dry ice blockage in an ultra-low temperature cascade refrigeration system using CO_2 as a working fluid, *International Journal of Refrigeration*, 34, 466-475.

DE GRUYTER
OPEN

DOI 10.1515/ama-2017-0049 acta mechanica et automatica, vol.11 no.4 (2017)

SIMULATION OF PROCESSES OCCURRING IN THE EXTRUSION HEAD USED IN ADDITIVE MANUFACTURING TECHNOLOGY

Artur PRUSINOWSKI*, Roman KACZYŃSKI*

*Faculty of Mechanical Engineering, Białystok University of Technology, 45C Wiejska Street, 15-351 Białystok, Poland

prusinowskiart@gmail.com, r.kaczynski@pb.edu.pl

received 6 June 2017, revised 5 December 2017, accepted 11 December 2017

Abstract: The purpose of this research is unsatisfactory state of knowledge of the abrasive wear of composites with thermoplastic polymer as matrix material and reinforcing material in the form of short and focused carbon fibers that can be used in additive manufacturing technologies. The paper presents a conceptual design of an extrusion head used in Fused Deposition Technology, which allows for the implementation of appropriately stacked fibers at the level of detail production. Finite element simulation was performed to simulate the thermal effect of the system to demonstrate the effect of head cooling on the system. The assumed extrusion temperature of the material was obtained at a uniform nozzle temperature and stable temperature of the entire system. Flow simulation of thermoplastic polymer was carried out in the designed extrusion nozzle. By supplying 0.5 mm wire of 1.75 mm diameter thermoplastic material to the nozzle, the extrusion rate was 0.192 m/s. The proper design of the extrusion head for the intended applications has been demonstrated and the purpose of further research in this field has been confirmed.

Key words: Additive Manufacturing, Fused Deposition Modelling, FEM Analysis, RFPC

1. INTRODUCTION

Additive manufacturing technologies are one of the main pillars of techniques related to Rapid Prototyping. Thanks to the constantly growing range of additive manufacturing methods and an ever-expanding number of available building materials it is possible to perform more and more specialized engineering details. Each manufacturing technology is characterized by some unique materials and components. One of the most widespread methods is Fused Deposition Modeling (FDM). It involves extrusion through a heated die of thermoplastic material and precisely laying it in the work space layer by layer until it reaches full detail.

Polymeric materials are widely used in many industries, among others in aviation and automotive because of the favorable weight to strength ratio of the components. It is possible to broaden the scope of possible application by using composite fiber reinforced composite polymers arranged in a non-accidental manner. Currently there is a shortage of composite plastics with uniformly oriented short fiber reinforcements that can be used in manufacturing devices using Additive Manufacturing. The development of this branch of materials will perform elements more resistant to wear than currently available. Carbon fiber reinforced polymer composites allow for high abrasion resistance while maintaining a low weight of the system.

The tensile strength of the detail made on FDM polymer composite with continuous carbon fiber has shown a significant increase in mechanical properties compared to polymeric material without fiber additions (Gardner et al., 2016). The study of wear of polymer composites with metal oxide additives (Boparai et al., 2016) showed a visible relationship between abrasion resistance and reinforcing additives of the composite. Lee and Huang (2013) fatigue analysis showed a significant effect of the layering of the material and its orientation relative to the main axis of the analysed parts on the strength values of the components. Abrasive wear of various polymers has been investigated - both for sliding friction and for rolling friction (Harrass et al., 2010), as well as the effect of temperature on abrasive wear on materials (Zhao et al., 2015).

Studies on the mechanisms of wear of polymer composites reinforced with carbon fibers (Kaczynski et al., 2014) indicate the important role of these materials in the production of elements working in different environments (Wilczewska and Kaczynski, 2009). Comparative studies on abrasive wear of vinyl matrix and carbon fiber reinforcements and polymeric copolymers with identical matrix material and fiberglass additives (Suresha et al., 2009) have been performed to show better properties of carbon fiber composites. The results of a study conducted by Kumar and Panneerselvam (2016) on abrasive wear in polymer composites based on Nylon 6 with different percent fiberglass showed a significant increase in abrasion resistance with increasing fiber content in the composite. Studies on polymer composites (Akinci et al., 2014) have shown a significant increase in abrasion resistance at various test speeds (Aigbodion et al., 2015). In addition, studies (Wenzheng et al., 2015) have shown the relationship between FDM filamentation and the strength properties of manufactured parts

At the same time, there is no in-depth research on the processes of wear of composite materials with oriented arrangement of fibers used in additive manufacturing technologies.

The authors devoted particular attention to the design of the FDM design with the possibility of application of short carbon fibers arranged in a targeted manner. Flow simulation of the ma-

DOI 10.1515/ama-2017-0049

trix material through the extrusion nozzle and thermal analysis of the system under various cooling conditions was performed. The presented results confirm the possibility of achieving the desired properties of the element by applying a suitable construction of the embossing head to the integrated feeders of the building materials. This will allow the targeted reinforcement fibers of a suitable length of the entire range of plastic having thermoplastic properties.

2. DESIGN OF EXTRUSION HEAD

2.1. Design assumptions

The main task facing the extrusion head in the incremental manufacturing apparatus is to obtain a strictly controlled flow of the building material, maintain the appropriate temperature and extrusion speed of the material, which determines the appropriate engagement of the subsequent layers and surface of the workpiece according to the requirements. The designed device should have a compact design and low weight due to the high acceleration generated in this type of manufacturing machine.

The authors have assumed that the designed head should be able to be installed on most FDM printing machines using a suitably complex control system for the entire device. This will allow the use of polymeric materials in the standard filament format used in FDM machines.

2.2. Matrix material

Correct selection of the matrix material in the composite polymer used in FDM technology allows to obtain a satisfactory mechanical property performed. Inappropriate selection of the used material can lead to premature degradation of the workpiece or lack of characteristic features.

Another factor influencing the choice of the appropriate material is its availability on the market in the form of a filament with fixed and well-defined diameter. This allows uncomplicated and precise dosing of the feed material. This also minimizes the cost of parts production due to the use of widely available materials.

Tab. 1. Materials used in FDM printing technology

Material	Melting temp. [℃]	Density g/cm^3	Abrasion resistance	Avaliable on the market
ABS	210 – 240	1.05	Good	Very Good
PLA	180 – 205	1.1	Poor	Very Good
Nylon PA66	240 – 260 (270)	1.14	Very Good	Good
HDPE	170 – 190	0.965	Good	Average

Tab. 1 shows one of the most commonly used FDM materials. It is evident that to achieve the proper model properties, the printhead must reach a temperature of 250 degrees Celsius. For further simulations, high density polyethylene (HDPE) and acrylonitrile-butadiene-styrene copolymer (ABS) were used as the matrix material.

2.3. Extrusion head model

Project extrusion head adapted to application-oriented reinforcement in the form of short carbon fiber was made in SolidWorks 2016. Fig. 1 shows the main elements included in the designed layout and its overall dimensions.

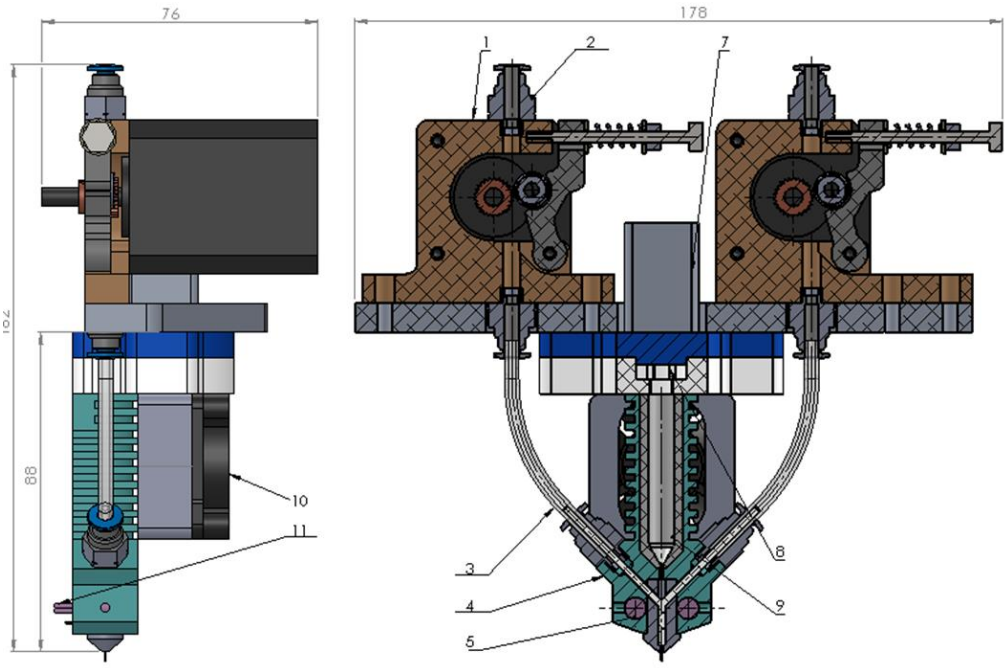

Fig. 1. Schematic Drawing of an Extrusion Head for use in FDM Technology

Building material in the form of a filament having a diameter of 1.75 mm passes through the plug-in connection – 2 – and then is drawn through the material feed roller – 1. The filament enters between a pinion gear mounted on the stepper motor shaft and

DOI 10.1515/ama-2017-0049

a bearing with a profiled outer race acting as a pressing element. This allows for a precise control of the amount of material fed with no slippage between the active elements. Then the material is carried out by Teflon tube – 3 – and reaches the base of the head – 4 . This detail serves as a basis for embedding further components and serves as a heatsink for the entire system. This prevents heat transfer to the top of the head and overheating of the precision stepper motors. The material hitting the nozzle – 6 – has the optimum temperature by heating the heating resistors arranged symmetrically – 5.

The head base is cooled by blowing air at ambient temperature caused by the fan – 10 – from a specially shaped cooling channel. This eliminates the phenomenon of excessive heat convection to the upper part of the head where there are stepper motors. In addition, it prevents premature plasticization of the material which could lead to the folding of the filament and, consequently, clogging of the head. The temperature of the extrusion nozzle is monitored by a thermistor – 11 – placed in direct contact with the nozzle. Control of the operation of the heating resistors is done by a computer with special software and a PID controller that minimizes temperature fluctuations.

Short carbon fiber sections are placed in the intermediate container – 9 – through the rotary feeder – 8. On the output shaft of the stepper motor – 7 – is mounted rack and pinion fiber storage. This system is designed to accurately control the amount of reinforcement fed to the composite. It also allows the administering of fibers only in the places where this is necessary and results from the operating conditions of the part produced which results in reduced use of expensive reinforcing material.

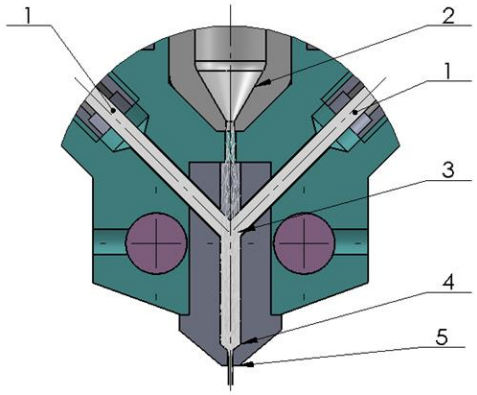

Fig. 2. Extrusion process of fiber reinforced composite from nozzle

Fig. 2 shows an extrusion nozzle fixed in the base of the head and heated with two heating elements. Extrusion head has two transport channels – 1 – arranged symetrically in relation to the composite extrusion axis feeding the thermoplastic material to the nozzle. Channel – 2 – is supplied with reinforcement fibers. In point – 3 – matrix material and fibers are mixed. At a short distance – 4 – from the nozzle exit, the fibers are set at the correct deviation. Properly selected geometric features of the nozzle output – 5 – opening ensure the alignment of the reinforcement fibers in the output material with a deviation from the extrusion axis by up to 20 degrees.

The head extrudes the circular cross section at the outlet due to the difficulty of producing nozzles with other output cross sections in the nozzle dimensions. The additional advantage of this cross sectional shape is the fact that Barus effect has been avoided by swirling the polymer stream leaving the head.

The authors used a symmetrical construction of the head and a doubling of the most important elements of the head because of the need to properly position the carbon fibers in the extruded material. Bringing both sides of the matrix material allowed for correcting the set of short fibers on one wall of the nozzle.

3. HEAD FEM ANALYSIS

Computer simulations made by the authors were aimed at demonstrating the rationality of the proposed head design and finding possible locations for improvement. Two types of simulation were performed: thermal simulation of the head during operation and flow of the matrix material through the extrussion nozzle. In both cases, the correct behavior of the system can be observed.

3.1. Thermal analysis

As part of the work, the authors performed a thermal simulation of the extrusion head. As the building material passing through the analyzed system, ABS was chosen because of the high plasticity temperature of up to 240 degrees Celsius, which is about 513.2 degrees Kelvin scale. It has been assumed that the components will be made of Aluminum PA6, Teflon, ABS and HSS tool steel.

SolidWorks 2016 software with Flow Simulation module was used to simulate the behavior of a heat treated element under normal conditions of use.

Two types of simulation were performed: without external cooling of the head base and with an external air flow directed at the head corresponding to the amount of air conveyed by a standard computer fan of these dimensions. This allowed us to check the suitability of the forced air flow in the head cooling.

Simulation time adopted in both cases is 300 seconds. Numerical analysis of simulated and experimental similar systems shows that after this time can be assumed that the system is in thermal equilibrium.

Two heat sources were installed at the locations of the heating elements. On both cylindrical surfaces, a constant temperature of 493.2 degrees Kelvin was applied which corresponds to the average actual temperature value needed to start the extrusion process for the material. The ambient temperature of the model during its operation was determined to be a constant value of 293.2 degrees Kelvin.

The model was simplified before simulations, which allowed for a significant reduction in numerical calculations. Due to the reduction of the stepper motors model, the authors have assumed that the safe value for the entire system measured at the top of the connecting plate is 380 K.

Fig. 3 shows the resulting temperature pattern in the embossing head after 300 seconds of simulation with two 493 K heat sources and without forcing the air circulation around the head radiator. It is evident uniform heating of the extrusion nozzle and its surroundings. With the distance from the heat source temperature is getting lower. The drop in temperature on the other ribs of the heat sink is noticeable.

A heat of 404.4 K. was provided to the upper connecting element of the designed head. This value is unacceptable because it results in higher temperature stepper motors which are particularly sensitive to improper temperature.

DOI 10.1515/ama-2017-0049

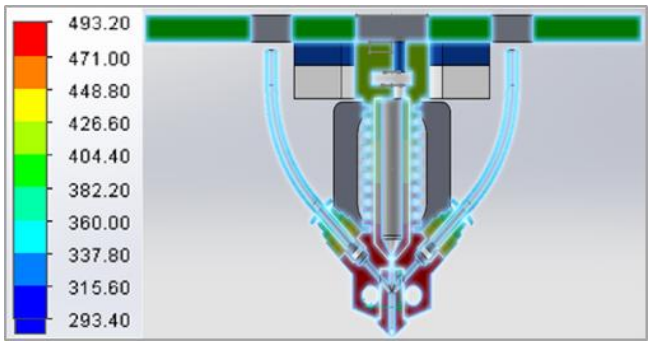

Fig. 3. Results of thermal analysis without external cooling

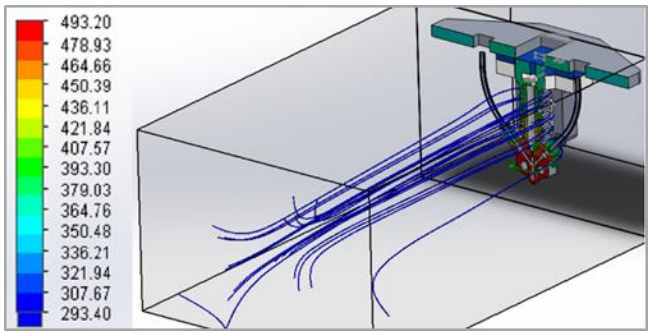

Fig. 4. Forced air flow stabilizing temperature of the extrusion head

In the second thermal simulation of the extrusion head, a cooling air flow was used to reduce the temperature in the upper part of the system. Other boundary conditions (e.g. heating surface temperature, material data) remained unchanged compared to the first simulation. Fig. 4 shows a simulated flow of air through the finned portion of the base of the head. The air flow rate was set at $Q = 8.0 \times 10^{-5}$ kg / s which corresponds to the value obtained from this type of fan. A temperature constant value of 293.4 K cooling air was adopted.

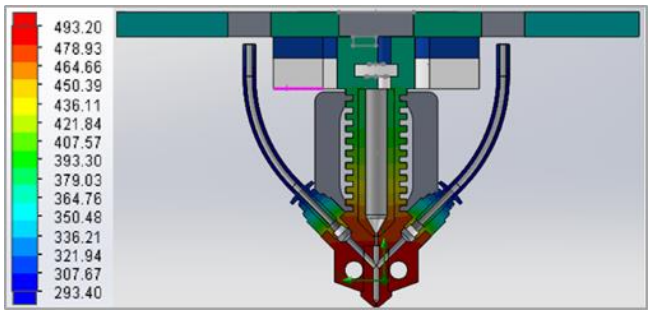

Fig. 5. Results of thermal analysis with additional cooling of the air stream

The temperature distribution of the system during simulation with additional cooling is shown in Fig. 5. As can be seen in the previous example, here also a homogeneous temperature field in the extrusion nozzle corresponding to the temperature emitted by the heat source is visible. It is easy to see that the system components are lower in temperature compared to the non-cooling system. The temperature of the upper connection plate is about 364 K which the authors have accepted for content that is satisfactory and safe for the operation of the whole system. In addition, the extruded material does not pass prematurely to the plastic state, which prevents clogging of the head and allows for proper properties.

3.2. Material flow analysis

As the second type of simulation performed, the authors adopted a simulated flow of building material through the designed extrusion nozzle. The material analyzed was high density polypropylene HDPE. Simulations were carried out using ANSYS R17.0 with Polyflow add-in dedicated for the extrusion and injection molding of materials.

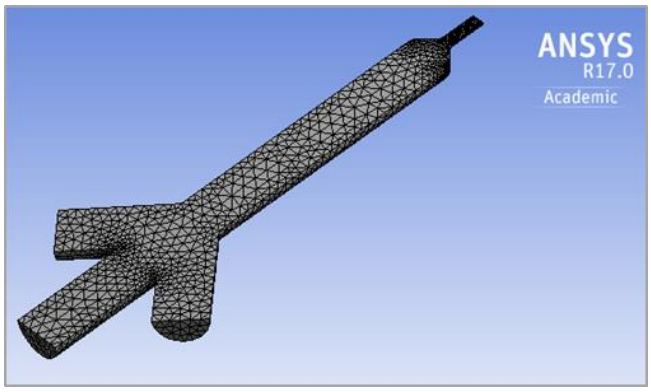

Fig. 6. Finite element mesh of extrusion nozzle flow channels

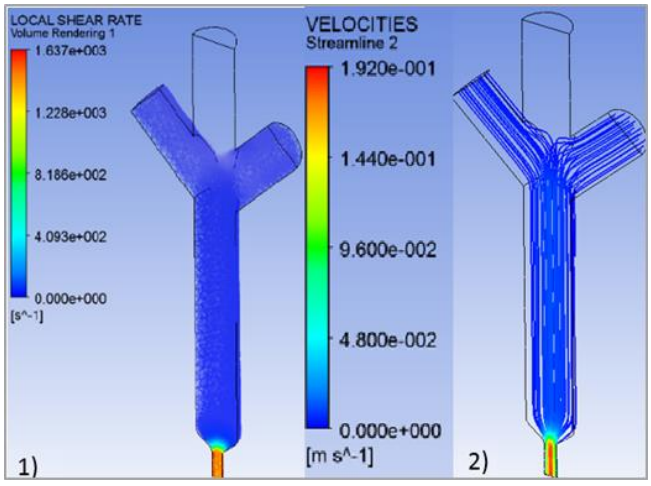

Fig. 7. Results obtained: 1) local shear rate and 2) velocity of extruded material

Fig. 6 shows the object on which the authors have studied the flow occurring in the head designed. This is the outline of the flow channels in the item. In order to shorten the computation time, a symmetry plane of the entire system is used.

On both sides of the nozzle is feeding a suitable temperature building material, while the central inlet channel is fed short carbon fibers. The outlet diameter of the system has a diameter of 0.4 mm. This value allows the behavior of the respective dimensional accuracy of the workpiece at an acceptable time of manufacturing an object.

As one of the assumptions for the simulation is that the volumetric flow rate for both inputs of the circuit is equal and is 4.8106×10^{-9} m^3/s. This value corresponds to the actual case of feeding on each side of a 0.5 mm filament segment of 1.75 mm

DOI 10.1515/ama-2017-0049

diameter in 1 second. In the simulation flow rate at the contact of the building material wall $v = 0$ m^3/s and the free flow of the material from the nozzle.

The results obtained by the authors are shown in Fig. 7. On the left side – subsection 1, the local shear rate of polymer material in the designed nozzle was determined. It is evident that at the upper part of the system no distinct velocity difference in material layers is evident. At the point of narrowing of the nozzle and passing into the final extrusion profile, it is clear that the local shear rate is significantly increased.

The velocity of extrusion of the building material from the nozzle is shown in Fig. 7, subsection 2. The flow of material is undisturbed. Extruded polymeric material shows no signs of stacking. The velocity of polymer material at the output of the head is 0.192 m / s which corresponds to the values obtained in such extruders used in Fused Deposition Modeling technology. This shows that the correct simulation conditions and the design of the head and nozzle are correct.

4. CONCLUSIONS

The authors have presented a design of a Fused Deposition Modeling extrusion head in which it is possible to add composite reinforcement in the form of targeted short carbon fibers at the manufacturing stage of the model. The described method allows for quick and trouble-free change of both matrix and reinforcement material without the need for material expenditure and time losses. It offers the possibility of obtaining a wide variety of components for the study of different pairs of composite plastic reinforcement in the form of fibers.

Simulations have shown the extrusion head components, the correctness of the structure and the validity of further work on this subject. The assumed extrusion temperature of the material was obtained at a uniform nozzle temperature and stable temperature of the entire system. Flow simulation of thermoplastic polymer was carried out in the designed extrusion nozzle.

It is planned to create a prototype of an extrusion head and to produce samples for research on wear mechanisms of composite polymer materials with targeted fiber reinforcement produced on Additive Manufacturing devices.

REFERENCES

1. **Aigbodion V.S., Hassan S.B., Agunsoye J.O.** (2012), Effect of bagasse ash reinforcement on dry sliding wear behaviour of polymer matrix composites, *Materials and Design*, 33, 322-327.
2. **Akinci A., Sen S., Sen U.,** (2014), Friction and wear behaviours of zirconium oxide reinforced PMMA composites, *Composites Part B: Engineering,* 56, 42-47.
3. **Boparai K.,Singh R., Singh H.** (2016), Wear behavior of FDM parts fabricated by composite material feed stock filament, *Rapid Prototyping Journal*, 22(2), 350-1357.
4. **Gardner J., Sauti G., Kim J., Cano R., Wincheski R., Stelter C., Grimsley B., Working D., Siochi E.** (2016), 3-D printing of multifunctional carbon nanotube yarn reinforced components, *Additive Manufacturing*, 12, 38–44.
5. **Harrass M., Friedrich K., Almajid A.A**. (2010), Tribological behavior of selected engineering polymers under rolling contact, *Tribology International*, 43, 635-646.
6. **Kaczyński R., Wilczewska I., A. Sfiridienok** (2014) Peculiarities of the wear mechanism of polymers reinforced with unidirectional carbon fibers, *Friction and Wear,* 35(6), 449-454.
7. **Kumar S., Panneerselvam K.** (2016), Two-body Abrasive Wear Behavior of Nylon 6 and Glass Fiber Reinforced (GFR) Nylon 6 Composite, *Procedia Technology*, 25, 1129-1136.
8. **Lee J., Huang A.** (2013), Fatigue analysis of FDM materials, *Rapid Prototyping Journal*, 19, 291-299.
9. **Suresha B., Kunigal N., Kumar S.,** (2009), Investigations on mechanical and two-body abrasive wear behaviour of glass/carbon fabric reinforced vinyl ester composites, *Materials & Design*, 30, 2056-2060.
10. **Wenzhueng W., Peng P., Guiwei L., Di Z., Haibo Z., Ji Z.,**(2015), Influence of layer thickness and raster angle of mechanical properties of 3D- printed PEEK and a comperative mechanical study between PEEK and ABS, *Materials*, 8(9), 5834-5846.
11. **Wilczewska I., Kaczyński R.,** (2009), Identification of friction and wear parameters of carbon fiber polymers in diferent working environments - in Polish, *Acta Mechanica et Automatica*, 3(2), 106-110.
12. **Zhao G., Hussainova I., Antonov M., Wang Q., Wang T., Yung D.L**. (2015), Effect of temperature on sliding and erosive wear of fiber reinforced polyimide hybrids, *Tribology International*, 82, 525-533.

DE GRUYTER
OPEN

DOI 10.1515/ama-2017-0050

DISPLACEMENT ANALYSIS OF THE HUMAN KNEE JOINT BASED ON THE SPATIAL KINEMATIC MODEL BY USING VECTOR METHOD

Marta GÓRA-MANIOWSKA[*], **Józef KNAPCZYK** [*,**]

[*]Cracow University of Technology, Al. Jana Pawła II 37 b, 31-864 Kraków, Poland
[**]State Higher Vocational School, ul. Staszica 1, 33-300 Nowy Sącz, Poland

mgora@mech.pk.edu.pl

received 6 June 2015, revised 7 December 2017, accepted 11 December 2017

Abstract: Kinematic model of the human knee joint, considered as one-degree-of-freedom spatial parallel mechanism, is used to analyse the spatial displacement of the femur with respect to the tibia. The articular surfaces of femoral and tibia condyles are modelled, based on selected references, as spherical and planar surfaces. The condyles are contacted in two points and are guided by three ligaments modelled as binary links with constant lengths. In particular, the mechanism position problem is solved by using the vector method. The obtained kinematic characteristics are adequate to the experimental results presented in the literature. Additionally, the screw displacements of relative motion in the knee joint model are determined.

Key words: Human Knee Joint Model, Kinematic Analysis, Parallel Mechanism, Constraint Equations, Vector Method

1. INTRODUCTION

The human knee joint (Fig. 1) provides a large relative movement of two bones (femur and tibia) that are constrained to remain in contact at two points and guided with three ligaments (ACL - anterior cruciate ligament, MCL – medial collateral ligament and PCL – posterior cruciate ligament), as mentioned in Sancisi, Parenti-Castelli (2010), Parenti-Castelli and Di Gregorio (2000) and Góra (2008). The knee is important in daily living activities and because of the high incidence of injuries and diseases involving this joint, which considerably affect locomotion. Restoration of normal knee joint function and range of motion, as pursued by reconstructive surgery and rehabilitation, can be achieved by re-establishing the natural relationship between the geometrical shape of the articular surfaces and the geometry of the ligaments, as presented in Woo et al. (2006). Kinematic models of the knee joint are very useful for defining diagnostic procedures, for pre-surgical planning, for functional assessment after knee surgery, and for designing prosthetic replacement devices.

Kinematic models presented as equivalent mechanisms (M1 – planar, M2 – spherical or M3 - spatial), with one degree of freedom (1-dof), can be used to analyse the relative motion of the femur with respect to the tibia, give in Parenti-Castelli and Di Gregorio (2000) and Sancis and Parenti-Castelli (2010). The considered mechanism contains two nonsymmetrical platforms (the femur and the tibia) with two contact points and four legs (ACL, PCL, MCL and PF- patella-femoral joint).The passive motion of the tibia-femoral joint (TF) is not constrained from that of patella-femoral chain if knee flexion is externally imposed. Thus the two sub-joints (TF an PF) of the knee can be analysed separately and in particular, tibio-femoral joint (with one degree-of-freedom) can be used to replicate the passive motion without taking patella-femoral (PF) joint into consideration. Since no loads are applied to the joint during passive motion, the muscles remain inactive, they do not guide the knee and, as a consequence, they are not considered in this study.

It has been observed that three ligaments (ACL, PCL and MCL) can be considered as isometric fibres (or cables) during the flexion of the unloaded knee. Thus, three ligaments are modelled as binary links, each connected to the tibia and femur by a spherical joint. The other bundles are not tight and reach the limit between laxity and tension at the most. As a consequence, only isometric bundles guide the passive motion of the knee, while the others can be ignored in the model.

More recent studies concern a knee joint modelling taking into account elasticity in ligaments, like in Sancisi and Parenti-Castelli (2011) or in Saldias et al. (2013).

Synthesis task, where for given functional characteristics wanted are selected dimensions of knee joint model, seems to be the most challenging. Innovative approaches are presented in Parenti-Castelli and Sancisi (2013) or in Saldias et al (2014).

The present paper aims to enhance the knowledge of knee joint mobility by equivalent 1-dof spatial mechanism, based on the knee model proposed in Parenti-Castelli and Di Gregorio (2000) and Sancisi (2013) and applied in Di Gregorio and Parenti-Castelli (2003). The surfaces of the femur and tibia condyles are modelled by rigid spherical and planar in point contact with one another. In particular, the scope was to use vector method, given in Morecki et al. (2002), to analyse position and displacement of the femur with respect to the tibia, and the path of the instantaneous screw axis.

2. FORMULATION OF KINEMATIC MODEL

Kinematic model (M3) of knee joint based on the measurement results from Parenti-Castelli and Di Gregorio (2000) was

DOI 10.1515/ama-2017-0050

used to analyse the relative position and displacement of the femur with respect to the tibia. There are two frames (Fig. 1) base reference system {*xyz*} embedded in the tibia and reference system {$x^by^bz^b$} fixed to the femur.

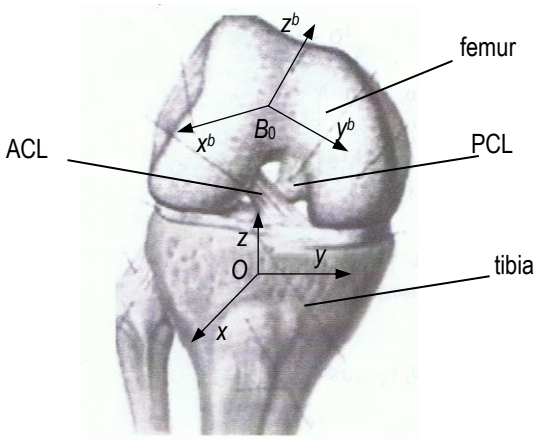

Fig. 1. Schematic anterior view of the knee in flexion (Woo et al., 2006)

The points A_i (i = 1, 2, 3) denote the centres of the joints, modelling the ligament insertions into the tibia; $\mathbf{a}_i$ – the position vector of point A_i with respect to the origin of the system{*xyz*}. The points B_i (i = 1, 2, 3) denote the centres of joints, modelling the ligament insertions into the femur and $\mathbf{b}_i^b$ – the position vector of the point B_i with respect to the origin of the system {$x^by^bz^b$}, $\mathbf{b}_i$ – the position vector with respect to the origin of the base system {*xyz*}. The respective relation is described by using the formula:

$$\mathbf{b}_i = \mathbf{b}_0 + \mathbf{R}^b\mathbf{b}_i^b, \qquad i = 1, 2, 3 \tag{1}$$

where $\mathbf{b}_0$ – position vector of point B_0 assumed as the origin of coordinate system {$x^by^bz^b$}, $\mathbf{R}^b$ – orientation matrix of the system {$x^by^bz^b$} with respect to the system {*xyz*}.

The position and displacement analysis of the spatial mechanism can be accomplished in the following way. The sphere surfaces are removed from contact points with the planes π_j (j = 4, 5) and the sphere centres B_j (j = 4, 5) are treated as coupler points of the transformed mechanism. The position of this mechanism (now with three degree of freedom) is described by three angles ϕ_i (i = 1, 2, 3), shown in Fig. 2, which can be treated as additional independent variables, with values to be find from closure equations. The position vectors $\mathbf{b}_4$ and $\mathbf{b}_5$ of the platform points B_4 and B_5 can be found using the vector method described below, and their respective distances from the planar surfaces (π_4, π_5) can be described as functions of ϕ_i giving the closure equations of the mechanism, as described below.

Since the sphere slides on the plane π_j (j = 4, 5) its centre point B_j (j = 4, 5) always belongs to a parallel plane and is located at a distance equal to the radius r_j. These conditions can be written, as in Sancisi, Parenti-Castelli (2010) [10] and Parenti-Castelli, Di Gregorio (2000) [5] and Góra (2008) [2], as follows:

$$F_j(\phi_1, \phi_2, \phi_3) = ||\mathbf{b}_j - \mathbf{o}_j|| - r_j = 0, \quad j = 4, 5 \tag{2}$$

$$F_j(\phi_1, \phi_2, \phi_3) = n_{jx}(b_{jx} - x_j) + n_{jy}(b_{jy} - y_j) + n_{jz}(b_{jz} - z_j) = 0 \quad j = 4, 5 \tag{3}$$

where: $\hat{\mathbf{n}}_j = [n_{jx}, n_{jy}, n_{jz}]^T$, $\mathbf{b}_j = [b_{jx}, b_{jy}, b_{jz}]^T$, $\mathbf{o}_j = [x_j, y_j, z_j]^T$,

$\mathbf{b}_j$ – position vector of point B_j (j = 4, 5), i.e. curvature centre of femur condyle surface described in the system {*xyz*};

$\hat{\mathbf{n}}_j$ – unit vector as the normal to the plane π_j,

$\mathbf{o}_j$ – position vector of the plane point O_j ($O_4 \in \pi_4$, $O_5 \in \pi_5$), described in the system {*xyz*} (tibia).

Additional angles ϕ_1, ϕ_2, ϕ_3 (Fig. 2) are defined respectively as the angles between the pairs of unit vectors: $(\hat{\mathbf{a}}_{21}, \hat{\mathbf{d}}_2)$, $(\hat{\mathbf{a}}_{23}, \hat{\mathbf{d}}_2)$ and $(-\hat{\mathbf{a}}_{21}, \hat{\mathbf{d}}_1)$, where:

$$\begin{aligned} &\mathbf{d}_1 = \mathbf{b}_1 - \mathbf{a}_1, \ \mathbf{d}_2 = \mathbf{b}_2 - \mathbf{a}_2, \\ &\mathbf{a}_{21} = \mathbf{a}_1 - \mathbf{a}_2, \ \mathbf{a}_{23} = \mathbf{a}_3 - \mathbf{a}_2, \\ &\mathbf{b}_{21} = \mathbf{b}_1 - \mathbf{b}_2, \ \mathbf{b}_{23} = \mathbf{b}_3 - \mathbf{b}_2, \\ &\mathbf{d}_{12} = \mathbf{b}_2 - \mathbf{a}_1, \ \mathbf{d}_{21} = \mathbf{b}_1 - \mathbf{a}_2. \end{aligned} \tag{4}$$

The general formula for finding one of three unit vectors can be treated as a subroutine used to calculate unknown unit vector $\hat{\mathbf{w}}$, when two unit vectors ($\hat{\mathbf{u}}$ and $\hat{\mathbf{v}}$) and two dot products of each these vectors with the unknown unit vector $\hat{\mathbf{w}}$ ($\hat{\mathbf{u}}\cdot\hat{\mathbf{w}}, \hat{\mathbf{v}}\cdot\hat{\mathbf{w}}$) are known. The unknown unit vector $\hat{\mathbf{w}}$ is determined by formula, given in Morecki et al. (2002):

$$\hat{\mathbf{w}} = [((\hat{\mathbf{u}}\cdot\hat{\mathbf{w}}) - (\hat{\mathbf{u}}\cdot\hat{\mathbf{v}})(\hat{\mathbf{v}}\cdot\hat{\mathbf{w}}))\hat{\mathbf{u}} + ((\hat{\mathbf{v}}\cdot\hat{\mathbf{w}}) - (\hat{\mathbf{u}}\cdot\hat{\mathbf{v}})(\hat{\mathbf{u}}\cdot\hat{\mathbf{w}}))\hat{\mathbf{v}} \pm \pm (\hat{\mathbf{u}}\times\hat{\mathbf{v}})\sqrt{D}\,](((1-(\hat{\mathbf{u}}\cdot\hat{\mathbf{v}}))(1+(\hat{\mathbf{u}}\cdot\hat{\mathbf{v}})))^{-1}$$

where

$$D = 1 - (\hat{\mathbf{u}}\cdot\hat{\mathbf{v}})^2 - (\hat{\mathbf{u}}\cdot\hat{\mathbf{w}})^2 - (\hat{\mathbf{v}}\cdot\hat{\mathbf{w}})^2 + 2(\hat{\mathbf{u}}\cdot\hat{\mathbf{v}})(\hat{\mathbf{u}}\cdot\hat{\mathbf{w}})(\hat{\mathbf{v}}\cdot\hat{\mathbf{w}})$$

By using this formula the following unit vectors can be determined in the specified order: $\hat{\mathbf{d}}_2, \hat{\mathbf{d}}_1, \hat{\mathbf{b}}_{23}, \hat{\mathbf{b}}_{24}, \hat{\mathbf{b}}_{25}, \hat{\mathbf{b}}_0$.

The position vectors $\mathbf{b}_m$ (m = 0, 1,...5) of points B_m are described in the base system {*xyz*}. The solution procedure for determining the position vectors $\mathbf{b}_m$ of the femur points in the base system is presented in Tab. 1.

Tab. 1. The following steps of the solution procedure for the direct position problem by using vector method

Step	$\hat{\mathbf{u}}$	$\hat{\mathbf{v}}$	$\hat{\mathbf{w}}$	$\mathbf{b}_m$
1	$\hat{\mathbf{a}}_{21}$	$\hat{\mathbf{a}}_{23}$	$\hat{\mathbf{d}}_2$	$\mathbf{b}_2(\phi_1,\phi_2) = \mathbf{a}_2 + d_2\hat{\mathbf{d}}_2$
2	$\hat{\mathbf{a}}_{12}$	$\hat{\mathbf{d}}_{12}$	$\hat{\mathbf{d}}_1$	$\mathbf{b}_1 = \mathbf{a}_1 + d_1\hat{\mathbf{d}}_1$
3	$\hat{\mathbf{b}}_{21}$	$-\hat{\mathbf{d}}_{32}$	$\hat{\mathbf{b}}_{23}$	$\mathbf{b}_3 = \mathbf{b}_2 + b_{23}\hat{\mathbf{b}}_{23}$
4	$\hat{\mathbf{b}}_{21}$	$\hat{\mathbf{b}}_{23}$	$\hat{\mathbf{b}}_{24}$	$\mathbf{b}_4 = \mathbf{b}_2 + b_{24}\hat{\mathbf{b}}_{24}$
5	$\hat{\mathbf{b}}_{21}$	$\hat{\mathbf{b}}_{23}$	$\hat{\mathbf{b}}_{25}$	$\mathbf{b}_5 = \mathbf{b}_2 + b_{25}\hat{\mathbf{b}}_{25}$
6	$\hat{\mathbf{b}}_{23}$	$\hat{\mathbf{b}}_{24}$	$\hat{\mathbf{b}}_0$	$\mathbf{b}_0 = \mathbf{b}_2 + b_0\hat{\mathbf{b}}_0$

The analysed range of the permissible displacements was divided into a finite number of discrete positions. The system of nonlinear equations (2) may be solved for two unknowns ϕ_2 and ϕ_3 assuming the selected value of ϕ_1.

On the basis of the algorithm described above a computer program in MATLAB was written. The solutions satisfied the geometrical conditions are used to determine the successive positions of the considered mechanism and the respective femur displacements as the function of the knee joint flexion angle. This algorithm can be also used for the parameter estimation procedure of the equivalent mechanism, for example to determine the coordinates of the ligament insertion points, that satisfied the correct mobility of the joint knee.

Marta Góra-Maniowska, Józef Knapczyk DOI 10.1515/ama-2017-0050

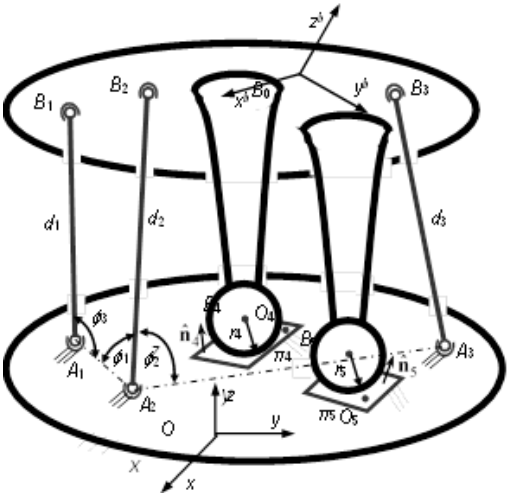

Fig. 2. Model of the knee joint. Notations: d_i (i=1, 2, 3) - isometric ligament modelled as binary link, with A_i – joint at the tibia, B_i – joint at the femur. The surfaces of the femur condyles are modelled by spherical (r_4 , r_5) surfaces and tibia condyles as planar (π_4 , π_5) surfaces in contact with one another. The coordinate system {xyz} is fixed to the tibia and the system {$x^by^bz^b$} is fixed to femur (Di Gregorio and Parenti-Castelli, 2003)

Position of the femur and its relative displacement with respect to the tibia, according to the model of the knee joint, can be described by using one input variable, for example flexion angle (α), like in Di Gregorio and Parenti-Castelli (2003). The solution for the position problem in the system {xyz} can be described by

- position vectors ($\boldsymbol{b}_m$, m = 0, 1,...5) of the femur points;
- position vector ($\mathbf{o}^b$) of the origin of the femur system;
- orientation matrix ($\mathbf{R}^b$) of the femur system with respect to the tibia system.

The femur orientation with respect to the tibia can be described by a sequence of three rotation angles: α – the flexion of the knee as the rotation angle around the y axis of the system {xyz}, β – rotation angle around the x axis, and γ – rotation angle around the z axis. In accordance with Parenti-Castelli and Di Gregorio (2000), the following yields:

$$\mathbf{R}^b = \mathbf{R}_z(-\gamma)\,\mathbf{R}_x(\beta)\,\mathbf{R}_y(\alpha) \tag{5}$$

Moreover these three angles are assumed equal to zero in the full extension configuration. The considered orientation matrix, defined in Di Gregorio and Parenti-Castelli (2003) and Parenti-Castelli and Di Gregorio (2000), has the following expression:

$$\mathbf{R}^b = \begin{bmatrix} c\alpha\, c\gamma + s\alpha\, s\beta\, s\gamma & c\beta\, s\gamma & c\gamma\, s\alpha - c\alpha\, s\beta\, s\gamma \\ c\gamma\, s\alpha\, s\beta - c\alpha\, s\gamma & c\beta\, c\gamma & -c\alpha\, c\gamma\, s\beta - s\gamma\, s\alpha \\ -c\beta\, s\alpha & s\beta & c\alpha\, c\beta \end{bmatrix} \tag{6}$$

where the following notation is used: $c = \cos$, $s = \sin$.

If the elements of the matrix (6) are known:

$$\mathbf{R}^b = \begin{bmatrix} l_x & m_x & n_x \\ l_y & m_y & n_y \\ l_z & m_z & n_z \end{bmatrix} \tag{7}$$

then the orientation angles can be calculated as follow:

$$\beta = \{\arcsin(m_z),\ \pi - \arcsin(m_z)\}$$

$$\alpha = \{\arcsin(-l_z/\cos\beta),\ \pi - \arcsin(-l_z/\cos\beta)\} \tag{8}$$

$$\gamma = \{\arcsin(m_x/\cos\beta),\ \pi - \arcsin(m_x/\cos\beta)\}$$

Equating the respective elements of the matrices (6) and (7) the values of the orientation angles (8) are calculated.

3. NUMERICAL EXAMPLES

The point coordinates and the link lengths of the knee joint model (Fig. 2), assumed as data according to Parenti-Castelli and Di Gregorio(2000), are given in Tab. 2 and 3.

Tab. 2. Coordinates of the vectors $\mathbf{a}_i$ described in the system {xyz}, $\mathbf{b}_j^b$ – in the system {$x^by^bz^b$}, the lengths d_i and r_j [mm]

i, j	$\mathbf{a}_i$	$\mathbf{b}_j^b$	d_i	r_j
1	$[-3\ \ 0\ \ 0]^T$	$[19.2; 16.9; 26.8]^T$	38.8	-
2	$[20.2\ \ 12.2\ \ -18.3]^T$	$[16.8; -6.5; 10.8]^T$	34.8	-
3	$[-11.4\ \ -2.4\ \ -53.6]^T$	$[8.2; -34.1; 13.8]^T$	77,0	-
4	-	$[5.1; -15.6; 19.1]^T$	-	24.6
5	-	$[3.0; 35.5; 27.1]^T$	-	30.3

Tab. 3. Coordinates of the vectors $\boldsymbol{o}_j$ and the unit vectors $\hat{\mathbf{n}}_j$ of the planes π_4, π_5 described in the system {xyz}

j	$\mathbf{o}_j$ [mm]	$\hat{\mathbf{n}}_j$ [-]
4	$[5.1\ -15.6\ 19.1]^T$	$[0.10\ \ -0.25\ \ 0.96]^T$
5	$[3.0\ \ 35.5\ 27.1]^T$	$[0.21\ \ \ 0.16\ \ \ 0.97]^T$

The position vectors $\boldsymbol{b}_m$ of the femur points calculated by using the algorithm presented in Table 1 are given in Tab. 4.

Tab. 4. Coordinates of the position vectors $\boldsymbol{b}_m$ of the femur points calculated for the determined values of additional angles

Additional angles	M	$\boldsymbol{b}_m$ [mm]
$\phi_1 = 45^o$	1	$[34.7;\ \ 8.2;\ \ 7.5]^T$
$\phi_2 = 101^o$	2	$[19.1; -15.1;\ \ 3.3]^T$
$\phi_3 = 51^o$	3	$[22.1; -43.6;\ \ 1.8]^T$
	4	$[28.9; -27.1; 11.2]^T$
	5	$[36.7;\ \ 20.9; 28.6]^T$
	0	$[\ 9.1;\ -14.3; 21.7]^T$

Orientation matrix of the femur system with respect to the base system, calculated by using the femur point coordinates is given by formula (7). The respective knee joint angles, calculated by using formula (8), are: α = 18^o, β = 1.2^o , γ = 2.5^o.

The femur pose with respect to the tibia is described by using the position vector $\mathbf{o}_k^b$ (k – number of poses) and the orientation matrix $\mathbf{R}_k^b$ dependent on the flexion angle as independent variable α_k (k = 1, …, n).

The determined coordinates of the system {$x^by^bz^b$} origin of the (femur) in relation to the flexion angle (α) are presented in Fig. 3. The obtained characteristics are compared to the simulation results from Parenti-Castelli and Di Gregorio (2000). The greatest displacement in z direction, reaching 17 mm, is adequate to the reference model curve from Parenti-Castelli and Di Gregorio (2000). The obtained characteristics of the knee displacements

DOI 10.1515/ama-2017-0050

in *x* and *y* directions have the same profiles but are biased by ca 1 mm with respect to the reference study.

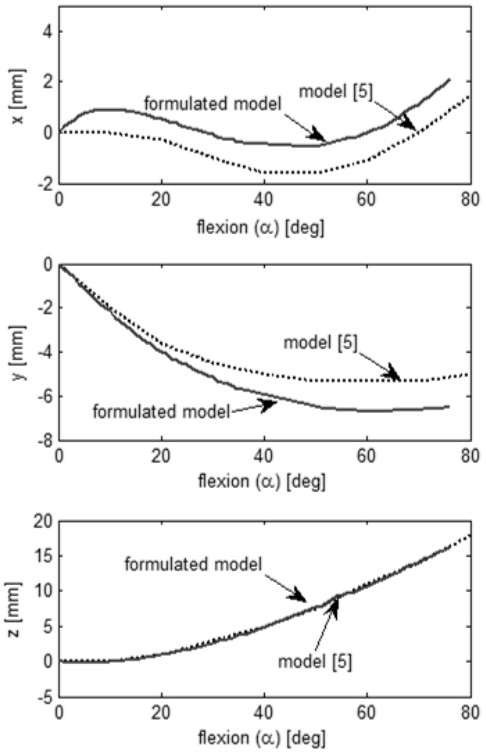

Fig. 3. The coordinates of the position vector $\boldsymbol{b}_0$ of the femur point B_0 in relation to the flexion angle α. Comparison of the own results with simulation from Parent-Castelli and Di Gregorio (2000)

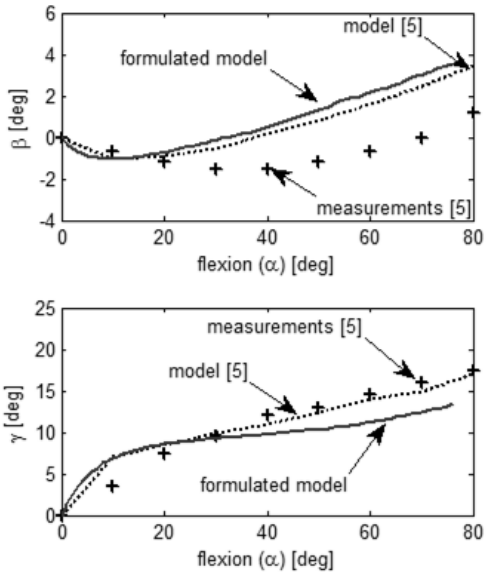

Fig. 4. Orientation angles (β and γ) of the femur with respect to the tibia in relation to the flexion angle (α). Comparison of the own results with simulation and meausurements from Parent-Castelli and Di Gregorio (2000)

The knee joint angles β and γ as functions of the flexion angle α are illustrated in Fig. 3. These characteristics, achieved by using the formulated knee model, are compared to the results from Parent-Castelli and Di Gregorio (2000) consititng of simulation and experimental results in Wilson et al. (1998). Generaly, the formulated model gives adequate results to the reference model. However, at flexion angles above 40° some deviation is noticeable, especially for γ angle. This can be a consequence of an error propagation in the utilized numerical approach.

4. SCREW DISPLACEMENTS FOR KNEE FLEXION

For a finite femur body displacement, the screw parameters can be determined by using the coordinates of three non-collinear points fixed to a body in some initial (n) and final (n+1) positions.

The screw axis of the finite displacement of the body between its two positions (with the upper left index ^{n} and $^{n+1}$) can be determined by using the formula, given in Morecki et al. (2002):

$$\hat{\mathbf{e}}_{n,n+1}\, tg\frac{\theta_{n,n+1}}{2}=\frac{(^{n+1}\mathbf{b}_{jk}-{}^{n}\mathbf{b}_{jk})\times(^{n+1}\mathbf{b}_{ji}-{}^{n}\mathbf{b}_{ji})}{(^{n+1}\mathbf{b}_{jk}-{}^{n}\mathbf{b}_{jk})\cdot(^{n+1}\mathbf{b}_{ji}+{}^{n}\mathbf{b}_{ji})} \tag{9}$$

where:

$^{n}\mathbf{b}_{jk}={}^{n}\mathbf{b}_{k}-{}^{n}\mathbf{b}_{j}$ – position vector of point B_j relative to B_k, corresponding to n –th position of the body;

$\hat{\mathbf{e}}_{n,n+1}$ – unit vector of the screw displacement axis;

$\theta_{n,n+1}$ – angular displacement of the body from position n to position n + 1 around this axis

Position vector of the axis point is described as

$$\mathbf{p}_{n,n+1}=\frac{1}{2}[^{n+1}\mathbf{b}_{j}+{}^{n}\mathbf{b}_{i}+\hat{\mathbf{e}}_{n,n+1}\times(^{n+1}\mathbf{b}_{i}-{}^{n}\mathbf{b}_{i})ctg\frac{\theta_{n,n+1}}{2}+ -\hat{\mathbf{e}}_{n,n+1}\cdot(^{n+1}\mathbf{b}_{ji}+{}^{n}\mathbf{b}_{ji})\hat{\mathbf{e}}_{n,n+1}] \tag{10}$$

($\boldsymbol{p}_{n,n+1}$) - position vector of this axis with respect to the base system and

($u_{n,n+1}$) - body displacement along this screw axis (Fig. 5).

The value ($u_{n,n+1}$) of the linear displacement of the body along the screw axis is determined by the formula:

$$u_{n,n+1}=\hat{\mathbf{e}}_{i}\cdot(^{n+1}\mathbf{b}_{i}-{}^{n}\mathbf{b}_{i}) \tag{11}$$

Linear displacement of the body along the screw axis is determined by the formula

$$u_{n,n+1}=\hat{\mathbf{e}}_{n,n+1}\cdot(^{n+1}\mathbf{b}_{i}-{}^{n}\mathbf{b}_{i}) \tag{12}$$

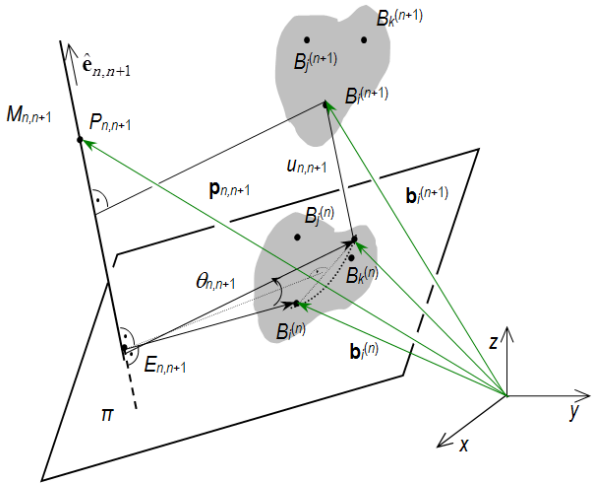

Fig. 5. Axis of the screw displacement of the body, described by using the unit vector ($\hat{\boldsymbol{e}}_{n,n+1}$) and the position vector ($\boldsymbol{p}_{n,n+1}$) of the axis with respect to the base system

DOI 10.1515/ama-2017-0050

According to the described procedure, axes of the femur screw displacements are determined with respect to the base system. Selected screw parameters (**e**, **p**, *u*) are given in Tab. 5, where for example *n*=1 corresponds to a finite displacement of the flexion angle between α=25° and α=30°. The obtained screw pitches (*u*) have relatively small magnitudes, what corresponds to a pure rotation about the screw axis.

Tab. 5. Parameters of the femur screw displacement with respect to the base frame {*xyz*} determined for different flexion angles α_n

n	α_n [°]	$\mathbf{e}_{n,n+1}$ [-]	$\mathbf{p}_{n,n+1}$ [m]	$u_{n,n+1}$ [m]
1	25	$\begin{bmatrix}0.2185\\0.9740\\-0.0602\end{bmatrix}$	$\begin{bmatrix}0.8949\\-6.9560\\4.9147\end{bmatrix}$x10^{-3}	-0.6800 x10^{-3}
2	30			
8	60	$\begin{bmatrix}0.2692\\0.9585\\-0.0938\end{bmatrix}$	$\begin{bmatrix}9.1315\\-40.3760\\7.6747\end{bmatrix}$x10^{-3}	0.0279 x10^{-3}
9	65			
14	90	$\begin{bmatrix}0.3536\\0.9278\\-0.1190\end{bmatrix}$	$\begin{bmatrix}12.9343\\-38.6413\\9.9044\end{bmatrix}$x10^{-3}	0.5702 x10^{-3}
15	95			

The following graphical representation of the screw axes enables better understating of a spatial character of this joint motion.

The femur screw displacements with respect to the tibia reference system are illustrated in Fig. 6 by the screw axes with direction unit vectors ($\mathbf{e}_a$, $\mathbf{e}_b$, $\mathbf{e}_c$) and position vectors (P_a, P_b, P_c) for the three finite displacements (α = 25^0 and 30^0; α = 60^0 and 65^0; α = 90^0 and 95^0). It can be noticed, that the screw axes are mainly directed along lateral (*y*) axis of the base reference frame. Simultaneously, the screw axis position changes slightly for each knee flexion, what corresponds to a position change of an instantaneous rotation point in the knee joint. Additionally, the screw axes are positioned inside the joint, it means between the three ligaments.

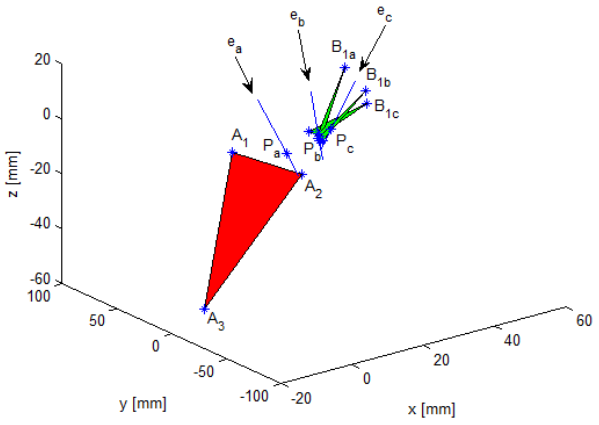

Fig. 6. Axes (e_a, e_b, e_c) of the femur screw displacements with respect to the base frame. Notations: *a*) α = 25^0 and 30^0; *b*) α = 60^0 and 65^0; *c*) α = 90^0 and 95^0

For further explanation of the knee joint model displacement (Fig. 2), the linear displacements of the curvature centres B_4 and B_5 of the femur condyle surfaces are investigated. Their coordinates are presented in Fig. 7 in the tibia reference system {*xyz*} as functions of the flexion angle. The obtained changes in the coordinates are related to a quasi-rolling of the considered bones.

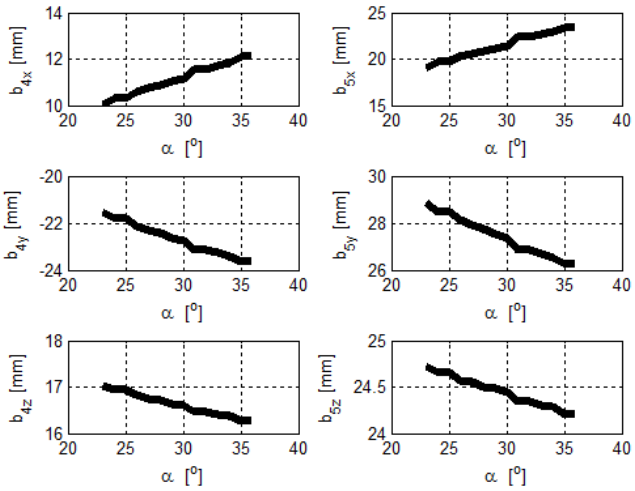

Fig. 7. Coordinates of point B_j (*j*=4,5), i.e. curvature centre of femur condyle surface, described in the system {*xyz*}as functions of the flexion angle α

5. CONCLUSIONS

Kinematic model of the human knee joint, considered as parallel mechanism, was formulated to determine the spatial displacement of the femur with respect to the tibia. The vector method was utilized for solving the direct position analysis (DPA) of the considered mechanism. The parameters of finite screw displacements are derived for better explanation of the knee joint spatial motion.

Numerical simulations proved effectiveness of the prepared algorithm. The elaborated algorithm can be used in the parameter estimation procedure of the equivalent mechanism, for example to determine the coordinates of the ligament insertion points, that satisfied the correct mobility of the joint knee. The formulated model enables to determine allowed ranges of the knee displacements and possible collision between the ligaments and the bones.

This algorithm can also be used for sensitivity analysis of the dimension tolerances on accuracy of the equivalent mechanism.

It seems useful to consider the linear displacement along the instantaneous screw axis of the joint motion, as it is allowed in the actual joint. Estimation of the model parameters can improve the results from the numerical analysis.

Further extensions of the kinematic model may led to solve static and elasto-static problems. The modified equivalent mechanism with femur and tibia condyles modelled as spherical or general shape surfaces may give better agreement with experiments.

REFERENCES

1. **Di Gregorio R., Parenti-Castelli V.** (2003), A spatial mechanism with higher pairs for modelling the human knee joint, *Trans. ASME Jnl of Biomechanical Eng.*, 125, 232-237.

DOI 10.1515/ama-2017-0050

2. **Góra M.** (2008), *Kinematic analysis of the multi-rod suspension mechanisms of the cars*, Doct. Diss, Cracow University of Technology.
3. **Morecki A., Knapczyk J., Kędzior K.** (2002), *Theory of mechanisms and manipulators*, WNT, Warsaw 2002.
4. **Ottoboni A., Parenti-Castelli V., Sancisi N.** (2010), Articular surface approximation in equivalent spatial parallel mechanism models of the human knee joint: an experiment-based assessment, *Proc. IMechE, Part H: Engineering in Medicine,* 224, 1121-1132.
5. **Parenti-Castelli V., Di Gregorio R.** (2000), Parallel mechanisms applied to the human knee passive motion simulation, *Advances in Robot Kinematics, Kluwer Academic Publ.* Dordrecht, 333-343.
6. **Parenti-Castelli V., Sancisi N.** (2013), Synthesis of spatial mechanisms to model human joints. In: McCarthy J. (eds) *21st Century Kinematics*, Springer, London.
7. **Saldias D., Martins D., de Mello Roesler C., da Silva Rosa F., Ocampo Moré A.,** (2013), Modeling of human knee joint in sagittal plane considering elastic behavior of cruciate ligaments, 22nd *International Congress of Mechanical Engineering*, November 3-7, 2013, Ribeirão Preto, SP, Brazil.
8. **Saldias D., Radavelli L., Roesler C., Martin D.** (2014), Kinematic synthesis of the passive human knee joint by differential evolution and quaternions algebra: a preliminary study, 5th IEEE RAS & EMBS *International Conference on Biomedical Robotics and Biomechatronics* (BioRob), 12-15 Aug. 2014, Brazil.
9. **Sancisi N., Parenti-Castelli V.** (2010), A 1-Dof parallel spherical wrist for the modelling of the knee passive motion, *Mechanism and Machine Theory*, 45, 658-665.
10. **Sancisi N., Parenti-Castelli V.,** (2011), A sequentially-defined stiffness model of the knee, *Mechanism and Machine Theory*, 46(12), 1920-1928.
11. **Wilson D.R., Feikes J.D., O'Connor J.J.** (1998), Ligaments and articular contact guide passive knee flexion, *Journal of Biomechanics*, 31, 1127-1136.
12. **Woo S., Abramowitch S., Kilger R., Liang R.,** (2006), Biomechanics of knee ligaments: injury, healing, and repair, *Journal of Biomechanics*, 39(1), 1–20.

DOI 10.1515/ama-2017-0051

WASHING MACHINE CONTROLLER WITH A NEW PROGRAMMING METHOD

Andrzej MILECKI*, Roman REGULSKI*

*Poznan University of Technology, ul. Piotrowo 3, 60-965 Poznań, Poland

andrzej.milecki@put.poznan.pl, roman.regulski@put.poznan.pl

received 10 October 2016, revised 7 December 2017, accepted 11 December 2017

Abstract: In the paper the newly designed at Poznan University of Technology (PUT) washing machine controller is presented. The commonly used in washing machines sensors, drives and other input-output elements are briefly described. The designed at PUT controller is based on 32-bit STM32 microcontroller. The used in this controller modules are described and their input/output signals and basics of operations are presented. The developed in the controller user-machine communication devices, elements and methods are described. The paper presents new washing machine programming methods and implementation software, such as voice recognition and intelligent programming of washing machine that were applied in the new controller.

Key words: Washing Machine, Programming, Communication, Mechatronics

1. INTRODUCTION

In the last two decades the expansion of sector producing house equipment in Poland is observed. The production quantities and assortment of produced refrigerators, washing machines, cookers, etc. have increased significantly. Also new devices like dishwashers have been introduced to production. In Poland such big and famous companies like Indesit (Łódź), Whirpool (Wrocław), Electrolux (Świdnica, Żarów), BSH (Łódź, Wrocław), Samsung EPM (Wronki), Amica, Beko, Candy, Gorenje, Indesit have started production factories. Nowadays, Poland is one of the biggest producers of "white goods" in Europe. The export of sector producing house equipment in Poland is about 3% of the total polish export. In the first quarter of 2016 in Poland about 5.6 million of so-called "big-white-goods" devices have been produced.

Recently a new group of household electronics is strongly developed, which may work in a network called Internet-of-Things. Continuous miniaturization in electronic packages and growth in microcontroller performance causes new concept of an environment where everyday objects are connected to the Internet. This will lead users to consume resources more efficiently (Bourgeois et al., 2014; Risteska Stojkoska and Trivodaliev, 2017).

Due to the growing demand for natural Human Machine Interfaces, a lot of concepts for robotic system that allows users to program an industrial robot using gestures and speech are proposed. Examples using ASR (automatic speech recgniotion) are described by (Anusuya and Katti, 2010; Neto et al., 2010; Norberto Pires, 2005).

In the field of medical systems very futuristic applications can be found. In the paper (Gundogdu et al., 2017) ASR was developed to control the prosthetic robot arms. These solutions can be also applied in Smart Homes such as voice interface for the elderly people (Portet et al., 2013) or for improved comfort and autonomy at home (Chahuara et al., 2017).

Gestures are another natural form of communication between humans. In the robotics field, several works have been done in order to identify and recognize motions and gestures performed by humans (Tsarouchi et al., 2016a; Tsarouchi et al., 2016b).

In 2009 at Poznan University of Technology (PUT) a project financed by polish National Centre of Research and Development was started. Its main goal was to design of a new, advanced washing machine microcontroller. In this project some new solutions have been proposed, tested and implemented in the controller.

In most commonly produced washing machines simple 8-bit microcontrollers are applied. For the last ten years, there are 32-bit microcontrollers on the market (Brown, 2012; Mallikarjun, 2006), cost of which compared to the cost of 8-bit microcontrollers, is not significantly higher. However the design of controllers based on 32-bit microcontrollers is much more difficult and time consuming. This applies especially to startup process of 32-bit microcontrollers, which is much more complex. Moreover the available to such microcontrollers library is big. The design of printed circuit board (PCB) for 32-bit microcontroller requires high experience of the designer. The programming, testing and debugging processes are also slightly different and more complicated.

At the beginning of the paper the washing machine description is given. Its basic operation. processes and control methods are shortly described (Milecki and Pittner, 2015).Then the structure of designed at PUT washing machine controller is presented. In this controller a 32-bit STM32 microcontroller is used. In order to achieve flexibility the controller hardware structure is modular-based. The individual modules are shortly described. Basic structure, the modules connection, their communication protocols and basics of cooperation between them are also briefly characterized. Also the used in the controller most important electronic circuits are described. In the next point the applied methods for communication between the user and the controller are presented. The main functions and possibilities of washing machine programming are described. The so called "intelligent" programming method is

DOI 10.1515/ama-2017-0051

presented. Also the voice communication in washing program settings is described. The most important advantages of a new controller are emphasized.

2. WASHING MACHINE INPUT AND OUTPUT ELEMENTS

In the modern washing machines several sensors and actuators are applied (Bascetta et al., 2012). Some sensors can measure the parameters, giving analog electrical signals on the outputs. This enables control of the water level and temperature, spin speed, cycle program, load balancing, child lock systems, and noise reduction systems. For example, a push button switch is used as a "door-closed" sensor, that allows a complete circuit when the closed door pushes on it. Another example is a pressostat called as "fill-level" sensor, which measures the level of the water in a drum. This is in fact a linear pressure sensor, in which there are two chambers separated with elastic membrane. The upper chamber is directly connected to the atmosphere and the lower chamber is connected through a pipe with the bottom of the drum, where the pressure is proportional to the level of the water. As a result the diaphragm bends in proportion to the difference of pressures in both chambers. The membrane moved the connected to it a ferromagnetic core, which is located in the middle of the coil supplied by sinusoidal generator.

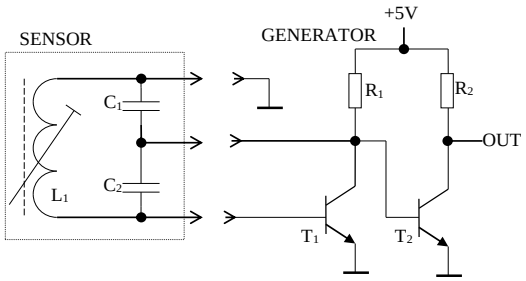

Fig. 1. Pressostat and its electronic circuit

The pressostat electric circuit is shown in Fig. 1. It consists of a NPN transistor, which input (Base) is connected to the coil, which inductance changes by ferromagnetic core according to the level of the water. The coil is connected to two capacitors, which creates a resonance circuit. This circuit creates a Colpitts generator, which frequency changes proportionally to the coil inductance changes. The output signal from generator is given to analog input of the microcontroller. If there is no water in a drum the generated frequency is equal to 26.7 kHz and when the drum is fully filled its frequency is equal to 20.8 kHz.

Nowadays in most washing machines, for temperature measurement the NTC thermistor is used. This is a semiconductor element with a non-linear resistanc-temperature characteristic (Fig. 2). This characteristic may be approximated by the following equation:

$$T = -28.8\ln(R) + 294.3 \tag{1}$$

where: T – temperature in °C, R – NTC thermistor resistance in Ohms.

In washing machine controller designed at PUT, this curve is reversed as shown in Fig. 2, stored in microcontroller's memory and used for linearization.

In cheap washing machines single phase brash AC motor is used, which typically is supplied by 230 VAC. The velocity of this motor is controlled by changing the supply voltage. Usually to this end a simple triac is used, which is switched on by pulses generated by the controller.

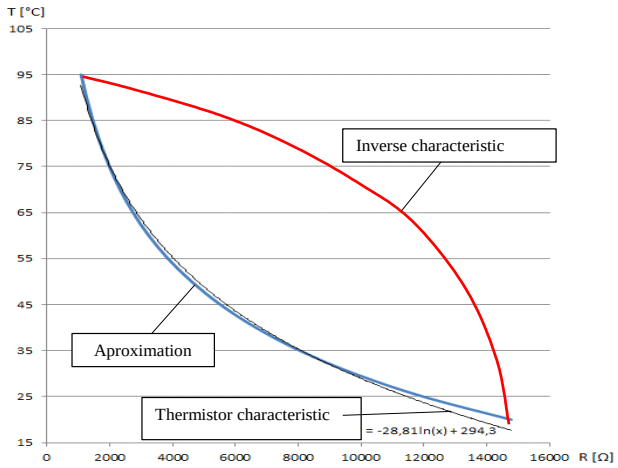

Fig. 2. NTC thermostat characteristic, its approximation (blue) and inverse curves (red)

Nowadays in advanced modern washing machines the mentioned above single phase AC motor is replaced by special inductive motor or by a multi poles brushless DC motor, which construction is similar to torque motor. In this motor there are several coils on a stator and permanent magnets mounted in a rotor. The position of the rotor is measured by Hall sensors, which output signals are used to control of coils switching. These type of motors are called "direct drive" and can rotate with low velocity. Thanks to this the application of a belt transmission is not necessary. For control of this motor a specialized and complicated controller should be applied.

Other output elements used in washing machines are: water pump, electro-valves, heater and door lock electromagnet. Typically these elements are switched on and off by relays or by triacs. In some washing machines also MEMS acceleration sensors are used, which enable the measurement of drum oscillations. Thanks to this the balance of laundry in the drum is controlled and the rotational velocity is adjusted accordingly, assuring safe and silent work. In some washing machines following sensors are used: leak detector, spin out-of-balance detector and mains failure sensor. They generate only on/off type signal, which is connected to the digital inputs of the controller. The heater is also controlled by triac, which is a very durable low-cost semiconductor element. Furthermore triacs are used for switching on and off of the electro valves and pump motor. In many washing machines produced nowadays, a commutated one-phase AC motor is applied, velocity of which is controlled using a triac in a wide range.

3. STRUCTURE OF 32-BIT WASHING MACHINE CONTROLLER

Since 1980 the microcontrollers are used as the washing machine controllers. This enabled the application of LED or LCD displays and creation of some buttons for programming and washing process supervision. Thanks to the application of microprocessors the washing process can be controlled much more accu-

DOI 10.1515/ama-2017-0051

rately. Thanks to advanced control algorithms applied in microcontrollers, washers use less electricity to run the machine and also to set the water to the right temperature levels. The scheme block diagram of a new washing machine controller, which is designed at Poznan University of Technology is presented in Fig. 3. It is based on 32-bit microprocessor.

In order to achieve flexibility the modular structure of the controller was proposed. The basis is main board, on which the CPU board, input sensor block, communication ports like RS485 and USB, EEPROM and buzzer module were implemented. The heart of the controller is CPU board which is connected to the mainboard with a slot, enabling its easy replacement. In the CPU board the microcontroller type STM32F103ZET6 is installed. It is a 32-bit microcontroller based on CortexM3 core. The main board may communicate with different users interfaces. The simplest is the on/off switching panel and the most advanced is a color touch-panel. The next controller board was high power unit, which is responsible for constant velocity control of the drum motor, and for switching on/off of such elements like: heater, valves, pump, door lock electromagnet etc.

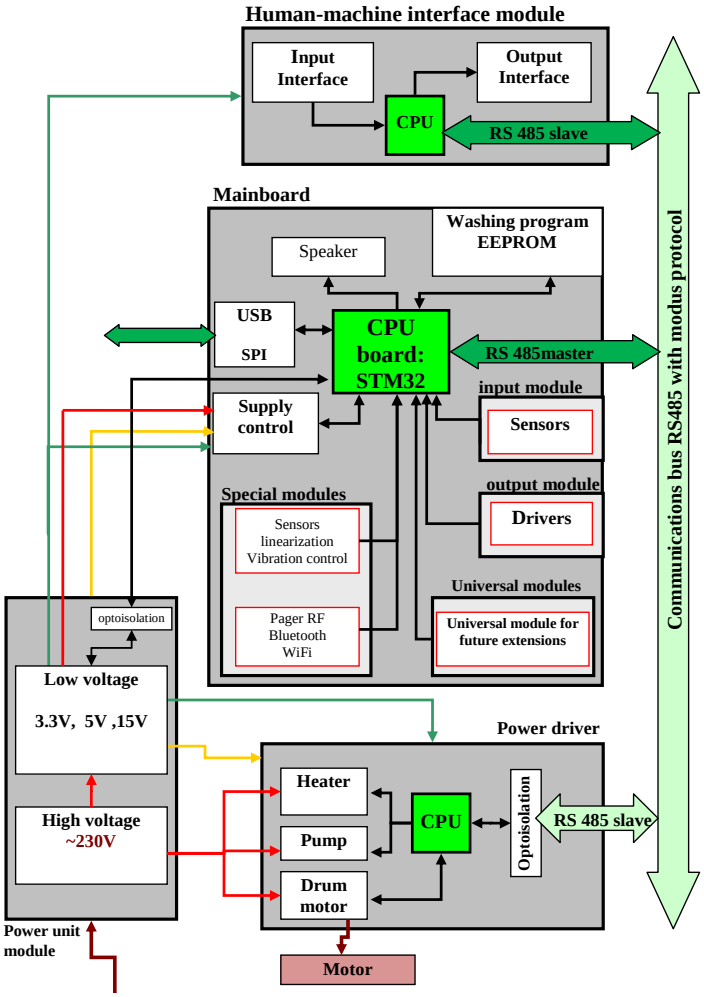

Fig. 3. Washing machine controller block scheme

All modules communicate with each other using serial interface network. In the developed solution, different single electronic modules can be used. Thanks to this the controller may be easy adopted to different requirements, which is an important advantage. Each module may be autonomous, individually programmed unit assuring more safety work. In this approach, the user may design and create the controller's structure, its capacity and ability and finally set its price. Moreover, the same main controller may be used in different washing machines but with different types of additional modules, for example drive controller or user interfaces. Thanks to such solution, the testing and in particular certification process is facilitated. In the designed prototype the digital outputs are connected through relays or through linear amplifier type ULN2003A. All digital inputs and outputs are opto-isolated.

4. COMMUNICATION BEETWEEN MODULES IN THE WASHING MACHINE CONTROLLER

In the described here washing machine controller three serial busses were implemented: SPI, RS-485 and USB, which assured internal communication between modules. The SPI was used for programming purposes, testing and commissioning, debugging and communication with EEPROM. The RS-485 was used for communication with High Power Controller like drive controller, relay modules, with user interfaces (LCD) and with Wireless Interfaces Controller. Throughout the project a few human-washing machine interfaces were designed, built and tested. The first one was a mechanical one with typical to washing machines rotary switch and LCD display. The last one was a color touch-screen

DOI 10.1515/ama-2017-0051

(Fig. 4). The controller was also equipped with a voice interface module which could be used for communication with, for example, blind users. The last interface was a USB, which enabled the wire communication with a PC based computer and was used for testing and diagnosis of the washing machine. In the project our proprietary direct drive controller was designed and built, but almost every other washing machine drive system could be used, i.e. single phase serial motor with triac, direct drive or synchronous PM motor.

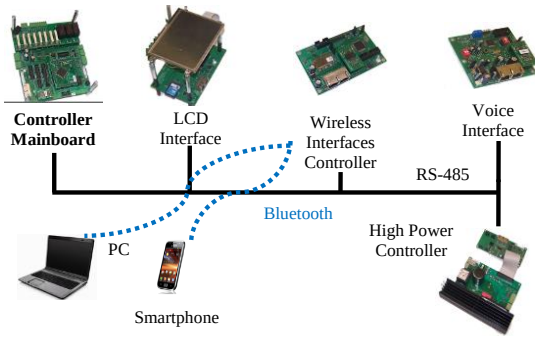

Fig. 4. View of the controller communication RS-485 interface

Additionally the wireless communication card was designed and connected to the controller. It enabled the connection with any device using Bluetooth system, for example with smartphone, PC, or pager. The special software for smartphone (Samsung S5) and PC (laptop) was written and implemented. It enabled the programming and supervision of washing machine using standard programs or user-customized ones. Smartphone or PC may be used instead of typical washing machine interface. Moreover, a so-called by us "intelligent programming" method was proposed and implemented. It enabled settling of the washing parameters using questions and answers. This method utilized control methodology based on fuzzy logic. The next interface was a USB, which enabled the cable communication with PC. Additionally a special software for the service purposes thus for diagnostic, was worked at PUT. It could be activated and all washing machine elements could be tested in the diagnostic mode. Such solution is very useful and enable fast testing and washing machine diagnosis.

5. VOICE COMMUNICATION AND INTELLIGENT WASHING MACHINE PROGRAMING

The new possibilities to connect washing machine controller with PC or smartphone provide further flexibility and enhanced user experience. The voice communication enables the intuitive programming of a washing machine. In the designed controller the Google Speech Recognition System was adapted and used. This system is easy to use and assures the acceptable quality of voice recognition.

The software for PC was written in Microsoft Visual Studio 2010 environment, using object programming language C#. A start/stop algorithm was used for voice recognition, which enabled the recognition of word starting and ending points. The voice signal from the microphone was constantly analyzed using RMS values calculation. For every ongoing 20 ms frame, the RMS value was calculated and compared with the previous one. If the set up threshold was exceeded, the starting or ending point of word would be detected. In the algorithm additional security tools like: minimum and maximum saying time were used. The command saying time and silence time were set basing on average value of energy, calculated as voice signal RMS during the time 200 ms. These rules were implemented into an algorithm, which eliminated the false recognition of short brakes between words, which may be taken by the algorithm as stop. The scheme of the described above algorithm is shown in Fig. 5. The same algorithm was implemented on a smartphone with Android operating system, but in this case the program was written in Java.

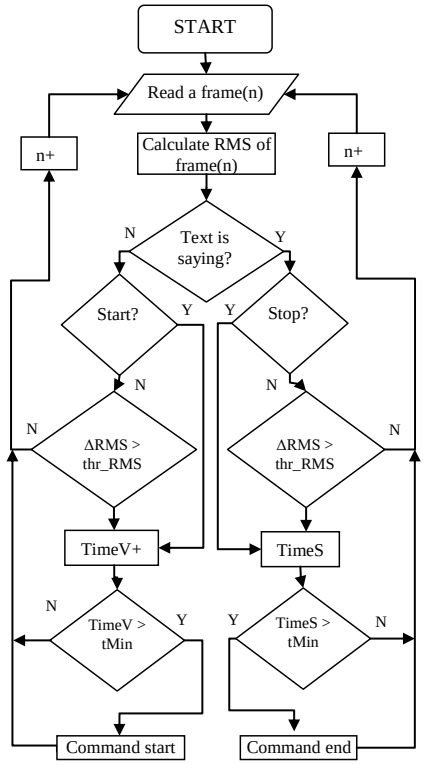

Fig. 5. Start/stop word recognition algorithm scheme

In order to check the efficiency of the voice recognition, the system was tested. In the investigations 5 people were involved. All of them used the same 6 words i.e. commands, repeated 20 times. In these tests following parameters were considered (see Tab. 1): server response time, confidence of recognition and recognition efficiency, defined as a proportion of properly recognized command to saying commands.

The investigations have shown that the recognition efficiency was almost 90% and the server response time was about 1.3 s, which is quite acceptable.

For the designed washing machine controller a few new programming methods were implemented. The first one is "Classic", which enabled to choose the ready to use, useful washing programs. This programs are commonly prepared by the producers, like: Synthetics, Cottons, Wool, Delicate, Sensitive, Quick and so on. The user may only chose one of them using mouse when PC is applied or pressing the touch-screen when smartphone is connected. There is also a possibility to change parameters using keyboard.

The second method utilizes the advantages of voice communication. In this case the user can "tell" the controller the name of the program and the values of parameters. For example, the user may only tell: "cotton, temperature 60, rotation speed 1200, dirt medium, rinsing 2, delay 60". The controller repeats every

DOI 10.1515/ama-2017-0051

word after recognition and the user has the opportunity to improve it repeating the last mentioned word.

Tab. 1. Speech recognition investigation results

User	Response time [ms]	Confidence (0 ÷ 1)	Efficiency [%]
# 1	1206	0.56	94.16
# 2	1257	0.65	84.17
# 3	1192	0.60	90.83
# 4	1301	0.54	80.00
# 5	1251	0.58	98.33
Average	1242	0.59	89.50

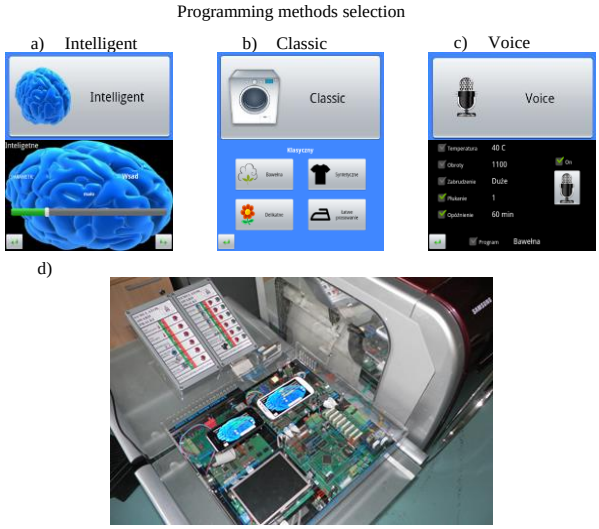

Fig. 6. View of the controller communication interfaces and view of the controller electronics

Finally, a special washing machine programming method, called "Intelligent", was proposed and implemented. It resembles the dialog between human and washing machine and is based on "Fuzzy Control" approach. During the programming phase the user has the possibility to set all parameters like: temperature, spin velocity, washing time, number of rinsing etc. in full range of washing machine possibilities. In the programming the graphical interface is used, which displays slider potentiometers on a screen. The user may move the slider, settling the washing parameters this way. All mentioned above programming methods are presented in Fig. 6. The software enables to switch intuitively and automatically between these three methods. For example, if the user starts to speak, the system is immediately going to voice recognition mode and so on. During the washing process its status is presented on a screen, and the user may stop the execution of the program, change some parameters and continue the washing process. The settled program and its parameters may be stored in the memory and induced again at any time. In Fig. 6d the view of the controller and smartphones during programming process are shown.

6. SUMMARY

The new 32-bit microcontroller designed and built at PUT was developed and implemented on the washing machine. Several prepared washing programs were tested, verified and approved. In the build controller both simple and advanced human-machine interfaces were developed. As a result the controller may be equipped with one, chosen for a client interface, like: typical interface with switches and LCD, mono or color touch-screen. Alternatively, the user may opt out of typical modules and may decide to use only smartphone or laptop for washing machine programming. Additionally the user may use the voice communication, programming and parameters setting. In the project also special intelligent methods of washing machine programming have been developed. All prepared methods were successfully tested. The proposed human washing machine interfaces may be implemented. The washing machines with such interfaces may be successfully offered on the market and find many clients.

REFERENCES

1. **Anusuya M.A., Katti S.K.** (2010), Speech recognition by machine, a review, *ArXiv Prep,*. ArXiv10012267.
2. **Bascetta L., Rocco P., Zanchettin A.M., Magnani G.** (2012), Velocity control of a washing machine: A mechatronic approach, *Mechatronics*, 22, 778–787.
3. **Bourgeois J., van der Linden J., Kortuem G., Price B.A., Rimmer C.** (2014), *Conversations with my washing machine: an in-the-wild study of demand shifting with self-generated energy*, ACM Press, 459–470.
4. **Brown G.** (2012), Discovering the STM32 Microcontroller, Indiana University
5. **Chahuara P., Portet F., Vacher M.** (2017), Context-aware decision making under uncertainty for voice-based control of smart home, *Expert Syst. Appl., 75, 63-79.*
6. **Gundogdu K., Bayrakdar S., Yucedag I.** (2017), *Developing and modeling of voice control system for prosthetic robot arm in medical systems*, J. King Saud Univ. - *Comput. Inf. Sci.*
7. **Mallikarjun S.** (2006), 32-bit MCUs offer high integration, high functionality, *Electron. Prod.*, 49, 40–43.
8. **Milecki A., Pittner G.** (2015), Design of 32-bit washing machine controller, *Solid State Phenomena*, 220-221, 463–469.
9. **Neto P., Pires J.N., Moreira A.** (2010), High-level programming and control for industrial robotics: Using a hand-held accelerometer-based input device for gesture and posture recognition, *Ind. Robot Int. J.*, 37, 137–147.
10. **Norberto Pires J.** (2005), Robot-by-voice: Experiments on commanding an industrial robot using the human voice, *Ind. Robot Int. J.*, 32, 505–511.
11. **Portet F., Vacher M., Golanski C., Roux C., Meillon B.** (2013), Design and evaluation of a smart home voice interface for the elderly: acceptability and objection aspects, *Pers. Ubiquitous Comput.*, 17, 127–144.
12. **Risteska Stojkoska B.L., Trivodaliev K.V.** (2017), A review of Internet of Things for smart home: Challenges and solutions, *J. Clean. Prod.*, 140, 1454–1464.
13. **Tsarouchi P., Athanasatos A., Makris S., Chatzigeorgiou X., Chryssolouris G.** (2016a), High level robot programming using body and hand gestures, *Procedia CIRP*, 55, 1–5.
14. **Tsarouchi P., Makris S., Chryssolouris G.** (2016b), Human robot interaction review and challenges on task planning and programming, *Int. J. Comput. Integr. Manuf.*, 29, 916–931.

Acknowledgements: The research work reported here was supported by the Polish Ministry of Science and Education grants no. 02/22/DSPB/1389 .

DE GRUYTER
OPEN

DOI 10.1515/ama-2017-0052 acta mechanica et automatica, vol.11 no.4 (2017)

NUMERICAL SIMULATION OF SHEAR SLITTING PROCESS OF GRAIN ORIENTED SILICON STEEL USING SPH METHOD

Łukasz BOHDAL*, Katarzyna TANDECKA*, Paweł KAŁDUŃSKI*

*Faculty of Mechanical Engineering, Koszalin University of Technology, Racławicka 15-17 str., 75-620 Koszalin, Poland

lukasz.bohdal@tu.koszalin.pl, katarzyna.tandecka@tu.koszalin.pl, pawel.kaldunski@tu.koszalin.pl

received 5 April 2017, revised 10 December 2017, accepted 12 December 2017

Abstract: Mechanical cutting allows separating of sheet material at low cost and therefore remains the most popular way to produce laminations for electrical machines and transformers. However, recent investigations revealed the deteriorating effect of cutting on the magnetic properties of the material close to the cut edge. The deformations generate elastic stresses in zones adjacent to the area of plastically deformed and strongly affect the magnetic properties. The knowledge about residual stresses is necessary in designing the process. This paper presents the new apprach of modeling residual stresses induced in shear slitting of grain oriented electrical steel using mesh-free method. The applications of SPH (Smoothed Particle Hydrodynamics) methodology to the simulation and analysis of 3D shear slitting process is presented. In experimental studies, an advanced vision-based technology based on digital image correlation (DIC) for monitoring the cutting process is used.

Key words: Shear Slitting, Smoothed Particle Hydrodynamics, Grain Oriented Silicon Steel, Digital Image Correlation

1. INTRODUCTION

The process of forming parts from sheet metal using shearing frequently includes blanking, piercing, slitting, and trimming operations. This operations realized with high speed, are a very complicated technological processes in which material undergoes plastic deformations. Grain oriented and non-oriented electrical steels are widely used for the manufacture of transformer cores, power reactors, hydro-generators, turbo-generators and other electrical equipment and apparatuses. Cutting operations for example: blanking, guillotining, edge trimming, shear slitting, or punching induce stresses in electrical steels and consequently magnetic properties are partially deteriorated. According to many authors, the reason for the deterioration of the magnetic properties is to change the distribution of flux density and hysteresis loss (Godec, 1977; Gałęzia et al., 2012; Gontarz and Radkowski, 2012).

The strong deformations are generated in tool-workpiece contact zones which affect on its magnetic properties. The another problem of shearing processes is deterioration of cut surface quality by forming of burrs and rollover which may include increasing the metal core eddy current loss. The burr also strongly difficult the packetizing. The analysis of state of stresses and strain in sheet after shearing using experimental methods is very problematic. This analysis is determined by invasive methods (Eg. by drilling a series of small openings through which wound measuring winding) which increase the error margin and in many cases is impossible when thin sheets are analyzed. There are no known non-invasive methods of appointment.

At the moment knowledge of the slitting of electrical steels is very limited and based mainly on experimental methods, which are often expensive and unable to be extrapolated to other cutting configurations. TeNyenhuis et al., (2000) analyzes the effect of slitting grain-oriented electrical core steel on iron loss which was investigated by comparing measurements performed by several prominent electrical core steel suppliers with a developed theoretical model. Measurements showed loss increases that were very dependent on sheet width, somewhat dependent on flux density, and practically independent on material type or power frequency. The influence of slitting on core losses and magnetization curve of grain-oriented electrical steel was analyzed by Godec (1977).

Analysis of current literature suggested the main challenge when cutting electrical steels is to obtain high quality products characterized optimum sheared edge condition, minimum surface damage, freedom from burrs, slivers, edge wave, distortion and residual stresses. Simulation of shear slitting processes in which the strip material is highly deformed is a major challenge of FEM codes which number is limited in current literature. The principal problem in using a conventional FE model with Langrangian mesh are mesh distortion in the high deformation (Golovashchenko, 2006, Kałduński and Kukiełka, 2007, 2008, Kukielka et al., 2010). Classical Lagrangian, Eulerian and ALE methods such as finite element methods (FEM) cannot resolve the large distortions very well. Recent developments in so called mesh-free or meshless methods provide alternates for traditional numerical methods in modeling the technological processes (Bagci, 2011; Gąsiorek, 2013; Jianming et al., 2011).

In this paper, first, the applications of mesh-free SPH (Smoothed Particle Hydrodynamics) methodology to the simulation and analysis of 3-D slitting process is presented. This method combines the advantages of mesh-free, Langrangian, particle methods and eliminate most of difficulties. At the moment in current literature applications of mesh-free methods to modeling of shear slitting and other shearing processes is lacking. Developed model is used to analysis of residual stresses in grain oriented electrical steels during and after process under different conditions. Next, the developed model is validated with experimental research by using vision-based solutions. The effect

DOI 10.1515/ama-2017-0052

of selected process technological parameters on the mechanically affected zone on the workpiece is analyzed.

2. BASIS OF THE SPH METHOD

SPH is total Langrangian and is a truly mesh-free technique initially developed by Gingold and Monaghan (1977) for the analysis and simulation of astrophysics problems. The idea of this method is to divide a continuum into discrete elements, called particles which are placed at some distance d from each other. This distance is called particle density *d* (Fig. 1).

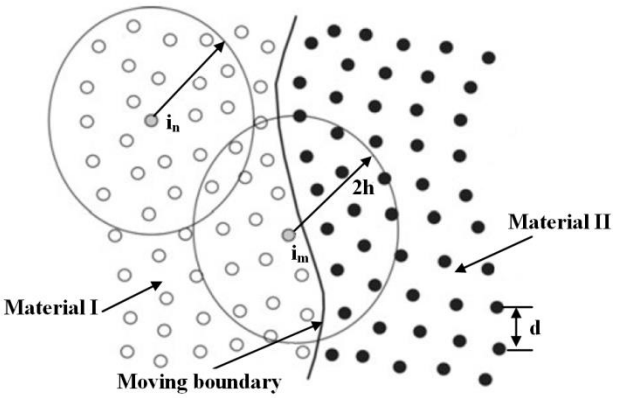

Fig. 1. Smoothing kernel in material volume and at the boundary

The smoothing of field variables is performed in the area with radius *h*, called the smoothing length, over which the variables are smoothed by a kernel function. This means that the value of a variable in any spatial point can be obtained by adding the relevant values of the variables within two smoothed lengths. Sometimes relative to particle density smoothing length $\bar{\mathrm{h}} = \mathrm{h}/\mathrm{d}$ is used. In contrast to mesh methods such as, e.g., the FEM, in which the mesh distorts in the case of large deformations, the SPH method can be used to model processes accompanied by large deformations. The SPH approximation of the equation for continuum mechanics uses the following approaches. A function $\mathrm{f}(\mathrm{x})$ is substituted by its approximation $\mathrm{A_f}(\mathrm{x},\mathrm{h})$, characterising a body condition. For example, the velocities of a body's points in a particular area are approximated with the following expression:

$$A_f(x,h) = \int f(y) \cdot W(x,h)dy, \tag{1}$$

where $\mathrm{W}(\mathrm{x},\mathrm{h})$ is a smoothed kernel function (Heisel et al., 2013). The size of the smoothing kernel is defined by the function of Θ :

$$W(x,h) = \left(\frac{1}{h(x)^p}\right) \cdot \Theta(x), \tag{2}$$

where p is the dimension of space.

The majority of the smoothing kernels used in the SPH method is represented as cubic B-spline, determining the selection of the function Θ as follows:

$$\Theta(x) = C \cdot \begin{cases} 1 - \frac{3}{2}\cdot x^2 + \frac{3}{4}\cdot x^3, & if |x| \le 1 \\ \frac{1}{4}\cdot (2-x)^3, & if\ 1 \le |x| \le 2 \\ 0 & if\ 2 \le |x| \end{cases} \tag{3}$$

where C is the normalisation constant. Integration time step can be determined by the following equation:

$$\Delta\tau = C_{\Delta\tau} \cdot \min_i \left(\frac{h_i}{C_i + v_i}\right), \tag{4}$$

where i is the particle number; $\mathrm{C_{\Delta\tau}}$ is the time step increase coefficient; $\mathrm{v_i}$ is the velocity of particle i. It is important to notice that coefficient $\mathrm{C_{\Delta\tau}}$ directly influences the integration time step.

The smoothing length in LS-DYNA solver used in this work dynamically varies so that the number of neighbouring particles remains relatively constant. It is realized by recalculating the smoothing length in accordance with the average particle density:

$$h = h_0 \left(\frac{d_0}{d_i}\right)^{1/p}, \tag{5}$$

or by solving the continuity equation:

$$\frac{dh}{dt} = \frac{1}{d} \cdot \frac{h}{d} \cdot \frac{\partial d}{\partial t}, \tag{6}$$

where $\mathrm{d_0}$ and $\mathrm{h_0}$ are the initial density and the initial smoothing length.

A quadratic approximation of the particle motion is mainly used for the SPH method. A motion of the particles can be described here with the following equation:

$$\frac{\partial v_i^\alpha}{\partial t} = \sum_{j=1}^{N} m_j \cdot \left(\frac{\sigma_i^{\alpha\beta}}{d_i^2} + \frac{\sigma_j^{\alpha\beta}}{d_j^2} + A_{ij}\right) \cdot \frac{\partial W_{ij}}{\partial x_i^\beta}, \tag{7}$$

where j is particle number; N is the number of neighbouring particles; $\mathrm{v_i^\alpha} = \frac{\mathrm{dx_i^\alpha}}{\mathrm{dt}}$ is the velocity of particle i; $\mathrm{m_j}$ is the mass of particle j; $\sigma_\mathrm{i}^{\alpha\beta}$, $\sigma_\mathrm{j}^{\alpha\beta}$, are the stress tensors of i and j particles respectively; $\mathrm{d_i}$ and $\mathrm{d_j}$ are the densities of i and j particles respectively; $\mathrm{A_{ij}}$ are the specific external forces; $\mathrm{W_{ij}} = \mathrm{W}(\mathrm{x_i} - \mathrm{x_j}, \mathrm{h})$ is the smoothing kernel.

3. CONSTITUTIVE MODEL FOR MATERIAL

In slitting models, accurate and reliable flow stress models are considered as highly necessary to represent workpiece materials constitutive behavior. The constitutive material model reported by Johnson and Cook (1985) was employed in this study, it is often used for ductile materials in cases where strain rate vary over a large range and where adiabatic temperature increase due to plastic heating cause material softening. The model can be represented by Eq (8):

$$\sigma_Y = [A + B(\bar{\varepsilon}^p)^n][1 + C\ln\dot{\varepsilon^*}][1 - (T^*)^m], \tag{8}$$

where σ_Y is the equivalent flow stress, $\bar{\varepsilon}^\mathrm{p}$ is the equivalent plastic strain, A, B, and n are strain hardening constants; C is the strain rate hardening constant, and m is the thermal softening constant that modifies the homologous temperature term, $\mathrm{T^*}$. The homologous temperature is defined as, $\mathrm{T^*} = \frac{\mathrm{T} - \mathrm{T_r}}{\mathrm{T_m} - \mathrm{T_r}}$, where T is the temperature of the material, $\mathrm{T_r}$ is a reference temperature (typically room temperature), and $\mathrm{T_m}$ is the melt temperature of the material. The term, $\dot{\varepsilon^*}$, is the normalized strain rate of the material or $\dot{\varepsilon^*} = \frac{\dot{\bar{\varepsilon}}^\mathrm{p}}{\dot{\varepsilon}_0}$, where $\dot{\varepsilon}_0 = 1.0\mathrm{s}^{-1}$. A dilatation of the material is based on the value of equivalent plastic strain at element integration points. Failure occurs when *D* = 1. The damage parameter follows a cumulative damage law given by Eq (9):

DOI 10.1515/ama-2017-0052

$$D = \sum \frac{\Delta \bar{\varepsilon}^p}{\varepsilon_f}, \tag{9}$$

where $\Delta\bar{\varepsilon}^p$ is the increment of the equivalent plastic strain during an integration cycle and ε_f the equivalent strain to fracture under current conditions of strain rate, temperature, pressure and equivalent stress (Bohdal et al., 2015, Gontarz and Radkowski, 2012, Heisel et al., 2013). ET 122-30 (0,3 mm thick) grain oriented steel which is often employed for industry, is used to simulate typical production conditions. The mechanical and physical properties of material are shown in Tab. 1. The Johnson-Cook constitutive model constants are shown in Tab. 2.

Tab. 1. Mechanical and physical properties of work material (Bohdal et al., 2015)

Density [kg/dm^3]	Silicon content [%]	Yield point [MPa]	Tensile strength [MPa]	Elongation [%]	Hardness [HV$_5$]
7.65	3.1	300	370	11	160

Tab. 2. The Johnson-Cook constitutive model constants for ET 122-30 steel (Bohdal et al., 2015)

A [MPa]	B [MPa]	C	N	M
104.3	445.6	0.041	0.46	0.54

4. SPH MODEL OF SHEAR SLITTING PROCESS

Slitting differs from the other shearing operations such as blanking and punching as it involves the rotation of blades and hence the material is cut in two directions simultaneously instead of one. A thorough understanding of the process of slitting would thus require that a three-dimensional analysis of the process be conducted. A three-dimensional SPH model of slitting was developed in the general purpose finite element software package LS-DYNA and presented in Fig. 2a. The model is created based on the experimental configuration and the geometrical parameters of the test stand shown in Fig. 2b. For the monitoring of slitting process, a high-speed camera i-SPEED TR with zoom lens and light sources are used.

The slitting machine (KSE 10/10) consists of two rotary knives (where: r_1 = r_2 = 15 mm, r_3 = 20 mm) driven by the engine. The contact between the knives and sheet (where: l = 80 mm, w_i = 40 mm) is considered non-sliding contact that uses a polyurethane roll, which move the sheet in the horizontal direction. The kinematics of the different components is as follows: first the upper knive moves vertically with the constant velocity v_1 in order to cut the sheet thickness. Then, the sheet moves along Z axis with the constant velocity v_2 = 3 m/min as a result of knives and roll rotations. In order to reduce the model size and shorten the computational time the strip is modeled by SPH particles while the tools (knives) are considered as rigid bodies, and modeled by the traditional finite element method. The contact between tools and the deformable sheet metal is described using Coulomb's friction model, and constant coefficients of static friction μ_s = 0.08 and kinetic friction μ_d = 0.009 are accepted.

A series of numerical simulations are carried out to determine the optimal parameters of the solver, and to obtain a minimum prediction error of slitting variables and minimal simulation cost. The computer simulations are executed for different initial particle densities: d_1 = 0.025 mm, d_2 = 0.02 mm, d_3 = 0.016 mm, d_4 = 0.014 mm, d_5 = 0.0125 mm. As a simplifying assumption the flat state of the deformation is assumed (Fig 3).

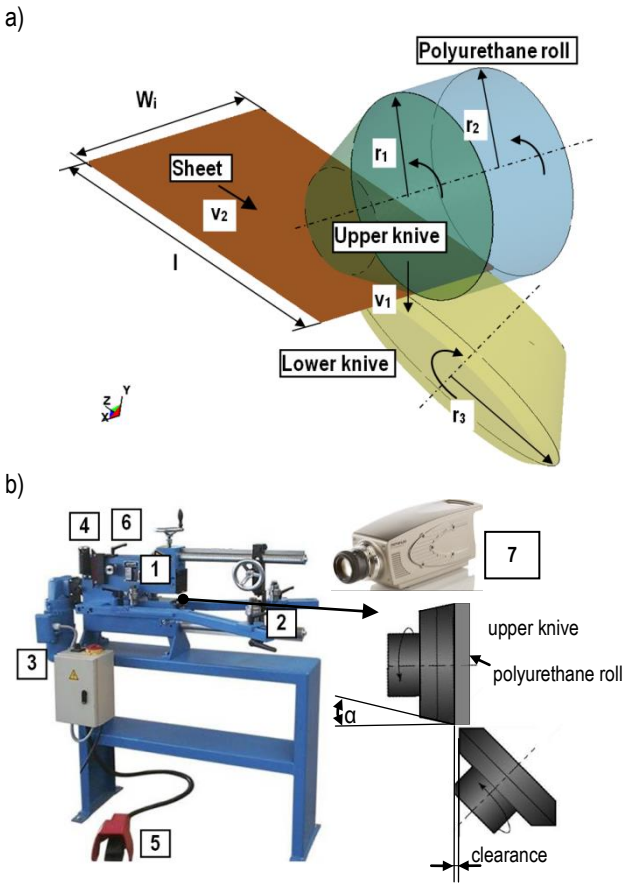

Fig. 2. a) SPH simulation model of shear slitting process, b) experimental test stand: 1 – knives, 2 – sheet holder, 3 – engine, 4 – clearance regulator, 5 – drive pedal, 6 – slitting velocity regulator, 7 – high-speed camera

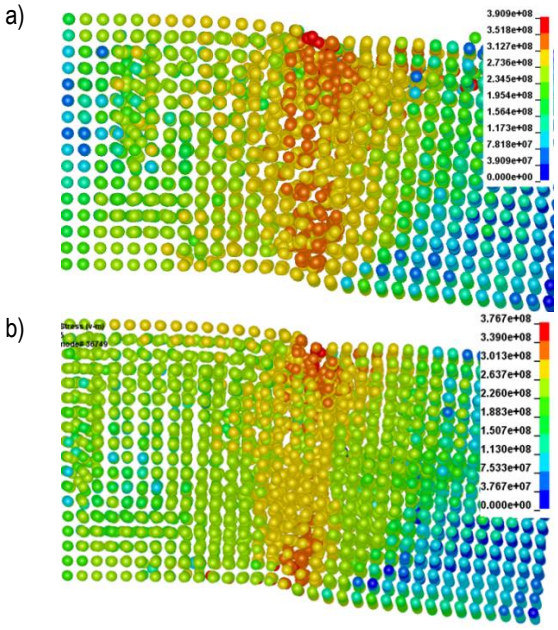

Fig. 3. Stress intensity distribution in plastic flow phase of the process for different initial particle density: a) d_2 = 0.02 mm, b) d_3 = 0.016 mm

DOI 10.1515/ama-2017-0052

An initial particle density of d_4 = 0.014 mm is selected as a optimal SPH particle density for used model dimensions. This initial particle density is selected so as to have a reasonable number of particles at the thickness of the sheet (Fig. 3). Larger density does not illustrate the material flow features and stress distributions appropriately becouse the material consist of many empty spaces beetwen particles (Fig. 3a). Smaller initial particle density strongly increase the computing time. Stabilization of the stress distribution, its values and slitting force in each time step is reached when $d \leq 0.014$ mm.

From our previous researches it's clear that changing the values of smoothing length between h = 1.05 ÷ 1.3 (recommended by solver options) has a small influence on stress distribution, its values and deformation state (Bohdal, 2016). Higher values of smoothing length strongly increase the simulation time, without significant effect on maximum stress variables and deformation state during process. For presented analyses in this paper a value of h = 1.2 is used.

5. SIMULATION RESULTS

5.1. Analysis of slitting mechanism

Proposed method using advanced vision based system allows for analysis of states of deformations in cutting area, propagation of cracking and analysis of its trajectory. An analysis of areas of high displacements and strains taking into account geometrical and physical nonlinearities of the process is possible.

Example results are given at Figs. 4 – 7.

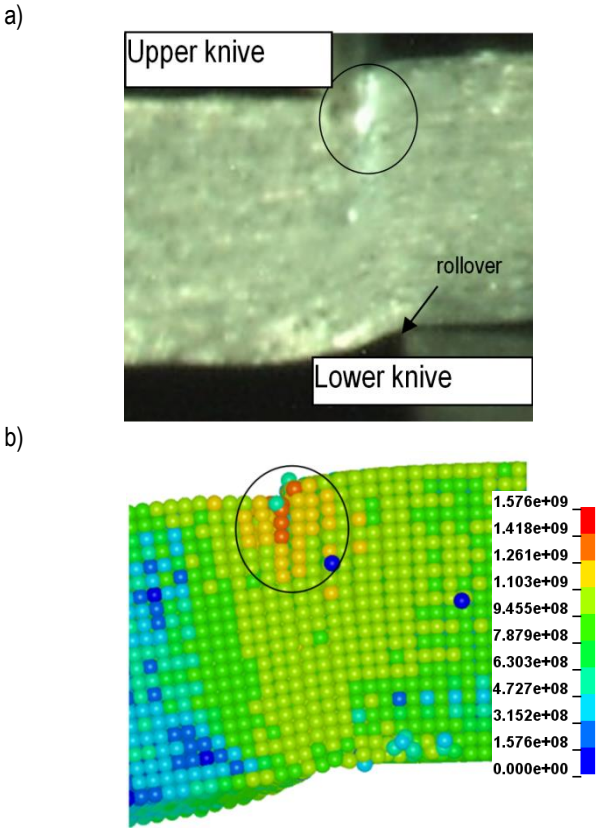

Fig. 4. Elastoplastic phase of the slitting process: a) image from camera, b) SPH simulation (equivalent stress distribution)

During the slitting process four main phases can be observed: elastic, elastoplastic, elastoplastic in which damage occurs, initiation and propagation of cracks leading to final rapture. During the first part of the process at crack front area, the upper and lower knives indent the sheet, pulling down some surface material. The greatest deformation of material occurs near the cutting edges of the tools in this phase (Fig. 4). First step of formation of rollover can be observed.

During the second phase the intensive plastic flow of the material in the surroundings of the cutting surface can be observed (Fig. 5a). A characteristic distortion of SPH particles in this areas can be seen (Fig. 5b). Both in numerical model and experimental investigations the plastic strain localization zones propagate much faster from the lower knive blade than from the upper knive (Figs. 5a, b). The deformation zone is non-symmetric with respect to the top and bottom knives. It can be observed the large distortions of the SPH particles near the bottom edge of sheet just before burr formation (Fig. 5b). The mechanically affected zone in this area is extended along the x direction. Since the crack will initiate and propagate through the localization zone, the cut surface will be curved and the burr will form because the crack will not run to the bottom blade tip (Fig. 5c). Comparison of the characteristic features of material separation geometry obtained from numerical model and experiment shows good agreement in the length of burnished and rollover areas (Fig. 5c). Some differences occur in the measurement of the fracture area, because in the SPH model moment of separation of material is delayed.

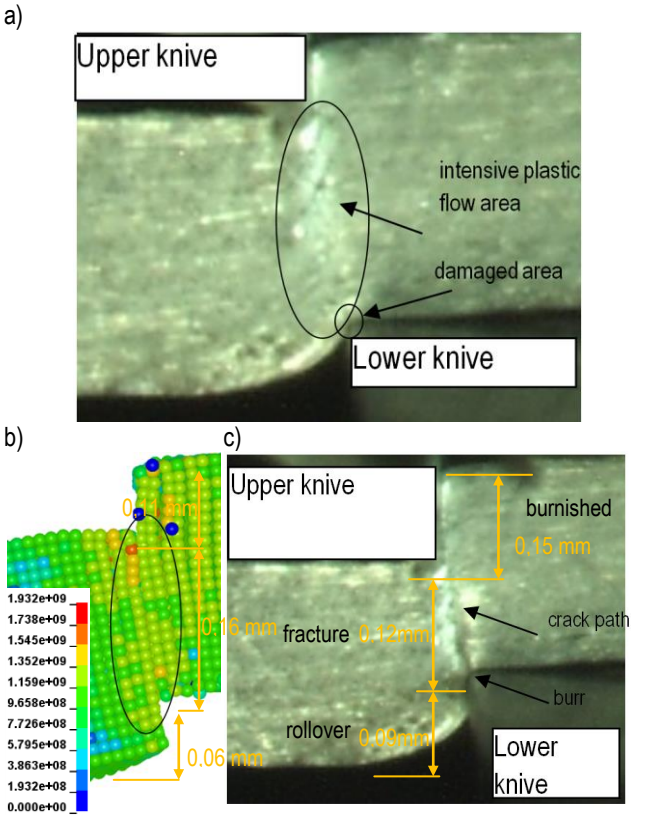

Fig. 5. Elastoplastic phase in which damage occurs: a) image from camera, b) SPH simulation (equivalent stress distribution), c) image from camera with visible initiation and propagation of cracks

DOI 10.1515/ama-2017-0052

As the sheet slits, it moves tangentially to the blade (Fig. 6). This causes the area of contact with the knive blade on the sheet to be inclined to the horizontal at an angle. It can be seen that the stresses form some bending moments. The sheet is bent twice to conform to the shape of the knives (Fig. 6a). The highest equivalent stress appears in the primary deformation zone, and a large plastic deformation also exists around this zone. A characteristic shear stress distribution extended along the *x* direction is observed under the upper knive edge (Figs. 6a and b). At the final stage of the process the tool - sheet contact zone is reduced (Fig. 6c). The bending moment increases which may cause rapture of the material at the end of the shearing line and burr formation.

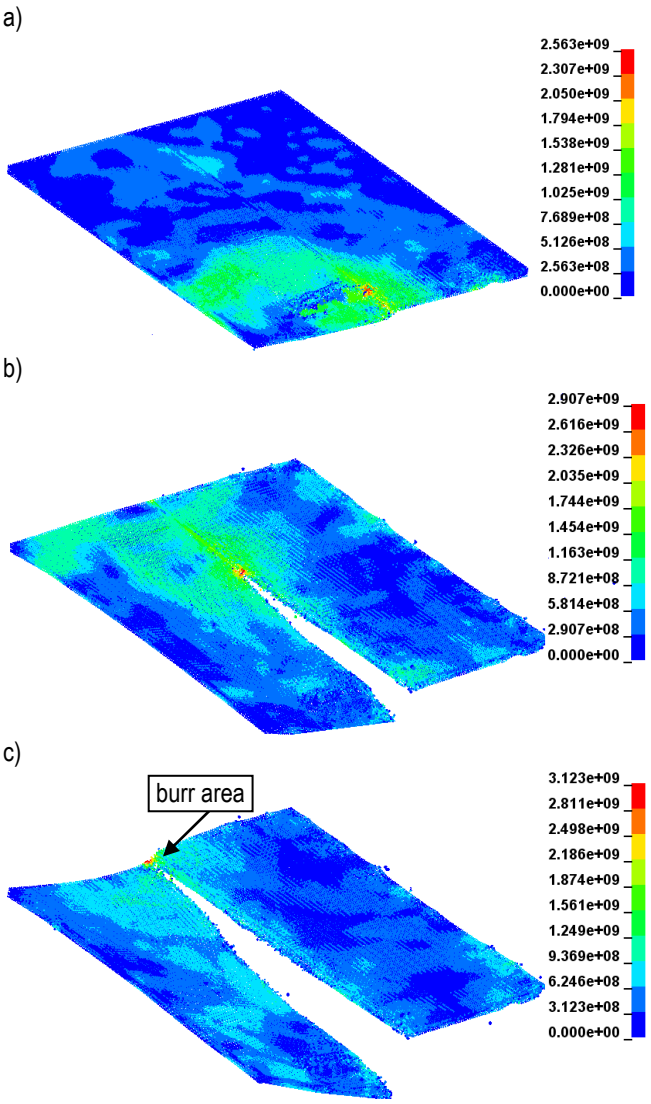

Fig. 6. Equivalent stress distribution in various stages of process: a) 5% step time, b) 60% step time, c) 95% step time

5.2. Parametric study

In this section, we illustrate the present solution procedure's capability to reproduce the effects of chosen process technological parameters such as the rake angle of the upper knive α, and clearance hc on the mechanically affected zone on workpiece. According to works (Meehan and Burns, 1996; TeNyenhuis et al., 2000; Pluta et al., 2004; Chodor and Kukielka, 2007; Chodor and Kukielka, 2014; Kulakowska et al., 2014) the deformation-affected zone after cutting process extends to several millimeters away from the cut edge and possibly occupies the entire sample volume. Thus, understanding the local degradation of the material due to the cutting process is crucial for improving the fabrication process and also for the design and simulation of electrical machines.

The computer simulations and experiments are executed for different rake angle values of $\alpha = 5 \div 40^{\circ}$, and clearance values of $h_c = 0.02 \div 0.1$ mm. Figure 7 shows the influence of analyzed process parameters on the extend of deformation affected zone. As the horizontal clearance increases, the deformation affected zone increases. The maximum width of deformation affected zone was found using a horizontal clearance of $h_c = 0.1$ mm. Reducing the clearance to $h_c = 0.02$ mm significantly reduced the affected zone for used rake angles. Unfavourable deformation conditions occur when the rake angle is set to the middle range (20 - 25°). The width of deformation affected zone carry out then approximately 170 - 190 μm. Increasing the rake angle from α = 25° to α = 40° significantly reduces this area at the analysed velocities and vertical clearances.

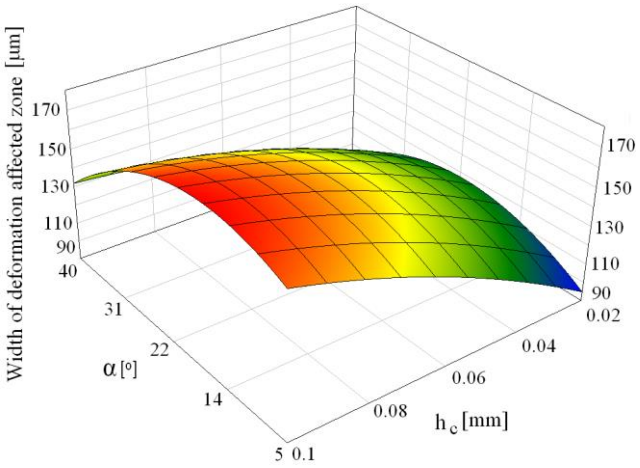

Fig. 7. Influence of rake angle α and clearance h_c on the width of deformation affected zone

6. CONCLUSIONS

The paper presents a possibility to apply the mesh-free SPH method for the analysis of the shear slitting operation. The objective of this study was to develop a three-dimensional model of the slitting process of grain oriented electrical steel. This model should provide insight into this process, which can be used to improve the quality and productivity of slitting. Obtained results showed a significant effect of selected process parameters on the residual stresses and width of deformation affected zone on workpiece. Knowledge about residuals stresses and deformation zone is very important in designing process. The good agreement between simulation results and the experimental data have confirmed the correctness and credibility of the model. Actual investigations concern the analysis of slitting parameters both on residual stress fields and magnetic properties of electrical steels. In modeling using SPH further work is still to be done in order to introduce some other effects concerning the behavior of the rolled metal sheets as the damage induced anisotropy and the springback effects.

REFERENCES

1. **Bagci E.** (2011), 3-D numerical analysis of orthogonal cutting process via mesh-free method, *International Journal of Physical Sciences*, 6, 1267-1282.
2. **Bohdal L.** (2016), The application of the smoothed particle hydrodynamics (SPH) method to the simulation and analysis of blanking process, *Mechanika*, 22(5), 380-387.
3. **Bohdal Ł., Gontarz S., Kukiełka L., Radkowski S.** (2015), Modeling of residual stresses induced in shear slitting of grain oriented silicon steel using SPH method, *Intelligent Methods in Surface Forming*. Gorzów Wlkp. – Poznań, 13-25 (In Polish).
4. **Chodor J., Kukielka L.** (2007), Numerical analysis of chip formation during machining for different value of failure strain*, PAMM* 7 (1), 4030031-4030032.
5. **Chodor J., Kukielka L.** (2014), Using nonlinear contact mechanics in process of tool edge movement on deformable body to analysis of cutting and sliding burnishing processes, *Applied Mechanics and Materials,* 474, 339-344.
6. **Gałęzia A., Gontarz S., Jasiński M., Mączak J., Radkowski S., Seńko J.** (2012), Distributed system for monitoring of the large scale infrastructure structures based on analysis of changes of its static and dynamic properties, *Key Engineering Materials*, 518, 106-118.
7. **Gąsiorek D.** (2013), The application of the smoothed particle hydrodynamics (SPH) method and the experimental verification of cutting of sheet metal bundles using a guillotine, *Journal of Theoretical and Applied Mechanics,* 51(4), 1053-1065.
8. **Gingold RA., Monaghan JJ.** (1977), Smooth particle hydrodynamics: theory and application to non-spherical stars, *Monthly Notices of the Royal Astronomical Society*, 181, 375-389.
9. **Godec Z.** (1977), Influence of Slitting on Core Losses and Magnetization Curve of Grain Oriented Electrical Steels, *IEEE Trans. Magn.,* 13 (4), 1053-1057.
10. **Golovashchenko S.F.** (2006), A study on trimming of aluminum autobody sheet and development of a new robust process eliminating burrs and slivers, *International Journal of Mechanical Sciences*, 48, 1384-1400.
11. **Gontarz S., Radkowski S**. (2012), Impact of various factors on relationships between stress and eigen magnetic field in a steel specimen. Magnetics, *IEEE Transactions on,* 48 (3), 1143-1154.
12. **Heisel U., Zaloga W., Krivoruchko D., Storchak M., Goloborodko L.** (2013), Modelling of orthogonal cutting processes with the method of smoothed particle hydrodynamics, *Production Engineering Research and Development*, 7, 639-645.
13. **Jianming W., Feihong L., Feng Y., Gang Z.** (2011), Shot peening simulation based on SPH method, *International Journal of Advanced Manufacturing Technology*, 56, 571-578.
14. **Johnson G.R., Cook W.H.** (1985), Fracture characteristics of three metals subjected to various strains, strain rates, temperatures and pressures, *Engineering Fracture Mechanics,* 21(1), 31-48.
15. **Kałduński P., Kukiełka L.** (2007), The numerical analysis of the influence of the blankholder force and the friction coefficient on the value of the drawing force, *PAMM* 7 (1), 4010045-4010046.
16. **Kałduński P., Kukiełka L.** (2008), The sensitivity analysis of the drawpiece response on the finite element shape parameter, *PAMM* 8 (1), 10725-10726.
17. **Kukielka L., Kulakowska A., Patyk R.** (2010), Numerical modeling and simulation of the movable contact tool-worpiece and application in technological processes, *Journal of Systemics, Cybernetics and Informatics*, 8/3, 36-41.
18. **Kulakowska A., Patyk R., Bohdal Ł.** (2014), Application of burnishing process in creating environmental product, *Annual Set The Environment Protection*, 16, 323-335 (In Polish).
19. **Meehan R. R., Burns S. J**. (1996), Mechanics of slitting and cutting webs, *Experimental Mechanics* 38, 103-109.
20. **Pluta W., Kitz E., Krismanic G., Rygal R., Soinski M., Pfützner H**. (2004), Rotational power loss measurement of Fe based soft magnetic materials; *Poster: 2DM 1&2 Dimensional Magnetic Measurement and Testing,* Ghent University; 27.09.2004 - 28.09.2004; in: 8th International Workshop on 1&2 Dimensional Magnetic Measurement and Testing, S. 9.E.
21. **TeNyenhuis E., Girgis R.** (2000), Effect of slitting electrical core steel on measured iron loss. *Journal of Magnetism and Magnetic Materials,* 215-216, 110-111.

ABSTRACTS

Łukasz Jastrzębski, Bogdan Sapiński
Experimental Investigation of an Automotive Magnetorheological Shock Absorber

The study summarises the experimental examination of an automotive magnetorheological (MR) shock absorber under electrical and mechanical excitations, investigates its current and force responses and the energy dissipation in the system. The aim of experiments was to acquire measurement data that allows in next step of the research program to engineer an energy harvesting device for the absorber. The work covers basic technical data of the absorber, description of the experimental set-up, scenario of testing program and test results of the device. Of particular importance is the influence the operating current, piston displacement amplitude and piston velocity have on the absorber's response.

Aleksandr Blokhin, Arcadiy Nedyalkov, Lev Barakhtanov, Aleksandr Taratorkin, Abram Kropp
Multistage Mechanical Transmissions with Automatic Control for Advanced Trucks and Buses

The study considers the basic trends of development of modern mechanical transmissions of trucks and buses. It provides the developed various series of multispeed transmissions with automatic control and a number of transmissions from 6 to 16 for trucks and buses. The paper shows the basic parameters of the standard series of new transmissions received on the basis of innovative technical solutions. It provides the results of experimental studies of 16-speed transmissions on a special test stand and on the road as part of a truck transmission. Theoretical and experimental data on the gear change time are compared.

Paweł Skalski, Klaudia Kalita
Role of Magnetorheological Fluids and Elastomers in Today's World

This paper explains the role of magnetorheological fluids and elastomers in today's world. A review of applications of magnetorheological fluids and elastomers in devices and machines is presented. Magnetorheological fluids and elastomers belong to the smart materials family. Properties of magnetorheological fluids and elastomers can be controlled by a magnetic field. Compared with magnetorheological fluids, magnetorheological elastomers overcome the problems accompanying applications of MR fluids, such as sedimentation, sealing issues and environmental contamination. Magnetorheological fluids and elastomers, due to their ability of dampening vibrations in the presence of a controlled magnetic field, have great potential present and future applications in transport. Magnetorheological fluids are used e.g. dampers, shock absorbers, clutches and brakes. Magnetorheological dampers and magnetorheological shock absorbers are applied e.g. in damping control, in the operation of buildings and bridges, as well as in damping of high-tension wires. In the automotive industry, new solutions involving magnetorheological elastomer are increasingly patented e.g. adaptive system of energy absorption, system of magnetically dissociable [hooks/detents/grips], an vibration reduction system of the car's drive shaft. The application of magnetorheological elastomer in the aviation structure is presented as well.

Mojtaba Biglar, Magdalena Gromada, Feliks Stachowicz, Tomasz Trzepieciński
Synthesis of Barium Titanate Piezoelectric Ceramics for Multilayer Actuators (MLAs)

In this paper the characteristics of BaTiO3 ceramics synthesized by solid state method is presented. In order to receive the monophase ceramics the double activation and calcination were applied. A spray drier was used to granulate the powder of BaTiO3. Isostatic and uniaxial pressing were applied to manufacture the barium titanate pellets. The properties of fabricated BaTiO3 ceramics were determined at different stages of production. After the sintering phase, the hardness, the bending strength, the fracture toughness, and the coefficient of thermal expansion of barium titanate sinter were estimated. The BaTiO3 powder is characterized by spherical grains and the average size of 0.5 μm. The small value of the specific surface area of granulate ensured good properties of material mouldability and finally allowed to receive sinters of high density.

Katarzyna Topczewska
Thermal Stresses Due to Frictional Heating with Time-Dependent Specific Power of Friction

In this paper influence of temporal profile of the specific friction power (i.e. the product of the coefficient of friction, sliding velocity and contact pressure) on thermal stresses in a friction element during braking was investigated. Spatio-temporal distributions of thermal stresses were analytically determined for a subsurface layer of the friction element, based on the model of thermal bending of a thick plate with unfixed edges (Timoshenko and Goodier , 1970). To conduct calculations, the fields of dimensionless temperature were used. These fields were received in the article (Topczewska, 2017) as solutions to a one-dimensional boundary-value problem of heat conduction for a semi-space heated on its outer surface by fictional heat flux with three, different time profiles of the friction power.

Oleg Ardatov, Algirdas Maknickas, Vidmantas Alekna, Marija Tamulaitienė, Rimantas Kačianauskas
The Finite Element Analysis of Osteoporotic Lumbar Vertebral Body by Influence of Trabecular Bone Apparent Density and Thickness of Cortical Shell

Osteoporosis causes the bone mass loss and increased fracture risk. This paper presents the modelling of osteoporotic human lumbar vertebrae L1 by employing finite elements method (FEM). The isolated inhomogeneous vertebral body is composed by cortical outer shell and cancellous bone. The level of osteoporotic contribution is characterised by reducing the thickness of cortical shell and elasticity modulus of cancellous bone using power-law dependence with apparent density. The strength parameters are evaluated on the basis of von Mises-Hencky yield criterion. Parametric study of osteoporotic degradation contains the static and nonlinear dynamic analysis of stresses that occur due to physiological load. Results of our investigation are presented in terms of nonlinear interdependence between stress and external load.

Alok Dhaundiyal, Suraj B. Singh
Asymptotic Approximations to the Non- Isothermal Distributed Activation Energy Model for Biomass Pyrolysis

This paper describes the influence of some parameters significant to biomass pyrolysis on the numerical solutions of the non-isothermal nth order distributed activation energy model (DAEM) using the Gamma distribution and discusses the special case for the positive integer value of the scale parameter (λ), i.e. the Erlang distribution. Investigated parameters are the integral upper limit, the frequency factor, the heating rate, the reaction order, and the shape and rate parameters of the Gamma distribution. Influence of these parameters has been considered for the determination of the kinetic parameters of the non-isothermal nth order Gamma distribution from the experimentally derived thermoanalytical data of biomass pyrolysis. Mathematically, the effect of parameters on numerical solution is also used for predicting the behaviour of the unpyrolysized fraction of biomass with respect to temperature. Analysis of the mathematical model is based upon asymptotic expansions, which leads to the systematic methods for efficient way to determine the accurate approximations. The proposed method, therefore, provides a rapid and highly effective way for estimating the kinetic parameters and the distribution of activation energies.

acta mechanica et automatica, vol.11 no.4 (2017)

Andrzej Waindok, Paweł Piekielny
Transient Analysis of a Railgun with Permanent Magnets Support

The calculation and measurement results of transients for an electrodynamic accelerator with permanent magnet support have been presented in this paper. The calculations have been made using the magnetostatic model in the Maxwell software, as well as using a Matlab/Simulink transient model. The waves of mechanical parameters (projectile velocity and acceleration, force) and electric ones (excitation current and capacitor voltage) have been analyzed for different supply conditions (voltage value, capacitance). The efficiency and projectile energy have been studied as well. The mathematical models have been verified experimentally using the original laboratory stand. A good conformity between calculation and measurement results has been obtained.

Iaroslav Pasternak, Heorhiy Sulym
Boundary Element Analysis of Anisotropic Thermomagnetoelectroelastic Solids with 3D Shell-Like Inclusions

The paper presents novel boundary element technique for analysis of anisotropic thermomagnetoelectroelastic solids containing cracks and thin shell-like soft inclusions. Dual boundary integral equations of heat conduction and thermomagnetoelectroelasticity are derived, which do not contain volume integrals in the absence of distributed body heat and extended body forces. Models of 3D soft thermomagnetoelectroelastic thin inclusions are adopted. The issues on the boundary element solution of obtained equations are discussed. The efficient techniques for numerical evaluation of kernels and singular and hypersingular integrals are discussed. Nonlinear polynomial mappings are adopted for smoothing the integrand at the inclusion's front, which is advantageous for accurate evaluation of field intensity factors. Special shape functions are introduced, which account for a square-root singularity of extended stress and heat flux at the inclusion's front. Numerical example is presented.

Jan Górecki, Ireneusz Malujda, Krzysztof Talaśka, Dominik Wojtkowiak
Dry Ice Compaction in Piston Extrusion Process

The article presents the results of research on the effect of extrusion tube geometry on the axial force being the key parameter of the dry ice piston extrusion process. The tests were carried out with the experimental set-up based on a cylindrical extrusion tube used alone and supplemented with reducer (orifice). The focus of the experiments was to determine the effect of compression tube reducer on the value of the force of resistance FOP in the dry ice compression process. Its value can subsequently be used as the basis for establishing guidelines for designing and building machines for compression and pelletizing of dry ice.

Artur Prusinowski, Roman Kaczyński
Simulaton of Processes Occurring in the Extrusion Head Used in Additive Manufacturing Technology

The purpose of this research is unsatisfactory state of knowledge of the abrasive wear of composites with thermoplastic polymer as matrix material and reinforcing material in the form of short and focused carbon fibers that can be used in additive manufacturing technologies. The paper presents a conceptual design of an extrusion head used in Fused Deposition Technology, which allows for the implementation of appropriately stacked fibers at the level of detail production. Finite element simulation was performed to simulate the thermal effect of the system to demonstrate the effect of head cooling on the system. The assumed extrusion temperature of the material was obtained at a uniform nozzle temperature and stable temperature of the entire system. Flow simulation of thermoplastic polymer was carried out in the designed extrusion nozzle. By supplying 0.5 mm wire of 1.75 mm diameter thermoplastic material to the nozzle, the extrusion rate was 0.192 m/s. The proper design of the extrusion head for the intended applications has been demonstrated and the purpose of further research in this field has been confirmed.

Marta Góra-Maniowska, Józef Knapczyk
Displacement Analysis of the Human Knee Joint Based on the Spatial Kinematic Model by Using Vector Method

Kinematic model of the human knee joint, considered as one-degree-of-freedom spatial parallel mechanism, is used to analyse the spatial displacement of the femur with respect to the tibia. The articular surfaces of femoral and tibia condyles are modelled, based on selected references, as spherical and planar surfaces. The condyles are contacted in two points and are guided by three ligaments modelled as binary links with constant lengths. In particular, the mechanism position problem is solved by using the vector method. The obtained kinematic characteristics are adequate to the experimental results presented in the literature. Additionally, the screw displacements of relative motion in the knee joint model are determined.

Andrzej Milecki, Roman Regulski
Washing Machine Controller with a New Programming

In the paper the newly designed at Poznan University of Technology (PUT) washing machine controller is presented. The commonly used in washing machines sensors, drives and other input-output elements are briefly described. The designed at PUT controller is based on 32-bit STM32 microcontroller. The used in this controller modules are described and their input/output signals and basics of operations are presented. The developed in the controller user-machine communication devices, elements and methods are described. The paper presents new washing machine programming methods and implementation software, such as voice recognition and intelligent programming of washing machine that were applied in the new controller.

Łukasz Bohdal, Katarzyna Tandecka, Paweł Kałduński
Numerical Simulation of Shear Slitting Process of Grain Oriented Silicon Steel using SPH Method

Mechanical cutting allows separating of sheet material at low cost and therefore remains the most popular way to produce laminations for electrical machines and transformers. However, recent investigations revealed the deteriorating effect of cutting on the magnetic properties of the material close to the cut edge. The deformations generate elastic stresses in zones adjacent to the area of plastically deformed and strongly affect the magnetic properties. The knowledge about residual stresses is necessary in designing the process. This paper presents the new apprach of modeling residual stresses induced in shear slitting of grain oriented electrical steel using mesh-free method. The applications of SPH (Smoothed Particle Hydrodynamics) methodology to the simulation and analysis of 3D shear slitting process is presented. In experimental studies, an advanced vision-based technology based on digital image correlation (DIC) for monitoring the cutting process is used.